(10)

Liquid Dynamic Compaction Spray Deposition of Commercial and Modified 3003 Al-Alloy: Process Application and Materials Characterization

by

Ali M. Farah

B.S. Mechanical Engineering, Somali National University (1985)
M.S. Materials Engineering, American University in Cairo (1989)

Submitted to the Department of
Materials Science and Engineering in Partial
Fulfillment of the Requirements for the Degree of

DOCTOR OF SCIENCE IN MATERIALS ENGINEERING
at the
MASSACHUSETTS INSTITUTE OF TECHNOLOGY

June 1996

Signature of Author____________________________________
Department of Materials Science and Engineering
May 3, 1996

Certified by____________________________________
Professor Nicholas J. Grant
Professor of Metallurgy
Thesis Supervisor

Accepted by____________________________________
Professor Michael F. Rubner, Chairman
TDK Professor of Materials Science and Engineering
Chair, Departmental Committee on Graduate Students

Liquid Dynamic Compaction Spray Deposition of Commercial and Modified 3003 Al-Alloy: Process Application and Materials Characterization.

by

Ali M. Farah

Submitted to the Department of Materials Science and Engineering
On May 3, 1996 in partial fulfillment of the requirements for the
Degree of Doctor of Science in Materials Engineering

Abstract

The Liquid Dynamic Compaction (LDC) rapid solidification process was applied on the production of 3003 Al-alloy sheets using new, linear, ultrasonic gas atomizers (USGA). A modified 3003 alloy (Al-1Mn-2Mg-1.5Cu-1.7Fe-1.7Si) was also atomized to investigate the increased tolerance to impurity elements imparted by this process and its applicability to scrap recycling. The effects of the modified gas delivery design of the new atomizers on the uniformity of the aspiration pressure along the length of the melt exit, and on the deposit thickness profile, were studied. The effects of the aspiration pressure and the atomization gas pressure on the melt atomization efficiency, the deposit microstructure, and the deposit thickness profile were also studied. The alloys were atomized with nitrogen and spray deposited on a grit-blasted mild steel substrate producing as-deposited grain sizes of 20 - 50 μm and densities of 95±4%. The deposits were rolled at temperatures from 25 to 500°C and annealed at various temperatures and times. Selected samples from both alloys were homogenized at 600°C for 8 hours prior to the rolling. Optical microscopy and TEM studies showed that the samples did not completely recrystallize, even when annealed at 500°C for 5 hours, and microstructures ranging from fine equiaxed (15 μm to 40 μm) grains, to elongated grains were observed. Depending on the rolling and annealing temperatures and times, the commercial 3003 Al-alloy possessed high yield strength, tensile strength and elongations (31 ksi, 40 ksi, and 32%, respectively), whereas the modified alloy had 33 ksi, 43 ksi and 18%, respectively. Although the specimens of the modified alloy had good elongations, its tensile specimens failed without necking. The homogenization treatment was observed to reduce the tensile properties of these alloys to values comparable to those of commercial ingot metallurgy 3003 Al-alloy.

Thesis Supervisor: Nicholas J. Grant, Professor of Metallurgy

Table of Contents

List of Figures

List of Tables

ACKNOWLEDGEMENTS

I would like to express my deeply felt gratitude to a number of people who helped me reach this stage of life and complete this thesis. My sincere thanks goes to Professor Nicholas J. Grant for his invaluable and continuous guidance, support, and encouragement. You have been an inspiration. I am also thankful to the other members of my thesis committee, Professor August Witt, Professor Andreas Mortensen and Professor David Dunand, for their advices and recommendations.

My special thanks goes ALCOA, whose cooperative agreement with DOE (DE-SC07-94ID13233) funded this research, and the King Faisal Foundation of the Kingdom of Saudi Arabia, whose fellowship I was privileged and honored to have received.

No words can express my gratitude toward my great friends, Daniele Marzaro, Peter Vrooman, and their families, without whose support I would not be here to pursue this degree. There were also many other wonderful people, who helped in my long journey toward this degree: Mr. Abdirashid Abdi Gire and his family, Ms. Carol Emert, Dean Isaac Colbert, Dr. Ralph Mason, Dr. Ibrahim Ücok, Mr. Mike Zody, Dr. Teiichi Ando, Dr. Saturo Matsuo, Dr. Xiaoman Duan, Ms. Elaine Tirrell, Ms. Kate Berkman Dr. Nam Hoe, Mr. Bill Chernicoff, Mr. Joshua Bennett, Mr. Holly Gates, Mr. Ryan Kershner, Mr. Pat Kearney, Mr. Fred Wilson, Mr. Guenther Ardt, Ms. Yin-Lin Xie, Mr. Joseph Adario and Mr. Michael Frongillo. To these friends and all the others I may have forgotten to mention here, I extend my special thanks and best wishes.

Last but not the least, I am extremely grateful to have had a wonderful, supporting and loving family. To my mother, Asli Olad; my wife, Jolanda Farah; my late father; Mohamed Farah, My step Father, Abdi Ahmed; and my numerous siblings and in-laws, I dedicate this thesis.

1. INTRODUCTION

In conventional ingot metallurgy (IM), the formation of large grains and severe segregation of alloying elements are attributed to the low solidification rates experienced in the large ingots. This characteristic structure has led to materials with inferior strength, toughness, corrosion resistance, stiffness, thermal stability, and other mechanical properties. In the 1970's, efforts were undertaken in the aluminum industry to improve on the IM technology. These efforts, which led to the development of high strength Al-alloys such as 7050 and 7475,[1] were primarily directed toward increased alloy content of elements such as Cu and Zn, new thermomechanical treatments (TMT), and reduced impurities from elements such as Fe and Si.[2] In wrought Al-alloys, metallic inclusions rich in Fe and Si, which are related to scrap practices and ingot solidification processing, are detrimental to the fracture toughness, fatigue life, formability and corrosion resistance of the alloys. However, improvements in IM alloys, by higher purity and/or additional TMT, are reaching a point of economic infeasibility because of increased processing costs.[3]

Rapid solidification (RS) processes are being introduced in order to achieve attractive combinations of structural control and improvements of mechanical properties, and to satisfy the critical needs for cost-effective structural materials with superior performance.[4] The properties attainable by RS processing are better than those of IM alloys due to sharply decreased segregation, the absence of coarse constituent phases and increased alloying capabilities, which permit unusual alloying potential.[3, 5, 6, 7, 8]

The majority of RS work have been directed toward the production of powders and powder metallurgy (PM) processing. PM processing requires handling and consolidation steps that are costly and hazardous. The improvements expected from the RS in PM technology have also been adversely effected by the formation of surface oxides that complicate powder consolidation and are later detrimental to the mechanical properties of the consolidated parts. To overcome these problems and maintain the advantages of RS, spray deposition (SD) techniques that produce consolidated preforms have been developed.[3, 9]

In the rapid solidification spray deposition (RS/SD) process, a molten metal stream is atomized into droplets. These droplets, while partially liquid, are deposited onto a cooled, high thermal conductivity surface to form deposits of different shapes. One of these RS processes is Liquid Dynamic Compaction (LDC), which was developed in the High Temperature Materials Laboratory of Professor N. J. Grant at MIT. This process is a simultaneous spray atomization and compaction process, where a molten stream of metal is atomized by a high velocity pulsed gas jet and the undercooled semi-solid droplets are compacted against a cold metallic substrate. Due to the small sizes of these droplets, high solidification rates in excess of 10^3 K/sec are achieved. And when the droplets deposit on the substrate, solid state cooling rates of 10 to 10^2 K/sec were recorded.[10, 11, 12, 13, 14]

By producing semi-finished products in one atomization step, the LDC rapid solidification process has the advantages of eliminating many processing steps, increasing production rates and lowering processing costs compared to the conventional IM and PM processes. The highly dense LDC products, which are formed in an inert atmosphere, have lowered oxidation levels of one to two magnitudes lower than that of PM (0.010 to 0.015 wt.%.) [15, 16]

A variety of alloys based on Fe, Al, Mg, Cu and other elements have been successfully produced with the LDC process to improve their physical and chemical properties. LDC deposits have shown a very fine equiaxed microstructures with uniformly distributed, fine second phases and increased solid solubility of alloying elements. The LDC application to Al-alloys has been focused on three areas: (a) room temperature high strength alloys, (b) low-density-high modulus alloys, and (c) high temperature high strength alloys.[194] These alloys are mostly precipitation and dispersion strengthened.

An ultrasonic gas atomization (USGA) nozzle, either circular or linear, is used in the LDC application. The linear type atomizer was developed to increase the production rate by either using one long nozzle or an assembly of multiple shorter ones. The nozzles can be arranged either in parallel or in series in order to increase the width or the thickness of the deposit. Hybrid layers of materials with different chemical composition can also be produced with series arrangements of the nozzles. The linear nozzle was developed more recently and has undergone improvements in its design and geometry to realize uniform atomization parameters across the length of its opening, in order to deposit a preform with more uniform thickness and reduced inherent Gaussian profile.

In this study, LDC processing parameters of a linear atomizer with new, gas feeding geometry and design were investigated. The aspiration pressure at the tip of the metal delivery slit created by different gas atomization pressures, the gas to metal flow ratio for optimal deposition rate, and the deposit thickness profiles were studied. The melt breakup, droplet sizes in the spray plume, and the overspray powder sizes and distribution were characterized as functions of the parameters of the new atomizers. Water and tin (for its low melting point) were used to simulate and optimize the process with the help of high speed photography. For the first time, the LDC process was applied on the 3003 low-alloyed work-hardenable high-tonnage commercial Al-alloy, since it was targeted by ALCOA as part of the LDC aluminum sheet production pilot plant. The thickness profile, deposit density, porosity shape and content, grain sizes, and rolling of this alloy were examined. The effect of temperature during rolling and annealing on the microstructure, and the mechanical properties of this alloy were investigated. To assess the tolerance for impurities in Al-alloys produced with LDC, the 3003 alloy was modified with the addition of Fe, Si, Cu, and Mg to Al-2.2Mg-1.75Si-1.7Fe-1.5Cu-1Mn composition. This alloy was then spray deposited, rolled, and its mechanical properties tested and compared to those of 3003 Al-alloy.

2. LITERATURE SURVEY

2.1 Rapid Solidification Technology (RST)

A minimum classification of a process as "rapid solidification" is an arbitrary minimum solidification rate of 10^2 °K/s, which excludes processes such as conventional continuous casting.[17] High cooling rates during solidification can be achieved by increasing the surface to volume ratio of the melt into powder, wire, ribbon and sheet forms. RST is well established as an effective means of reconstituting alloys by forming new phases, extending and modifying equilibrium phase fields and refining microstructures.[5] The aerospace and other industries are well aware of the potential for improvement through RST. [18]

Improvements achieved by RS processing include: avoidance of large dendritic, oriented structure, decreased grain size, extended solid solubility, refinement of the second phase particle sizes, increased chemical homogeneity by reducing segregation, elimination of large brittle constituent phases by replacing them with fine stoichiometric intermetallic compounds, and production of new metastable structures and amorphous phases.[8, 17, 19] These improvements led to increased strength, thermal stability, ductility, fatigue life, and corrosion resistance to pitting, exfoliation and stress corrosion cracking of the material.[4, 19, 20] In Figure 1, The secondary dendrite arm spacings and estimated solidification rates are plotted against the average particle sizes for various Al-alloy powders.[21] In Figure 2, the secondary dendrite arm spacing of high-speed steel versus its cooling rates for an atomization process (i.e. the consolidated spray deposition - CSD) is shown.[22]

Some of the RS processes are also near net shape forming technologies that save about 15-40% of the production cost by eliminating intermediate production and processing steps. In RS sheet forming processes, the first 10 large rolling stands in conventional IM sheet production can be eliminated.[9] There are different types of RS processes, some of which are based on melt spinning, splat quenching and atomization techniques.

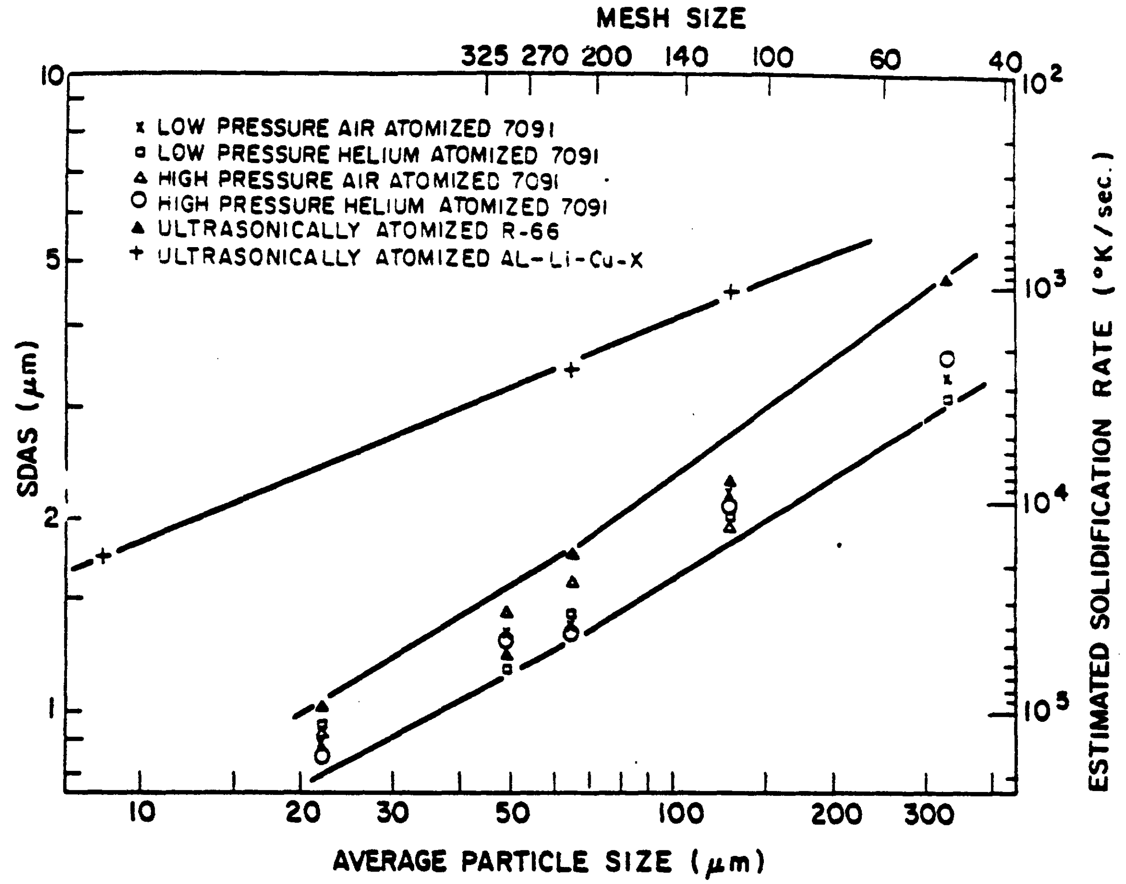

Figure 1. Secondary dendrite arm spacing (SDAS) or estimated solidification rate versus average particle size of various Al-alloy powders.[21]

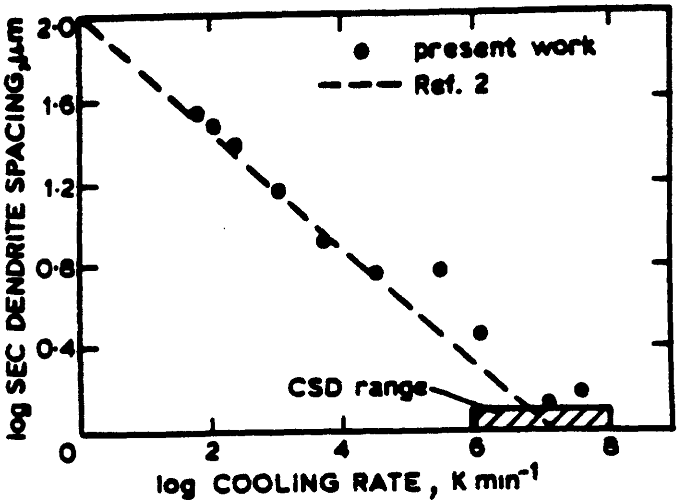

Figure 2. Measured dendrite arm spacing for M2 high-speed steel versus cooling rates during CSD processing.[22]

2.1.1 Atomization Processes

The atomization processes are flexible techniques that allow the production of a broad range of alloy compositions with extensive control over the structures and properties of the products.[3] These processes involve a forced breakup of a melt in flight into very fine droplets, which are either solidified in flight to produce powder or deposited into a shape before they completely solidify. The melt breakup takes place in one of three mechanisms: Liquid cylinder breakup, liquid film breakup, and liquid droplet breakup by additional interference. [23]

Atomization targets the production of particles (on average) in the range of 1000 μm to 1 μm sizes that can undergo high cooling rates. These cooling rates contribute to the formation of materials with homogeneous structures. Powder produced by atomization methods possess better characteristics in size, shape, cooling rate, and cleanliness compared to powder produced in other methods such as chemical reduction and mechanical grinding.[24] However, most of the atomization techniques are incapable of producing powders with narrow useful size distribution, thus lowering the yield of useful powder and increasing the cost of production.

Examples of atomization processes are: 1. Gas atomization 2. Water atomization, 3. Steam Atomization, 4. Centrifugal atomization, with numerous configurations (perforated rotating cup, rotating electrode, rotating cup and dish, Singer roll) 5. Vacuum atomization, 6. Vibrational atomization, etc.[18,24,25]

The predominant industrial methods of atomization are water, gas and centrifugal atomization.The centrifugal atomization produces acicular and tear-drop shaped powder with high production rates and cleanliness. Water atomization is associated with severe oxide formation and other reaction products in highly alloyed materials, which need additional drying and reduction steps. In gas atomization, air atomized powder is irregular in shape, while nitrogen, argon and helium form finer, spherical powder.[17, 24, 26] Gas atomized powder in the range of 45 to 200 μm sizes with production rates in the order of 50 Kg/min is produced at Hoeganaes, ALCOA and Special Metals.[24]

A general overview of the operating variables in various atomization process are discussed elsewhere,[27,28] and more detailed experimental studies of controlling variables are also available.[29-32]

2.1.1.1 Gas Atomization Processes

A rudimentary form of an atomization process was first patented in Germany in 1882 to produce lead powder used in accumulators.[33] Two American patents granted in 1924 and 1925 were based on a compressed gas atomization nozzle with the gas delivery annulus concentric with the metal delivery orifice.[3,34]

In conventional subsonic atomization, metal powder is produced in a three step melt breakup process, where the final powder formation is well removed from the point of gas/melt impingement. Collisions between the droplets by the inherent turbulent flow, wide range of droplets sizes, aided by the relatively low solidification rates of the process, cause the formation of heavy satellite population and coalesced droplets.[8,35-39] In ultrasonic gas atomization, studies by means of high speed cameras and video machines point to a single step atomization process. The formation of satellites is reduced by the high solidification rates, which reduce the number of collisions that can take place before the droplets are completely solidified.[3,40]

2.1.2 Rapid Solidification Powder Metallurgy (RS/PM)

Powder metallurgy has found many applications in the field of hard metal cutting tools such as tungsten carbide that can not be machined to shape. RS/PM powders solidify at rates between 10 to 10^5 °K/s, producing grain sizes in the micron to submicron ranges.[17] Fine Al-Alloy powders produced in the Swedish Institute for Metal Research had an average diameter of 9 μm with

97% of the powder smaller than 50 μm, while the powder of a ferritic alloy had an average diameter of 26 μm and 86% of it was less than 50 μm in size.[41] Sometimes amorphous powders can be produced at higher cooling rates, for example $Cu_{0.6}Zr_{0.4}$ USGA powder, where powder of 60 μm or less were fully amorphous.[42] Cu-Zr and Fe-B alloys were also atomized to amorphous powders.[43] Figure 3 shows cumulative and differential particle size distribution of $Cu_{0.6}Zr_{0.4}$ powder and the powder size range for amorphous , mixed, or microcrystalline phase formation.[42]

Ideally RS/PM should provide high quench rates (>10^3 K/sec), high productivity, spherical shaped particles to reduce surface area and oxygen contamination, and controllable powder size distribution.[3,24] The solidification rates, the atomization gas type and pressure, and atomization environment control the shape, size and size distribution of the powder, which, in turn, determine the compressibility, forgibility, and toughness of the final product.[44] Figure 4 shows droplet solidification time-dependency on the droplet diameter and atomization gas type of an aluminum alloy.[45] The powder is consolidated into fully dense bars, plates, sheets, strip and other shapes. The consolidation steps include: cold compaction (60-80% density), vacuum degassing, and hot compaction to full density. These steps, which involve canning, decanning, hot pressing, extruding, forging, and powder milling, are recipes for high production cost.

The fracture toughness of Al-Cu-Li alloys prepared by PM was seen to be lower than that of IM processed alloys.[46] However , in terms of fatigue behavior, the S-N data from smooth specimens prepared from 7XXX PM extrusions equaled and sometimes exceeded those of the corresponding IM material. The fine constituent particle sizes and the much finer grain sizes achieved in PM processing are believed to be the primary reasons for the increase in resistance to crack initiation.[3,47- 51]

Satellite formation in powder metallurgy is one of the problems that hinders initial separation of the powder and their later consolidation. Gas entrapment in the droplets and easy oxidation of powders with Mg, Al, Li, Si, Ti,

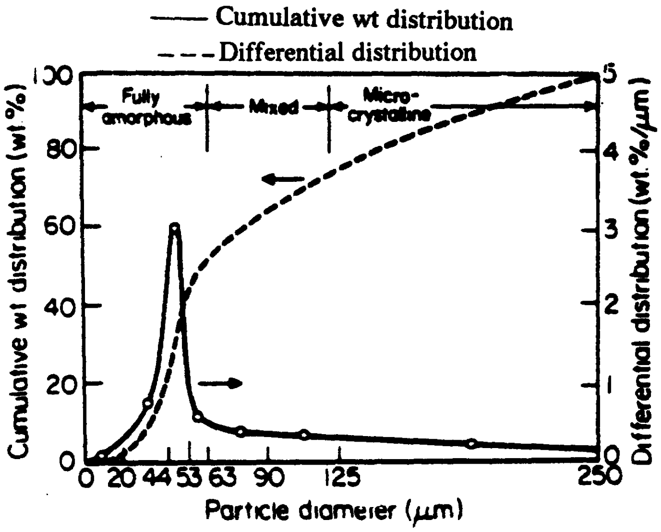

Figure 3. Cumulative and differential particle size distribution of $Cu_{0.6}Zr_{0.4}$ powder, and the range of amorphous phase formation.[42]

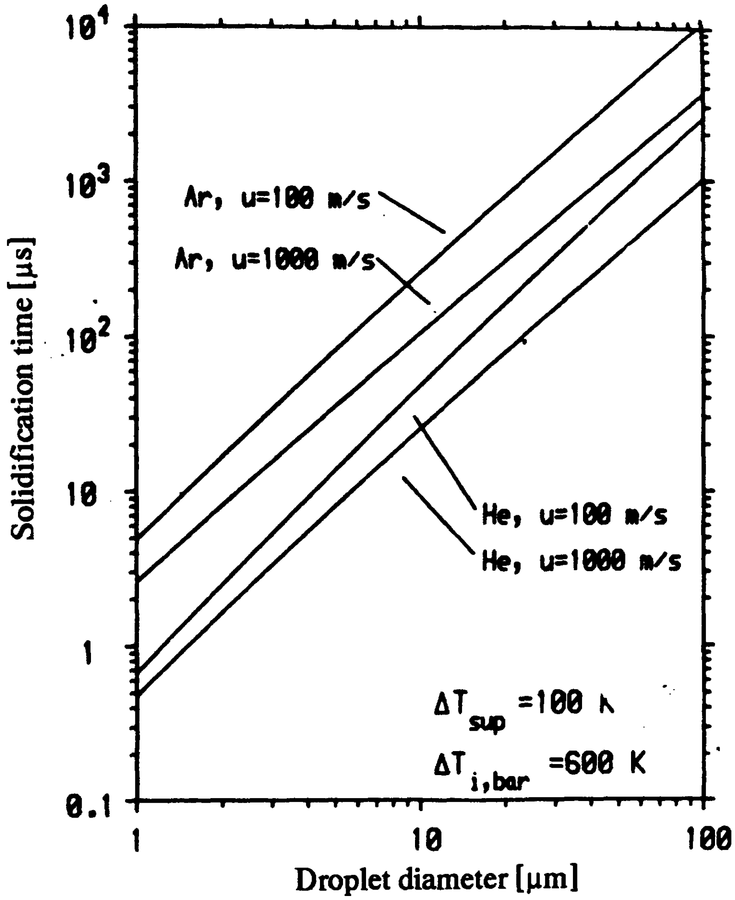

Figure 4. Predicted dependence of droplet freezing time on powder diameter, for aluminum atomization with He and Ar.[45]

Zr, Hf, Be, V, and rare earth elements are other factors that limit the commercialization of RS/PM techniques.[18] Air atomized powder was not spherical and contained about 0.38% oxygen. Table 1 lists the oxide content of several alloys processed with various PM techniques.[3] These oxides are detrimental to crack initiation and growth resistance, fracture toughness, pitting corrosion, and magnetic characteristics of the product.[52-55] Crack nucleation at the continuous oxide film along prior flake boundaries, in splat cooled flakes of Al-Li-Cu, alloys was observed.[56] These oxides films and stringers also serve as paths for easy crack growth. When powders that contained hydrates were compacted and treated in the range of 500°C, the hydrates broke down and coarsening of the billets and blistering were experienced.[20,57] Al-Li alloys have ten times the hydrogen content of other Al-alloys due to the formation of LiH, Li_3AlH_6.[24]

In general, cost, poor quality, and problems of reproducibility and consistency limit the PM technology to the application of only high performance materials. Although the oxidation of metals is relatively inevitable even in atmospheres with very low oxygen partial pressure, such as 10^{-53} atm for Al-alloys. The oxygen content of a product can be reduced by using alternate processing routes such as: spray rolling [58] and spray deposition. [22,37, 59 - 65]

2.1.3 Rapid Solidification Spray Deposition (RS/SD)

The principle of spray deposition was pioneered during 1970's by A. Singer at the Swansea University, UK.[66] However, Schoop first invented a form of metal spray in 1910.[9,67] Singer proposed direct production of a rolled strip from the molten metal, with the advantage of eliminating all the conventional intermediate steps between the caster and the roll stand, including heating.[68] Singer's spray deposited sheet had porosities in the range of 15% to 20% and needed rolling well in excess of 50% reduction, soon thereafter, in a protective environment, to produce about 95% of the theoretical density,[66] which is not acceptable for commercial alloy.

Table. 1. Oxygen Content of Selected Alloys Produced by Various RS Processes.[3]

Alloy Type	Processing	Weight Percent O_2
7075 Al	H_2O atomization*	0.457
7075 Al	Inert gas atomization*	0.209
7075 Al	Rotating Cup Process**	0.0066
7075+Ni+Zr	LDC + Extrusion**	0.011
X2020-B	LDC + Extrusion**	0.010
MERL 76	LDC + HIP**	0.0080
Fe-Nd-B	LDC + Extrusion**	0.050
Al-3Li-1.5Cu-1Mg-0.2Zr	PM + Extrusion***	0.051
Al-3Li-1.5Cu-1Mg-0.2Zr	IM***	0.005
Al-3.2Li-2.1Cu-0.83C	Mechanically Alloyed + Extrusion	0.65
7090	PM + Extrusion	0.2 - 0.5
Al-3.7Ni-1.5Fe	Air Atomized***	0.386
Al-3.7Ni-1.5Fe	Splat Flakes***	0.139
Al-3.7Ni-1.5Fe	Centrifugal Atomization***	0.020

* Wt% O_2 calculated from measured wt% of Al_2O_3, $MgAl_2O_4$, MgO, using Neutron Activation Analysis.

** Wt% O_2 analysis was performed using an Inductively Coupled Argon Plasma technique by Arnold Green Labs, MA.

*** Wt% O_2 analysis was performed using Fast Neutron Activation Analysis.

In spray deposition, the deposit is built up layer by layer from successive impacting molten or semi molten droplets. The thermal history and the resultant structure can be highly variable with the location in the deposit.[5] Three mechanisms were proposed for the microstructural evolution in spray deposits:[10,69]

1. Incremental solidification, where partially solidified incoming droplets impact on a cold substrate and develop a thin film of liquid that contributes to the formation of high density deposits.
2. Growth/coarsening of nuclei in a partially liquid layer consisting of 80% solid.
3. Splat solidification at a microscopic level, where the droplets arrive and spread into splats in nanoseconds and solidify instantaneously via gas convection and substrate conduction. Splats with arrival rates of 10-20 m/s solidify in milliseconds.

Depending on the gas to metal flow rate ratio and the flight distance, the droplets from gas atomization spray deposition (GA/SD) processes may freeze into incoherent powder agglomerates of high porosity and very fine microstructures, or form a thick mostly liquid layer with reduced porosity, larger microstructures and non uniformly dispersed second phases. Cooling during deposition, is mainly by either conduction to the substrate or radiation and convection to the surroundings, depending on the thickness of the existing deposit layer at a given time.[10] The GA/SD deposits show a non uniform thickness profile across its width depending on the uneven droplet density and deposition rate in this direction. Singer has suggested the use of either multi-nozzle arrangement or a scanning type nozzle to solve this problem.[70] The later suggestion become one of the spray deposition processes called Osprey process. GA/SD processes include the Osprey process,[71] the Consolidated Spray Deposition (CSD) process,[22] and the Liquid Dynamic Compaction (LDC) process.[3,17,72]

Lately, a pilot scale study of the Osprey process to produce sheet, plates and different shaped preforms was undertaken. In this process liquid metal is spray deposited into highly dense metallic preforms.[73] depending on the location of the preform, almost full density of about 99.8% was reported for nitrogen atomized Rene' 95 (Ni-based) alloy. However, the density was relatively lower when Ar was used.[74] The collector is fixed to a mechanism that is programmed to move in sequence within the spray to achieve the definitions of a preform. A 450 kg roll was spray deposited on a mandrel in 6 minutes. Also an IN-100 (Ni-based) superalloy was deposited into a cylindrical preform of 6.3 kg with 10.5 cm OD, 1.3 cm wall thickness and 19.3 cm length. The overspray powder of the Osprey process was seen to be clean and spherical, and can be considered a useful by-product, that increases the yield of the process.[75]

Aurora steel Ltd.[22,76] developed the CSD process which is similar to the Osprey except for the deposition of coarse liquid droplets with cooling rates of 10^3 - 10^4 K/sec. The deposit had micron size porosities, was free of interconnected oxides, showed no evidence of splat boundaries, and had densities of about 96-98%.

The LDC process, which is a spray atomization and deposition process that utilizes an ultrasonic gas atomization (USGA) technique was developed in the High Temperature Materials Laboratory at MIT.

2.1.3.1 Liquid Dynamic Compaction (LDC)

LDC is an inert gas atomization spray deposition process that utilizes the high velocity pulsed gas jet from the USGA nozzle. The USGA was studied in Sweden a few decades ago by Nilsson of Kohlswa AB for the atomization of low melting point alloys.[61,77 - 79] However it was not until extensive development on the nozzle has been done at MIT that it became possible to produce rapidly solidified powders and deposits in potential commercial sizes. A broad range of alloys have been atomized into selected powder sizes and deposit thicknesses by the USGA technique at MIT. High pressure gas is accelerated through the resonance cavities of USGA nozzle to stimulate pulses in the ultrasonic gas jet in a mechanism similar to a whistle, like the Hartman tube. In conventional subsonic gas atomization, the gas and the liquid droplets travel at about Mach 0.5, while the USGA atomization die accelerates them to velocities in the range of Mach 2 and produces powder whose average size was around 10-50 μm, with 99% of it smaller than 250 μm.[21,57,79, 80]

Different Kohlswa ultrasonic gas atomization (USGA)[77] nozzle geometries, based on the Hartman shock-wave generator with axially symmetrical convergent nozzles and resonator cavities of various sizes and forms were developed at MIT in the last 20 years. Figure 5 shows a schematic illustration of the region around the USGA atomization die.[3] Circular and linear nozzles[72] have been in use for a variety of experiments. A linear nozzle with 50 mm X 2 mm slit opening has provided laboratory production rates of 5 - 10 tons per hour.[17,80] For higher tonnage production, a longer linear nozzle or a multiples of small ones either in series or parallel can be used. However, it would be more economical to use a multiple set of shorter atomizers, since it is easier and cheaper to replace a short segments of the assembly instead of a longer one in case the gas nozzle is plugged or damaged by liquid metal impingement.

During the LDC atomization process, the fine pulverized droplets travel in a conical shaped path when circular atomizer is used or in a prismatic tent-like path when linear atomizer is used. The semisolid droplets are later collected in the form of splats against cold metallic substrate at a certain flight distance to form a deposit or let to solidify in flight to form powder. The LDC deposition process is a hybrid rapid solidification process where the metal experiences an initial rapid solidification from the atomization gas followed by rapid, solid state cooling from the water cooled substrate. The cold substrate minimizes structural coarsening and precipitation from the supersaturated solution.[9,80]

The high solidification rates of 10^3-10^6 °K/s reported for gas atomization processes,[19] make the USGA process very attractive for fine metal powder production. These high rates are essential for the control of the final structure and properties of the highly alloyed and complex metal compositions. Cooling rates of about 10^5 K/sec were realized in alloys based on Pb, Sn, Zn with

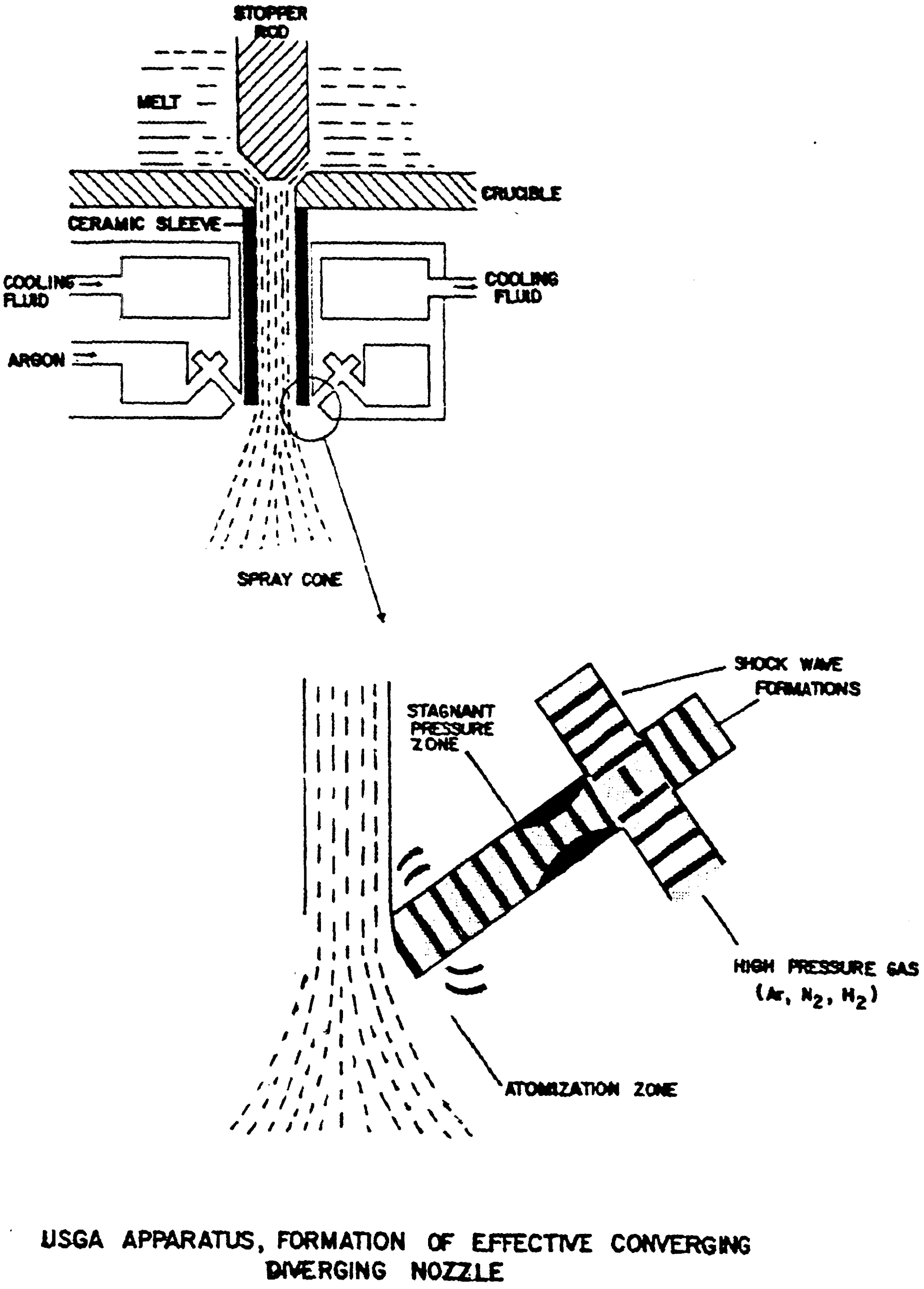

Figure 5. A schematic representation of relative positions of atomization die, pour tube, crucible and stopper rod for USGA. And details of shock wave formation.[3]

1-10 µm average powder sizes and Al-alloys with 30 to 70 µm average sizes, yielding highly refined structures. The high cooling rates are attained by high relative velocities between the gas and the metal droplets, small droplet sizes, and gas chilling factor from the expansion of the highly pressured gas.[18, 79, 81]

Depending on the atomization gas pressure, the USGA nozzle generates gas jets with high supersonic velocities and frequencies that reach more than 50 KHz compared to sonic converging nozzles. This has been experimentally confirmed by high speed photography of the shock waves generated by a USGA die. For argon gas at 425 psig, the gas jet had twice the velocity of sound with a corresponding frequency of approximately 58 KHz. It was also seen that increasing the gas pressure reduced the apex angle of the conical path of the gas jet.[3,81] Figure 6 shows the atomization gas frequency in terms of atomization gas pressure, while Figure 7 shows the effect of gas pressure on the included spray cone.[81] An USGA atomizer with a frequency of 80 KHz was reported to produce finer powder than other atomizers with divergent/convergent geometries at equal amount of gas atomization energy.[24]

Most atomization devices are based on the principle that high velocity fluids readily disintegrate liquid metals due to their very low shear resistance at high velocities. When the pressurized gas is delivered through the USGA nozzle with the Hartman configuration, the gas flow leads to a Bernoulli effect and the flow velocity becomes supersonic.[82] In addition, the interference mechanism at the Hartman shock wave generators introduces primary and secondary waves of high amplitudes and frequencies.[82] Details on the operation of the Hartman generator are found in several references,[26,79, 82] where it is shown that the frequency of the pulsed jets depends on the cavity dimensions of the Hartman generator.[79] For efficient atomization of the molten metal, the USGA process makes use of its high velocity pulsed gas jets to generate a narrower range of fine droplet sizes.[77, 83]

As the frequency of the pulsed gas is increased, the distance between the adjacent wave crests is shortened. During atomization, these waves transfer

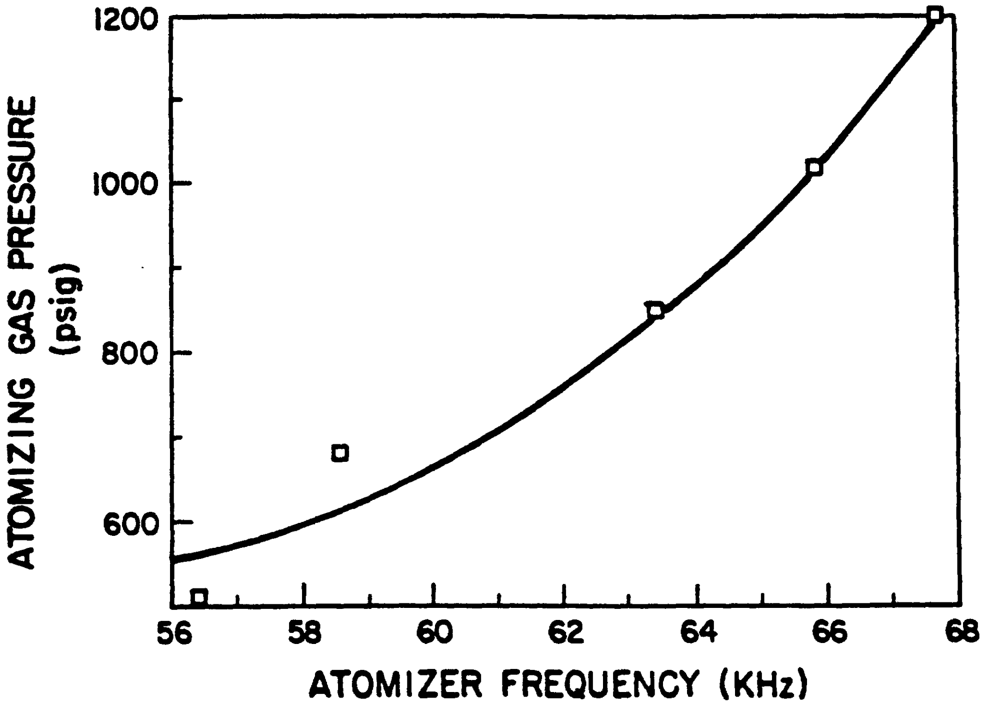

Figure 6. Calculated gas jet frequency versus the atomization gas pressure.[81]

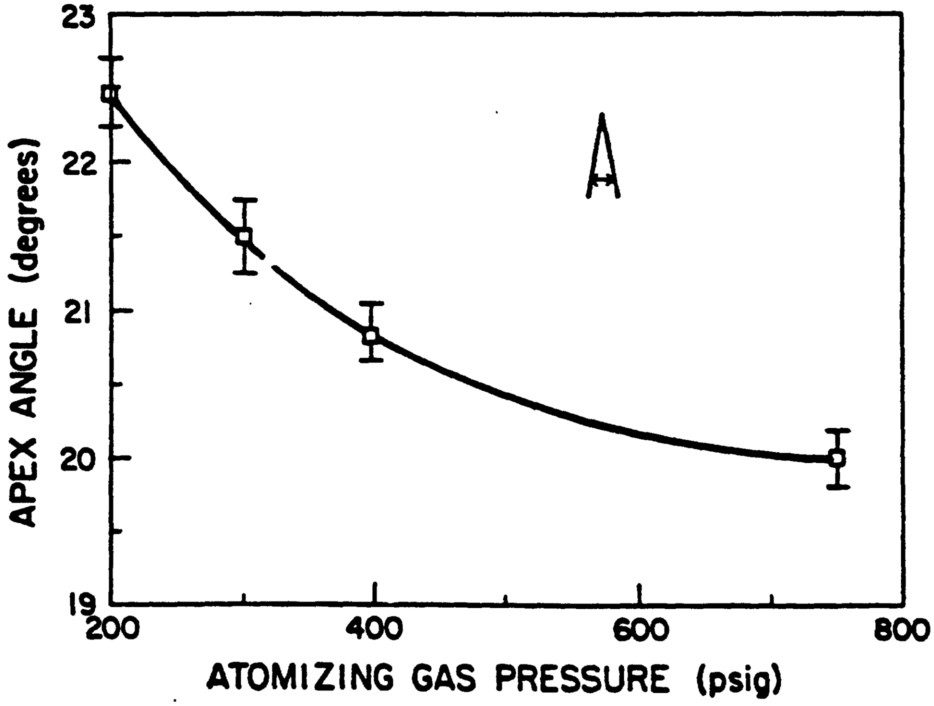

Figure 7. Variation in the included angle of the spray cone as a function of the atomizing gas pressure.[81]

their energy in the form of wave disturbances into the melt stream. As the amplitude of the metal disturbances increases the wave peaks become unstable and separate. The broken liquid takes the form of droplets smaller than or equal to the wave crests on which they are formed. And since the wave length is inversely proportional to the frequency, higher frequencies promote smaller droplets. Wave perturbations on the surface of metal left and frozen in the metal delivery tube at the end of an atomization experiment, spacing 100 - 200 μm, were reported.[3, 40, 84] The crests of these waves showed high disturbance and evidence of droplet formation. A frequency of 10^5 - 10^6 Hz was calculated from the interoscillation distance of 100-200 μm, which matches the 10^5 Hz range reported in the Swedish USGA Kohlswa research.[77, 78]. Several investigators are reported to have observed what appeared to be shock wave formation during USGA atomization using Schlieren Photography.[85]

The LDC process has been investigated to produce a variety of alloys based on Al, Fe, Mg, Cu and others that included superalloys.

A high strength 7075 Al-alloy with addition of Ni and Zr was atomized using a circular atomizer. Refined grain structure with fine Al_3Ni and Al_3Zr dispersoids contributed to highly improved mechanical properties of the alloy.[3, 61] An Al-Li LDC deposited alloy showed increased resistance to fatigue crack growth and improved toughness compared to its RS/PM processed counterpart.[3, 86] A 2024 Al-alloy was spray deposited with a linear LDC atomizer into a plate shaped preform with 96% density. This deposit contained equiaxed grains of 45 μm average size and oxygen content of about 0.006 ± 0.002 w/o. After consolidation and T4 treatment, this alloy showed higher strength and comparable ductility to commercial 2024.[87] Additions of 2 wt.% of Fe and Ni into the LDC 2024 Al-alloy resulted in increased strength values both at room temperature and, especially, at elevated temperatures compared to the commercial 2024 and LDC 2024 Al-alloys.[88, 89]

For LDC processed AISI 1020 and 1008 steels,[80,90] higher strength and excellent ductilities were reported compared to the commercial grade alloys.

Microalloying the 1020 steel with aluminum stabilized the grain size of the LDC processed metal, where, with controlled rolling at temperatures above A3, grain sizes of 2-3 μm were achieved.[91] Al-microalloying of an AISI 316L stainless steel by LDC processing achieved significant improvement in its hot and cold rolling, and in its mechanical properties in general.[9] A spray deposited 9Cr-1Mo ferritic steel with LDC circular atomizer has shown ductility values higher than those of IM processed alloys.[65]

LDC processed MERL 76 superalloy showed similar strength levels to those of RSPM.[62] An IN-100 LDC spray deposited superalloy had room and elevated temperature strength, and rupture strength levels comparable to those of RSPM.[92] Both alloys had lower oxygen content than the RSPM ones.

Since the intrinsic coercivity of permanent magnetic materials is improved by refinement of their microstructures through high quenching rates during solidification, Fe-Nd-B alloys were sprayed deposited via LDC. The intrinsic coercivity values of these alloys were increased, although they were lower than those realized by melt spinning and splat quenching.[64, 93-95]

The circular and the linear LDC atomizers were also used to produce deposits of alloys of Mg, Sn, low carbon steel, titanium, Zn and others. Tandem parallel linear atomizers were used to enlarge the deposit across its width and improve its thickness uniformity in that direction.[9,80] Metal matrix composites (MMC) were also processed with LDC. The metal matrix is melted and then atomized into a spray of fine droplets into which one or more jets of the strengthening phases are injected.[96] Tin coating on a freshly exposed surface of low carbon 1005 steel plates was accomplished by LDC spray deposition, in order to evaluate the development of a commercially competitive process that could replace the current commercial electroplating process, and eliminate its high cost and associated environmentally hazardous solvents and baths.[97,98]

2.1.3.1.1. Advantages of the LDC Process

As mentioned before, the LDC process can be used to produce either powder or deposits. However, spray deposition with LDC has a number of advantages over IM and RSPM processes as listed below:

- Lower atomization gas pressure are used for spray deposition, i.e. gas pressures of about 50-200 psig (345-1380 kPa) compared to the powder atomization pressures in the range of 900 psig (6210 kPa).
- Higher material yield than PM.
- Lower post-deposition processing temperatures relative to that of PM consolidation.
- Lower reactivity, lower oxide content and reduced risk of inflammability compared to PM. The short duration of spray flight to the substrate in an inert atmosphere and the high density of the LDC deposit sharply minimizes the opportunity of oxidation. The oxygen content in PM products is about one or two orders of magnitude higher (0.40%) than that in LDC deposits.[19]
- Fine and uniformly distributed equiaxed grain morphology, extended solid solubility of alloying elements, formation of quasicrystalline intermediate phases and non-equilibrium crystalline phases, production of metallic glass, refined and uniformly distributed second phases, absence of macrosegregation, and increased chemical homogeneity can be realized with LDC compared to IM.
- Improved magnetic properties, fracture behavior, fatigue life, increased ductile to brittle transition temperatures, and overall higher mechanical properties. [17,62]
- Potential for near net shaping, reduced number of processing steps and lower production cost compared to both PM and IM.[61] Calculations show that LDC saved about 40% of the production cost of superalloy billets compared to equivalent P/M processes.[72]
- Versatility in producing strips, sheets, tubes, discs, coating/cladding, metal matrix composites and dispersion strengthened materials.

2.1.3.1.2. LDC Process Parameters

Different aspects of the LDC production steps are influenced by a large number of variables that determine the eventual properties and shape of the deposit and/or powder. Table 2 lists these variables, while in Figure 8 the relative areas of influence of these variables are shown on a schematic representation of the LDC atomization chamber. A good understanding of how these variables operate is necessary in order to achieve consistent and reproducible results.

The importance of these parameters and their effects on the atomization process are variable. A large number of experimental studies on these variables have resulted in empirical equations that attempt to predict the characteristics of the atomization process and those of its products. Since the experimental data involve a complex interrelation between fluid dynamics, heat transfer and mass transfer, dimensionless group analysis of the variables, which is analogous to the theory of similarities in fluid mechanics, has been employed. By evaluating the equivalent dimensionless numbers of two fields subject to the same phenomena, a comparison could be drawn. Some of the important dimensionless numbers encountered in these empirical equations are:

Reynolds number: $Re = \rho v l/\mu$ (1)

Weber's number: $W = v^2 \rho l/\sigma$ (2)

The Biot number: $Bi = hl/k$ (3)

The Prandtl number: $Pr = \mu c_p/k$ (4)

where: v = velocity
ρ = density of fluid
l = linear dimension
μ = Dynamic viscosity
σ = surface tension
k = melt (droplet) conductivity
h = heat transfer coefficient
c_p = melt heat capacity

Table. 2: Atomization Variables in LDC

Atomization Chamber:	Ambient gas type and pressure
	Oxygen partial pressure
Melting Unit:	Power of the induction heating unit
	Melt pouring orifice (circular or linear)
The Melt:	The composition of the metal
	Viscosity
	Surface tension
	Volume - Metallostatic head pressure
	Melting temperature range
	Melt superheat
	Mass flow rate (melt exit area)
Atomization gas:	Gas type
	Gas pressure (static and dynamic)
	Velocity
	Viscosity
	Heat capacity
	Gas flow rate (exit area)
Melt breakup and cooling:	Aspiration pressure at the pouring slit tip.
	Gas/metal mass flow rate ratio
	Gas to droplet Relative velocity
	Flight distance to the substrate
	The gap between the atomizer halves
Deposit profile and cooling:	Spray plume spread
	Heat transfer coefficient
	Gas jet apex (included) angle
	Substrate material - heat conductivity
	Substrate material - thermal expansion
	Substrate temperature
	Substrate velocity
	substrate surface roughness: Adhesion

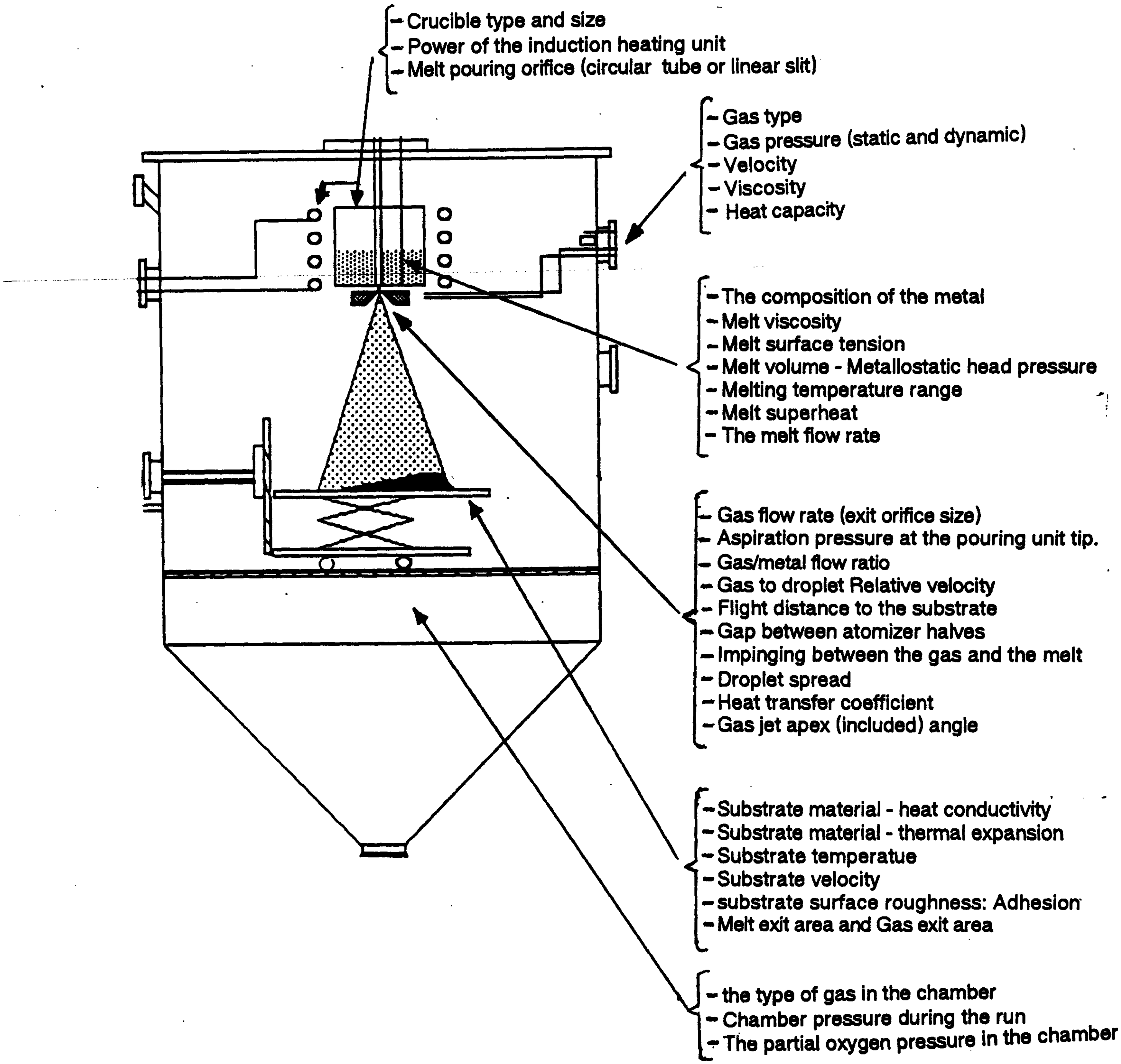

- Crucible type and size
- Power of the induction heating unit
- Melt pouring orifice (circular tube or linear slit)

- Gas type
- Gas pressure (static and dynamic)
- Velocity
- Viscosity
- Heat capacity

- The composition of the metal
- Melt viscosity
- Melt surface tension
- Melt volume - Metallostatic head pressure
- Melting temperature range
- Melt superheat
- The melt flow rate

- Gas flow rate (exit orifice size)
- Aspiration pressure at the pouring unit tip.
- Gas/metal flow ratio
- Gas to droplet Relative velocity
- Flight distance to the substrate
- Gap between atomizer halves
- Impinging between the gas and the melt
- Droplet spread
- Heat transfer coefficient
- Gas jet apex (included) angle

- Substrate material - heat conductivity
- Substrate material - thermal expansion
- Substrate temperatue
- Substrate velocity
- substrate surface roughness: Adhesion
- Melt exit area and Gas exit area

- the type of gas in the chamber
- Chamber pressure during the run
- The partial oxygen pressure in the chamber

Figure 8 Schematic representation of the LDC atomization chamber showing the relative position of the process variables.

The Reynolds number gives a measure of the turbulence in the fluid flow of the process, while the Weber number relates the critical dependence of the droplet diameter to the surface tension of the atomized melt. The Biot number compares the convective heat transfer of the gas at the droplet surface to the conductive heat transfer in the droplet. When the Biot number is < 0.1 the temperature gradient in the droplet is negligible and the heat flow is controlled by convective heat transfer at the boundary between the droplets and the gas. However, if it is > 10 then the heat flow is primarily limited by the heat conduction in the droplet. The Prandtl number represents the ratio of the ability of the fluid to transfer momentum to its ability to transfer thermal energy.

The following is a brief discussion on the influence and importance of the LDC process parameters:

The melting unit

The shapes and dimensions of the crucible, tundish and the pouring unit determine the level of the melt on which the resultant metallostatic head pressure depends. This metallostatic pressure and the aspiration pressure at the tip of the pouring unit, as will be discussed later, determine the metal mass flow rate during atomization.

The Melt: Superheat, viscosity and surface tension

For efficient atomization, a very close proximity between the atomization gas and the metal pouring unit is necessary. However, due to the Joule-Thompson cooling effect from the expansion of the high pressure atomization gas, the melt pouring unit may be subject to high heat losses. These losses can cause the melt to freeze in the pouring unit and interrupt the process. In order to eliminate this problem, a superheat of 100-200 °C has been practiced in the LDC process. The amount of superheat used was reported[70,99] to affect the melt breakup efficiency and the droplet size ranges. However, no effect of the superheat was detected in other researches.[38,100]

In some PM processes, the superheat was seen to promote finer powder size and reduced satellite formation. The powder of an aluminum alloy became progressively finer with increasing superheat up to 820 °C, while the satellite formation in other alloys was reduced by 15% with a superheat of 150 °C.[81] However, increased superheat of a copper alloy showed limited powder refinement.[101] The volatility, oxidation rate, impurity pickup and the prolonged time of heat removal before the onset of droplet solidification associated with higher superheat counter the purpose of the atomization processes. The droplet solidification time can be calculated from the droplet heat balance partial differential equation:

$$\rho_m C_{pm} \frac{\partial T}{\partial t} = K_m \nabla^2 T \tag{5}$$

where: ρ_m = melt density
C_{pm} = melt heat capacity
$\partial T/\partial t$ = cooling rate of the droplet
K_m = molten metal heat transfer coefficient

And the time to cool a superheated droplet from an initial temperature (T_i) to temperature (T) is derived as [102]:

$$t = \frac{d \rho_m C_{pm}}{6h_c} \ln\left(\frac{T_i - T_g}{T - T_g}\right) \tag{6}$$

where: T_g = gas temperature
d = droplet diameter
h_c = heat transfer coefficient

In an atomization process with a Biot number < 0.1, the droplet internal temperature gradient is negligible and convective heat transfer at the boundary between the droplet and the gas is the controlling mechanism. This heat transfer coefficient is shown to depend on the droplet size (d):[103]

$$h_c = \frac{k_g}{d\left(2 + 0.6\,Re^{0.5} Pr^{0.33}\right)} \tag{7}$$

where: k_g = thermal conductivity of the gas
Re = Reynolds number
Pr = Prandtl number

Equations 6 and 7 show that the cooling time of a droplet is proportional to the square of the droplet size. In atomization processes, the melt is atomized into droplets of large size distribution. The finer droplets freeze early in flight and in their particle shape in the deposit.

The viscosity and the surface tension of the melt influence the efficiency of melt breakup.[3,24] It was found from different metals and alloys that these parameters influence the shapes of the atomized powders, where the tendency to form spherical powders was favored by lower viscosity and higher surface tension.[101,104] The effect of the viscosity was reported to be more pronounced than the surface tension, and that higher melt viscosity resulted in coarser powder [32,34] Other research, however, reported no significant effect of the viscosity.[105]

Atomization gas

The atomization gas pressure determines the velocity of the gas and the melt disintegration energy and efficiency during atomization. Increased gas pressure, when other parameters are kept constant, resulted in decreased average powder size and narrower powder size distribution, as shown in Figure 9.[3] Using mechanical energy conservation of a turbulent flow at steady state, the gas velocity can be calculated from the pressure as follows:[106]

$$\overline{U} = \sqrt{\frac{2g_c(P_1 - P_2)}{\varphi\left(1 - \frac{A_2}{A_1}\right)}} \qquad (8)$$

where: $\overline{U}$ = average gas velocity
$P_1 - P_2$ = pressure gradient
g_c = force of gravity
φ = gas density
A_2/A_1 = area ratio of orifice

Figure 9. Effect of gas pressure on the powder size distribution of 7075 Aluminum alloy, when other parameter are kept constant.[3]

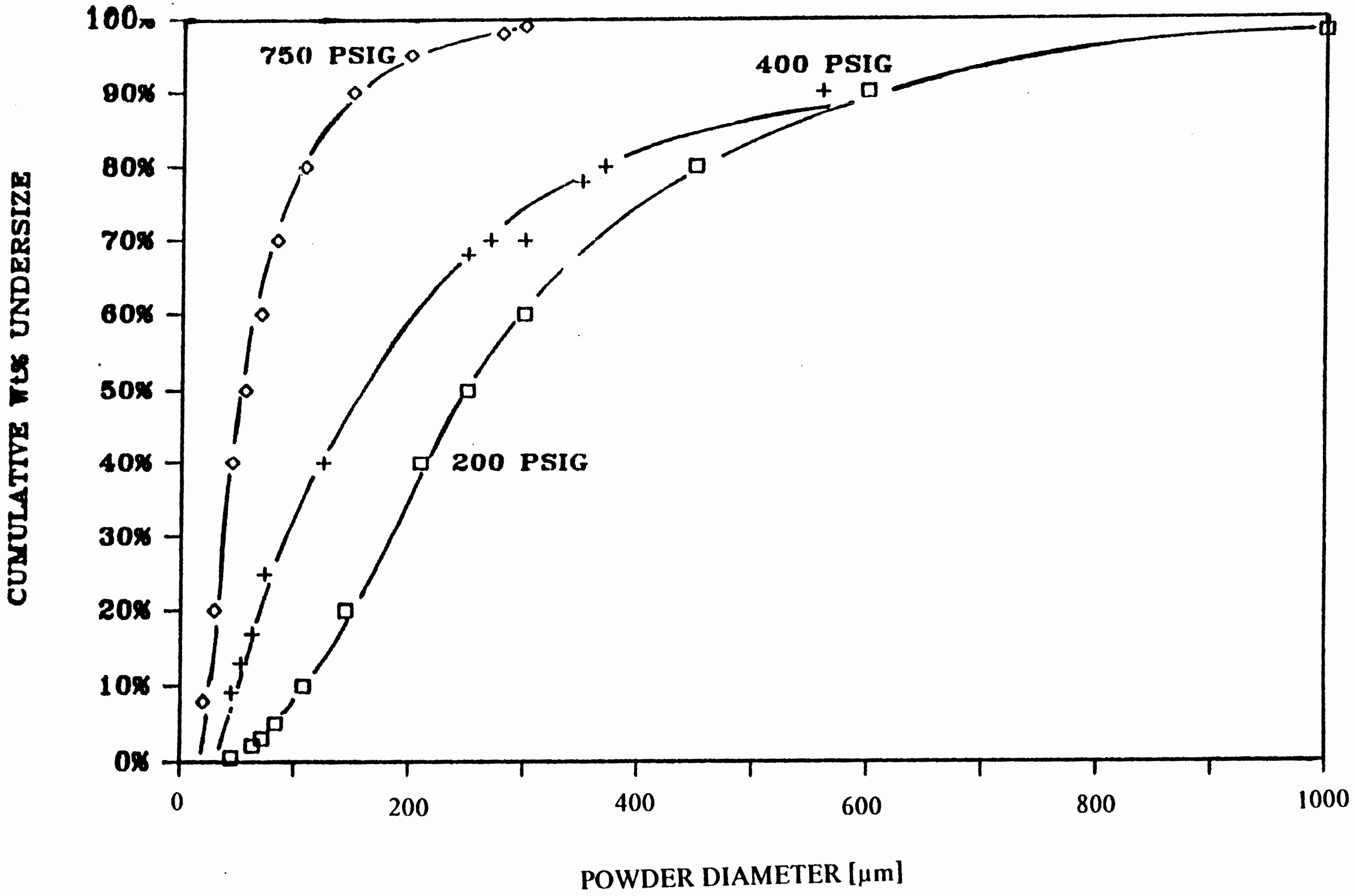

The gas pressure and gas energy are very important parameters since the kinetic energy of the gas is transferred into melt surface energy during atomization. The gas flow rate is used as a good measure of these variables, and its ratio with the melt flow rate is one of the most important parameters in LDC, as will be discussed later.

The type of atomization gas affects the droplet sizes, cooling rates, oxidation rates, and powder shape. Air, as an atomization gas, produces irregular shaped particles due to the surface oxide films that form while the particles are solidifying in flight.[82] Inert gases, reducing gases and semi-inert gases such as nitrogen (depending on the melt composition) are used to produce spherical powders and to limit oxidation. The viscosity of the atomization gas has a pronounced effect on powder refinement. A 60% reduction in gas viscosity resulted in a corresponding 60% reduction of average powder size. However, when the gas density was decreased by a seventh, the average powder size was increased by a factor of two despite increased gas velocity.[107] For the same atomization gas pressure, helium produced finer powder than argon due to its lower viscosity and higher gas power output.[26]

The relative vertical level between the atomizer gas exit and the pouring tube/slit melt exit, in conjunction with the atomization gas pressure, creates a condition of either lowered (aspiration) or raised pressure (back-pressure) at the zone right underneath the pouring unit tip. At a constant relative positioning between these orifices, increasing the atomization gas pressure increases the existing aspiration or back-pressure condition. For Al-alloys, an aspiration pressure of 1 psi is equivalent to about 25 cm increase in the metallostatic head pressure.[25]

Melt breakup and cooling:

The velocity difference between the droplets and the atomization gas, regardless of which one is faster, is a very important parameter both in melt breakup efficiency and droplet cooling rate. This is one of the reasons why high gas pressures and velocities result in finer droplet sizes. From extensive measurements of various liquids atomized with a converging pneumatic atomizer, a relationship to predict the mean particle diameter was derived.[108] The average droplet diameter is calculated in terms of the relative velocity between the gas and the liquid, the gas to liquid volume flow rate ratio, the liquid surface tension, and the melt viscosity, as:

$$d = \frac{585}{V}\sqrt{\frac{\gamma}{\varphi}} + 597\left(\frac{\mu}{\gamma}\right)^{0.45}\left(1000\frac{Q_L}{Q_A}\right)^{1.5} \qquad (9)$$

where: d = mass mean particle diameter
V = relative velocity between the gas and the liquid
γ = surface tension of the liquid
μ = viscosity of the liquid
Q_l = liquid flow rate
Q_g = Gas flow rate

The calculated result from this equation agreed very well with water atomization experiments.[107] The equation was also used in supersonic gas atomization, but was rarely applied on the atomization of liquid metals .[109] Another equation, based on equation 9, was derived for the gas atomization of molten metals.[110]

$$d_m = d_M\, K\sqrt{\frac{v_m}{v_g}\,\frac{1}{W}\left(1 + \frac{J_m}{J_g}\right)} \qquad (10)$$

where: K = constant
d_m = mass mean diameter
d_M = metal stream diameter
W = Weber number
v_m, v_g = Kinematic viscosities of the liquid metal and gas
J_m, J_g = mass flow rates of metal and gas

It could be seen from this equation that finer droplets can result from increasing gas to metal mass flow rate ratio (i.e. J_g/J_m), increasing gas viscosity and decreasing melt viscosity.

In order to use the gas at its highest velocity, it is necessary to place the atomizer gas exit very close to the melt stream, which makes the gap between the atomizers an important parameter. The gap is limited by the size of the pouring unit. And it should be made as narrow as possible to reduce gas spreading before it comes in contact with the melt stream. The setup geometry between the atomizer, such as the gas jet apex (included) angle also influences the distance the gas travels before impinging on the melt. The average powder size decreases as this angle is increased.[111] However, at an angle greater than 60°, the melt was prevented from exiting the pouring unit due to back pressure created at its tip.

Applying fluid mechanics dimensionless analyses on the atomization of molten waxes and wax-polyethlene mixtures, a correlation of the median droplet diameter as a function of the viscosity, gas/melt mass flow ratio, and relative velocity was developed:[112]

$$\frac{d}{T} = f\left(\frac{D_a}{D_L}, W_L, \frac{M_a}{M_L}, \frac{\mu_L}{\sqrt{D_L \rho_L \sigma}}, \frac{\mu_L}{\mu_a}, \frac{\rho_L}{\rho_a}\right) \tag{11}$$

where: d = droplet diameter
T = turbulence parameter
D_a/D_L = diameter ratio of the air and liquid nozzles
W_L = Weber's number
M_a/M_L = air to liquid mass flow ratio
μ_l/μ_a =liquid/air viscosity ratio
ρ_L/ρ_a = liquid/air density ratio

The experimental data showed that the liquid/gas mass flow rate ratio and the gas dynamic forces are the most important variables.[9]

Atomization Chamber

The atomization chamber atmosphere controls the aerodynamic modes of atomization. The atmospheric pressure depends on the initial chamber pressure and temperature, the heat pump rate from the melt during atomization and the relative flow rate between the entering atomization gas and the exiting exhaust gas. Care should be exercised right at the end of an atomization run when there is no further heat flow from the melt and suddenly the chamber atmosphere cools and the pressure inside the chamber drops, causing a reverse flow of the outside fluids into the chamber through the exhaust line. An initial vacuum condition of the chamber was reported to show a different melt breakup mechanism in a centrifugal atomization chamber.[80] An increase in the ambient pressure reduces the velocity and spreading of the melt spray plume and the atomization gas jets, increases the drag forces on the droplet and promotes the formation of coarser droplets. The type of the gas in the chamber also influences the shape and oxidation rate of the droplets. It was observed that tin oxidized in an air atmosphere resulted in irregularly shaped powder although it was atomized with nitrogen.[97]

Theoretical analyses showed and experimental observations verified that the average droplet size decreases with increased droplet flight velocity.[90] Newton's second law for an accelerated particle in a fluid becomes:[113]

$$\frac{\partial v_d}{\partial t} = \frac{3\rho_g}{4\rho_d} C_D (v_g - v_d) |v_g - v_d| + g \qquad (12)$$

where: v_d = droplet velocity
v_g = gas velocity
ρ_d = droplet density
ρ_g = gas density
g = acceleration due to gravity
C_D = drag coefficient which is given as:

$$C_D = 0.28 + 5\,Re^{-0.5} + 21\,Re^{-1}$$

Re = Reynolds Number

The droplet velocity is seen to increase to a maximum and then decrease as the flight distance of the droplet increases. The finer droplets accelerate faster to a higher maximum velocity than the larger ones.[113]

Deposit profile and cooling

The flight distance, droplet sizes and the droplet-spray-plume-spread greatly influence the amount of heat contained in the deposit. Efficient heat transfer through the substrate depends on the thickness and the density of the deposit layer existing at a given time. The cooling rate during deposition depends on the heat removal rate per unit area. The heat transfer coefficient (q) can be calculated as:[26]

$$q\beta^2 d_m t_s = \frac{1}{2}\left(d_m{}^2 \rho_m C_{pm}(T - T_{mp}) + d_m{}^3 \rho_m H\right) \tag{13}$$

where: β = the ratio of splat radius to droplet radius
d_m = droplet diameter
t_s = solidification time
ρ_m = melt density
C_{pm} = melt heat capacity
T = temperature of liquid droplet
T_{MP} = melting point
H = latent heat of fusion

Other factors that influence the heat transfer are the substrate temperature, substrate velocity and the adhesion between the substrate and the deposit. These factor influence the deposit profile and adhesion to the substrate.

The complex fluid dynamics and the large number of variables involved in the ultrasonic gas atomization demand a careful analysis of the process and data before any conclusion is drawn. It should be realized that in a particular investigation the results are limited to the specific experimental variables and alloy characteristics.[41]

3. Aluminum alloys

Aluminum (Al) and its alloys have found increasing applications in the transportation, military, chemical, food storage and other commercial industries. Aluminum is a metal with an f.c.c. structure that melts at 660.3°C and has a density of 2.70 g/cm ^{3} at room temperature. In Table 3 some of the thermophysical properties of aluminum are listed.[114] There are only eight elements that have solubilities higher than 1% in aluminum. These elements (Mg, Si, Li, Cu, Zn, Ga, Ge and Ag,[115] form Al-alloys that have relatively low thermal stability due to their low melting point and high diffusivity.[19,114,115] However, copper (Cu), manganese (Mn), silicon (Si), magnesium (Mg) and zinc (Zn) are the main alloying elements in commercial Al-alloys. The commercial Al-alloys are divided into three main categories which are: age-hardened (heat treatable), cast, and work-hardened alloys.[116] In Table 4 the notations for wrought Al-alloys and their main alloying elements are listed;[115] whereas in Table 5 the maximum solubility of certain elements in aluminum are shown.[114]

The mechanical properties of Al-alloys are mostly influenced by the volume percent, size and distribution of the secondary phase particles that form during solidification, and subsequent thermomechanical treatments (TMT). These particles are conventionally classified into three groups:[19]

1. Constituent particles: which are Fe, Si, and Cu rich inclusions of 0.1-10 μm sizes. Fe and Si are usually present as impurities, whereas Cu is added as an alloying element.
2. Dispersoid particles: which are Cr, Mn and Zr rich particles of 0.05-0.5 μm sizes. They are utilized in controlling recrystallization and grain growth because of their sizes, and their stability during hot working and/or annealing.
3. Precipitate particles: Which are Cu, Mg and Zn rich particles of 0.01-0.1 μm sizes. They are secondary phase matrix strengtheners.

Metallic elements from among the transition metals, which have moderate solubilities in aluminum form fine, stable dispersoid particles. These particles stabilize the grain and subgrain boundaries and can improve the strength, toughness and corrosion resistance of the alloys. Elements with solubilities in the solid state that increase significantly with increasing temperature, such as Cu, are the source of the third type precipitates. When alloys containing these elements are quenched from high temperatures, where maximum solubility is achieved, a supersaturated matrix is formed. Subsequent aging at low to moderately higher temperatures results in fine precipitates. The strengthening of all age-hardened Al-alloys is due to these types of precipitates.

Table 3. Condensed Physical Properties of Aluminum.[114]

Property	Value
Thermal neutron cross section	0.21 barn (10^{-24} sq cm)
Lattice constant	4.04958 ± 0.000025 A at 25 C (77 F)
Density (solid)	2.698 g/cu cm at 25 C 0.0975 lb/cu in. at 77 F
Density (liquid)	2.368 g/cu cm at 660 C 0.0856 lb/cu in. at 1220 F
Linear coefficient of thermal expansion	22.5 × 10^{-6} cm/cm/°C 12.5 × 10^{-6} in./in./°F
Average coefficient of linear expansion	23.6 × 10^{-6} cm/cm/°C from 20–100 C 13.1 × 10^{-6} in./in./°F from 68–212 F
Thermal conductivity	0.59 cal/sq cm/cm/sec/°C at 25 C 142.7 Btu/sq ft/hr/ft/°F at 77 F
Volume resistivity	2.6548 microhm-cm at 20 C (68 F)
Volume conductivity	64.94% IACS
Mass temperature coefficient of resistance	0.00429 at 20 C (68 F)
Magnetic susceptibility	0.6276 × 10^{-6} per g
Reflectance (electrolytically brightened), visible light	85 to 90%
Emissivity at 9.3 microns	3%
Surface tension	900 dynes/cm at 700 C (1292 F)
Viscosity	0.01275 poise at 700 C (1292 F)
Melting point	660 ± 1 °C (1220 ± 1.8 °F)
Heat capacity	5.82 cal/mole/°C at 25 C
Boiling point	2452 C ± 15 °C 4445 F ± 27 °F
Solution potential, standard hydrogen scale	−1.66 v
Heat of fusion	397 J g^{-1}
Heat of vaporization	1.08 × 10^{-4} J g^{-1}

Table 4. Notations of Wrought Al-Alloys[114]

Designation	Major alloying element
1XXX	None(a)
2XXX	Cu
3XXX	Mn
4XXX	Si
5XXX	Mg
6XXX	Mg and Si
7XXX	Zn
8XXX	Other than above
9XXX	Unused

(a) 99.00% aluminum, minimum.

Table 5. Max Solubilities in Binary Al-Alloys[114]

Element	Temperature(a) °C	°F	Liquid solubility wt%	at.%	Solid solubility wt%	at.%
Ag	570	1060	72.0	60.9	55.6	23.8
Au	640	1180	5	0.7	0.36	0.049
B	660	1220	0.022	0.054	<0.001	<0.002
Be	645	1190	0.87	2.56	0.063	0.188
Bi	660(b)	1220(b)	3.4	0.45	<0.1	<0.01
Ca	620	1150	7.6	5.25	<0.1	<0.05
Cd	650(b)	1200(b)	6.7	1.69	0.47	0.11
Co	660	1220	1.0	0.46	<0.02	<0.01
Cr	660(c)	1220(c)	0.41	0.21	0.77	0.40
Cu	550	1020	33.15	17.39	5.67	2.48
Fe	655	1210	1.87	0.91	0.052	0.025
Ga	30	80	98.9	97.2	20.0	8.82
Gd	640	1180	11.5	2.18	<0.1	<0.01
Ge	425	800	53.0	29.5	6.0	2.30
Hf	660(c)	1220(c)	0.49	0.074	1.22	0.186
In	640	1180	17.5	4.65	0.17	0.04
Li	600	1110	9.9	30.0	4.0	13.9
Mg	450	840	35.0	37.34	14.9	16.26
Mn	660	1220	1.95	0.97	1.82	0.90
Mo	660(c)	1220(c)	0.1	0.03	0.25	0.056
Na	660(b)	1220(b)	0.18	0.21	<0.003	<0.003
Nb	660(c)	1220(c)	0.01	0.003	0.22	0.064
Ni	640	1180	6.12	2.91	0.05	0.023
Pb	660	1220	1.52	0.20	0.15	0.02
Pd	615	1140	24.2	7.5	<0.1	<0.02
Rh	660	1220	1.09	0.29	<0.1	<0.02
Ru	660	1220	0.69	0.185	<0.1	<0.02
Sb	660	1220	1.1	0.25	<0.1	<0.02
Sc	660	1220	0.52	0.31	0.38	0.23
Si	580	1080	12.6	12.16	1.65	1.59
Sn	230	450	99.5	97.83	<0.01	<0.002
Sr	655	1210	...	...	...	...
Th	635	1180	25.0	3.73	<0.1	<0.01
Ti	665(c)	1230(c)	0.15	0.084	1.00	0.57
Tm	645	1190	10.0	1.74	<0.1	<0.01
U	640	1180	13.0	1.67	<0.1	<0.01
V	665(c)	1230(c)	0.25	0.133	0.6	0.32
Y	645	1190	7.7	2.47	<0.1	<0.03
Zn	380	720	95.0	88.7	82.8	66.4
Zr	660(c)	1220(c)	0.11	0.033	0.28	0.085

(a) Eutectic reactions unless designated otherwise. (b) Monotectic reaction. (c) Peritectic reaction.

Rapid solidification processing increased the mechanical properties of Al-alloys by decreasing their grain size and second phase particles, while at the same time eliminating complex constituent particles such as AlCuMnFe intermetallics.[19] So far, the rapid solidification processing of Al-alloys has been largely directed to specialized alloys that fall in one of three classes:

1. Room-temperature, high-strength alloys
2. Elevated-temperature, high-strength alloys
3. Low-density, high-modulus alloys

3.1. Room-Temperature High-Strength Al-Alloys

Precipitation hardening is the primary source of strengthening for the room-temperature, high-strength aluminum alloys. The introduction of dispersions of insoluble intermetallic phases combined with controlled amounts of strain hardening provide supplementary strengthening. Based on their superior strength, high fracture toughness, good fatigue and corrosion resistance, these alloys have found extensive application in the aerospace industry, specially the 2XXX and the 7XXX series. In conventional ingot-metallurgy, overaged tempers of these alloys are used in order to improve their stress-corrosion and exfoliation resistance. However, in this condition the metal loses about 15-20% of peak strength.[19] The room temperature strength and corrosion resistance of these alloys have been improved by applying rapid solidification processing and selected thermomechanical treatments (TMT). The first successful RS processing of these alloys was the PM processing of a 7XXX alloy by subsonic air atomization in 1961.[117] Lately, the 7XXX series (Al-Zn-Mg-Cu) with small additions of Fe, Co, or Ni have been rapidly solidified by different processes. Table 6 lists selected mechanical properties data for some of these alloys.[118] Improved properties were recorded for the 7XXX alloys with additions of Co, Zn or Fe+Ni.[68] The phases containing Co, Fe and/or Ni were seen to be more resistant to coarsening during fabrication and subsequent TMT compared to others containing Cr, Ti, V, Mo and Co.[19]

The 2XXX series have also shown parallel improvements when processed by RS, as seen in the LDC alloy 2024+2Fe+2Ni.[119] The LDC 2XXX and 7XXX

Table 6. Comparison of Room Temperature Tensile Data for Various 7XXX Alloys.[118]

Alloy and Condition	Heat Treatment*	Yield Strength (ksi)	Tensile Strength (ksi)	Elongation (%)
Conventionally Processed Standard Alloy				
7075 Ingot Commercial Bar	(a)	74	83	13.0
IM·7075 + 1 pct Ni + .08 pct. Zr Extrusion	(a)	104	107	1.5
Rapidly Solidified Standard Alloy				
7075 Melt Spun + Extruded	(d)	84	92	16.0
7075 Twin Rolled + Extruded	(b)	72	87	9.0
Rapidly Solidified Modified Alloys				
7075+1 pct Fe+0.6 pct Ni USGA+Ext.	(b)	83	100	6.0
7075+1 pct Ni+1 pct ZR USGA+Ext.	(d)	91	99	10.0
7075+1 pct Ni+1 pct Zr LDC+Ext.	(e)	107	118	9.0
7075+2 pct Zn Twin Roller Quench + Ext.	(b)	72	87	9.0
7075+1 pct Ni+1 pct Fe Twin Roller Quench + Ext.	(c)	92	104	9.0
7075+1 pct Ni+0.8 pct Zr USGA + Ext.	(a)	91	99	10.0
X7091 (Aloca) Air Atomized + Ext.	(a)	85	89	12.0
X7090 (Alcoa) Air Atomized + Ext.	(e)	93	97	11.0
X7091 USGA + Ext.	(c)	85	90	12.0
MA67 Air Atomized + Ext.	(f)	95	99	4.5
X7091 Air Atomized + Ext.	(f)	83	95	13.0
X7091 Powder Strip	(a)	83	93	13.4
X7091 Air Atomized + Ext.	(g)	79.6	—	15.9

*Heat Treatment Legend (K/h):

(a) Solution Treated: 773/1; Aged: 393/24.
(b) Solution Treated: 733/1; Aged: 393/24.
(c) Solution Treated: 748/1; Aged: 393/24.
(d) Solution Treated: 763/1; Aged: 393/24.
(e) Two Step Treatment.
(f) Solution heat treated @ 761/1 hour; cold water quench; age at room temperature, 4 days minimum; artificial age 24 hours @ 394K; second step age 14 hours @ 436K.
(g) Solution heat treated @ 761/1 hour; cold water quench; age at room temperature, 4 days minimum; artificial age 24 hours @ 394K.

Source: Charles River Associates.
Source: Charles River Associates based upon data from E. J. Lavernia and N. J. Grant, Massachusetts Institute of Technology, 1984.

had as-deposited with densities of 95-97%, which needed about 70% total hot rolling reduction for complete densification and was achievable in two rolling passes.[120]

These high strength Al-alloys account for about 80% of the commercial aircraft structural materials.[121] They compete very well against composite materials in aircraft structures due to their low manufacturing costs, availability of manufacturing facilities and the vast know-how procured during their extensive early use in the aircraft industry.

3.2. Elevated-Temperature High-Strength Al-Alloys

The presence of fine, stable dispersoids in Al-alloys was seen to increase their strength at high temperatures. In early efforts, oxide and carbide particles were introduced into Al-alloys by mechanical alloying, and by sintered aluminum powder (SAP) processes. Additions of transition metals were also seen to increase the thermal stability of the Al-alloys by forming particles resistant to coarsening at high temperature due to their low diffusivity and low solubility in the aluminum matrix.[3] The extended solubility of the transition elements in aluminum and refinement of their dispersoids by rapid solidification processing and TMT offer the opportunity of utilizing Al-alloys modified by these elements to serve as elevated-temperature high-strength alloys.[19] RS/SD of these alloys has produced a high volume fraction of about 20-30% of fine stable intermetallic precipitates.[20,122] Incoherent particles, such as Co_2Al_9 particles, were effective in hindering the slip and increasing high temperature strength.

PM processing of fine air atomized powders containing Mn, Co, Fe, Si, Ce, and Cr was undertaken in ALCOA. The Al-Fe-X type alloys have shown the best high temperature strength of these alloys. The most promising of the Al-Fe-X alloys were the Al-Fe-Ce and Al-Fe-Cr series, of which the Al-8Fe-4Ce was the most exceptional. Fe addition was reported to be more effective up to 8% maximum content, although this value depends on the rapid solidification method used.[19] LDC application on modified 2024 with additions of 2%Fe and 2%Ni was seen to result in higher strength at temperatures up to 250°C than those of the ALCOA developmental alloys. The elevated temperature high strength Al-alloys in general show useful strength up to 300 °C.[123]

3.3. Low-Density High-Modulus Al-Alloys

The search for light weight materials for aircraft structural parts has prompted the introduction of low-density high modulus Al-alloys. The density of Al-alloys can be decreased by the addition of elements such as Li, Mg, Si, Be, B, C, and Ca, whereas other elements such as Co, Cr, Cu, Fe, Mn, Ni, Ti, Zn, and Zr may be added in the alloys for other purposes than for density control. Li and Be are the only elements that reduce the density and at the same time increase Young's modulus of the Al-alloys. The high modulus is a result of the volume fraction and properties of the second phases that are present in these alloys;[46] however, Be is not used due to its cost and toxicity.[19] Figures 10 and 11 show the influence of selected elements on the density and modulus of Al-alloys.[124]

In Al-Li alloys, 1 wt% addition of Li has resulted in 3-4% reduction in density and a 6% increase in Young's modulus.[124,125] Weight saving in aircraft structural parts of 15-18% were estimated to result from using Al-Li alloys.[126,127] The first Al-Li alloy in an aircraft application, made by conventional Al-alloy processing, was the X2020 alloy used in the structure of the Navy RA-SC Vigilante aircraft in 1957.[126] However, due to the sharply lower ductility and toughness that resulted from segregation and coarse particles that formed during conventional IM, it was withdrawn from commercial production. Larger volumes of fine second phase dispersoids such as the ∂' (Al_3Li), higher solid solution of the alloying elements, and/or texture modifications of the Al-Li alloys were seen to be very critical in realizing their potential.[19] Rapid solidification processing of these alloys is instrumental in achieving improved properties, such as increases in elastic modulus of 20-40% higher than those of the IM products.[122]

Other elements such Mn, Zr and Co were added to rapidly solidified Al-Li to form Al-Li-X alloys. These elements were useful in introducing secondary

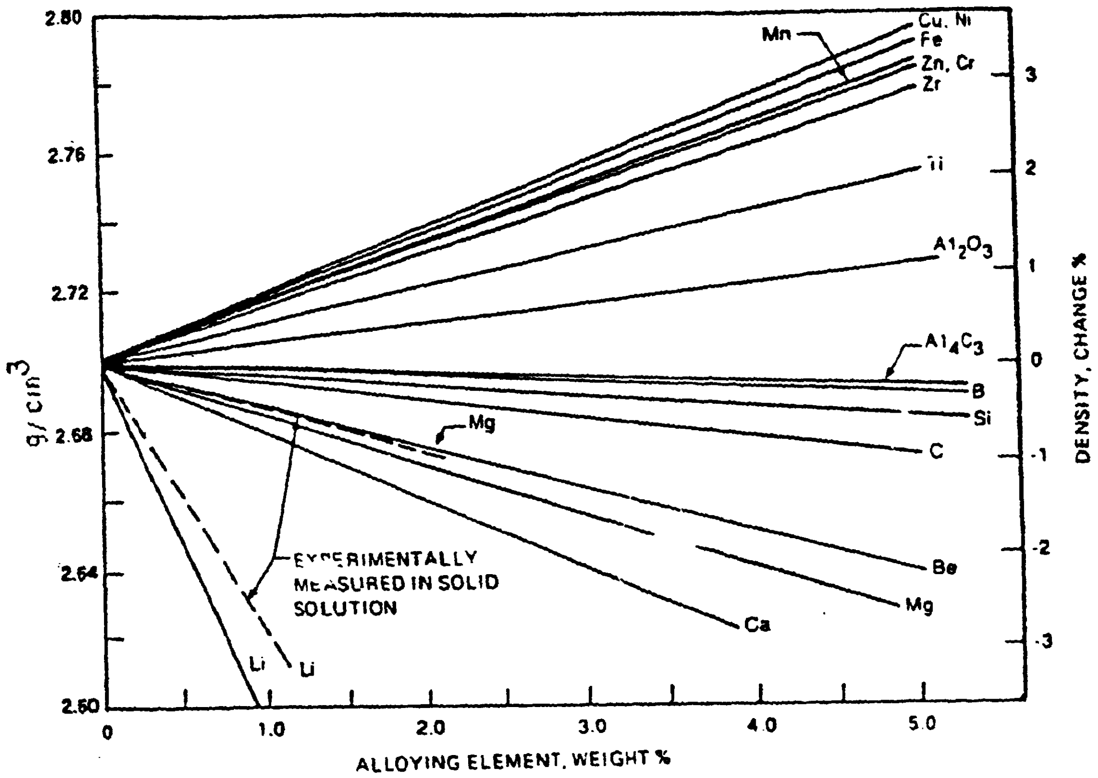

Fig. 10. Influence of the alloying elements on the density of Al-alloys .[124]

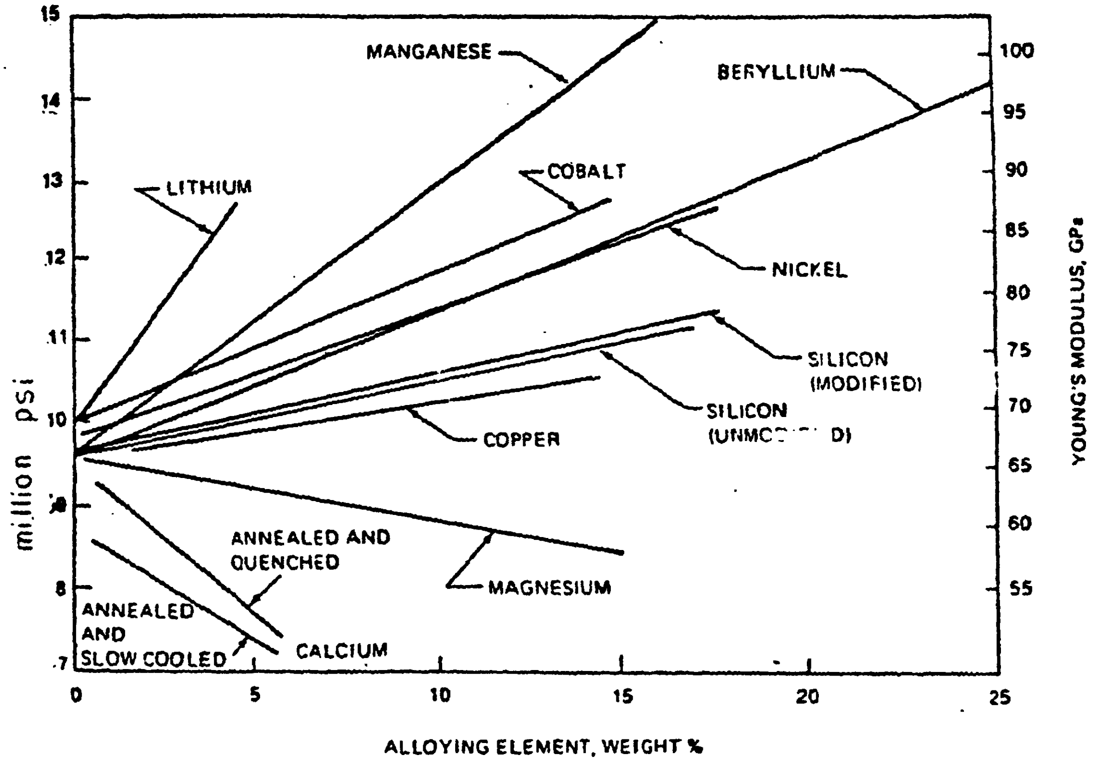

Figure 11. Calculated Influence of alloying elements on Young's Modulus of aluminum.[124]

precipitation, dispersion hardeners and grain refining phases. Additionally, the content of tramp elements such as K, Na and S was minimized in order to improved alloy toughness.[19,128,129] However, the coarse Mn rich particles at interdendritic boundaries were found to provide easy fracture paths that lead to extremely low ductilities in such Al-Li alloys.[128] Extrusions and rolled sheets of LDC processed Al-4Li-1Cu-0.2Zr alloy possessed increased ductility and reduced notch sensitivity due to the reduction of oxide usually present in this alloy.[130]

As was mentioned earlier, the application of LDC has been limited to the above mentioned groups of Al-alloys. In this project, the LDC process is applied to sheet production of a non-heat treatable (work-hardenable) 3003 Al-alloy.

3.4. Strain Hardenable Al-Alloys (3003)

The non heat treatable Al-alloys, which include the 1XXX, 3XXX, 4XXX, 5XXX and 6XXX series, constitute the largest percentage of aluminum alloy production. In 1985, about 95% of all sheet, plate and foil aluminum products were made from these types of alloys. Their applications range from food packaging and the huge volume beverage can market to specialized products that take advantage of the combination of reflectivity, corrosion resistance, thermal and electrical conductivity.[131] The increased application of these alloys in the food packaging industry is due to their non-toxicity, good thermal conductivity, resistance to light, oxygen, moisture and micro-organisms;[132] and to the advent of high speed rolling mills capable of economically producing thin foils with gages in the range of 0.000245 inches.[133]

A major advance in 1976 in can production, which involved the production of the two-piece all-aluminum can, allowed the Al-alloys to take over almost all the beverage can market. In this process the seamless body of the can is produced by sheet cupping, drawing and ironing.[134] The 12-ounce aluminum beverage can which was introduced in the 1960s', was able to capture 99.6% of the beer can, market by 1985 and effectively replaced steel cans. It was also reported that aluminum's soft beverage can market share reached 87.6% by

1985 and was rising. Innovations in design that reduced the aluminum can weight; advances in recycling furnaces that reduced melting energy, and improvement in fluxing operation that resulted in reduced dross losses have substantially reduced the cost of can production.[133] The recycling fraction of the aluminum cans has increased from 15.4 in 1972 to 52.8% by 1984.[133]

The excellent formability, low anisotropy and good mechanical properties, and excellent corrosion resistance of the non-heat treatable Al-alloys made them excellent candidates for the can industry.[134] These alloys are typically directionally cast, hot rolled, annealed and cold rolled prior to the can forming steps.[132] The emphasis of these steps is on the control of composition and structure to optimize the forming steps that follow the primary rolling.[134]

Mn has been known to be one of the most efficient elements that affect the deformability and recrystallization of aluminum.[135-137] Its influence derives from the alloy supersaturation and the size and distribution of particles that it forms. The grain size and texture of Al-Mn alloy sheet were seen to be related to its thermal and mechanical histories.[134] Commercially, the Al-Mn alloys are usually cast by the semi-continuous direct chill (DC) casting process. They are then heat treated at high temperatures for a "long time" in a process referred to as either "preheating" or "homogenization" in the literature. The plates are then hot rolled, subsequently cold rolled, and then annealed. Usually there is an intermediate annealing step between the hot and cold rolling steps.[134] The formation of fine grains in these alloys depends on the homogenization process and the presence of the fine intermetallic dispersions that form during the rolling and subsequent annealing steps.[138] Precipitation of Mn that forms on the subgrain boundaries prior to annealing causes the formation of undesired, coarse and/or elongated microstructures during recrystallization.[139] Figure 12 show the effect of Mn content on the hardness and electrical conductivity of Al-Mn alloys.[140] The Al-Mn alloys combine good flexibility during cold and hot working and low cost, which makes them ideal in the can industry.[141,142]

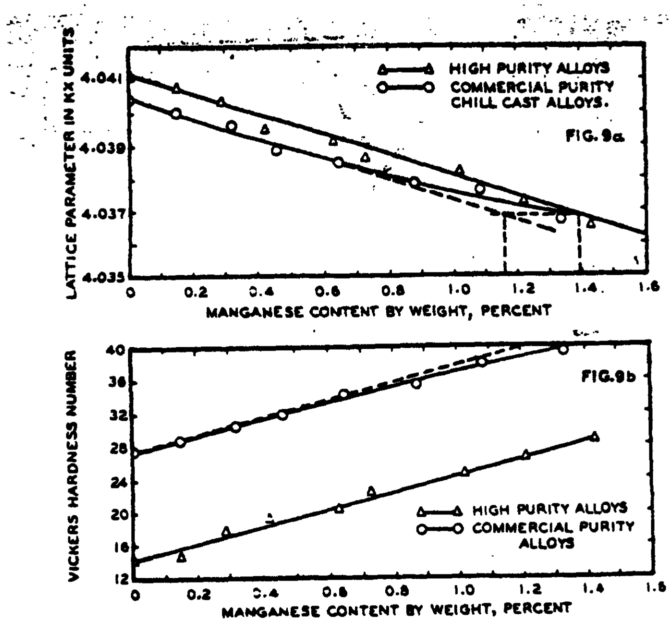

Figure 12. Hardness and electrical conductive variation with Mn content in aluminum.[140]

3.4.1. Homogenization

Homogenization or "homogenizing anneal" is a process in which segregation of the solute elements due to coring is eliminated or minimized by heating the alloy to high temperatures.[123] The relaxation time of the desegregation during homogenization varies as the square of the dendrite arm spacing (DAS), and hence the finer the structure the faster is the homogenization step.[123]

In unhomogenized 3003 Al-alloy produced by semi-continuous Direct Chill (DC) casting, an abnormal recrystallization behavior was noted that led to undesired final coarse grains, related to the fine and highly concentrated precipitates in the metal. However, when the metal was homogenized prior to hot rolling, recrystallization of fine grains occurred.[143] Almost all the Mn in the DC cast metal is in solid solution and has very low diffusivity.[144] As the 3003 alloy is heated to the rolling temperature, regardless of prior homogenization treatments, fine precipitates which are heavily concentrated in the primary aluminum dendrites, appear. The rate of precipitation, which depends on the rate of Mn dissolution, can be determined through resistivity measurements of the alloy. As the temperature is increased the Mn dissolves, steeper reduction in resistivity is experienced.[140,145-148] Figure 13 shows the resistivity as a function of Mn solute content in the as-rolled and as-annealed strip cast Al(Mn)FeSi alloy.[145] It was detected that the rate of solid solution breakdown and the number of these precipitates was significantly greater in the unhomogenized samples.[139,143] Although the unhomogenized samples retained less Mn in solution after hot rolling and annealing than the homogenized ones, the difference was not large enough to explain the abnormality in recrystallization of the unhomogenized material. The heavily concentrated fine precipitates of these samples are more likely to cause this abnormality.[143]

Homogenization treatment was observed to lead to: (a) globularization of the primary interdendritic particles, (b) precipitation of fine plate-like $Al_{12}(Fe, Mn)_3Si$ precipitates in the primary aluminum dendrites, and (c) reduced Mn in solid solution down to 0.55%. The result is the formation of fine precipitates remote from the large primary interdendritic particles and the development of precipitate free zones (PFZ) around these primary particles. The PFZ formation is due to Mn solute atom depletion by diffusion to the large primary particles which help the globularization of these particles.[134,149]

Due to the low diffusivity of Mn in aluminum, homogenization treatments are usually done at high temperatures (up to 635 °C) for long periods of times (up to 20 hours.)[144] The higher the temperature and the longer the time of homogenization of the samples prior to rolling, the finer the resultant recrystallized grains and the lower the recrystallization temperature when these samples are annealed after rolling. Figure 14 shows the effect of homogenization and annealing temperatures on the hardness of 3S (Al-1.15Mn) alloy.[144] When homogenization of an Al-Mn alloy at 625°C was done for 2 and 20 hours, it was observed that the recrystallized grains, from samples homogenized for 2 hours, were twice the size of the 20 hours ones. However,

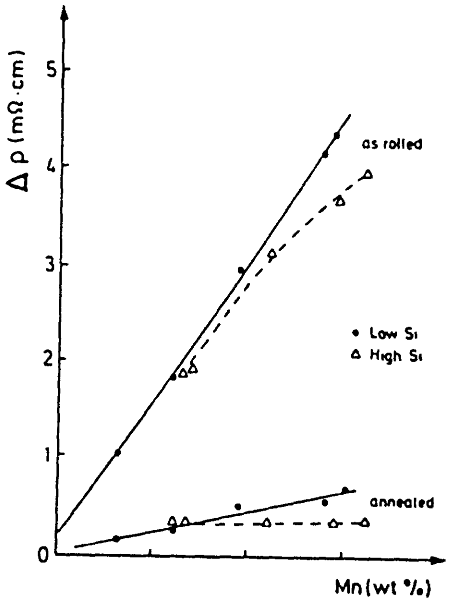

Figure 13. Resistivity vs Mn solute content in strip cast Al(Mn)FeSi alloy.[145]

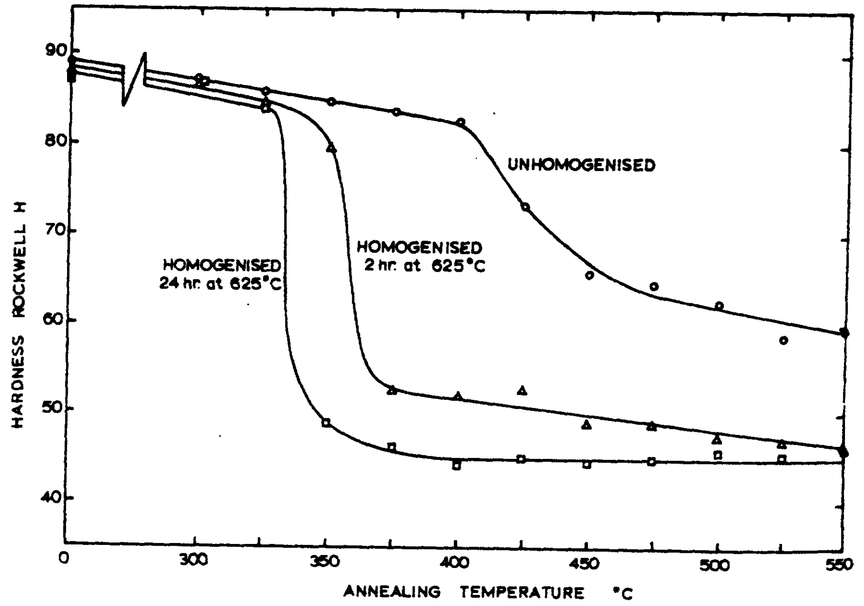

Figure 14. The effect of annealing temperature on the hardness of 3S alloy.[144]

the grains from the 2 hour homogenization were good enough to meet the desired objectives of fine final grain size and lowered recrystallization temperature for the hot and cold rolled materials. Unhomogenized samples in this work were seen to develop very coarse, slightly recrystallized grain structure.[144]

The effect of homogenization on recrystallization stems from: (a) the reduction of solute supersaturation and segregation, which reduces their effect on dynamic precipitation, and (b) the change in the size and morphology of the intermetallic primary particles. Due to the globular shape of these particles, the deformation zone around them becomes uniform. The uniformity of these zones and the coarsened globular intermetallics cause multiple nucleation sites of fine and equiaxed recrystallized grains.[141,150] On the other hand, due to the irregularly shaped primary particles in unhomogenized material, severe deformation is encountered at their sharp corners. During recrystallization, the grains first nucleate at the deformation zone around the large particles, which contain lower fine precipitates content; however, the presence of high volume fine precipitation in the rest of the matrix hinders the grain nucleation and growth through the rest of the matrix, promotes the formation of non uniform coarse grains and increases the recrystallization temperature.[134,150]

Hardness and tensile strength measurements of direct chill cast 3003 have shown that the unhomogenized material was harder and stronger compared to the homogenized, and that the chilled surface of the ingot had higher hardness compared to the interior of the samples, regardless of homogenization. The hardness difference between the surface and interior was observed to be more pronounced in the unhomogenized metal.[143,151] Although the unhomogenized materials had coarser grains, the higher strength and hardness may be attributed to the presence of the large volume fraction of fine secondary precipitates.[143,150,151]

3.4.2.Second Phases in 3003 Al-alloy

Prior to 1970's, all the features of the Al-Mn phase diagram were not definitely established, and all the observed phases and reactions were not accounted for in a consistent stable and metastable phase equilibria due to low purity, high vapor pressure and easy oxidation of Mn.[152] The maximum solubility of Mn in aluminum is 2% at the eutectic temperature of 658.5°C and decreases rapidly at lower temperatures.[147,152,153] However, due to the low diffusion rate of Mn in solid aluminum, there is a high tendency of Mn to remain in solution and to supersaturate during solidification. Fe and Si, even at low content, decrease markedly the solid solubility of Mn in aluminum.[143,145] 0.05% Fe solute content reduces the solubility of Mn from 1.82% down to 0.65%.[140,154] Microprobe analysis of solute concentration in DC cast 3003 showed Fe and Si solute contents of less than 0.05%, and Mn solute concentration of about 0.9%.[134]

The main primary constituent phases in the DC cast 3003 was $(Mn,Fe)Al_6$. At slower cooling rates, two additional reactions take place:

(Peritectic) Liquid + $(Mn,Fe)Al_6$ ------> α-$Al_{12}(Mn,Fe)_3Si$ + Al solid solution

(Eutectic) Liquid -------> α-$Al_{12}(Mn,Fe)_3Si$ + Al solid solution.

Any subsequent post-solidification heating continues the peritectic reaction, in which case the liquid phase is replaced by aluminum solid solution. This reaction continues until equilibrium proportions between the two phases, $(Mn,Fe)Al_6$ and α-$Al_{12}(Mn,Fe)_3Si$ are reached.[143,156] The precipitation of the α-$Al_{12}(MnFe)_3Si$ requires 0.1% Si concentration during solidification.[155] The dendrite arm spacing in the DC cast Al-Mn alloy varied from about 30 µm at the chilled surface to about 70 µm in the center of the ingot. The coarse primary particles also varied in size. 85% of the primary particles were the orthorhombic $(Mn,Fe)Al_6$, while the remaining 15% were the cubic phase α-$Al_{12}(Mn,Fe)_3Si$, most of which is formed by an eutectic reaction. The sizes of these particles varied between 1-4 µm[134] and 30-100 µm[141] with interparticle spacings of 5-20 µm depending on the solidification cooling rates. The $(Mn,Fe)Al_6$ phase forms parallelogram cross sectioned, long prisms, while the α-$Al_{12}(Mn,Fe)_3Si$ phase has a script-like appearance and polygonal shaped cross section.[157]

At lower solidification rates, secondary phases from the binary Al-Mn system and the ternary Al-Mn-Si system were suggested to be Al_3Mn and α-AlMnSi phases; however Al_3Mn reported for the phase diagram is shown to form at a higher Mn content of around 10%.[145,158] At high solidification rates, such as in the melt spinning process, precipitation of quasicrystal icosahedral and decagonal primary phases has been observed.[159,160] The icosahedral phase has a composition close to that of $MnAl_6$. While these types of quasicrystal phases were not detected at Mn concentrations below 6%, it was lately claimed to have been observed in an Al-3.95 at% Mn alloy.[159,161] It was also found that these quasicrystalline phases precipitated from the supersaturated Al solid solution as secondary precipitates during subsequent solid state heating.[161]

During homogenization, unidentified needle shaped precipitates of 0.005-0.01 μm in diameter and 0.1-0.2 μm in length were observed to form at about 250 °C and to disappear at 370 °C.[134,147] A plate-like metastable b.c.c phase called G-phase, which has an approximate stoichiometry of $MnAl_{12}$, has been identified at about 400°C.[,147,149,155,162] The formation of this phase was completely prevented by the presence of as little as 0.2% Fe or Si.[140,163] At higher temperatures this phase transforms into an equilibrium, secondary, plate-like $MnAl_6$ phase that precipitated around 550 °C. However, if Si concentrations greater than 0.1% were present, these plate shaped precipitates were both $MnAl_6$ and α-$Al_{12}(Mn,Fe)_3Si$ (or α-$Al_{12}Mn_3Si$) and had 0.2-0.3 μm diameters and 1-2 μm interparticle spacings.[134,149,164,165] The precipitation of the α-$Al_{12}Mn_3Si$ requires a minimum concentration of 0.06% Si during solid state precipitation around 500°C. The presence of about 0.01% Fe accelerates the $MnAl_6$ precipitation.[155,166] Microprobe analysis showed that the secondary α-$Al_{12}(Mn,Fe)_3Si$ precipitates were incoherent with the matrix, and that they were distributed either on the grain and subgrain boundaries or on dislocation lines, depending how fine they were.[149]

The homogenization reaction also causes the Fe and Si atoms to diffuse into the primary coarse particles and partially transform the $(Mn,Fe)Al_6$ particles into the α-$Al_{12}(Mn,Fe)_3Si$ phase.[134] After homogenization, the primary coarse particles were reported to consist of about 65% of α-$Al_{12}(Mn,Fe)_3Si$ to 35% of $(Mn,Fe)Al_6$.[134,143,167] The result of this reaction is an extreme depletion of Mn in an area of several microns of the matrix around these coarse particles, and the formation of the PFZ's. However, the Mn did not form new particles but rather diffused to the coarse primary particles and contributed to the α-phase formation.[144] The Mg_2Si phase that forms when Mg and Si are present dissolves at 500 °C, at which point the Si segregates to the primary $(Mn,Fe)Al_6$ phase and transforms it into α-$Al_{12}(Mn,Fe)_3Si$.[159]

Heating the alloy to the hot rolling temperature after homogenization slightly increases the number of fine secondary precipitates in the dendrites and decreases the width of the PFZ at the grain boundaries. However, these reactions do not appreciably change the microstructure.[134] A maximum of 0.1% of Mn in solution was observed to precipitate during hot rolling.[168]

3.4.3. Recrystallization in 3003 Alloy

During annealing of cold worked alloys, with high stacking fault energy, the high levels of dislocations ($>10^{12}$ cm^{-2}), and the small subgrain size ($<0.5\mu m$) give increased driving force for polygonization by subgrain growth.[134] The size of these subgrains is a function of the degree of cold rolling, annealing temperature, and annealing time. The growth of the subgrain boundaries takes place in one of two distinct modes: migration of sub-boundaries or subgrain coalescence. The sub-boundary migration results in growth similar to conventional grain growth, where growth of large subgrains occurs at the expense of smaller ones. The subgrain coalescence was divided into three subdivisions: collective migration, dislocation extraction and boundary dislocation emission.[169-171] The deformation temperatures and the Mg content were seen to influence the subgrain size. The subgrain size increases as the deformation temperature and/or Mg content are increased.[132,150] Aluminum alloys have shown preference to recovery during hot rolling rather than through dynamic recrystallization; however, static recrystallization could take place between hot rolling passes.[134,172] The subgrain growth of cold rolled Al-1%Mn, annealed at 300-400 °C, showed parabolic growth where a subgrain coalescence mechanism of collective migration of sub-boundary dislocations operated. At higher temperatures or longer annealing times, the subgrain growth was interfered with by recrystallization after it reaches a critical size.[170]

The coarse primary particles stimulate the recrystallization rate by acting as nucleation sites, while the fine secondary dispersions inhibit both grain nucleation and growth through a Zener drag mechanism by pining the boundaries.[131,173] In the unhomogenized material, fine, highly concentrated secondary precipitates form during the hot rolling or early annealing in the matrix away from the depleted (PFZ) zone around the large primary particles. These particles increase the complete recrystallization temperature of the alloy.[143,150] The non-uniform deformation zone around the irregular primary particles, the pinning forces from the fine secondary precipitates, and the high recrystallization temperature of the unhomogenized material, lead to the formation of large and elongated grains of an 8:1 aspect ratio.[143,173] These grains originally nucleated at the highly deformed zone around the large primary particles during annealing. At intermediate temperatures the subgrains in this deformed zone, which does not contain fine secondary particles, reach a critical size at which recrystallization can take place.[134,168] However, the rest of the matrix is stabilized by the fine secondary precipitates that retard grain nucleation or growth there.[168] As the recrystallization is continued a parasitic (secondary) grain growth takes place at the recrystallized zone around the large primary particles and large grains form there. On the other hand, the uniform deformation zone around the globularized primary particles, and the less concentrated fine secondary particles in homogenized material, lead to fine recrystallized grains.

The chilled side of the unhomogenized DC cast 3003 showed greater resistance to recrystallization than the interior, and resulted in incomplete recrystallization of coarse and elongated grains after an intermediate anneal between hot and cold rolling. A two hour annealing period of the DC 3003 alloy at various temperatures showed that when homogenized the alloy was completely annealed at about 345°C, whereas when in the unhomogenized condition, the interior of the material responded at 370°C and the chilled surfaces at 400°C.[143] As the annealing temperature is increased the recrystallized grain size difference between the chilled surface and the interior disappears and final grain size becomes finer;[134] although, few regions characterized by irregularly distributed dislocation did not completely recrystallize.

The classic Zener and Smith theory of particle pinning of grain boundaries has been modified for Al-Mn alloys. The original equation:[174]

$$\frac{D}{r} = \frac{4}{3f} \tag{14}$$

where: D = grain diameter
r = particle radius
f = particle volume fraction,

has been modified for an 3104 Al-alloy by 3-dimensional computation that resulted in the relationship:[175]

$$\frac{D}{r} = \frac{9}{f^{0.31}} \tag{15}$$

In another model, the ratio of limiting mean grain diameter (D_L) with particle radius (r) was calculated as:[176]

$$\frac{D_L}{r} = \frac{8}{9f^{0.93}} \tag{16}$$

The influence of Mn content on recrystallization was seen not to be monotonical. Complete recrystallization of 83% cold rolled sheets of Al-Mn alloys with 0.15%, 0.35% and 1.4% Mn content was seen to take place in 30 minutes at temperatures of 400°C, 350°C and 415°C, respectively.[140] Rapid rates of heating, high hot rolling temperatures, heavy deformation during cold rolling and high Fe content are factors that favor the development of fine annealed grains, while prolonged annealing time, higher annealing temperatures (>500 °C), and a high content of Si cause the reverse.[177]

Accelerated recrystallization was observed at fine precipitate spacings of 4µm,[178] while an interparticle spacing of 2 µm retarded substantially the recrystallization.[134] Fine grain sizes prior to deformation were reported to increase the annealing time or temperature for complete recrystallization.[179]

3.4.4. Al-Mn-Mg-Cu-Fe-Si Alloy

Conventional IM processing of Al-alloys results in the formation of coarse, complex, constituent particles that lead to lower strength, lower ductility, lower fracture toughness, and poorer fatigue life. During recycling of aluminum scrap, it is likely that a pickup of unwanted elements might form brittle second phases which fracture at lower strains by microvoids formation and coalesce. The most significant of these elements are Fe and Si, which require costly refinement during remelting.[180,181] However, rapid solidification processes that increase the solid solubility of these elements and form fine second phases could be employed in reducing or eliminating the cost of melt refinement. Al scrap with alloying/impurity levels of 14.8% (10.5Si-3.6Cu-0.6Zn-0.1Mg)[182] and 14.94% (7.6%Si-4.1Cu-1.4Zn-0.7Fe-0.23Mn-0.07Mg-0.04Cr,[183] obtained from scrap car shredder plants, were processed by RS and consolidation processes that consisted of melt spinning, compaction and hot extrusion. The processed Al scrap had mechanical properties comparable to that of 6061 and showed high workability. The effect of RS LDC processing of an Al-Mn-Mg-Cu-Fe-Si, with alloying content of around 1-2% of each element, will be investigated in this research.

The Al-1%Mn-1%Mg (AA3004) Al-alloy, which contains 1% of Mg more than does the AA3003 alloy, has been replacing the 3003 in the can industry due to its higher strength.[132,149] Mg in an Al-alloy forms Mg_2Si particles when Si is present. This phase is present on the grain boundaries as non-coherent particles, whereas inside the grains it is present as a fine, coherent hardening phase.[184] The Mg_2Si is precipitated at 300°C during heating. At temperatures between 400°C-500°C, some of the Mg_2Si redissolves to the solid solubility limit, whereas the remaining particles coalesce and spheroidize. At these temperatures, the Mg and Si contents in the cell boundaries and cell interiors reach higher homogeneity. Above 560°C, all the Mg_2Si goes into solution within 1-5 hours.[185]

The Hall processed aluminum contains less than 1% total of Fe and Si. The removal of these elements is costly, and they actually could function as useful alloying additions. However, the solid solubility of Fe is limited to 0.05% at the eutectic temperature, and the excess Fe reacts with Al and Si to form large constituent particles during solidification.[131]

Fe additions in Al-Mn alloys increases the quantity of the coarse primary constituent particles whose presence is attributed to the acceleration of recrystallization and fine final grain size.[168,177,186] An Al-1.4Fe-0.4Mn (AA8014) alloy with 1.5-5 μm grain size and 0.5-1.3 mm sheet, had excellent formability due to its high strain and strain rate hardening.[138] The hardening from solution treatment and aging for an Al-alloy with 4% Cu was seen to decreases with the addition of an amount as small as 0.3% of Fe. The Fe combines with the Cu and reduces the amount of Cu available for the treatment.[187]

Si additions increase the precipitation rate of the fine secondary particles in 3003 and lead to irregularly shaped grains.[168,177,186] When Si is added to an alloy containing Fe, the Si generally combines with the Fe to form very low solubility phase and thus decreases the effect of Fe.[187]

In Al-alloys, Fe and Si form $FeAl_3$, α-(Fe-Si) and β-(Fe-Si). The first two phases are tough and brittle, while the β phase, which contains more Si than the others, is brittle and readily crumbles. After hot or cold deformation, the $FeAl_3$ and the α-phase tend to remain in large fragments that are detrimental to the mechanical properties, whereas the β crumbles and becomes finely distributed throughout the matrix.[177] Larger additions of Si that accelerate the formation of the β phase should be beneficial.

All the phases that can occur in the binary, ternary, quaternary, quinary and senary phase diagrams that can result from any combination of Al-Mn-Mg-

Cu-Fe-Si were investigated in reference.[187] For the senary system of Al-Mn-Mg-Cu-Fe-Si, the crystal system, lattice constant, atomic arrangement and density of the second phases are tabulated in Table 7, however, the atomic arrangements of these phases are specified.[187]

Table 7. Phases Present in Al-Mn-Mg-Cu-Fe-Si Alloys[187]

Crystal Form	Lattice Constant				Density
	a_1, kX	a_2, kX	a_3, kX	a_2	g/cm^3
Octahedra {111}	5.147	....	....	....	....
Needle {110}	6.052	....	4.878	....	....
Needle {010} and {021} combined	4.00	9.23	7.14	....	....
Rhombic dodecahedra {110} modified by cubes {100}	14.28	....	....	....	....
Octahedra {111} sometimes modified by cubes {100}	6.391	....	....	....	2.21
Plates and lamellae {101}	6.32	....	14.78	....	>1.10
Needle, often twins	....	....	....	....	3.70
Trigonal tablets bounded by {001} and {100}	6.62	....	7.92	....	2.82
Needles	10.30	....	4.04	....	2.70
Needles {110} bounded at the ends by {001}	6.485	7.525	8.810	....	3.27
	6.482	7.183	8.810	....	....
	6.452	7.173	8.794	....	....
	6.428	7.449	8.768	....	3.66
Flat needles bounded by {110} and {100}. Needles axis {001}. Often twins on {110}	48.04	15.59	8.10	....	3.83
Cubes {100}	12.625	....	....	....	3.55
Rhombic dodecahedra {110}	12.523	....	....	....	3.61
Pseudo-tetragonal plates or lamellae {001}. Twins or {001}	6.11	6.11	41.4	91°	3.30
Tetragonal plates bounded by {001} and {110}	6.11	....	9.46	....	3.13

4. Experimental Procedure

4.1. Alloy Selection and Preparation

Work-hardenable 3003 Al-alloy was chosen for the investigation of LDC spray deposition by new (modified) USGA linear atomizers. The master alloys were supplied by Aluminum Company of America (ALCOA) in three shipments. The variations in chemical composition of these shipments were very small as shown by the results of chemical analyses listed in Table 8.

Al-alloys in aerospace applications are specified to contain < 0.5% of Fe and Si, which require refinement processes that contribute to higher materials production costs. Rapid solidification processing that refines the grain size, the second phase particles, and increases solid solubilities should extend the limits on impurity concentration levels that are tolerable in any alloys. To investigate the levels of tolerance of the alloy to impurities that result from LDC spray deposition, Fe and Si contents in the 3003 alloy were increased by 1% each. To also simulate the elemental pickup associated with recycling from shredded loads of Al-alloys, Cu and Mg were also added. A charge of the 3003 master alloy from the third shipment was first melted in an induction powered foundry unit and superheated to 1000°C under argon cover. Fe, Si and Cu were then added to the melt. In addition to the induction stirring, the melt was mechanically stirred to insure complete dissolution of these elements. Mg was added to the melt just before pouring it into ingots of 2.5" x 1" x 4" sizes. These ingots were then remelted in the LDC atomization chamber and spray deposited. The compositions of these deposits, referred to as "modified 3003", are shown in Table 9. The chemical analyses of all the alloys were done at ALCOA.

Water and pure tin were also used to simulate the influence of certain LDC atomization parameters and to characterize the improvements realized by the new nozzle geometry. Because of the low inflammability, toxicity and melting point of tin, the atomization runs were done at open air where instrumentation for the high speed photography was easier to assemble for a closer look, and preparation for the runs was faster.

Table 8. Chemical Compositions of the 3003 Aluminum Master Alloys.

Alloy Designation	Shipment No.	Atomization Run #	Mn %	Fe %	Si %	Cu %	Mg %	Zr %	Al %	Density [g/cm^3]
3003	1st	67, 69, 70, 73, 75	1.20	0.76	0.60	0.16	0.04	0.09	bal. = 97.15	2.7359
" "	2nd	76, 77, 78, 81, 82, 94, 95, 96, 98,99, 101,102,	1.12	0.69	0.57	0.15	0.04	0.09	bal. = 97.34	2.7332
" "	3rd	112, 113, 116, 120, 121	1.13	0.71	0.57	0.16	0.04	0.08	bal. = 97.29	2.7343

Table 9. Chemical Compositions of the Modified 3003 Al-alloys Deposits.

Alloy Designation	Atomization Run #	Mn %	Fe %	Si %	Cu %	Mg %	Zr %	Zn %	Al%	Density [g/cm^3]
Modified 3003	122	1.00	1.66	1.78	1.52	2.20	—	0.14	bal. = 91.70	2.7375
" "	126	0.98	1.73	1.74	1.46	2.10	—	0.14	bal. = 91,85	2.7379

4.2. LDC Atomization Apparatus

The atomization apparatus of the LDC process consists of an atomization chamber (tank), an induction heating unit, a gas supply assembly, a powder collection unit, and an exhaust line as shown schematically in Figure 15. The atomization chamber is made of stainless steel with an inside diameter of 90 cm and a wall thickness of 6.5 mm. The lower section of the tank is tapered to a conical shape with an end opening of 6.35 cm diameter, where a powder collection cyclone unit is attached. The tank is sealed by O-rings, gaskets, swage lock and pressure type tube connections; and can sustain both low vacuum and high pressure levels. The chamber houses the following main parts of the LDC process:

(a) The melting section, which consists of induction leads, induction coil, crucible, tundish, and resistance heaters.
(b) The atomization nozzle, which can be either linear or circular, and the respective gas feeding lines.
(c) The substrate assembly, which can be used with or without water cooling.
(d) The powder collecting unit, which consists of a cyclone that separates the powder from the exhaust gas, and a powder storage box.

Figure 16 shows a schematic representation of the chamber and its main parts. The chamber is also equipped with five pass-throughs (windows) that allow the transfer of gas, water and electricity into the chamber, and the collection of data and images from it during the atomization run. Four of these pass-throughs are on the sides of the tank at 90° angles from each other, with one facing pair (at 180°) near the top of tank and the other pair close to the mid-section. The fifth pass-through is at the center of the top cover of the tank. Figures 17 shows the configuration and the kind of inlets and outlets in use. The chamber has two exhaust lines. The main line is connected to the cyclone unit and is usually used alone, whereas the second exhaust line is employed in the case of pressure built-up inside the chamber. The pressure can built-up either due to clogging of the main exhaust line by loose matter such as insulation batches, or due to gas delivery into the chamber at higher rates than

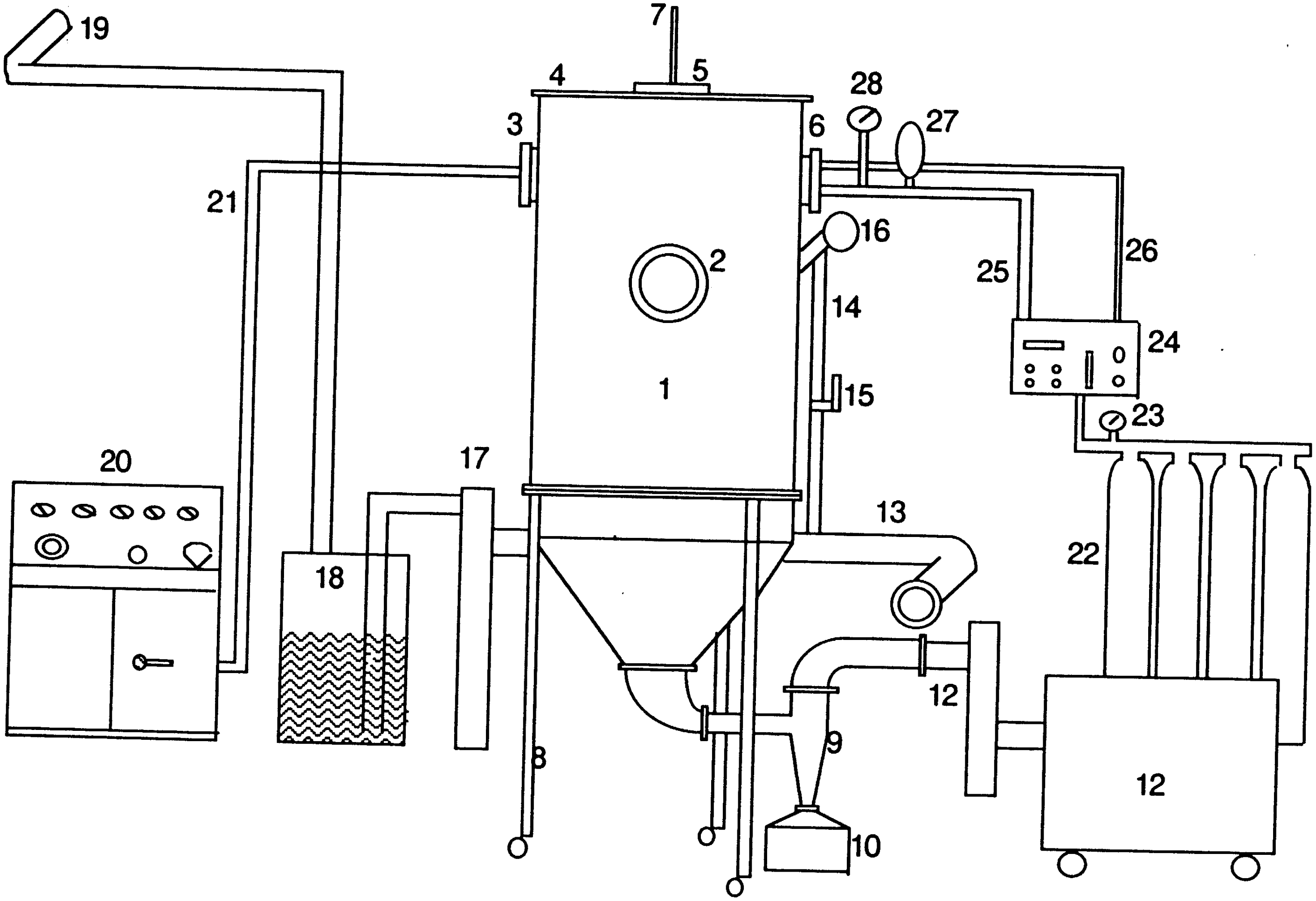

1. Atomization chamber
2. Front window
3. Left side window
4. Chamber top cover
5. Top center window
6. Right side window
7. Stopper rod extension
8. Chamber support legs
9. Cyclone
10. Powder collection box
11. Vacuum pump filter
12. Vacuum pump
13. Main exhaust line
14. Secondary exhaust line
15. Secondary exhaust valve
16. Safety rupture disc
17. Exhaust filter
18. Soap water exhaust filter
19. Exhaust into the ambient
20. Induction generator
21. Induction lines
22. Gas reservoir
23. Gas reservoir pressure gage
24. Gas assembly control board
25. Atomization gas line
26. Back-fill gas line
27. Atomization gas valve
28. Atomiz. gas pressure gage

Figure 15. Schematic Representation of the Atomization Facility.

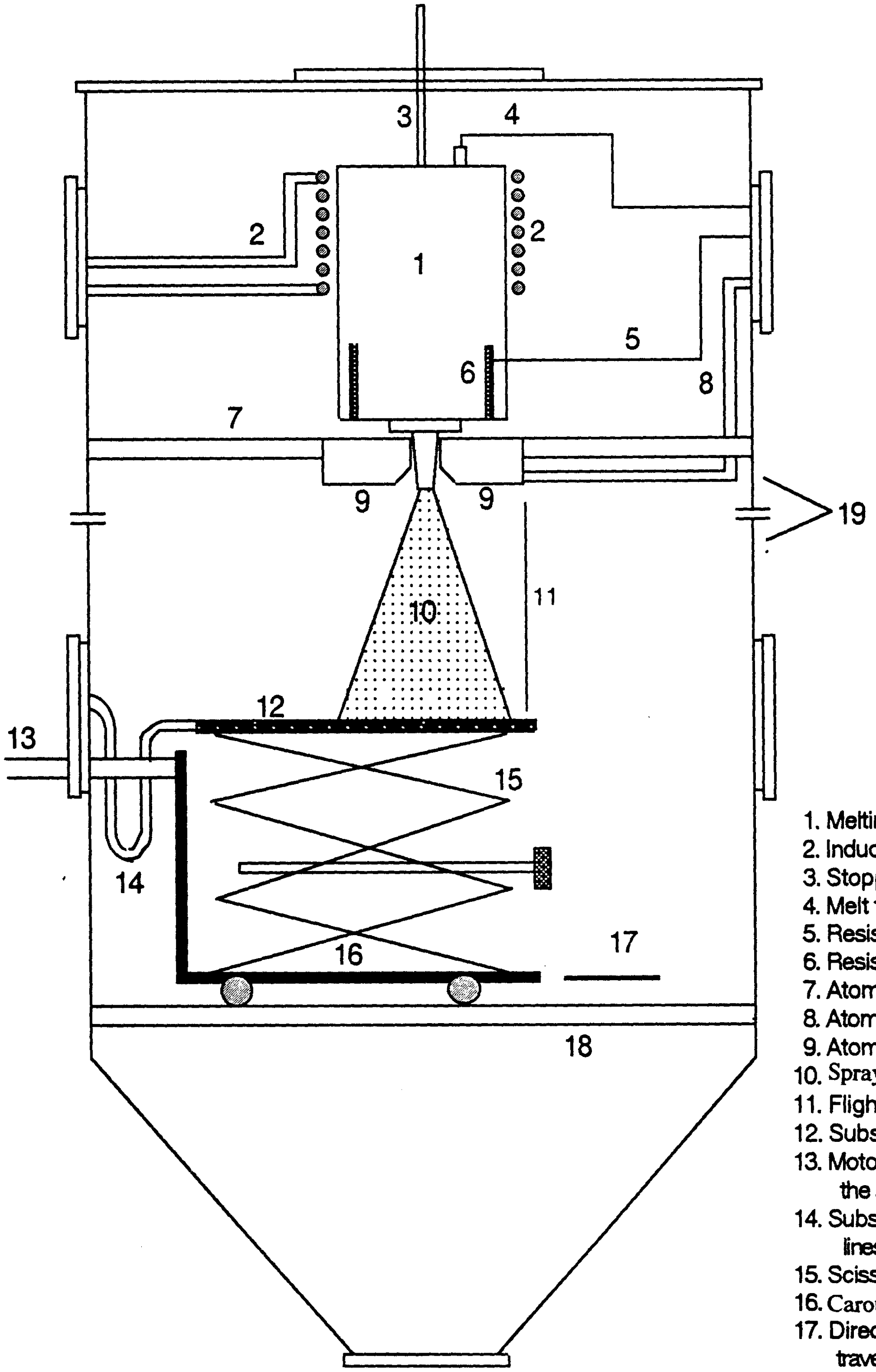

1. Melting unit
2. Induction lines and coil
3. Stopper rod extension
4. Melt thermocouple
5. Resistance heating line
6. Resistance heaters
7. Atomizers support
8. Atomizer gas lines
9. Atomizers
10. Spray plume
11. Flight distance
12. Substrate
13. Motor shaft that moves the substrate
14. Substrate water cooling lines
15. Scissor jack
16. Carousel
17. Direction of substrate travel
18. Support rails
19. These tank halves are at 90° rotation

Figure 16. Schematic Representation of the Atomization Chamber

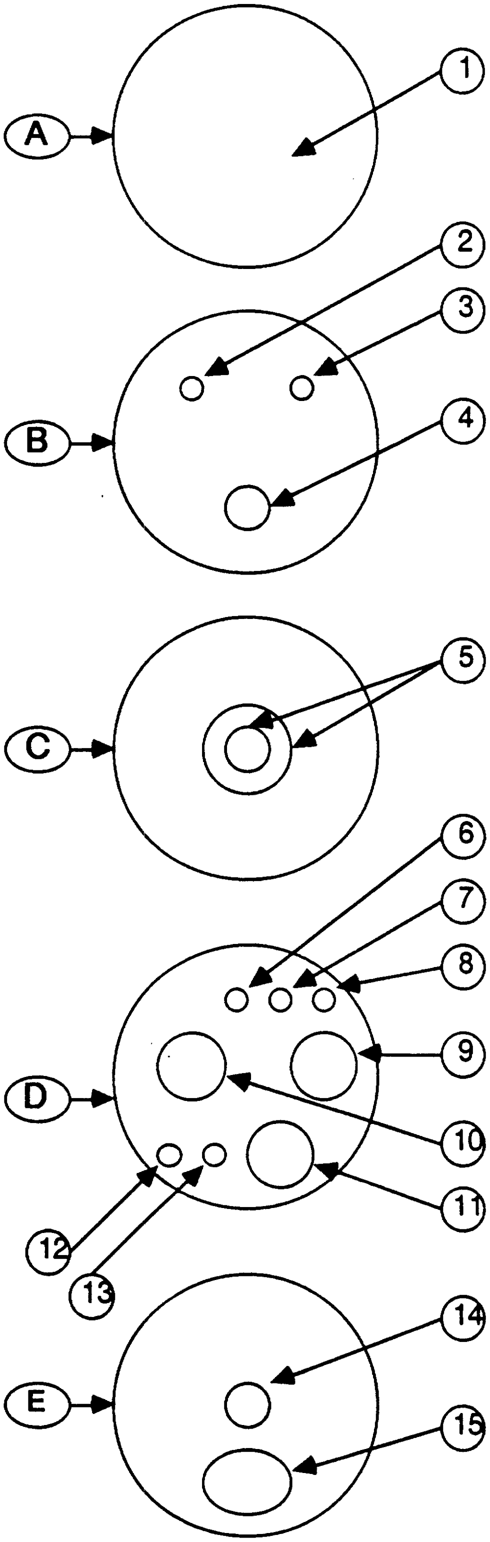

A. Front window

1. Transparent plexiglass for viewing

B. Back window

2. Substrate cooling water inlet
3. Substrate cooling water outlet
4. Motor shaft inlet

C. Left side window

5. Induction line inlet

D. Right side window

6. High vacuum pressure gage
7. Low-vacuum high-pressure pressure gage
8. Inert gas back fill line
9. Electricity connections lines
10. Thermocouple connection lines
11. Atomization gas inlet
12. Atomizer air cooling inlet
13. Atomizer air cooling outlet

E. Top center window

14. Stopper rod extension outlet
15. Plexiglass for observation

Figure 17. The configuration and types of inlets and outlets of the atomization chamber windows

the exhaust gas evacuation rate through the main exhaust line only. A safety rupture disc (4" CDCV, 316-Tef-316) that breaks at 8.5 - 16 psi is place at the top of the secondary exhaust line.

4.2.1. Linear LDC Atomization

The melting assembly and its parts in a linear atomization setup are schematically shown in Figure 18. A graphite/clay crucible of size #25 was used to melt the Al-alloys. At the bottom of the crucible, a funnel shaped hole with 12.7 mm major diameter, and a 6.35 mm minor diameter with a conical angle of 120° was drilled. Either a high density alumina or a graphite rod of 30 cm length and 15 mm diameter, with one end machined to a conical shape of 120° angle, is fitted into the crucible hole to prevent the melt from leaking. This rod, known as "stopper rod", is connected to a stainless steel extension by mechanical coupling. This extension comes out of the chamber through a Cajon O-ring vacuum fitting at the top window. The stopper rod is held in place until the melting and the necessary superheating is completed, then it is pulled out to deliver the melt into the tundish. The temperature measurements of the melt and other heated areas were measured with "K" type chromel (Ni-Cr) alumel (Ni-Al) thermocouples.

The tundish was made of high density, graphite cylinder halves that can be easily assembled, and dismantled if the melt freezes in it. The two halves are held together by pins and a support ring made of graphite. At the bottom of the tundish a rectangular hole of 25 mm x 110 mm was drilled. A linear slit which was also made of two halves that easily assemble is attached at the bottom of the tundish. The top end of the slit has the same opening as the bottom of the tundish, and tapers to 35-100 mm x 0.5-0.75 mm opening at its bottom. A ceramic deflector is placed inside the tundish to break the free fall of the melt toward the slit and evenly distribute it across the slit opening. A Fiberfrax (a Carborundum trademark), flexible alumina fiber insulation that contains SiO_2 as a binder is wrapped around both the crucible and the tundish except at their seating surfaces. The tundish sits on 1 cm thick ceramic blocks and a number of thin steel plates that are placed at the top of the atomizers. The ceramic blocks, which were cut from a porous brick, act as insulation

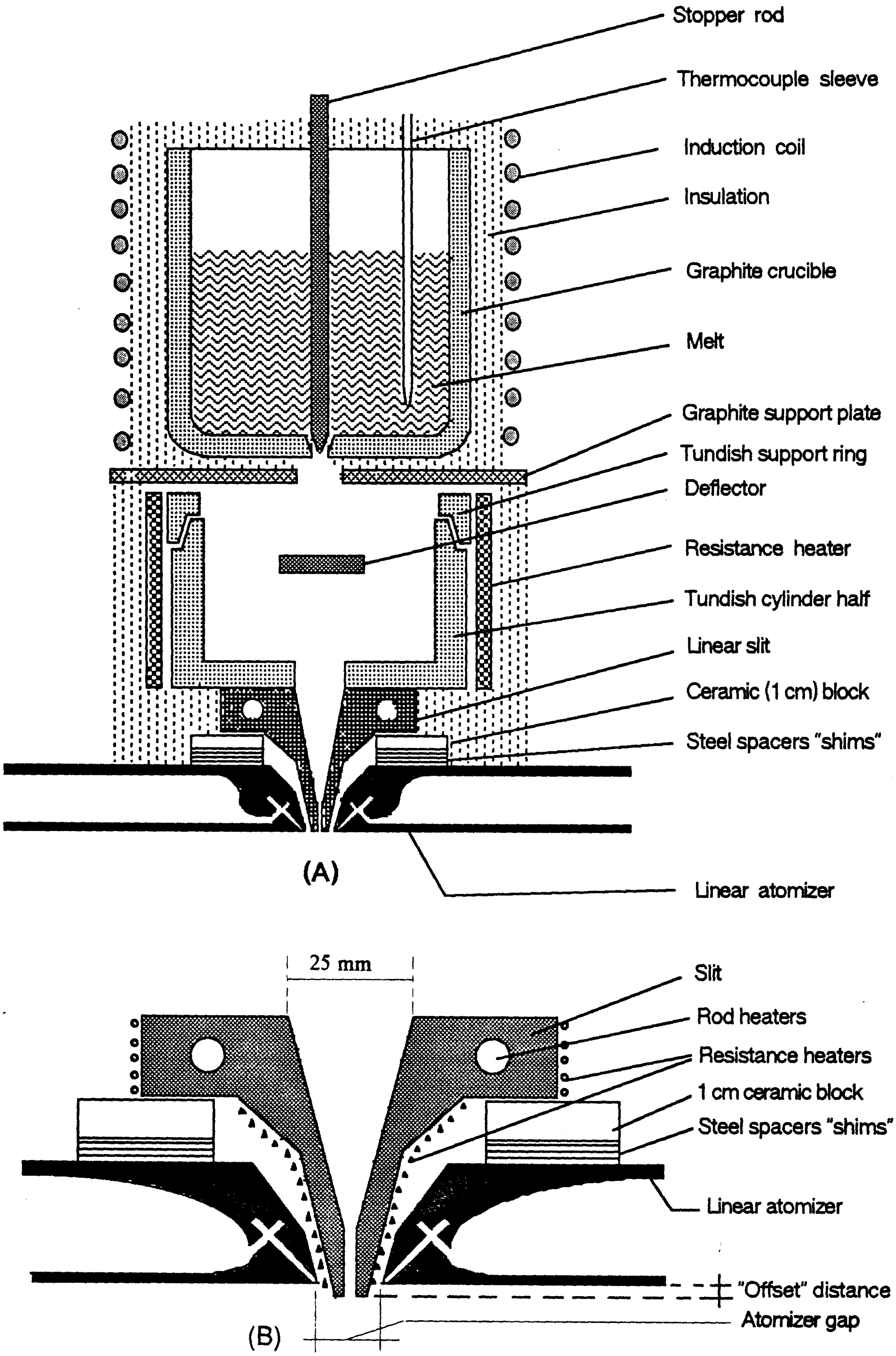

Figure 18. Schematic representation of (A) the melting assembly and (B) a close up view of the atomization zone.

between the bare bottom surface of the tundish and the atomizers. The thin steel plates are shims that are used to set the vertical spacing between the tundish and the atomizers. All the surfaces of the crucible, stopper rod, tundish and melt deflector that come in contact with the melt are coated with a zirconia wash.

The crucible and the charge are heated by induction in a coil with an inside diameter of 23 cm and a height of 20 cm. The coil is made of 9 rounds of 0.5 inch outside diameter (O.D.) copper tube. This coil is powered by a TEK MG-15 integral motor/generator unit with high frequencies of 9600 Hz output and 15 kW power supply. The assembly of the crucible and the induction coil sits at the top of a graphite plate, with a hole in the center that lies on the top of the tundish.

The tundish is heated by resistance heaters, a large one that is set around the upper cylindrical part of the tundish and a smaller one made of filament woven around the outer surface of the slit. There are additional rod heaters that are place in the long holes at top of the slit. Since it is very important to keep the atomizer as close as possible to the melt delivery exit, the total thickness of the slit and the surrounding heating filament and insulation should be kept as small as possible, without adversely affecting the heating efficiency of the filaments and the insulating efficiency against heat losses at the slit-atomizer contact areas.

As the melt is delivered through the slit, it is atomized by jets of gas from the linear (USGA) atomizers. The gas exit of these modified atomizers has Hartman configuration cavities as do the rest of linear and circular USGA atomizers. However, the design of the gas feeding geometry has been changed to improve the gas delivery efficiency as shown schematically in Figure 19A. The gas first enters at the back end of the atomizer through vanes that direct it evenly along the atomizer gas exit. In older linear atomizers, the gas was fed either from the side or from the back with configurations that restrict even distribution of the gas pressure across the length of the linear gas exit as shown in figure 19B. The atomizer gas exit area is 100 mm x 0.6 mm, where the 0.6 mm width can be varied by inserting spacers.

The atomization gas pressure is monitored by two pressure gages, a digital one located at the control board of the gas assembly, and an analog one placed close to the entrance of the gas line into the chamber. The gas reservoir consists of 16 cylinders on a holding rack, from which any number of cylinders can be used depending on the type of the atomizer and the necessary atomization gas pressure. The reservoir gas pressure level is read from an analog pressure gage. The gas pressure is set at the control panel by a high pressure regulator, while the gas is released (fired) by an electromagnetic solenoid valve (spring return pneumatic actuator).

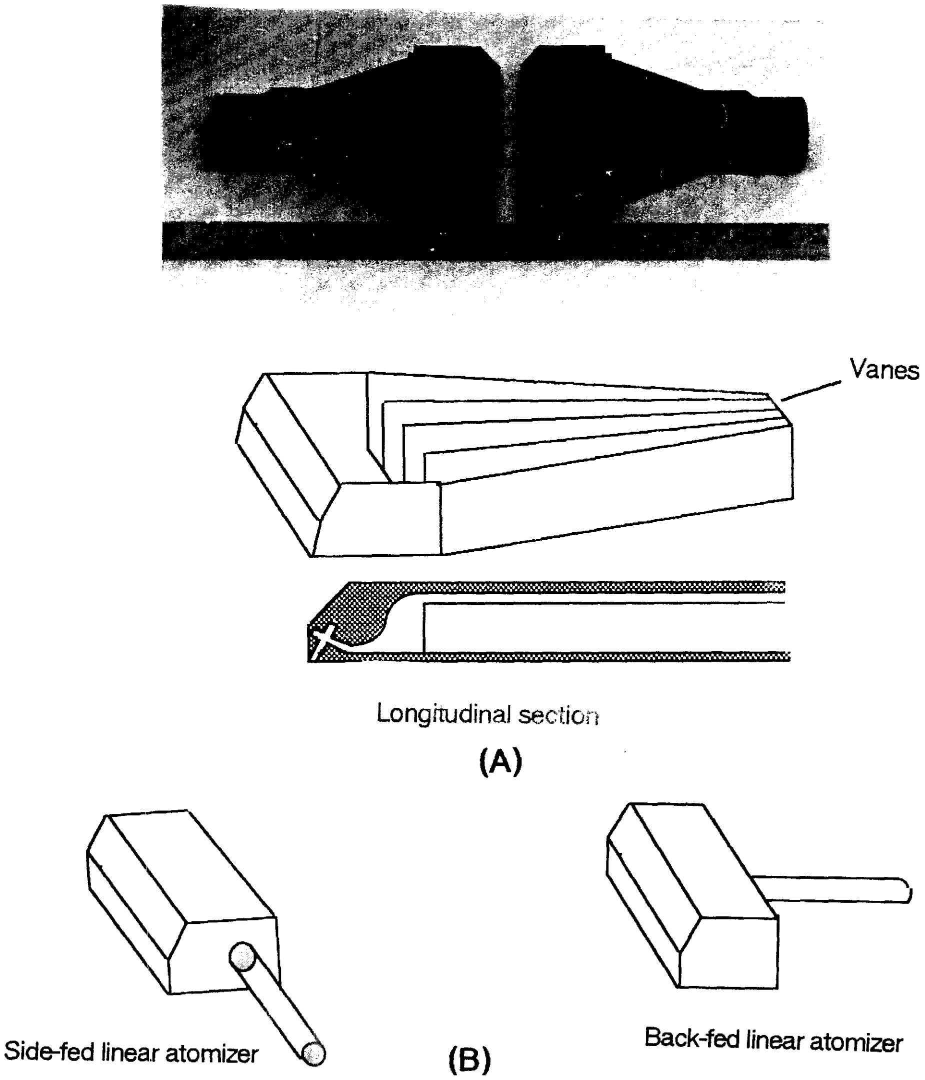

Figure 19. Schematic representation of (A) the geometry of the new linear atomizer and (B) The older linear atomizers and their gas feeding geometries.

The partially solidified droplets then deposit on the cooled substrate that lies at a predetermined distance, called "flight distance", from the atomizers. The substrate is cold rolled steel plate of 21 cm x 43 cm x 1 cm size with grit blasted surfaces of 15-16 μm roughness. At the bottom of the substrate, a brass jacket, through which high pressure cooling water runs, can be attached if desired. The cooling water enters the tank from the back window through vacuum fittings. LDC spray depositions were made with and without water cooling to investigate its effect on the deposit grain sizes.

The substrate and the brass jacket assembly is placed on laboratory scissor jack which is mounted on a carousel that travels on steel caster wheels on two "L" shaped beam rails. The carousel is driven by a Bodine (1/4 h.p., 45 lb.in torque) electric motor with variable speed control that is mounted outside the tank. A matched screw and nut mechanism converts the rotation of the motor to translational velocity of the stage through a shaft that connects them. This shaft enters the chamber from the back window through O-ring vacuum feed-throughs. The rails can be mounted at any of three vertical levels spaced at 16 cm to adjust large variations of the flight distance, whereas small variation of the flight distance can be set with the scissor jack.

4.2.2. Circular LDC atomization

The circular LDC atomization system has the same main parts as the linear LDC. The only difference exists in the melting section and the atomizer geometry. In the circular LDC, only the crucible is used for both melting and delivering the melt to the atomization zone, and there is no tundish as shown on Figure 20. A melt delivery tube made of alumina with 6.35 mm outer diameter (O.D.) and 5 mm inner diameter (I.D.) is fit into the hole at the bottom of the crucible. A larger alumina tube of 9.5 mm O.D. and 6.5 mm I.D. and a steel support ring are mounted at the bottom of the crucible, concentric with the smaller tube. This setup forms a double tube assembly that both delivers the melt and act as insulation against heat losses from the inner delivery tube. The crucible and the melt delivery assembly are held together by a ceramic glue called "Ceramabond 569" from Aremco. A stopper rod is also used to plug the bottom of the crucible. The crucible is then placed at the top of the circular atomizer, where the double tube fits into the annular space formed at the center of the atomizer. The atomizer is made of a circular tube with 18 gas delivery holes, of 9 mm^2 total exit area, lined on one pitch circle at the bottom of the ring. These holes converge into an included angle of 45°. A copper tube, through which either cooling water or gas runs, is wound around the circular atomizer to prevent overheating due to its close proximity to the crucible.

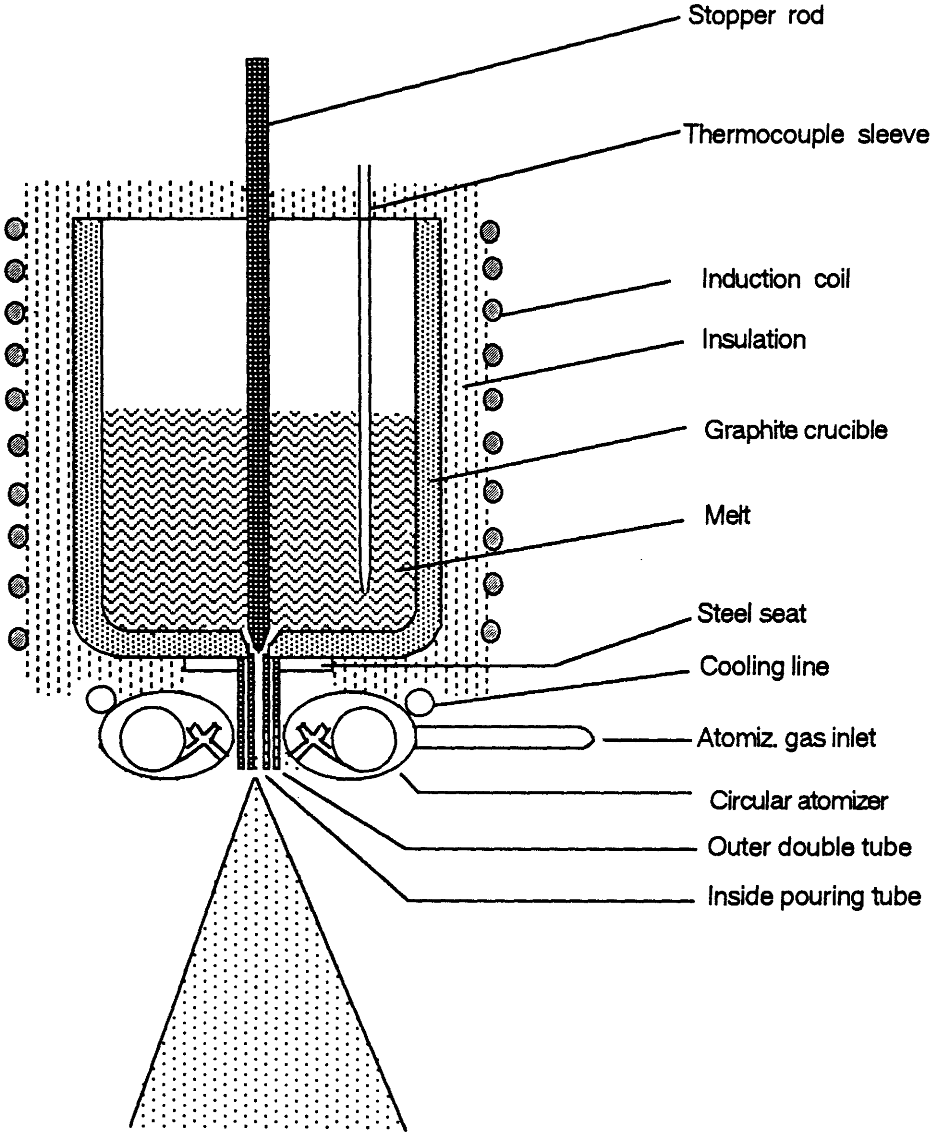

Figure 20. Schematic representation of the circular LDC melting and atomization setup.

4.2.3. Aspiration Gas Measurements

Depending on the relative vertical level between the atomizer gas exit and the melt delivery slit exit, variable pressure conditions are realized in the zone around the tip of the slit - atomization zone. This vertical distance is referred to as the "offset distance". The thin steel plates under the 1 cm thick ceramic plate, above which the tundish sits, are used to set the required off-set distance and hence the aspiration pressure. Close schematic representation of this area was shown in Figure 18b. Depending on the aspiration or back pressure created at the slit tip, the rate of melt delivery to the atomization region can either increase or decrease. If a back-pressure is large enough to overcome the melt head pressure then the melt delivery is completely stopped. Aspiration pressures that exist across the slit were measured at five positions along the slit opening. The average aspiration pressure that exists throughout the slit was also measured. A linear copper slit with five holes spaced at 20 mm was used for the aspiration measurements as shown on Figure 21. The aspiration pressure was measured as a function of the offset distance and the atomization gas pressure, while other variables such as the atomizer included angle (45°), gas exit area, and atomizer gap spacing were kept constant. The aspiration pressures were calculated from differences between ambient pressure and the pressure at the tip of the slit during atomization, measured with a barometer. These measurement are intended to map out the behavior of the new atomizers.

4.2.4. Atomization Procedure

The chamber is sealed after all the parts are completely assembled, and all the parameters, such as atomization gas pressure, aspiration pressure, and flight distance are set. The values for these parameters set for the atomization runs, both linear and circular, are listed in Table 10. The chamber is then evacuated down to about 100 mTorr vacuum pressure by a Sargent-Welch (mod.#1398) mechanical pump, with 1500 l/min pumping capacity, which is attached to the main exhaust line. During the early hours of vacuuming, the crucible, the tundish and the charge are heated to 300°C to facilitate the evaporation of any volatile matters and adsorbed water that may exist on these parts. The vacuuming is continued for a long period of time, usually overnight, to make sure any water adsorbed on the inner walls of the chamber during the cleaning the tank (washing) between runs is completely evaporated. After a good vacuum (50 mTorr) is achieved, the chamber is purged with either argon or nitrogen several times. First the chamber is back filled with inert gas to around 10 Torr and then vacuumed for 20-30 minutes. This cycle is repeated a couple or more times depending on how good the vacuum was and how reactive the alloy is. In the last cycle, the chamber is back-filled to 1 psi pressure above atmospheric to ensure no leakage of air into the chamber. The pump is then detached and the exhaust line is reattached to the rest of its line.

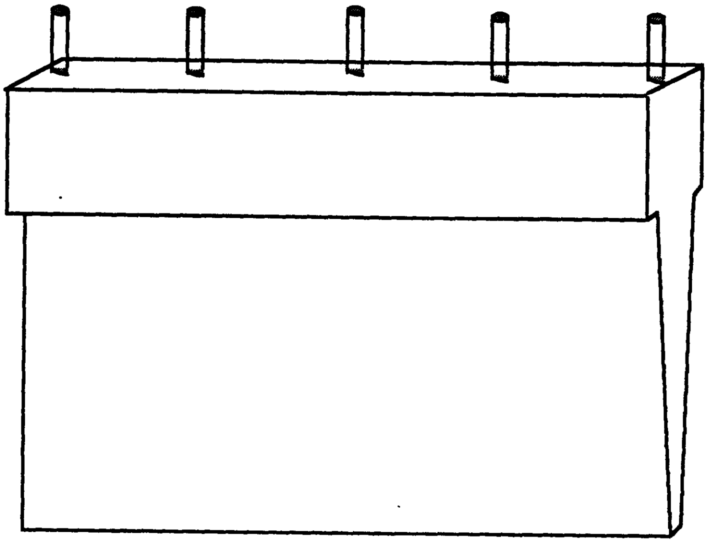

Figure 21. The copper slit showing the five aspiration measurements stations spaced 20 mm from each other along the length of the slit.

Table 10. Values of Parameters Set for the LDC Atomization Runs.

Run Number	#67	#69	#70	#73	#75	#76
Atomizer type	L-sidefed	L-sidefed	L-sidefed	1st Lin.	1st Lin.	1st Lin.
Atomization gas pressure*	100	80	70	70	70	100
Aspiration pressure [psi]	-0.30	-0.39	-0.35	-0.42	-0.44	-0.45
Alloy type	3003	3003	3003	3003	3003	3003
Charge weight [kg]	3.01	2.94	3.00	2.42	2.51	2.51
Melt pouring temperature [°C]	850	850	850	850	850	850
Slit openning size [mm X mm]	0.75 x 71	0.75 x 71	0.75 x 71	0.75 x 71	0.75 x 71	0.75 x 71
Flight distance [cm]	37	37	37	33	30	30
Substrate speed [cm/sec]	0.32	0.46	0.9	1.04	1.04	1.04
Substrate water cooling	yes	yes	yes	No	No	No

* Nitrogen gas was used for atomization and chamber backfilling except for run #67.

Table 10. Continue.........

Run Number	#77	#78	#81	#82	#94	#95	#96	#98	#99
Atomizer type	1st Lin.	1st Lin.	1st Lin.	1st Lin.	2nd Lin.	2nd Lin.	2nd Lin.	2nd Lin.	2nd Lin.
Atomization gas pressure	100	100	70	73	70	70	70	70	70
Aspiration pressure [psi]	-0.35	-0.33	-0.34	-0.33	-0.32	-0.22	-0.26	-0.24	-0.24
Alloy type	3003	3003	3003	3003	3003	3003	3003	3003	3003
Charge weight [kg]	2.08	2.11	2.08	2.19	2.40	2.41	2.46	2.51	2.29
Melt pouring temperature [°C]	800	800	800	800	800	830	820	820	820
Slit openning size [mm X mm]	0.75 x 71	0.75 x 71	0.65 x 71	0.51 x 71	0.5 x 100	0.5 x 100	0.5 x 100	0.5 x 100	0.5 x 100
Flight distance [cm]	30	30	38	42	41	41	41	41	41
Substrate speed [cm/sec]	0.95	0.95	1.52	1.52	2.10	1.52	1.30	2.00	2.00
Substrate water cooling	No	No	Yes	Yes	No	Yes	Yes	Yes	Yes

* Nitrogen gas was used for atomization and chamber backfilling except for run #67.

Table 10. Continue.........

Run Number	#101	#102	#112	#113	#116	#120	#121	#122	#126
Atomizer type	2nd Lin.	2nd Lin.	2nd Lin.	2nd Lin.	2nd Lin.	2nd Lin.	2nd Lin.	Circular	Circular
Atomization gas pressure	70	70	50	50	60	80	100	90	90
Aspiration pressure [psi]	-0.24	-0.29	-0.26	-0.28	-0.88	-1.41	-1.55	-0.34	-0.33
Alloy type	3003	3003	3003	3003	3003	3003	3003	Mod3003	Mod3003
Charge weight [kg]	2.46	2.38	2.65	2.61	2.68	2.84	2.78	2.57	2.50
Melt pouring temperature [°C]	820	820	820	820	820	820	820	770	800
Slit openning size [mm X mm]	0.5 x 100	0.5 x 15	0.5 x 100	0.5 x 100	0.5 x 64	0.5 x 64	0.5 x 64	ϕ 0.5 mm	ϕ 0.5 mm
Flight distance [cm]	41	41	35.6	35.6	N/A	N/A	N/A	35.6	35.6
Substrate speed [cm/sec]	2.12	N/A	2.12	2.12	N/A	N/A	N/A	0.40	0.40
Substrate water cooling	Yes	Yes	No	No	N/A	N/A	N/A	No	No

* Nitrogen gas was used for atomization and chamber backfilling except for run #67.

The charge is melted in a nitrogen environment and superheated to the required temperature. The tundish and the slit are also heated to that same temperature. When the melt is ready, all the heating units are turned down, the cooling lines are turned on, and the melt is atomized. Most of the atomized droplets deposit on the substrate whereas the ones that miss freeze in flight and form "overspray powders" that are collected at the cyclone box after separating them from the exhaust gas. The size, shape and distribution of the collected powders were analyzed by standard Tyler sieves of sizes down to 45 μm, and by optical microscopy. The cyclone may not be able to collect some of the overspray powder of sizes < 4μm which are therefore carried out with the exhaust gas. This lost powder is less than 5% of the total overspray and quite below the standard concentration limits specified in environmental codes. Even so, the gas is still run through a filter and a barrel filled with a solution of soap and water to insure the complete removal of the powder from the exhaust gas before it is released to the atmosphere. When the run is completed the exhaust lines are closed and the chamber is kept at positive pressure, > 1 psi above atmosphere, until everything cools down to avoid solid state oxidation of the deposit and the over-spray powder, and the burning of the graphite tundish. The chamber is then dissembled and cleaned.

4.3. High Speed Photography

During atomization, high speed photography by a Kodak video camera (Ektapro HS Motion Analyzer, Mod. 4540) and an IMACON camera with up to 10^6 frame/sec speed were used to freeze and resolve the mechanism of melt breakup and to determine droplet velocities.

4.4. Structural Examination of the Deposits

All deposits were examined for porosity (sizes and distribution), density, surface quality, deposit thickness profiles and microstructural characteristics. The density was determined by a water displacement method based on Archimedes' principle. An Olympus optical microscope was used for the porosity and microstructural analyses. Samples for optical analysis were mounted in bakellite and mechanically ground with silica grinding papers. Polishing of the samples was done either on a colloidal silica "Mastermet" soaked cloth, or by electropolishing in a solution of perchloric acid ($HClO_4$) and methanol (CH_3OH) in an 1:5 ratio. The samples were then etched for metallographic examination. Etching solutions ranging from Keller's reagent (1 ml HF, 1.5 ml HCl, 2.5 ml HNO_3, 95 ml H_2O), NaOH solution (10 gm NaOH, 90 ml H_2O), Graff-Sargent reagent (3 gm CrO_3, 0.5 ml HF, 15.5 ml HNO_3, 84 ml H_2O) and electroetching with a solution based on the same mixture of $HClO_4$ and CH_3OH were used. Micrographs from the Olympus optical microscope were taken with Polaroid-55 film. The grain sizes were measured from the bottom to the top of the central portion of the deposit cross section. The grain sizes were determined by the linear intercept procedure according to ASTM E112 standard.

An environmental scanning electron microscope (ESEM) operated at 15-30 kV was used to examine the fracture surfaces of the tensile specimens and the distribution of the second phase particles of polished samples with different TMT histories. Since an ESEM was used, coating of the samples with a thin conductive (gold) layer to prevent surface charging was not necessary. An energy dispersive X-ray analyzer (EDXA) mounted on the ESEM was used for compositional analysis of the second phases and the matrix.

Transmission electron microscopy (TEM) analysis was performed for several TMT conditions of the alloys to characterize the type, size and distribution of the second phases, the grain and subgrain sizes and their boundary features. The microscopes used were JEOL 200CX and high resolution scanning transmission electron microscope (STEM VG HB603) which operated at 100 kV and 200 kV, respectively. The TEM samples were first ground to plates 0.2 mm thick from which disks of 3 mm diameter were punched. These disks were further ground with a dimpler machine to around 10 μm thickness and were subsequently milled with an ion beam milling machine (Gatan-duo) at an angle of 10°. To identify the composition of the constituent particles and the matrix, selected area diffraction (SAD) analysis and an EDXA mounted on the STEM were also used.

Differential scanning calorimetry (DSC) analyses on the responses of samples with different TMT histories heated at a rate of 15 °C/min to high temperatures, in order to determine their phase transformation, were undertaken using a Seiko DSC-320.

4.5. Thermomechanical Treatments and Mechanical Tests

Densification of the LDC as-deposited preforms was achieved by hot and cold rolling to around 80% reduction. The as-deposited metals were either homogenized prior to the rolling step or were directly rolled. Rolling samples (rectangular cross sections and parallel surfaces) were cut and milled from the deposits. The first cold rolling pass was usually limited to about 15% reduction to eliminate the alligator type cracking or the severe edge cracking experienced at high first rolling pass reductions. However, the rolling reduction of successive passes could be increased without adverse effects. The hot rolled samples were sandwiched between mild steel plates of 5 mm thickness to reduce the temperature drop of the samples during the time it is removed from the furnace to when it is completely rolled. The cycle of sandwiching, heating, and rolling of the sample is repeated for each rolling pass. A "K" type thermocouple in contact with the sample reads the sample temperature. Rolling temperatures of 25-500 °C were selected to investigate the effect of rolling temperature on the mechanical properties of the alloys. A rolling mill with 15 cm roll diameter that operated at 16 rpm was used. The rolled samples were then annealed at temperatures between 300-500°C at various time periods.

The effects of annealing temperature and time on the samples were examined through hardness measurements, and optical and electron microscopy observations. Coupons were cut from the annealed samples and were ground to have parallel surfaces for hardness testing. The hardness measurements were done on a Wilson Rockwell hardness tester using the Rockwell 15T (15 kg and 1/16" steel ball indenter) surface hardness scale since the alloys were too soft for other scales.

Tensile specimens were cut from the annealed samples and tested on an Instron universal machine. Details and dimensions of the tensile specimens are shown in Figure 22. All tests were run at room temperature with constant head speeds of 0.01 and 0.02 inches per minute (strain rate of around 10^{-4} /sec) with a 1000 kg load cell. Tensile properties of the substandard sized smooth specimen were determined according to ASTM E 8. The general sequence of the thermomechanical treatments and mechanical tests are summarized in Figure 23.

4.6. Water and Tin Atomization

Water and tin were atomized in a setup similar to the one shown in Figure 24, using the modified new atomizers, the tundish and the slit. Different conditions of aspiration pressures and atomization gas pressures were used for simulation. The water flow rates at different levels of water head pressure were measured. The tin was first melted in a separate container then transferred to the tundish and atomized. Tin droplet velocities were determined by using the Imacon camera. The liquid breakup of the water and the tin were studied with a high speed Kodak video camera.

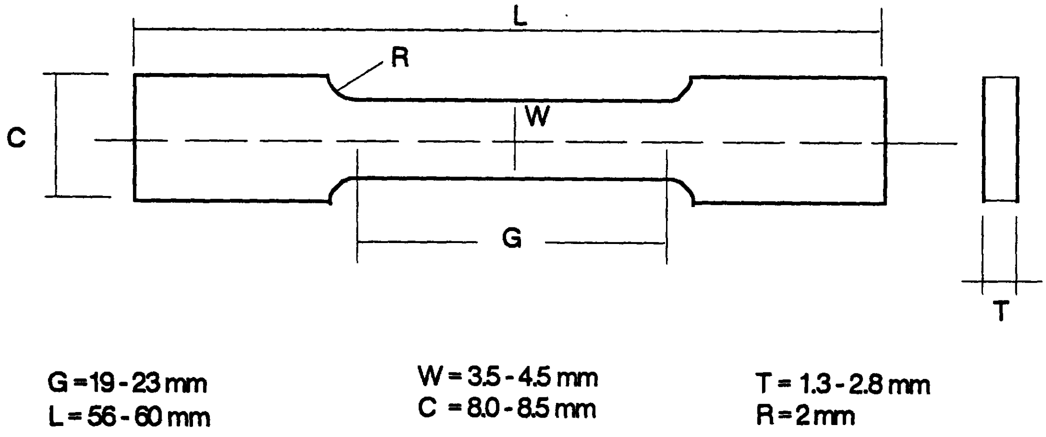

Figure 22. Dimension of the Room Temperature Tensile Specimen

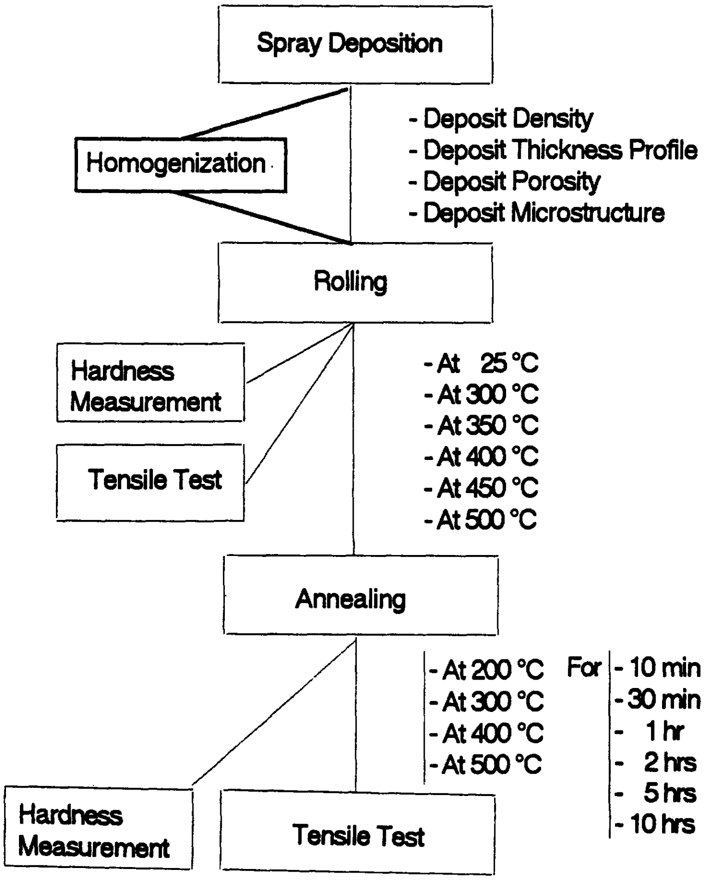

Figure 23. The general sequence of the thermomechanical treatments and mechanical tests.

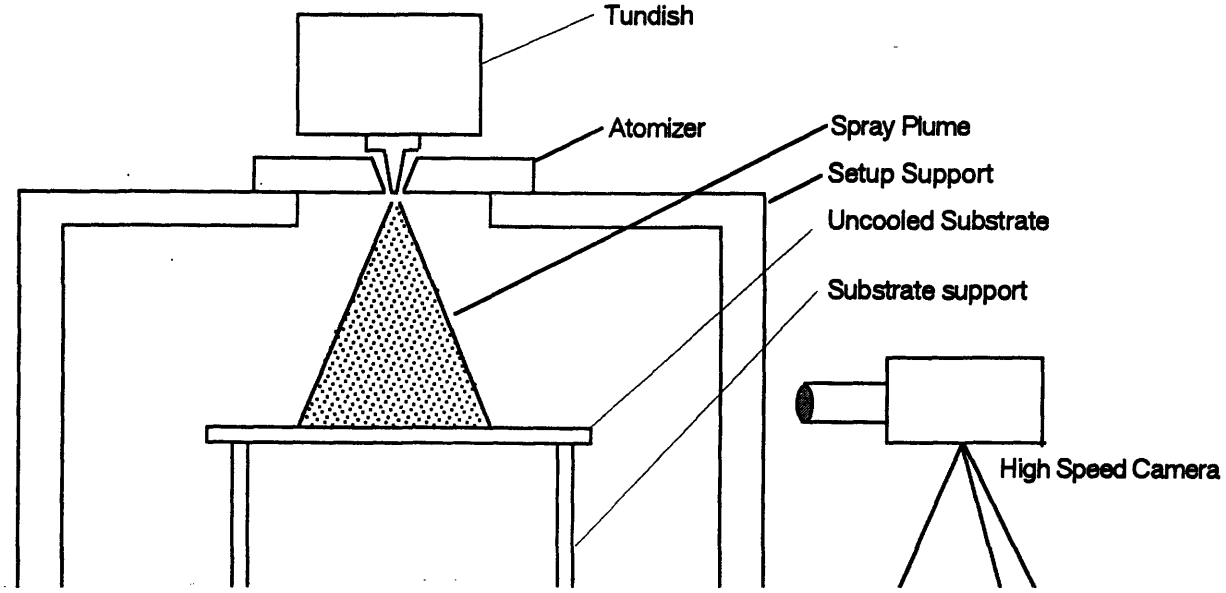

Figure 24. Schematic representation of the water and tin atomization setup

5. RESULTS AND DISCUSSION

5.1. LDC Spray Deposition

5.1.1. Aspiration Pressure Measurements

One of the most important parameters of the LDC atomization process is the pressure that is created at the tip of the metal delivery slit during the run. This area, which is also referred to as "the atomization zone", is where the gas impinges on and breaks up the metallic stream. Interference due to the presence of the melt delivery slit in the path of the atomization gas leads to various pressure magnitudes at this zone. Depending on the positioning of the melt delivery slit relative to the level of the atomizers gas exit, three different pressure conditions are realized:

(1) low pressure, which causes "aspiration" of the melt inside the slit,
(2) no change of pressure, which is similar to a "free fall condition", and
(3) high pressure, which causes pressurization and restriction of the melt flow. It is referred to as "the back-pressure regime".

The relative positioning between the atomizers and the slit in these three pressure conditions are shown in Figure 25A. When the path the gas is tangential to the corners of the slit tip, the free fall condition is realized. If the slit tip is raised above the free fall level, the gas jets impinge on each other below the slit tip, force part of upwards and create back-pressure at the slit tip. However, if the slit tip is below the free fall level, the gas jets first hit the slit sides, get deflected downward, drag out the fluid in the slit by creating aspiration pressure. As the slit is moved further down into the gas impinging zone, the aspiration pressure first increases, reaches a maximum, and then begins to decrease.

These pressure conditions influence, among other parameters, the melt flow rate. When there is no change of pressure at the tip of the melt delivery slit, the melt flow rate corresponds to free fall, driven only by the the melt height level in the tundish (the metallostatic pressure head). In the aspiration regime, the melt flow rate increases to more than the melt free fall rate due to the suction created at the tip of the slit. Whereas, in a back pressure condition, the melt flow rate is reduced. At a certain magnitude of back-pressure, the melt flow can be completely stopped.

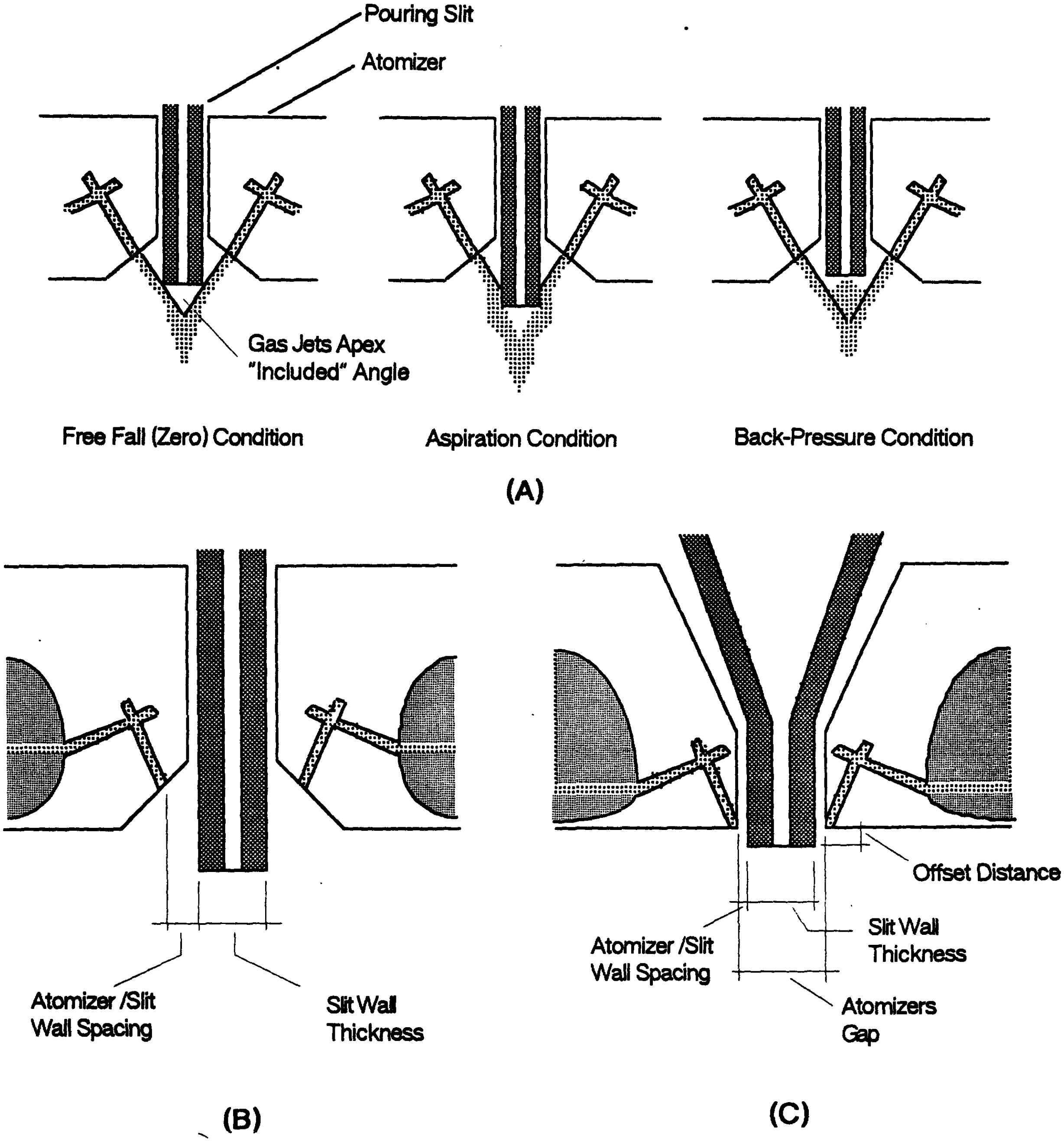

Figure 25. The positioning of the slit relative to the atomizers: (A) its effect on the pressure at the atomization zone, (B) old linear atomizer setup, and (C) the new linear atomizer setup.

In addition to the relative vertical level between the gas exit and the melt delivery tip (also knows as the "offset distance"), these pressure conditions depend on the atomization gas pressure, the gap between the atomizers, the apex (included) angle between the atomization gas jets, and the horizontal spacing between the gas exit and the slit wall. These parameters, some of which are geometrically defined in Figure 25A-C, determine the distance the gas jets travel before they reach the atomization zone and the extent the gas expands. The longer the travel distance the larger the expansion of the gas. As the gas expands, it creates velocity gradients and an increased gas impingement area. It also drags larger amounts of surrounding gas, thus reducing the gas power and the atomization efficiency.

Since the pressure condition at the atomization zone depends on the atomization gas pressure and the geometry of the atomizers and the melt delivery slit, the position of the free fall varies and corresponds to different offset distances. In earlier studies with the old side-fed linear atomizers that had the configuration and geometry shown in Figure 25B, one had to make few pressure measurements to determine the free fall level. This level was then referred to as the "zero vertical position." The pressure magnitude and type at different vertical levels of the slit tip were then measured. A representative curve of the variation of these pressures, which were similarly experienced for both the circular and linear LDC nozzles, is shown in Figure 26. From this curve, it can be seen that a certain aspiration pressure magnitude can be realized at two different slit height levels. The level with the shorter slit height is always selected in the LDC runs in order to reduce the area of the slit on which the gas impinges, and to prevent the melt from freezing in the slit.

In this study, the new atomizers and the slit have different geometries than those in the old linear setup, shown in Figure 25C. The gas exit, which is right at the corner of the atomizer, is very closer to the slit wall. Due to the reduced horizontal spacing between the gas exit and the slit wall, the zero offset distance was chosen to be the position where the gas and melt exits are at the same level instead of the free fall level. Setting the zero position geometrically gave a fixed reference point that simplified the measurements and reproducibility of the pressures at the tip of the slit. This approach eliminated

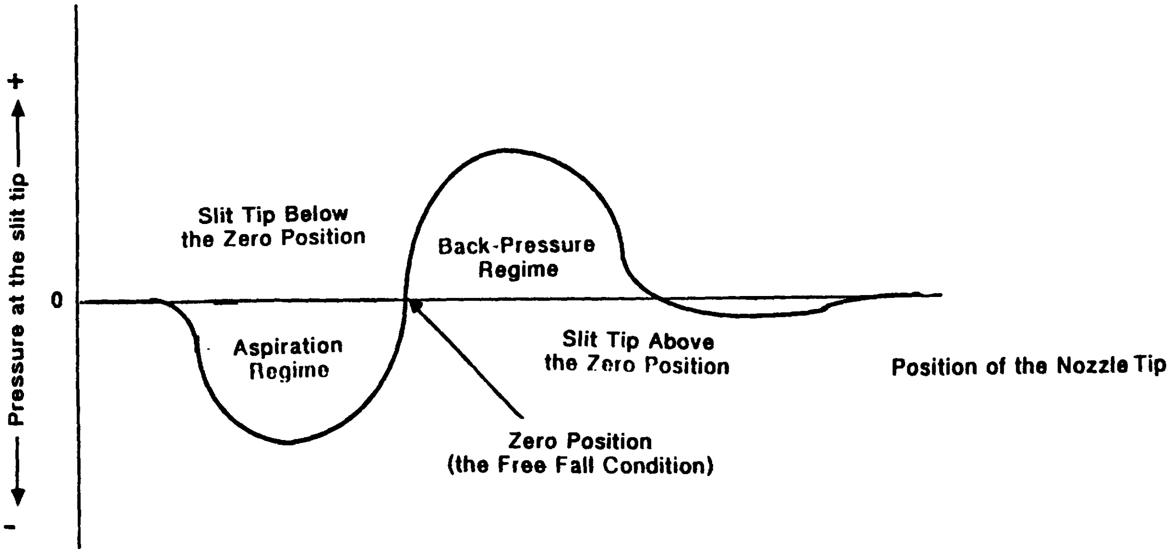

Figure 26. Schematic representation of the pressure at the tip of the melt delivery slit as a function of the position of the nozzle.

the number of measurements made routinely in earlier studies in order to determine the free fall level that was referred to as the zero position.

In a back-pressure condition, if the metallostatic pressure head is large enough to overcome the backpressure, the melt flows at a lower rate than the free fall condition. In addition, the melt will flow laterally to the sides of the melt exit and wet both the slit tip and the atomizers. This melt may then freeze both on the delivery slit and on the atomizers due to the temperature drop by the Joule-Thompson effect from the the expanding gas. When the melt freezes on the tip of the slit, it increases the slit length, the offset distance, and the magnitude of the back-pressure. If this melt freezes at the atomizers gas exit, it plugs the gas exit opening, and may ruin the atomizers. As the melt pressure head decreases in this type of run, the back pressure eventually overcomes the metallostatic pressure head, stops the run, and freezes the remaining melt in the delivery slit and the tundish.

Usually a slight aspiration pressure is utilized in the LDC process in order to insure a complete and smooth atomization run. A high aspiration pressure would increase the melt flow rate and lead to reduced melt break-up efficiency.

Only the aspiration regime at the atomization zone, created by the newly designed linear atomizers, were investigated in this study.

In the linear atomizer, the atomization gas velocity along the length of the gas exit is usually not uniform due to friction at the walls of the gas path. The gas is thus faster at the center and slower at the ends of the gas exit opening. In old linear atomizers, this effect was compounded by the non-uniform gas delivery along the gas exit due to non-ideal gas feeding geometry. The aspiration pressure, created by this non-uniform gas velocity, becomes variable along the length of the slit. In turn, this aspiration pressure, in addition to the friction at the walls of the melt path, and the melt surface energy, leads to a variable melt flow rate along the melt delivery slit. The variable melt flow rate, in turn, promotes non-uniform distribution of the atomized droplets in the spray plume, which eventually form a deposit of variable thickness profile.

To reduce the variation of the gas pressure along the linear atomizer gas exit, the gas delivery unit at the back of the atomizers was redesigned. In the new design, vanes were built in the gas path to form ducts that directs the gas more equally along the atomizer gas exit and lead to more uniform gas velocity. To investigate the improvements of these new linear atomizers, the aspiration pressures, at five stations, spaced 20 mm from each other along the length of the melt delivery slit opening, were measured as a function of the atomization gas pressure and the offset distance. The average aspiration pressure over the entire slit opening of 71 mm x 1 mm was also measured. The results of these measurements for a slit wall thickness of 5 mm and a gap between the atomizers of 5.5 mm are compiled and shown in Figure 27A-C. In Figure 28A-C, the aspiration measurements with a slit of 8 mm wall thickness and a gap of 10 mm between the atomizers is shown.

For a given offset distance, the aspiration pressure increased as the atomization gas pressure was increased. The increase in the aspiration pressure with the atomization gas pressure became greater as the offset distance was increased. From these curves, it can be seen that the aspiration pressure still varied along the length of the slit, from the center to the ends.

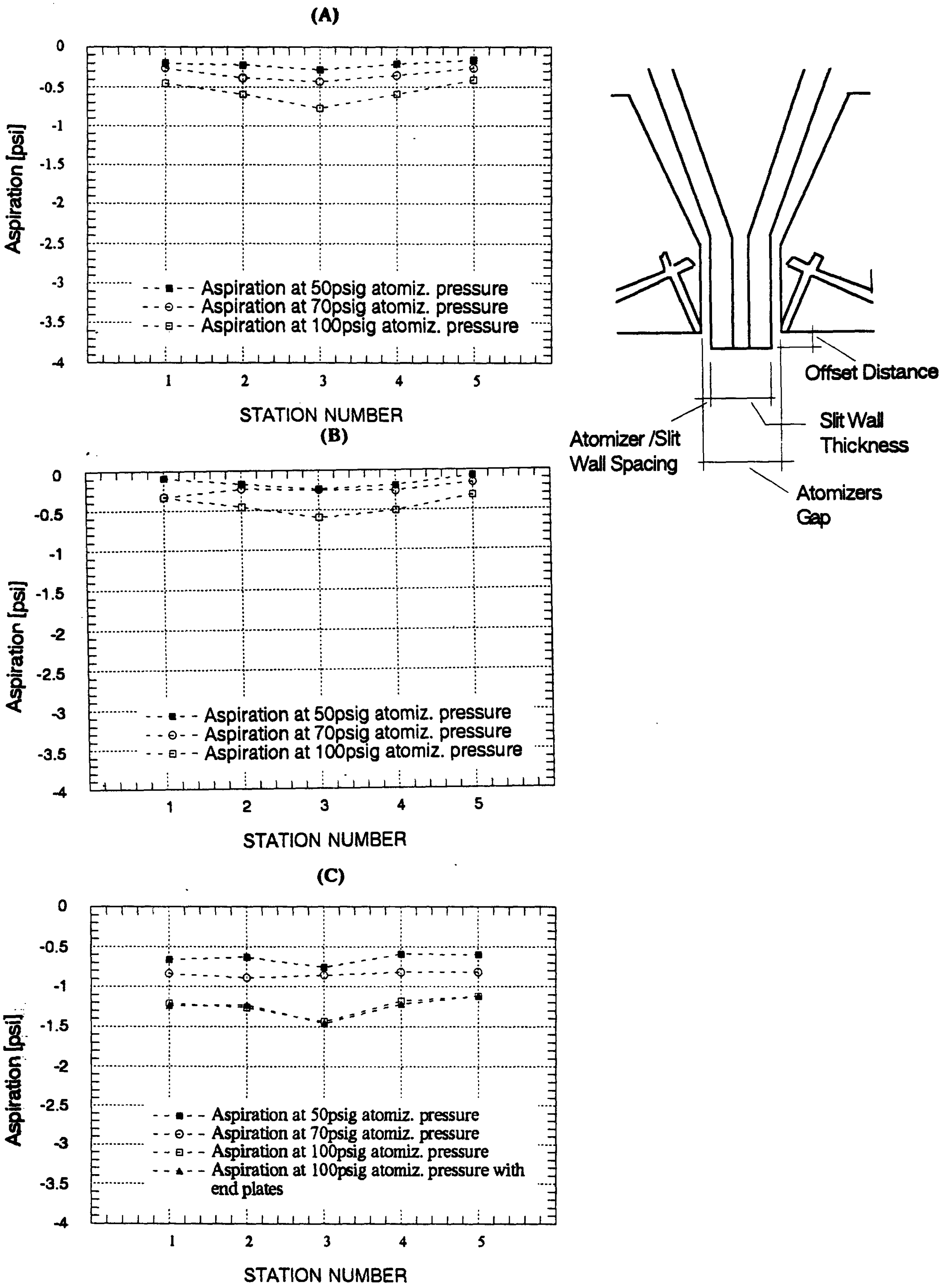

Fig. 27. The aspiration pressures at the stations along the slit with an Atomizers gap of 5.5 mm at offset distances of (A) 3.05, (B) 5.05 and (C) 7.85mm

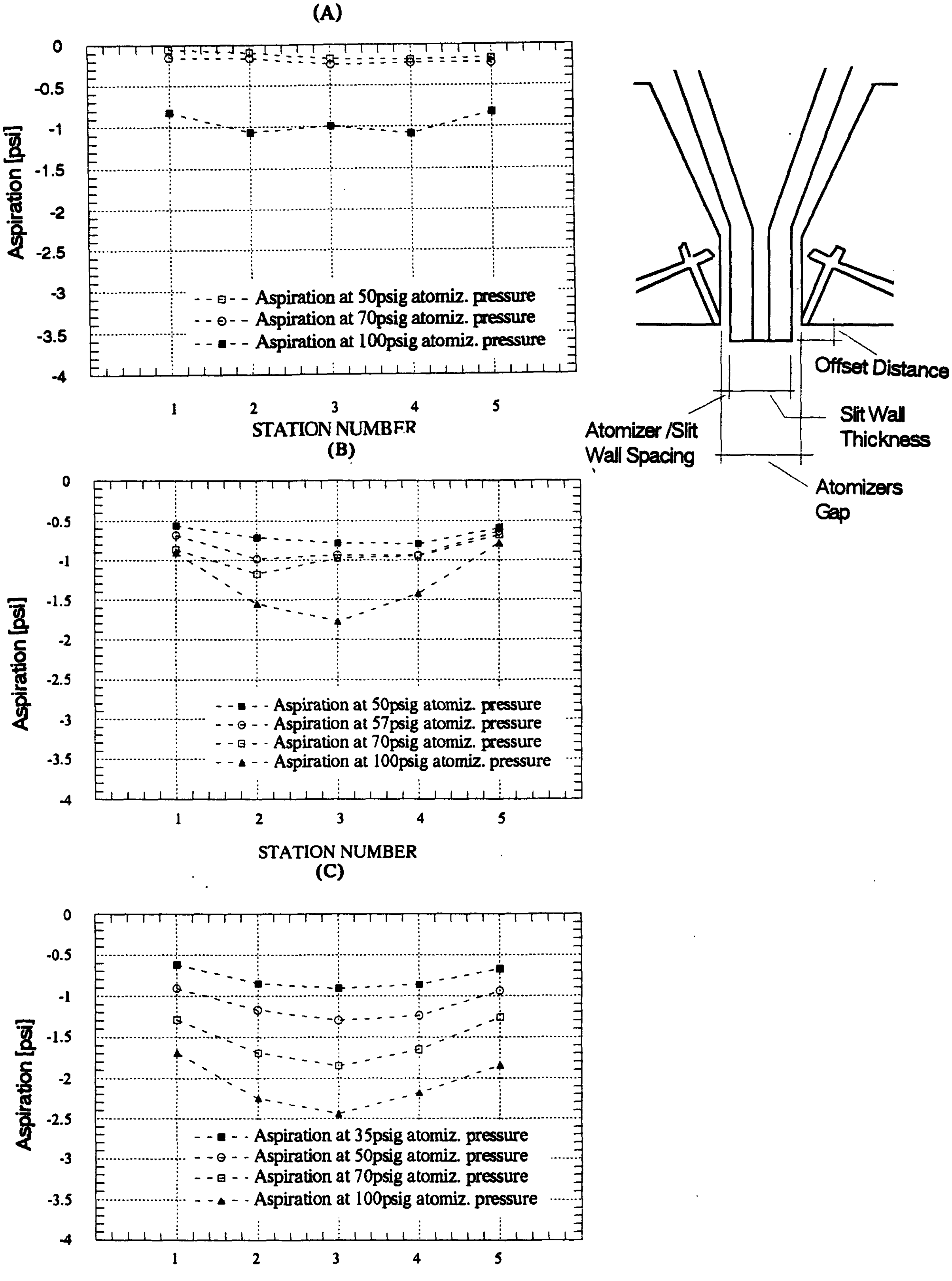

Fig. 28. The aspiration pressures at the stations along the slit with an Atomizers gap of 10 mm at offset distances of (A) 0.39, (B) 2.39 and (C) 9.39mm

Greater atomization gas pressure led to a greater aspiration pressure difference between the center to the ends along the length of the slit. This aspiration pressure variation along the slit was also larger the longer the offset distance. Comparing Figures 27 and 28, It can also be seen that the aspiration pressure increased less with the atomization gas pressure and the offset distance when the atomizer gap was larger. At the same time, the rate of variation of the aspiration pressure from the center to the ends of the slit due to increasing atomization gas pressure and offset distance was smaller when the gap between the atomizer was large.

Deflectors, made of graphite plates, were attached at the ends of the atomizers and the slit to confine the lateral expansion of the atomization gas and to inhibit dragging gas from these sides. These deflectors extended about 1.5 inches below the atomizers gas exit level. However, the aspiration pressures at the five stations along the slit, measured at 100 psig atomization gas pressure, with and without the presence of these deflectors, were identical, as shown in Figure 28C. These readings suggest that the deflectors had, at least, no influence on the aspiration pressures variation for these conditions.

The average aspiration pressure was measured along the length of a slit opening of 71 mm X 1 mm as a function of the offset distance and the atomization gas pressure. Results of these measurements, which were made with a slit thickness of 8 mm and a gap between the atomizers of 10 mm, are shown in Figure 29. It can be seen that at shorter offset distances, the average aspiration pressure varies less with atomization gas pressure compared to longer offset distances, reflecting the same trends shown in Figures 27 and 28. As the offset distance is increased, the average aspiration pressure increases in a steeper fashion at higher atomization gas pressures.

A second new set of atomizers with improved gas distribution vanes and shorter Hartman tubes was made in order to create more uniform aspiration pressures along the length of the slit. The results of the aspiration pressure measurements, made with this set, at the five stations along the slit, at different offset distances, and at atomization gas pressures of 70 and 100 psig, are

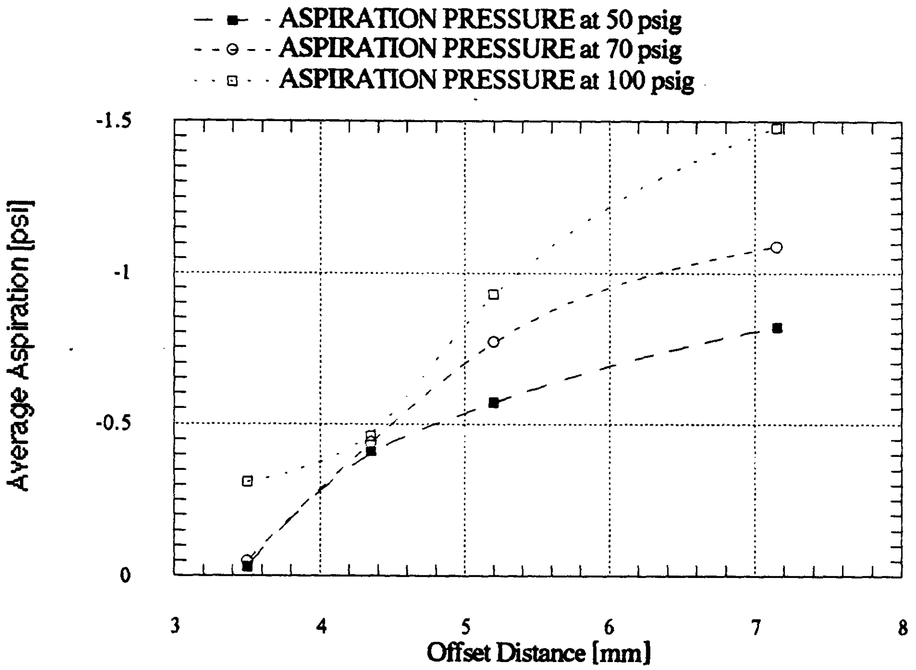

Figure 29. The average aspiration pressure by the first set of atomizers along a slit 71 mm long and a gap between the atomizers of 10 mm.

shown in Figures 30 and 31, respectively. These results show more uniform aspiration pressures along the slit relative to those of the first set of atomizers. The average aspiration pressure along the slit was also measured at different offset distances at atomization gas pressures of 70 and 100 psig. As expected, the average aspiration pressure increased first both with the offset distance and the atomization gas pressure, as shown in Figure 32, and then decreased at higher offsets distance, as the trends in Figures 30, 31 and 32 show.

The aspiration pressure at the tip of the melt delivery slit fluctuates during the atomization run with any type of small perturbation. The metallic head level in the tundish can overcome these fluctuations. An aluminum metallic head level of 10 inches produces a metallostatic head pressure of about 1 psi and can easily overcome small fluctuation of the aspiration along the slit.[24] However, large fluctuations may not be as easy to overcome.

The type of atomization gas slightly influences the pressure conditions, especially in the aspiration regime. The variation of the aspiration pressure with the atomization gas pressure was more pronounced for argon gas than

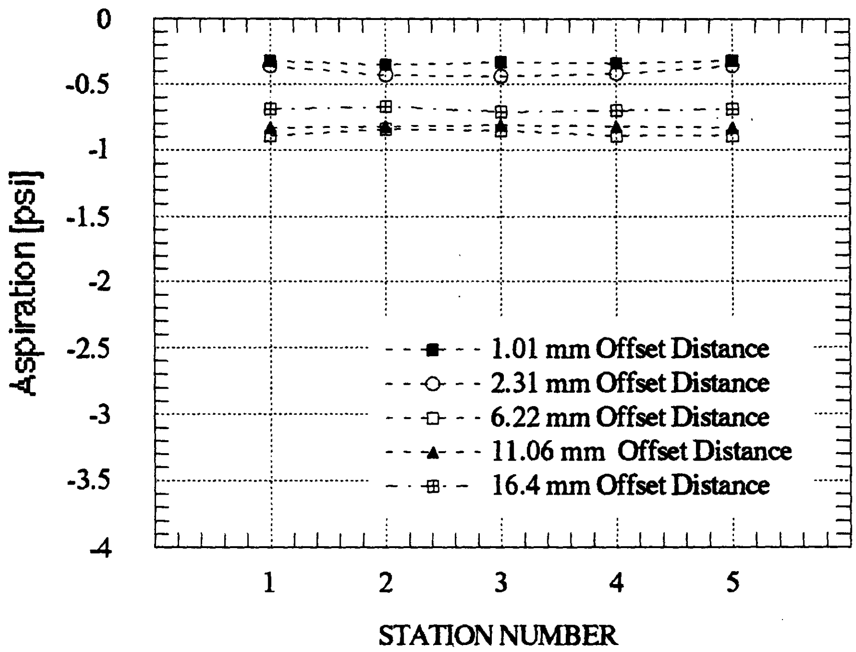

Fig. 30. The aspiration pressure at the five stations measured with the second set of atomizers at a gap of 10 mm and at 70 psi atomization gas pressure.

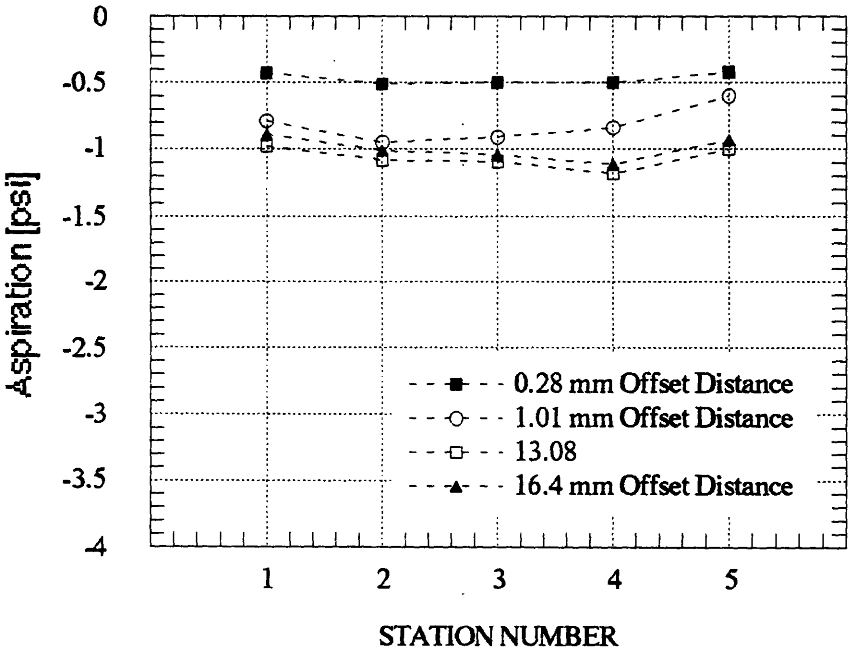

Fig. 31. The aspiration pressure at the five station measured with the second set of atomizers at a gap of 10 mm and at 100 psi atomization gas pressure.

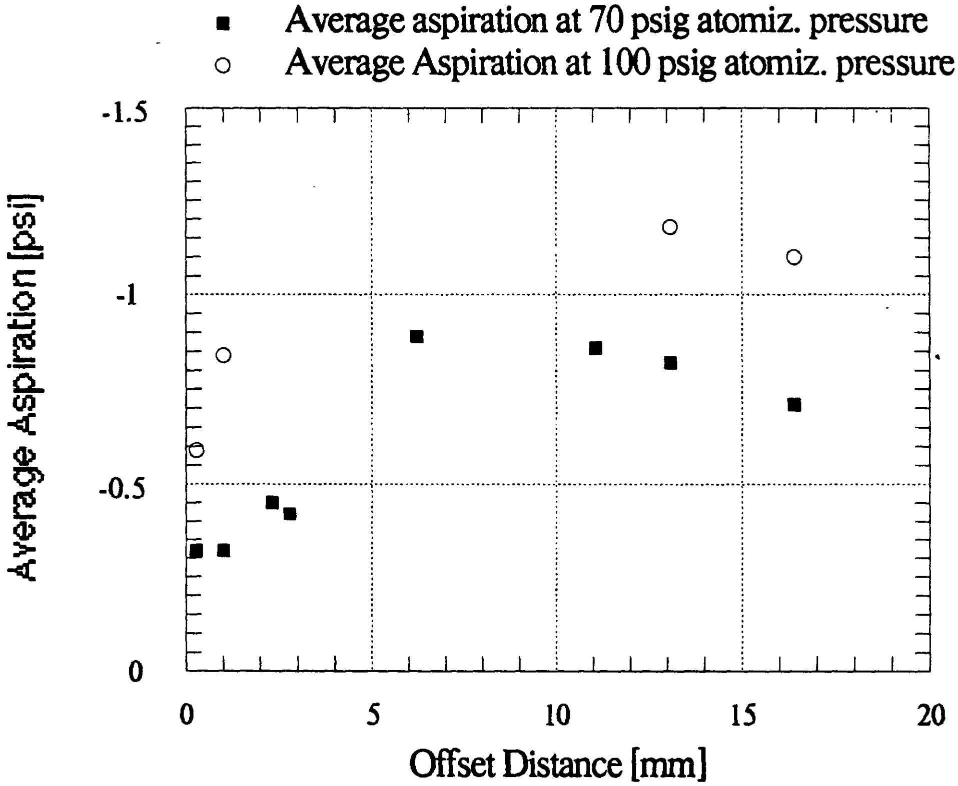

Figure 32. The average aspiration pressure along the length of the whole slit by the second set of atomizers at a gap between the atomizers of 10 mm along.

nitrogen.[80] This effect was thought to be related to the difference of their viscosities at constant atomization gas pressure. The difference in viscosity also explains why argon gas promotes higher melt flow rates compared to helium.[24]

5.1.2. LDC Atomization Parameters.

Some of the parameters that characterize the LDC atomization process, such as the atomization gas pressure, the aspiration pressure, the weight of the melt, the gas and the melt delivery exit areas, are set prior to the atomization run in order to control the LDC process and the properties of its products. The values set for these parameters were listed in Table 10. After the atomization runs were completed, additional parameters that influence the success of the process during the run were either measured or calculated. The values of these parameters are listed in Table 11.

Table 11: Values of the Characteristic Parameters Calculated and Measured for the LDC Runs

Run Number	#67	#69	#70	#73	#75	#76	#77	#78	#81
Initial Reservoir Pressure [psi]	1910	2010	1750	2010	1600	1610	2000	1600	1810
Final Reservoir Pressure [psi]	1200	1800	1500	1700	1260	1300	1600	1350	1620
Reserv. Press. Difference [psi]	710	210	250	310	340	310	400	250	190
Total Reservoir Volume [liter] = No. of cylinders X cyl. volume	4 x 48*	5 x 44*	5 x 44	4 x 44	4 x 44	4 x 44	4 x 44	5 x 44	4 x 44
Mass of the Gas Used [kg]	15.05	3.58	4.26	4.22	4.63	4.22	5.45	4.26	2.58
Gas Delivery Time [sec]	104	36	41	40.8	45	28	35	29.4	26.6
Gas Mass Flow Rate [kg/min]	8.68	5.97	6.23	6.21	6.18	9.05	9.39	8.69	5.83
Mass of the atomized Melt [kg]	2.27	2.88	2.94	2.35	2.46	2.46	2.03	2.07	2.05
Melt Atomization Time [sec]	98	30	31	38	40	22	24	20	22
Melt Mass Flow Rate [kg/min]	1.39	5.76	5.69	3.71	3.69	6.71	5.07	6.21	5.59
Gas Power [W]	13,556	13,272	13,874	13,830	13,750	20,152	20,802	19,348	13,001
Gas/Metal Flow Ratio	**6.25**	**1.04**	**1.09**	**1.67**	**1.67**	**1.35**	**1.85**	**1.40**	**1.04**
Total Metal Charge [kg]	3.01	2.94	3.00	2.42	2.51	2.51	2.07	2.11	2.08
Deposit Weight [kg]	1.90	2.03	2.40	1.76	1.90	2.00	1.65	1.73	1.70
Overspray Powder [kg]	0.23	0.64	0.40	0.21	0.33	0.21	0.18	0.22	0.15†
Metal Left in the Tundish [kg]	0.75	0.06	0.06	0.07	0.05	0.05	0.04	0.04	0.03
Deposition Efficiency	**84%**	**70%**	**82%**	**75%**	**77%**	**81%**	**81%**	**84%**	**83%**

* Volume of an argon cylinder is 48 liter while that of nitrogen is 44 liter.

† Most of the powder was wet with water and only 150 g were recovered.

Table 11: Continued ....

Run Number	#82	#94	#95	#96	#98	#99	#101	#102@	#112
Initial Reservoir Pressure [psi]	1640	1530	1380	1550	1360	1095	1420	1550	1540
Final Reservoir Pressure [psi]	1480	1330	1240	1490	1250	1020	1320	1400	1440
Reserv. Press. Difference [psi]	160	200	140	60	110	75	100	150	100
Total Reservoir Volume [liter] = No. of cylinders X cyl. volume	5 x 44*	4 x 44	5 x 44	10 x 44	5 x 44	8 x 44	5 x 44	9 x 44	5 x 44
Mass of the Gas Used [kg]	2.72	2.72	2.38	2.04	1.87	2.04	1.70	4.60	1.70
Gas Delivery Time [sec]	22.8	29.1	24.2	26.7	21	17.8	16.9	55.6	24
Gas Mass Flow Rate [kg/min]	7.17	5.61	5.91	4.59	5.35	6.89	6.05	4.96	4.26
Mass of the atomized Melt [kg]	2.16	2.30	2.34	2.34	2.41	2.11	2.32	—	2.23
Melt Atomization Time [sec]	22	29.1	20	20	16	16	15	—	17
Melt Mass Flow Rate [kg/min]	5.89	4.74	7.02	7.02	9.04	7.91	9.28	—	7.87
Gas Power [W]	15,967	12,510	13,163	10,226	11,918	15,339	13,463	11,049	9,480
Gas/Metal Flow Ratio	**1.22**	**1.18**	**0.84**	**0.65**	**0.59**	**0.87**	**0.65**	---	**0.54**
Total Metal Charge [kg]	2.19	2.40	2.41	2.46	2.51	2.29	2.46	2.66	2.65
Deposit Weight [kg]	1.81	0.40ƒ	0.88√	1.70	1.52	1.54	1.34	—	1.44ˆ
Overspray Powder [kg]	0.28	—	0.40	0.54	0.67	0.39	0.31	—	0.58
Metal Left in the Tundish [kg]	0.03	0.10	0.06	0.12	0.10	0.18	0.14	0.11	0.42
Deposition Efficiency	**84%**	---	---	**73%**	**63%**	**73%**	**58%$**	----	**65%ˆ**

* Volume of an argon cylinder is 48 liter while that of nitrogen is 44 liter.

ƒ Due to timing problem, we run out of substrate after depositing only 400 grams and had to pour the rest of the melt in a deflector.

√ About 950 grams of the melt were sprayed in a deflector at the back of the substrate.

$ About 400 grams were overflown into deflectors at the front and the back of the substrate.

@ This run was made for high speed photography, and was not part of the deposition experiments.

ˆ About 260 grams of the melt were sprayed in a deflector at back of the substrate.

Table 11: Continued.....

Run Number	#113	#116Σ	#120Σ	#121Σ	#122Å	#126Å
Initial Reservoir Pressure [psi]	1430	1980	1750	1420	1120	1460
Final Reservoir Pressure [psi]	1250	1820	1500	1120	1000	1330
Reserv. Press. Difference [psi]	180	160	250	300	120	130
Total Reservoir Volume [liter] = No. of cylinders X cyl. volume	5 x 44	6 x 44	6 x 44	6 x 44	2 x 44	2 x 44
Mass of the Gas Used [kg]	3.07	3.27	5.11	6.13	0.82	0.88
Gas Delivery Time [sec]	38.8	24.1	30	34	91	76
Gas Mass Flow Rate [kg/min]	4.74	8.14	10.25	10.82	0.54	0.70
Mass of the atomized Melt [kg]	2.46	2.58	2.74	2.69	2.32	2.23
Melt Atomization Time [sec]	17	20	25	28	83	64
Melt Mass Flow Rate [kg/min]	8.7	7.74	6.58	5.76	1.68	2.09
Gas Power [W]	10,555	18,127	22,752	24,091	1,200	1,557
Gas/Metal Flow Ratio	**0.55**	**1.05**	**1.56**	**1.88**	**0.32**	**0.33**
Total Metal Charge [kg]	2.61	2.68	2.84	2.78	2.57	2.51
Deposit Weight [kg]	1.70	—	—	—	1.41	1.61
Overspray Powder [kg]	0.62	1.89ø	2.36Ï	2.46π	0.84	0.46
Metal Left in the Tundish [kg]	0.15	0.10	0.06	0.09	0.25	0.28
Deposition Efficiency	**69%**	**73%øΣ**	**86%**	**91%**	**61%**	**72%**

Σ These are powder runs, and since there were no depositions, the efficiency here is powder yield efficiency.
ø Additional 387 grams of the powder agglomerated and deposited at a deflector at the bottom of the chamber.
Ï Additional 250 grams of the powder agglomerated and deposited at a deflector at the bottom of the chamber.
π Additional 140 grams of the powder agglomerated and deposited at a deflector at the bottom of the chamber.
Å Circular LDC atomization runs.

The values of the atomization gas mass flow rate in Table 11 are the average rates calculated from the ratio of the total mass of the gas consumed during the run and the gas delivery time. Assuming an ideal gas behavior, PV=nRT, the total mass of the gas consumed is determined from the initial and the final gas reservoir pressures. Since the reservoir volume and temperature are constant, the gas mass flow rate is thus:

$$M_g = \frac{\Delta n . Z}{t} = \frac{(P_i - P_f) V_r Z}{RTt} \qquad (17)$$

where: M_g = gas mass flow rate
Δn = total moles of gas used
Z = molar weight of the gas
t = gas delivery time
P_i, P_f = initial and final reservoir gas pressures
V_r = reservoir volume,
R = gas constant
T = reservoir temperature (298°K)

The gas power is calculated from the change in the gas reservoir internal energy, $\Delta E = n_i C_V T_i - n_f C_V T_f$. Assuming an ideal gas behavior, where $C_V = 1.5R$ and PV=nRT, the gas power is calculated as:

$$\text{Gas Power} = \frac{\Delta E}{t} = \frac{1.5 V_r (P_i - P_f)}{t} \tag{18}$$

where: ΔE = gas reservoir internal energy change
n_i, n_f = the initial and final moles of gas in the reservoir
C_V = atomization gas heat capacity at constant volume

The values of the melt mass flow rates listed in table 11 are the average rates calculated from the ratio of the weight of the atomized melt and the melt delivery time. The weight of the atomized melt is the difference between the initial weight of the metal charge and the leftover in the crucible and the tundish after the run.

The ratio of the gas and the melt mass flow rates is an important dimensionless process parameter, which is also referred to as the "G/M ratio".

Most of the droplets, which either missed the substrate or bounced off it, solidified in flight and formed the overspray powder, which was collected in the powder container at the bottom of the tank. This powder was weighed and then sieved.

The deposition efficiency was calculated from the ratio of the deposit weight to the atomized melt weight. In the case when only powder was made instead of a deposit, the value of the powder yield was recorded in place of the deposition efficiency.

5.1.3. Atomization Gas Mass Flow Rate

The atomization gas mass flow rate calculated accurately from equations of fluid dynamics, in an earlier LDC study[3] agreed very well with the values calculated from equation 17.

It should be noted that at gas reservoir pressures above 1000 psig, the atomization gas pressure, which is usually set prior to the atomization run, stayed constant during the run. However, as the reservoir pressure fell below 1000 psig, the atomization gas pressure became variable during the run, increasing by about 30% at a reservoir pressure in the vicinity of 500 psig. This variation was specially pronounced for the linear atomizers compared to the circular ones due to the greater gas flow rate associated with the larger gas exit area of the linear atomizer. For a constant mass of gas consumed in a run, the final pressure of a small gas reservoir drops more than a larger one. Thus, to keep the atomization gas pressure constant during a run, a large number of cylinders with initial gas reservoir pressures well above 1000 psig must be used.

5.1.4. Melt Mass Flow Rate

To calculate the exact melt flow rate, an equation for the melt mass flow rate was derived from the principle of a mechanical energy balance, Bernoulli's theorem, as:[80]

$$M_m = C_d A_2 \rho \left[2\left(gh - \frac{\Delta P}{\rho} \right) \right]^{1/2} \tag{19}$$

where M_m = melt mass flow rate

C_d = melt discharge coefficient, which depends on the melt height, exit area, melt velocity at the exit, and friction losses in the slit.

A_2 = metal delivery exit area

ρ = melt density

g = gravitational acceleration

h = melt height in the tundish and slit which is variable with time.

ΔP = aspiration (-) or or back-pressure (+)

The melt flow rate can also be calculated by monitoring the melt height in the tundish during the atomization run, as:

$$M_m = -\left(\frac{dh}{dt}\right) A_1 \rho \tag{20}$$

where: M_m = Melt mass flow rate
dh/dt = the variation of melt height in the tundish with time
A_1 = tundish inside area
ρ = melt density

The melt mass flow rate is variable during the atomization runs since, among other parameters, the melt height level and the melt discharge coefficient vary with time. The influence of the drop in melt height level on the melt flow rate was also seen to be variable depending on the magnitude of other parameters such as the pressure at the tip of the melt delivery slit. Simulation runs with water[T2] showed that the variation of the water flow rate was larger at small variations of back-pressure, while it was not affected as much in the aspiration regime.

The variation of the melt flow rate due to the drop in melt height level was also larger for a smaller melt delivery slit opening area. This shows that the effect of friction from the slit walls was larger for small melt exit width. The melt flow rate is also affected by the melt viscosity, especially with a small melt exit area. Making the slit melt exit opening wider reduced the effects of both the viscosity and the fluid head level drop on the melt flow rate.[80]

As the included angle between the atomizer halves was reduced from 45° to 30°, while other parameters were kept constant, the metal flow rate increased.[80] This effect is attributed to the variation of the offset distance with changing the included angle, which results in increased aspiration pressure. Increasing the gap between the atomizers also resulted in increased melt flow rate, which may again be due to increased aspiration pressure. In this study a constant 45° included angle was selected since it contributes to a flatter profile of the deposit.

The tundish and the slit in this study were designed to sustain an almost constant melt flow rate by keeping the melt height drop rate in the tundish negligible during most of the run. The tundish, which has a cylindrical shape with an inside diameter of 140 mm, feeds the melt into the slit. The inside opening of the slit is very narrow and has a very small volume of about 65 cm^3, but has a height that exceeds 117 mm. During the atomization run, most of the melt is in the tundish, while the slit contains only a very small portion (about 170 grams in the case of the 3003 Al-alloy.) Due to the large tundish opening area, the melt height drop rate is very small. For instance, the atomization of the 3003 Al-alloy, with a 2.74 g/cm^3 density, and at a melt flow rate of 6 kg/min (36.6 cm^3/sec), the melt height drop in the tundish is 2.4 mm/sec. Since, the melt height in the slit and the tundish is at least more than 117 mm, this height drop rate is less than 2% per second.

Since in this study a low aspiration pressure, which is uniform along the length of the slit was used, and the above discussed tundish/slit design was used, the average mass flow rate listed in Table 11 is a good first approximation, representative of the melt flow rate during the run.

The rate of the melt delivery from the crucible to the tundish controls the height of the melt in the tundish. Thus, to realize the above mentioned slow melt head level drop in the tundish, the melt delivery from the crucible to the tundish is required to be relatively fast. Simulation trials with tin and water were made to compare the rate of the melt delivery from the crucible and the tundish. The water flow rate from the crucible was seen to be retarded by a vortex flow that forms very early in the crucible. A plate, which was inserted in the crucible, effectively prevented the formation of the vortex in the water. It was seen that the presence of the plate increased the flow rate by a factor of two. The vortex was not experienced in the tin due to the dross at the top of the melt and due to its high viscosity. When this dross was removed, however, a small vortex seemed to form. The liquid flow rate from the crucible also depends on the diameter of the crucible bottom delivery hole. When the vortex fluid flow was restricted, crucible to tundish water flow rate ratios of 2:1, 3:1 and 4:1 were measured for crucible hole diameters of 9.5 mm, 12.7 mm and 17 mm, respectively. The tin simulation, on the other hand, resulted in crucible to tundish melt flow rate ratios above 5:1.

Water simulations were made to investigate the liquid flow rate as a function of the offset distance and aspiration pressure. The water flow rate at constant water head level was measured at different aspiration pressures using an atomization gas pressure of 70 psi. The water supply into the tundish was varied during the run until a constant water head level of 190 mm was realized. These water supply flow rates and the aspiration pressures for an atomizers gap of 9 mm are plotted against the offset distances in Figure 33.

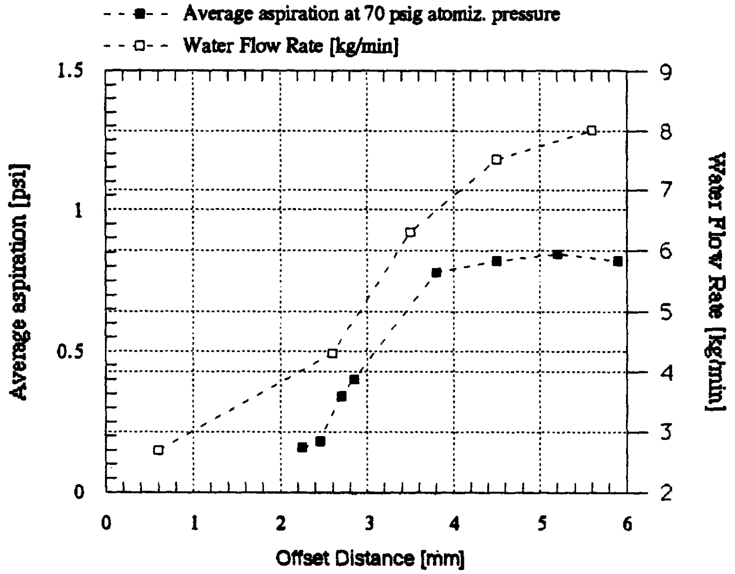

Figure 33. The average aspiration pressures and the water flow rates measured at different offset distances.

5.1.5. Gas/Melt Mass Flow Rate Ratio

The ratio of the gas/melt mass flow rates is a very important parameter on which the melt break-up efficiency and droplet cooling rates depend. It was shown in Equation 10 that the mean droplet size in an atomized spray plume depends on the inverse of the gas/melt flow ratio since a higher gas/melt flow ratio offers a larger energy of disintegration. The refined droplets are also subject to higher cooling rates and, at a constant flight distance, contain a higher solid fraction than the larger droplets. The G/M ratio is increased by any parameter that either increases the gas flow rate or decreases the melt flow rate. The gas/melt flow ratio decreases with increasing aspiration pressure, metal delivery exit area, and melt height level in the tundish; while it increases with increasing atomization gas pressure and atomization gas exit area. The influence of any particular parameter is, however, complicated unless all the remaining variables are kept constant. For instance, a higher atomization gas pressure increases the gas flow rate and thus the G/M ratio; however, it also increases the aspiration pressure, which increases the melt flow rate, which reduces this ratio. The influence of the G/M ratio on the droplet sizes and distribution in the spray plume and the deposit thickness profile and microstructures will be discussed later.

5.1.6. Melt Break-up

As the melt leaves the slit delivery tip, it is atomized by the impinging atomization gas. The melt, which is delivered in a sheet form, is disintegrated eventually into fine droplets by the high velocity, high frequency, pulsed gas jets. The perturbations in the gas jets, with 100-200 μm wavelengths and 10^5-10^6 Hz frequencies,[T1] seed instabilities that force the melt to break-up into droplets of narrow range of sizes proportional to the gas velocity, frequency and wavelengths. A high gas kinetic energy reduces the gas wavelength and leads to finer droplets. The melt break-up in the LDC process occurs just within few millimeters of the melt exit in contrast to subsonic atomization, as indicated by the sequence of photos from the high speed IMACON camera shown in Figure 34. The melt break-up continues in flight if the dynamic pressure due to the gas velocity exceeds the restoring force of the melt surface tension, also known as the "Maximum Stability Criterion."[3]

During the early stages of the LDC atomization, when the gas velocity (pulsed) is grossly faster than that of the droplets, the quenching of the droplets is at its highest rate. As the gas expands and slows down, and the droplets pick up speed, the relative velocity between the gas and the droplets decreases and the cooling rate is reduced, but due to the ultra fine droplet size (and large surface area), the quench rate are still very high.

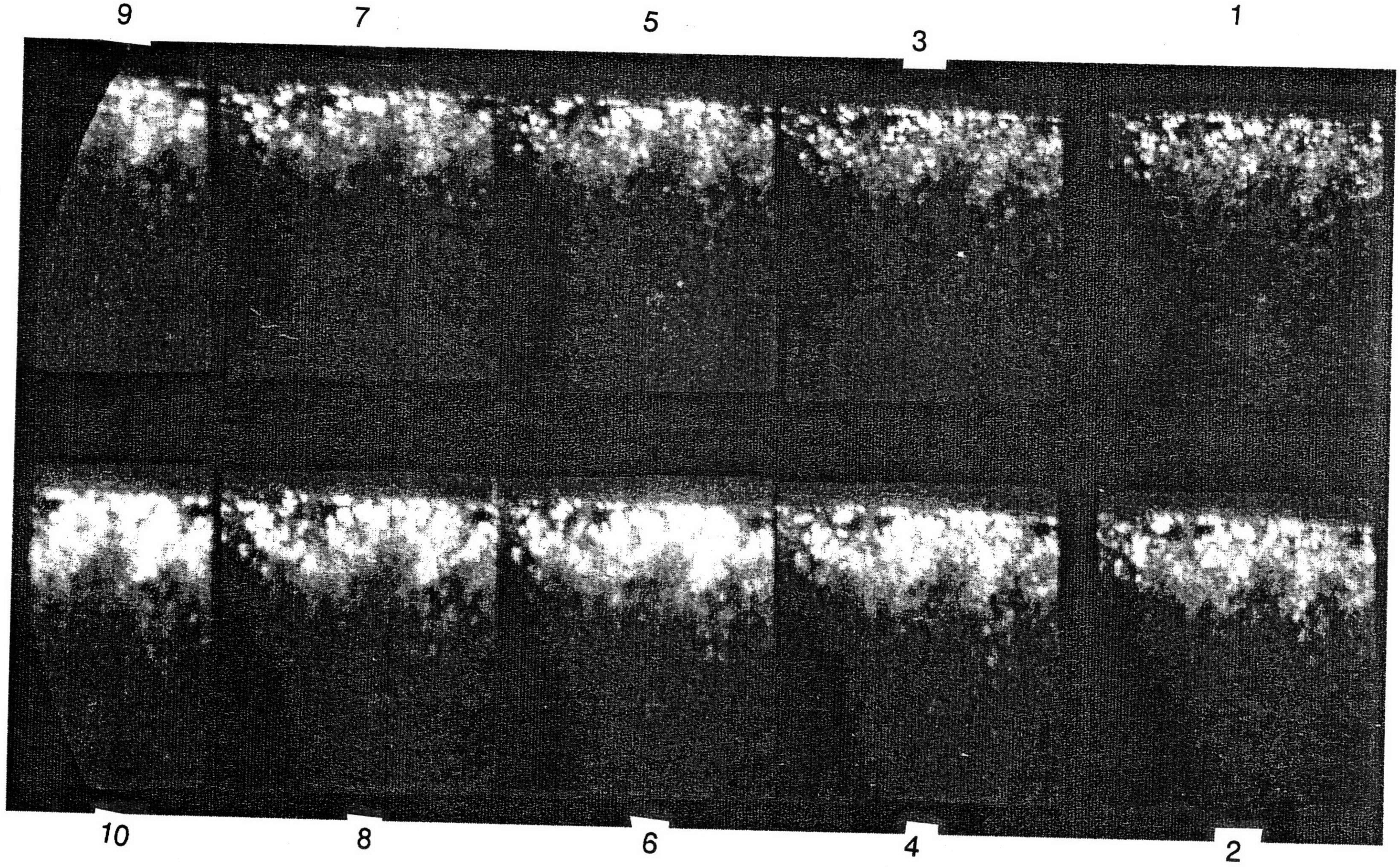

Figure 34. Instantaneous atomization of the melt into droplet within few millimeters of the melt exit shown by an Emicon photography taken at a speed of 10^5 pictures/second at a field of view of 1″ x 1″, in the sequence shown above.

The velocities of the atomized tin droplets were measured with high speed streak photography using the IMACON camera.[188] In this photographic method, the film moves horizontally in the camera at a constant speed (10 m/sec = 100 μsec/mm) while viewing a fixed area of the path of the droplets moving downwards, as shown schematically in Figure 35. Depending on the relative velocity between the droplets and the film, the images of the droplets appear as inclined streaks in the photograph, as shown in Figure 36.[188] From the streak angles and the horizontal film speed, droplet velocities of 12 - 25 m/sec were measured for tin droplets atomized with 30 psi gas pressure; whereas velocities of 18 - 30 m/sec were measured for those atomized with 60 psi gas pressure.[188] These droplet velocities were measured at 60 cm flight distance, where the droplets must had considerably slowed down. At higher atomization gas pressures, attempts to resolve the velocity of droplets with the streak photography method were not successful.

In the linear LDC process, the atomized droplets travel in a tent-shaped path and form a spray plume with the configuration shown in Figure 37. The sizes and distribution of the droplets in the spray plume are affected by the melt surface energy, the uniformity of the aspiration pressure and the atomization gas expansion. As the melt leaves the slit opening in a sheet form, the surface energy forces the melt to contract toward the center of the slit. A non-uniform aspiration pressure along the slit opening, which is higher at the slit center, promotes higher melt flow rate at the slit center due to the greater suction it creates there. Since the melt break-up suffers as the melt flow rate is increased, both the melt surface energy and the non-uniform aspiration pressure lead to a spray plume with higher concentration of larger droplets at its center. The expanding gas, on the other hand, drags the finer droplets toward the periphery of the spray plume thus exacerbating the uneven droplet size distribution across the plume.

The finer droplets at the periphery of the spray plume travel longer distances than the larger droplets at the center. Due to their smaller sizes and longer flight distances, these droplets reach the substrate with a higher solid fraction and deposit a somewhat more porous preform there. If the droplets are

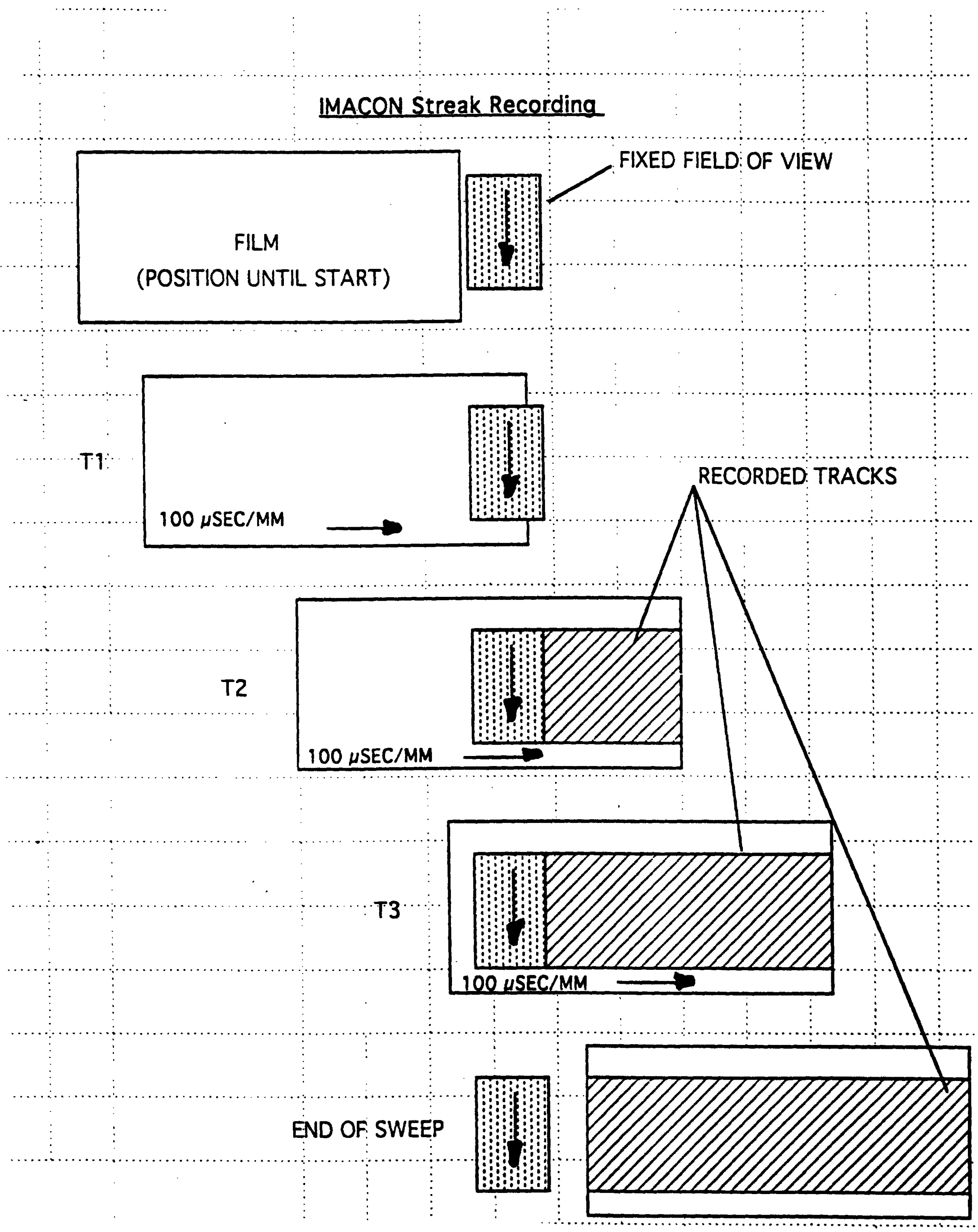

Figure 35. Schematic representation of the streak photography method by the IMACON Camera.[188]

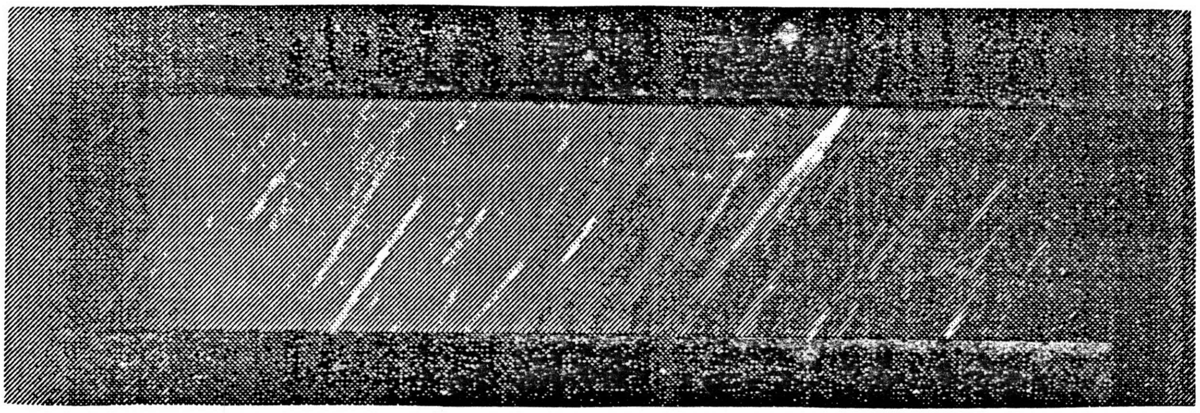

Figure 36. Photo of the streak paths of tin droplets atomized at 30 psi at a horizontal film speed of 10m/sec.[188]

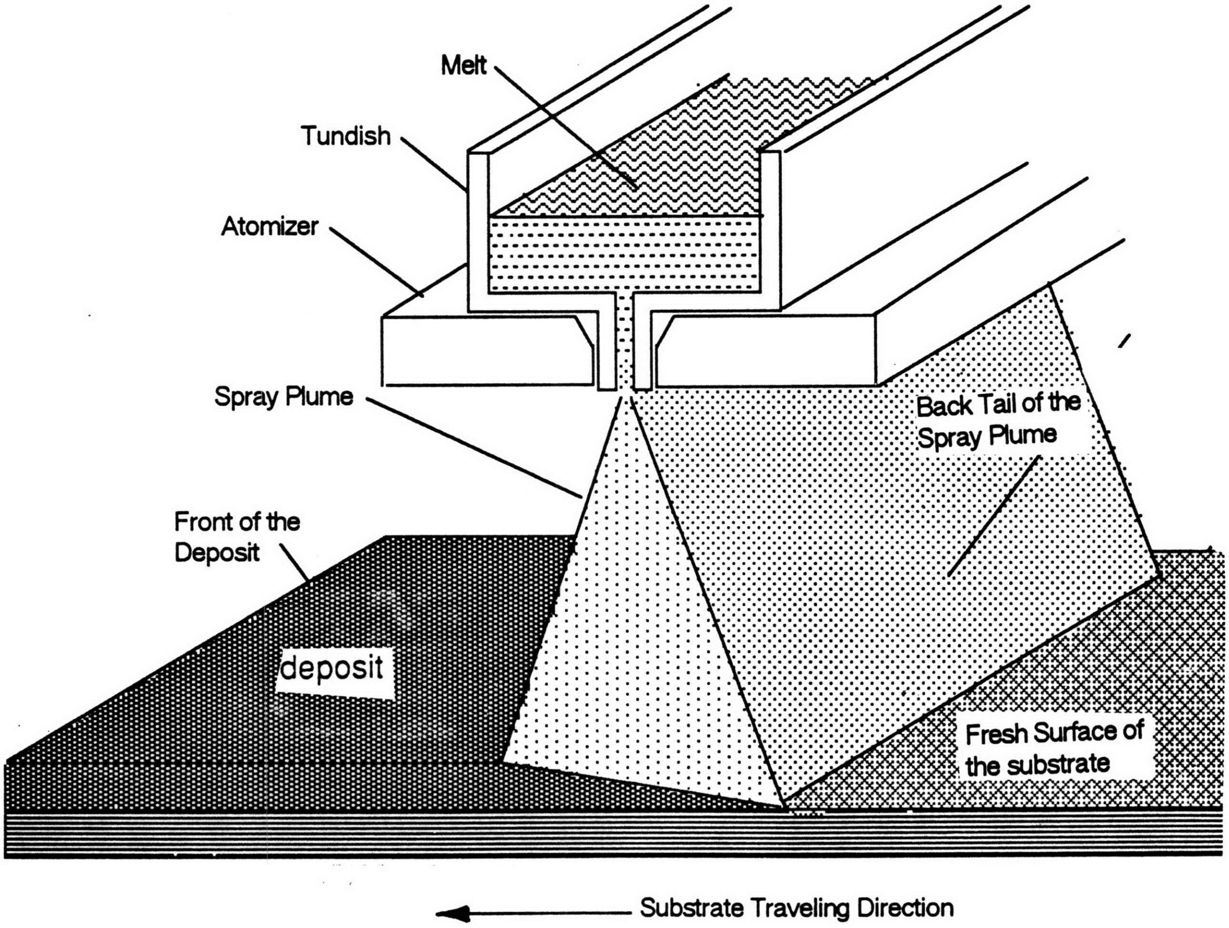

Figure 37. Schematic representation of the spray plume.

completely solidified, they may bounce off the substrate and become part of the over-spray powder. The larger droplets at the center of the melt plume travel shorter distances, and reach the substrate at higher liquid fraction. To determine the influence of the process parameters on the melt breakup efficiency and the size of the droplets, the over-spray powder of the LDC runs were studied.

5.1.7. The Over-spray Powder

The over-spray powders from selected LDC deposition runs were separated with Tyler sieves. The cumulative weight distribution curves of these over-spray powders were plotted in two separate diagrams depending on whether the runs were made with the first set of the new (modified) linear atomizers (#73 - #82), or the second set of the new atomizers that had improved gas delivery vanes and smaller Hartman tubes (#94 - #121), as shown in Figure 38A-B.

Three atomization runs (#116, #120 and #121) were made without the presence of a substrate in order to solidify all the atomized droplets into powder. These powder runs were made at a constant offset distance of 3.8 mm and a constant gap between the atomizers of 7 mm. Atomization gas pressures of 60 psi, 80 psi and 100 psi, which generated aspiration pressures of -0.88, -1.41 and -1.55 psi, respectively, were chosen. These runs were made in order to study the effect of the atomization gas pressure and the aspiration pressure on the melt breakup efficiency. These powders were sieved and their cumulative weight distribution plotted in Figure 39.

The mean powder size, which corresponds to 50% of the cumulative weight distribution, was determined from the distribution curves. These mean powder size values, the gas atomization pressure, the aspiration pressure, the melt flow rate, the gas/melt flow ratio and the flight distance of the runs are listed in Table 12. The melt breaks-up into finer droplets when the aspiration pressure and the melt flow rate are low, and the G/M ratio and the gas power are high. An increase in the gas power, on the other hand, results in increased

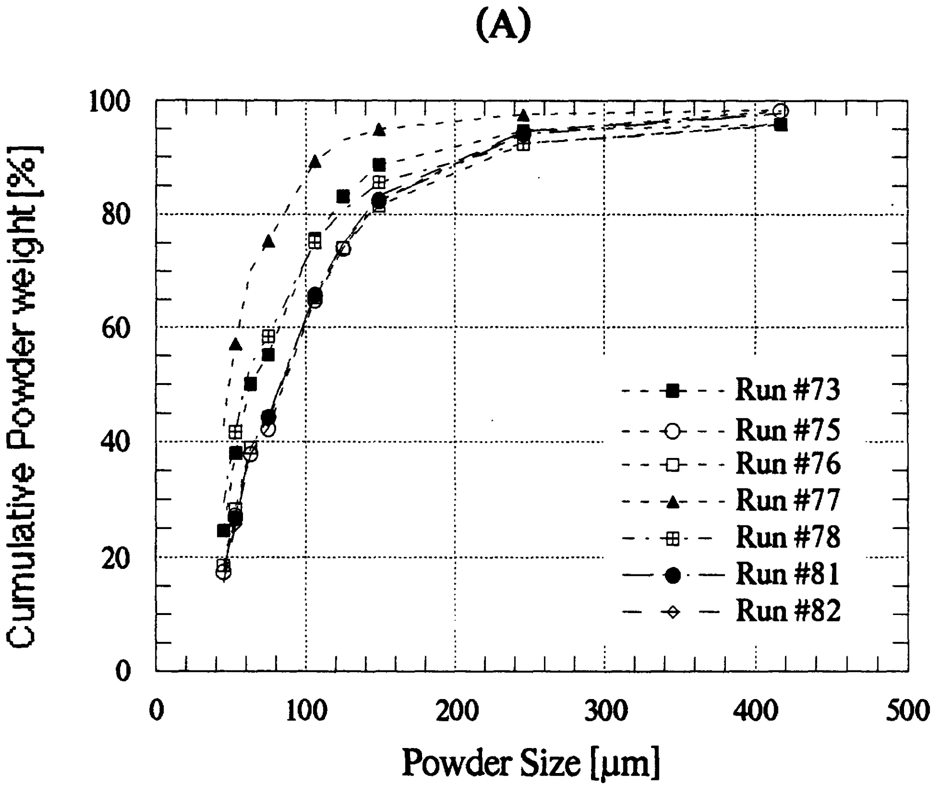

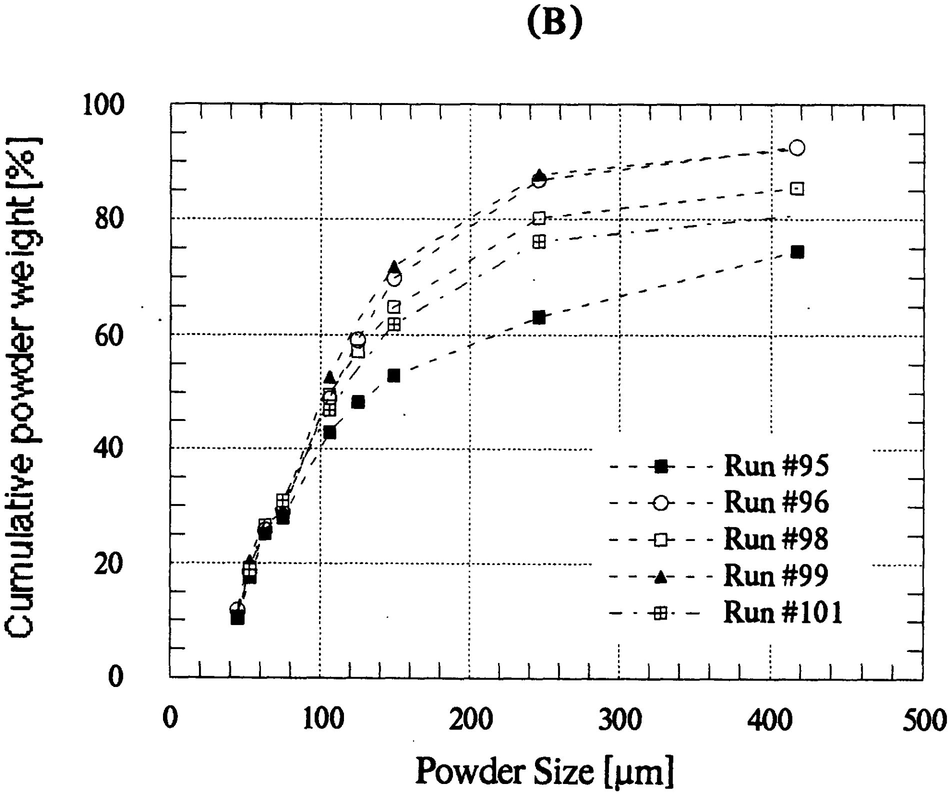

Figure 38. The cumulative weight percent of over-spray powders from runs made with (A) the first set of the new atomizer and (B) second set of atomizers.

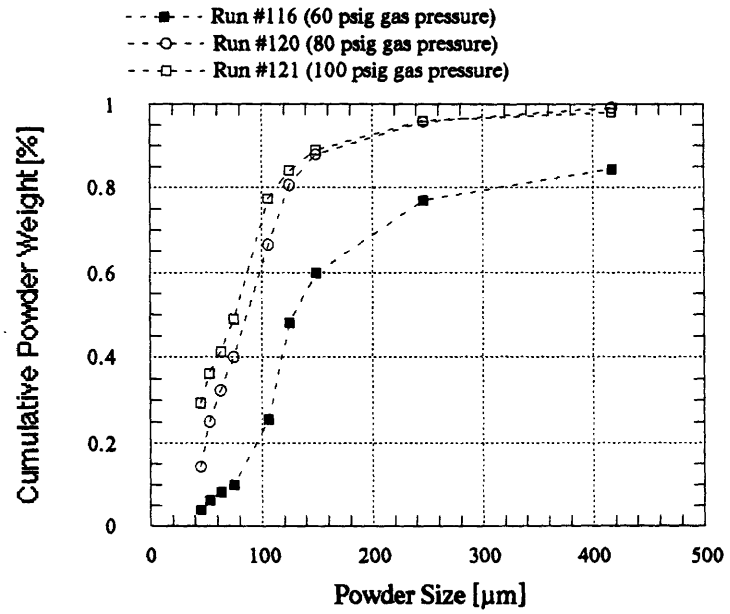

Figure 39. Cumulative weight percent distribution of the three powder runs.

Table 12. Summary of the Mean Powder Size and other Process Parameters Values of Selected Runs.

Run #	Atomization Pressure [psi]	Aspiration Pressure [psi]	Melt flow rate [kg/min]	Gas /Melt flow rate Ratio	Gas Power [Watt]	Flight Distance [cm]	Average Powder Size [μm]
73*	70	-0.42	3.71	1.67	13,830	33	63
75*	70	-0.44	3.69	1.67	13,752	30	90
76*	100	-0.45	6.71	1.35	20,152	30	85
77*	100	-0.35	5.07	1.85	20,802	30	48
78*	100	-0.33	6.21	1.40	19,348	30	60
81*	70	-0.34	5.59	1.04	13,001	38	85
82*	70	-0.33	5.89	1.22	15,967	42	85
95†	70	-0.22	7.02	0.84	13,163	41	135
96†	70	-0.26	7.02	0.65	10,226	41	110
98†	70	-0.24	9.04	0.59	11,918	41	110
99†	70	-0.24	7.91	0.87	15,339	41	102
101†	70	-0.24	9.28	0.65	13,463	41	115
116†	60	-0.88	7.74	1.05	18,127	—	130
120†	80	-1.41	6.58	1.56	22,752	—	90
121†	100	-1.55	5.76	1.88	24,091	—	78

* Atomized with the first set of atomizers

† Atomized with the second set of atomizers

melt break-up efficiency and reduced spray droplet sizes, due to the increased melt disintegration energy. A longer flight distance leads to more of the droplets to miss the substrate due to the expanding spray plume. In this situation, more of the larger droplets at the core of the spray plume could miss the substrate and lead to a greater mean over-spray powder sizes.

The over-spray powders of the runs, made with the first set of the new atomizers, had, in general, finer sizes and narrower distributions than those of the second set. Although the aspiration pressures for these runs were higher, the atomization gas pressure, the gas power and the gas/melt flow ratio, were also high and could account for the finer over-spray powders of these runs. On the other hand, as the atomization gas pressure was lowered, the average droplet size increased and the droplet size distribution became wider, as was shown by the curves of the second set of atomizers in Figure 38B. The flight distances for this second group of runs were also longer and, to a certain extent, contributed to their larger mean overspray powder sizes. However, for any one group of runs by the same set of atomizers, both a higher gas/mass flow ratio and gas power from higher atomization gas led to finer over-spray powders with a narrower distribution. This fact is actually more clear for the runs of the second set of atomizers (#95 - #101), which were made at relatively constant aspiration pressure and flight distance. On the other hand, as the atomization gas pressure was lowered, and the G/M ratio and the gas power decreased, the average droplet size increased and the droplet size distribution became wider.

The aspiration pressures of the runs with the first set of atomizers were initially set higher than the usual range of -0.2 to -0.3 psi used in earlier studies in order to increase the production (melt flow) rates. However, the melt flow rates of these runs were lower than those of the second set, although their aspiration pressures were 30 to 50% higher. Although the melt exit area of the two group were almost equal, the second group had longer melt exit (100 mm X 0.51 mm) than the first (71 mm X 0.75 mm), which may have accounted to the higher flow rate due to the fluid boundary conditions that may have over-shadowed the effect of the wider slit. It was shown earlier that smaller aspiration pressure leads to more uniform aspiration pressure along the length of the slit, and, as will be explained later, leads to flatter deposit thickness profiles. Higher production rates should be achieved by increasing the melt exit area rather than increasing the aspiration pressure and risking non-uniformity.

It should be noted that the sizes and distribution of these over-spray powders did not always reflect the structure of their deposits. For instance the deposit of run #95, with the over-spray powder of the largest mean powder size and wide distribution, contained a large number of pre-solidified fine particles and fine porosities, as shown in Figure 40. This deposit had 90% density at the front of the deposit and 89% at the back.

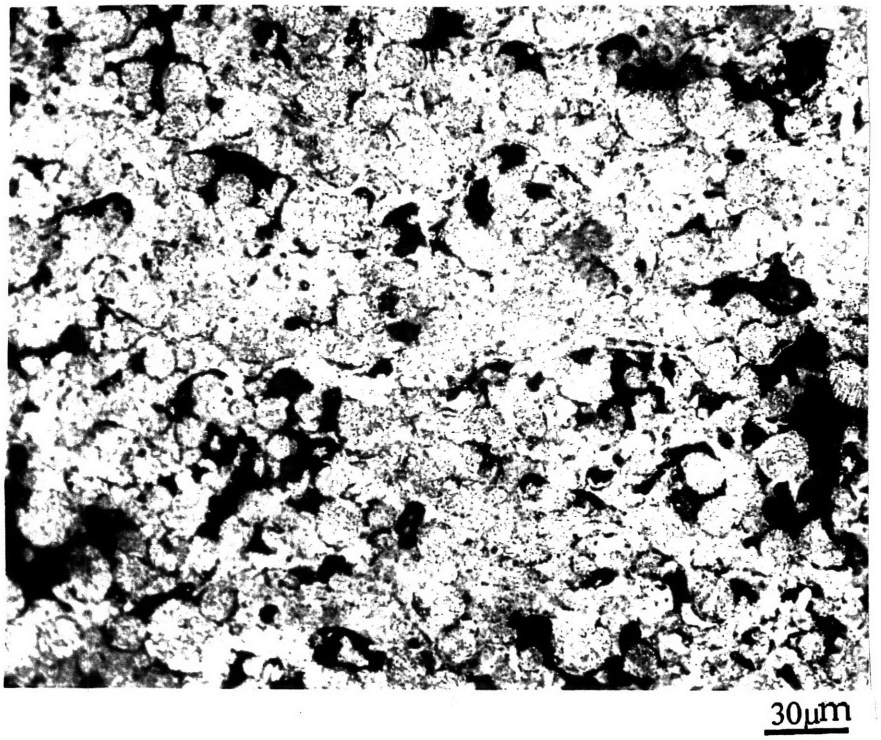

Figure 40. As-deposited micrograph from the center-front of deposit run #95 showing pre-solidified particles. [X165]

In the powder runs #116, #120 and #121, where the offset distances were kept constant and the aspiration pressure increased progressively with the atomization gas pressure, the powder sizes decreased and the distribution became narrower at higher atomization gas pressures. Although the aspiration pressure increased with the atomization gas pressure, the melt flow rate, inexplicably, decreased. The higher gas/melt flow ratio and gas power associated with the higher gas pressure again seem to dominate the aspiration pressure and produce the finer and more narrowly distributed powders in these runs.

5.1.8. Substrate/Deposit Adhesion

The atomized droplets eventually deposit on a substrate at a selected flight distance. These droplets built up into a deposit whose properties depend on their interaction with the substrate.

In this study, a mild steel plate with a grit blasted surface, is used as a substrate. The parameters associated with the substrate, which influence the LDC deposit properties, are the substrate conductivity, temperature, moving speed, thermal expansion and surface roughness. The conductivity and the temperature of the substrate influence the microstructures of the deposit. The speed of the substrate, in conjunction with the melt flow rate, determines the thickness of the deposit. The surface roughness of the substrate promotes mechanical interlocking between the deposit and the substrate. All of these parameters affect the deposit/substrate adherence and the heat transfer efficiency. During deposition, the interaction of 4 stresses determine the adherence of the deposit onto the substrate.[T2] These stresses are: (1)The adhesive stress between the deposit and the substrate (σ_a), (2) the deposit fracture strength (σ_y), (3) the deposit yield strength (σ_f), and (4) the thermal contraction stress that results from the thermal differences between the deposit and the substrate (σ_c). Depending on the magnitude of the stresses, the following condition can arise:

- If $\sigma_c > \sigma_a$, then the deposit peels off the substrate. However,
- if $\sigma_c < \sigma_a$, then one of these three conditions can take place:
- If $\sigma_c > \sigma_f$, the deposit adheres well but cracks.
- If $\sigma_f > \sigma_c > \sigma_y$, the deposit adheres well but deforms plastically.
- If $\sigma_f > \sigma_y > \sigma_c$, the deposit adheres well but deforms elastically.

The thermal contraction stress, σ_c, creates stresses at the deposit/substrate interface due to their thermal expansion difference and due to the temperature difference across the variable deposit thickness. Since the temperature change of the substrate is very small, especially when water cooled, the stresses at the interface depend only on the deposit contractions.[9]

If the deposit peels off during deposition, it becomes warped with a wavy bottom surface due to the interactions of different contractions resulting from its variable thicknesses. However, if the deposit adhered well onto the substrate, one of two behavior patterns is expected when it is later peeled off the substrate. The bottom surface either stays flat if the deposit deformed plastically, or becomes curved if it deformed elastically during the deposition. Ferrous (iron based) alloys were seen to have little adhesion on the substrate and were more likely to peel off during the deposition. This peeling was more pronounced when the substrate was water cooled.

The deposit may crack when it is expected to either deform plastically or elastically. The cracks usually take place at the outer, thin and porous region of the deposit, which cannot sustain that much of a stress. This cracks, however, are rare occurrence, especially in the Al-alloys.

In this study, the mild steel substrate, which has a low expansion coefficient, good thermal conductivity, and a grit blasted rough surface, promoted good adherence of the Al-alloys during deposition. It also permitted easy separation of the deposit from the substrate after it cooled down. Cracking was rarely experienced in these deposits.

5.1.9. Deposit Thickness Profile

The variable distribution of the atomized droplets, in terms of size and location, across the spray plume, leads to the deposition of deposits with variable thickness profiles. Some of the deposits had agglomerates of powder at their edges and bottom. These features, known as "feathering," form from deposition of fine droplets that have almost completely solidified in flight.

The runs with high melt break-up efficiency and finer droplet sizes are the more likely candidates to have feathering. The photographs of the top surface, and cross sections of deposits from runs #78, #101 and #113 are shown in Figure 41A-C. Deposit of run # 78 had the highest concentration of feathering both on its sides and bottom, while that of #101 had relatively less, and #113 did not have any at all. Selected parameters that characterize these runs are summarized in Table 13.

Table 13: Important LDC Parameters of Runs #78, #101 and #113

Run number	#78	#101	#113
Atomization gas pressure [psig]	100	70	50
Aspiration pressure [psi]	-0.35	-0.24	-0.28
Pouring temperature [°C]	800	820	820
Gas/Metal mass flow ratio	1.4	0.65	0.55
Gas power [Watts]	19,348	13,463	10,555
Melt flow rate [kg/min]	6.21	9.28	8.70

As mentioned earlier, the aspiration pressure of the early runs was kept high in order to increase the melt flow and, hence, the production rates. The atomization gas pressure was also kept high in order to compensate for the expected high melt flow rate and keep the melt break-up efficient. However, a high aspiration pressure, as discussed earlier, results in non-uniform aspiration along the length of the slit that leads to increased suction at the center of the slit. The high atomization gas pressure of run #78 resulted in high gas power and G/M ratio that led to excessive refinement of the droplets. Both the high aspiration and atomization gas pressures led to the atomization of very fine droplets that were more concentrated at the center of the spray plume.

The first fine droplets reach the substrate at a high solid fraction and form a porous preform of agglomerated powder. The very small early layer of these

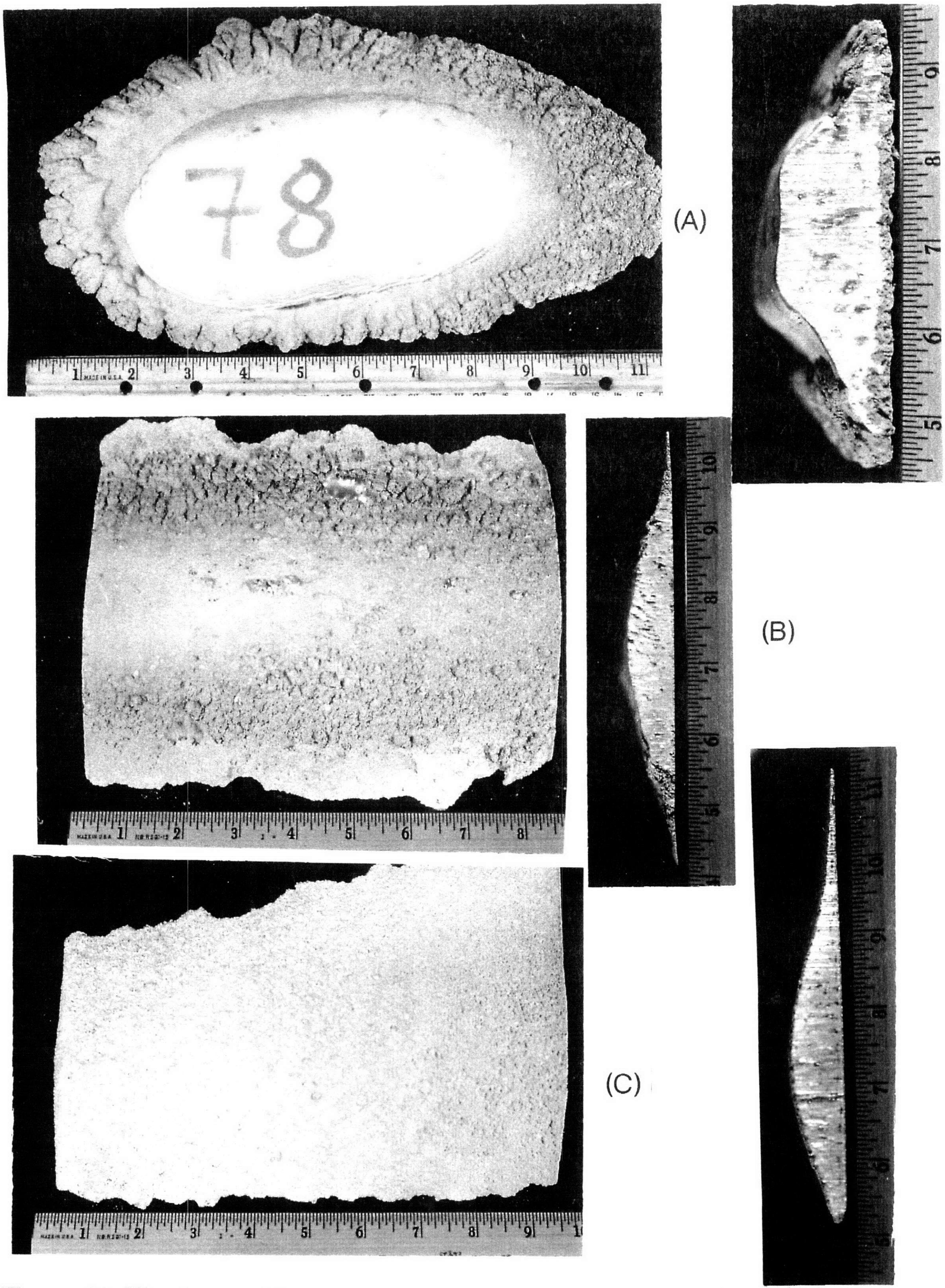

Figure 41. The top and transverse cross sectional view of deposits from run (A) #78, (B) #101 and (C) #113.

agglomerates hindered the heat transfer to the substrate. The successive deposition of the highly concentrated fine droplets at the center of the substrate and the reduced heat transfer to the substrate by the early layer led to the formation of a narrow, oval-shaped, thick semi-liquid layer at the center of the deposit. The force of the atomizing gas moves this liquidous layer to the sides, where it solidifies with traces of liquid ripples at its top, as that at the top of run #78. The lightly concentrated finer droplets at the outer edges of the spray plume, on the other hand, led to the built-up of the feathering. These two features, the oval liquidous center and outside feathering, existed in most of the early runs, similar to run #78.

The uneven distribution of the atomized droplets in the spray plume, the spray plume expansion angle, and the substrate speed contribute to the deposition of deposits of variable thicknesses and bell-shaped (Gaussian) thickness profiles. The thickness profiles along the width (transverse cross section) of selected deposits in both actual and normalized sizes are shown in Figure 42A-B.

The deposit thickness along the longitudinal direction, which is parallel with the substrate moving direction, was relatively constant, as shown in Figure 43. The negligible melt height drop in the tundish during most of the atomization run, as discussed earlier, and the constant substrate speed contributed to the uniform, longitudinal thickness profile. In industrial practice, the melt would be poured into the tundish at a constant flow rate in order to keep the melt height in the tundish constant. The process would then be at steady state, and a deposit of a constant longitudinal thickness profile would be continuously deposited on a cooled conveyor-belt-type substrate.

Comparing the structures and shapes of runs #78, #101 and #113 in Figures 41A-C, and their characteristic parameters in table 12, it is evident that the feathering was reduced and the deposit became flatter and wider as the atomization gas pressure, G/M ratio, the gas power and the aspiration pressure were reduced. One, however, should be careful no to go down to values of these parameters that reduce the melt break-up efficiency and compromise the

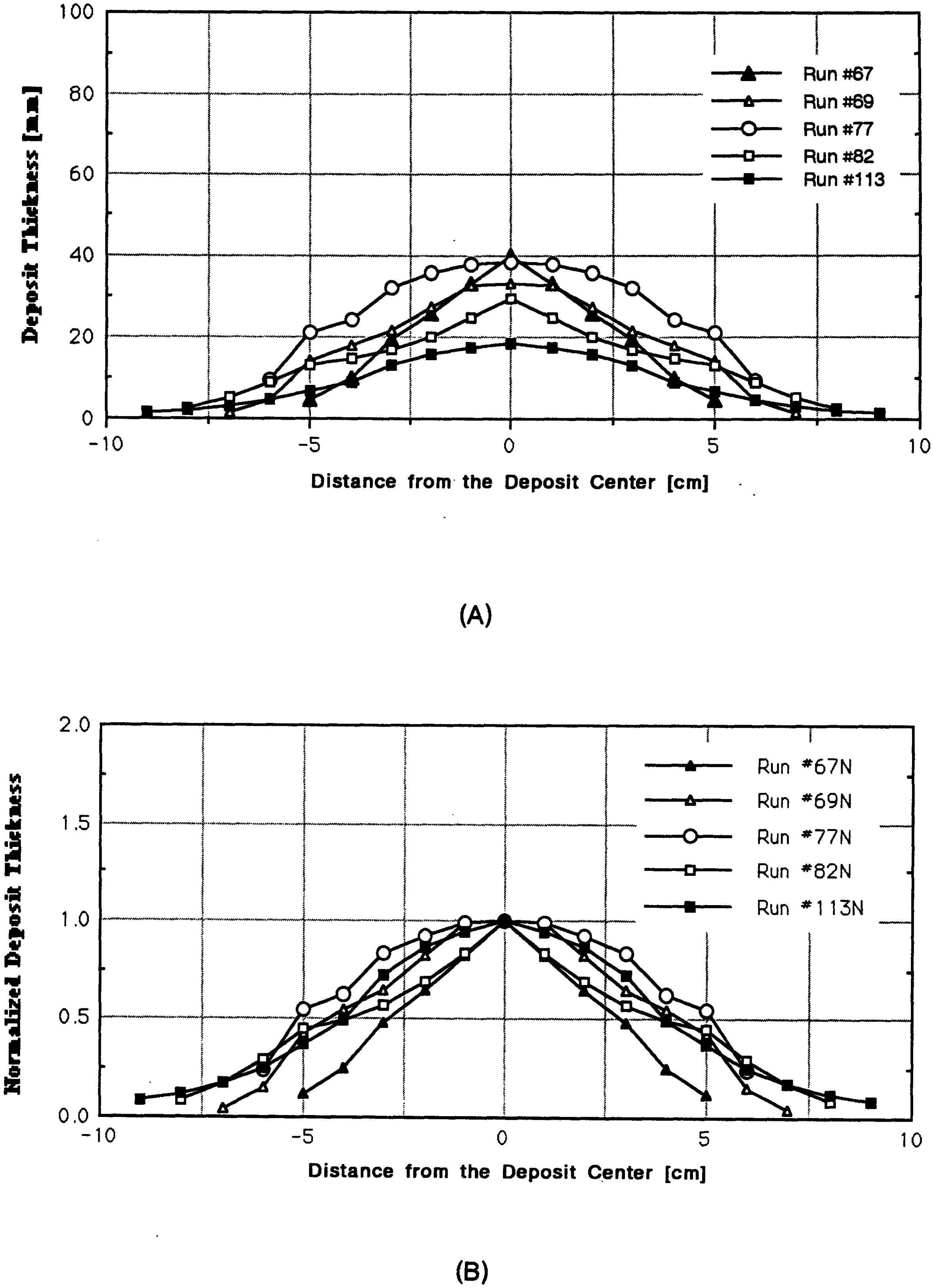

Figure 42. The transverse cross section thickness profiles of selected deposits in (A) actual sizes and (B) normalized sizes.

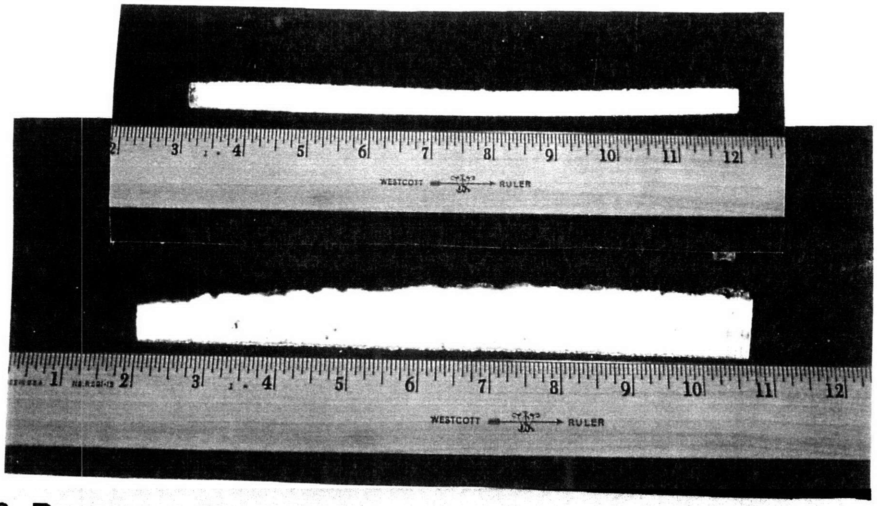

Figure 43. Representative longitudinal thickness profiles of the LDC deposits

characteristic rapid solidification behavior of the LDC process. An atomization gas pressure of 50 psi, an aspiration pressure of -0.2 to 0.30 psi, and a G/M ratio of 0.55 seem to lead to better results.

Models that characterize and predict the thickness profiles of LDC deposits were derived from the equation that formulates the density of natural (Gaussian) distribution:

$$T(x) = \alpha \exp(-\beta x^2) \qquad (21)$$

where: $T(x)$ = thickness of the bell shaped profile
α and β = constant
x = distance from the center of the profile

Including the variation of the distribution in the transverse and longitudinal directions and in time, equation 21 becomes:[80]

$$T(x,y,t) = \int D_m(t) \exp(-\beta_x x^2 - \beta_y y^2)\, dt \qquad (22)$$

The above equation was solved[T2] for a constant melt flow rate, where the maximum local deposition rate, $D_m(t)$, is constant, and a moving substrate at a constant speed, as:

$$T(x,y,t) = \frac{\sqrt{\pi}}{\sqrt{\beta_y}} \left(\frac{D_{m,avg}}{2v}\right) \exp(-\beta_x x^2) \left\{ \mathrm{erf}(\sqrt{\beta_y}\, y) - \mathrm{erf}[\sqrt{\beta_y}\,(y - vt)] \right\} \tag{23}$$

where: $T(x,y,t)$ = deposit thickness at a given time
$D_{m,avg}$ = average maximum local deposition rate
β_x = transverse thickness distribution coefficient
β_y = longitudinal thickness distribution coefficient
v = substrate speed
t = deposition time

This model shows that the spray distribution, the melt flow rate across the spray plume, the substrate speed, and the deposition time determine the thickness profile of a deposit. The aspiration rate, the melt delivery exit area and the melt breakup efficiency are represented in this equation by the melt flow rate across the spray plume. The thickness distribution coefficient, β, was observed to be very useful in determining the uniformity of the thickness profile in any direction.[89] Smaller β values corresponded to flatter deposits. β is a function of parameters such as: the flight distance, atomization gas pressure, the included angle between gas jets, the gap between the atomizers, and the melt flow rate; and represents the effect of these parameters. For instance, a large included angle and/or increased flight distance reduced the values of β, thus making the deposit flatter. However, for a constant flight distance and a predetermined substrate width, as β decreased and the deposit was flattened, the deposition efficiency (yield) became smaller. This reduced yield of product that is related to the flatter deposits is against the LDC process goals.

Earlier studies of the LDC process made efforts, such as installing gas jets at the ends of the linear atomizer to confine the gas spread; and/or arranging the atomizers in tandem sets of two or more, in order to produce flat deposit profiles. It was reported that the effect by the secondary gas jets on the thickness profile was very small.[9,80]

Using a tandem of two sets of linear atomizer, the resulting thickness profile is expected to be equal to adding the two individual bell-shaped profiles produced by a single set of atomizers. The addition of the two deposit profiles is done with their centers spaced the same distance as the centers of the tandem atomizer. Two transverse thickness profiles of run #113, made with gas atomizers of 2(0.5 mm X 100 mm) gas exit area and melt delivery exit area of 0.5 mm X 100 mm, were added at different center to center spacings, as shown in Figure 44A-C. It can be seen that a center to center spacing of 8 cm gave the closest to a flat profile, and a tandem of two set of atomizers spaced 8 cm should give this same results. Three profiles of this deposit with center to center spaced also at 8 cm from each other also give a wider deposit with larger flat section, as shown in Figure 44D.

In an earlier study[9,80] the profile of water, tin, 7150 and 2024 Al-alloys atomized with a tandem of two sets of linear atomizers resulted in a wider flat central portion of the deposit than when a single set of the same length as the tandem sets was used. Simulation of tandem linear atomizers[9,80] showed that they were better suited than a single set of long linear atomizers, because of the difficulty of maintaining a uniform gas pressure along the opening of the single set, and because they are cheaper in terms of building and maintenance, if a short section was to be replaced instead of the single, long linear set.

5.1.10. Deposit Microstructure

The solidification of the LDC spray deposition process takes place in incremental fashion, as shown schematically in Figure 45.[10,80] During the deposition, the LDC process results in the formation of a very thin liquid layer on the top of the growing solidified deposit. As more droplets land on this solidifying surface and the thickness of the deposit increases, the deposited liquid layer solidifies and is replaced by newly deposited liquid splats. This liquid layer feeds the growing equiaxial structure at its bottom and inhibits most of the solidification shrinkage, thus contributing to the formation of a dense layer. This advancing thin layer distinguishes the LDC process from the

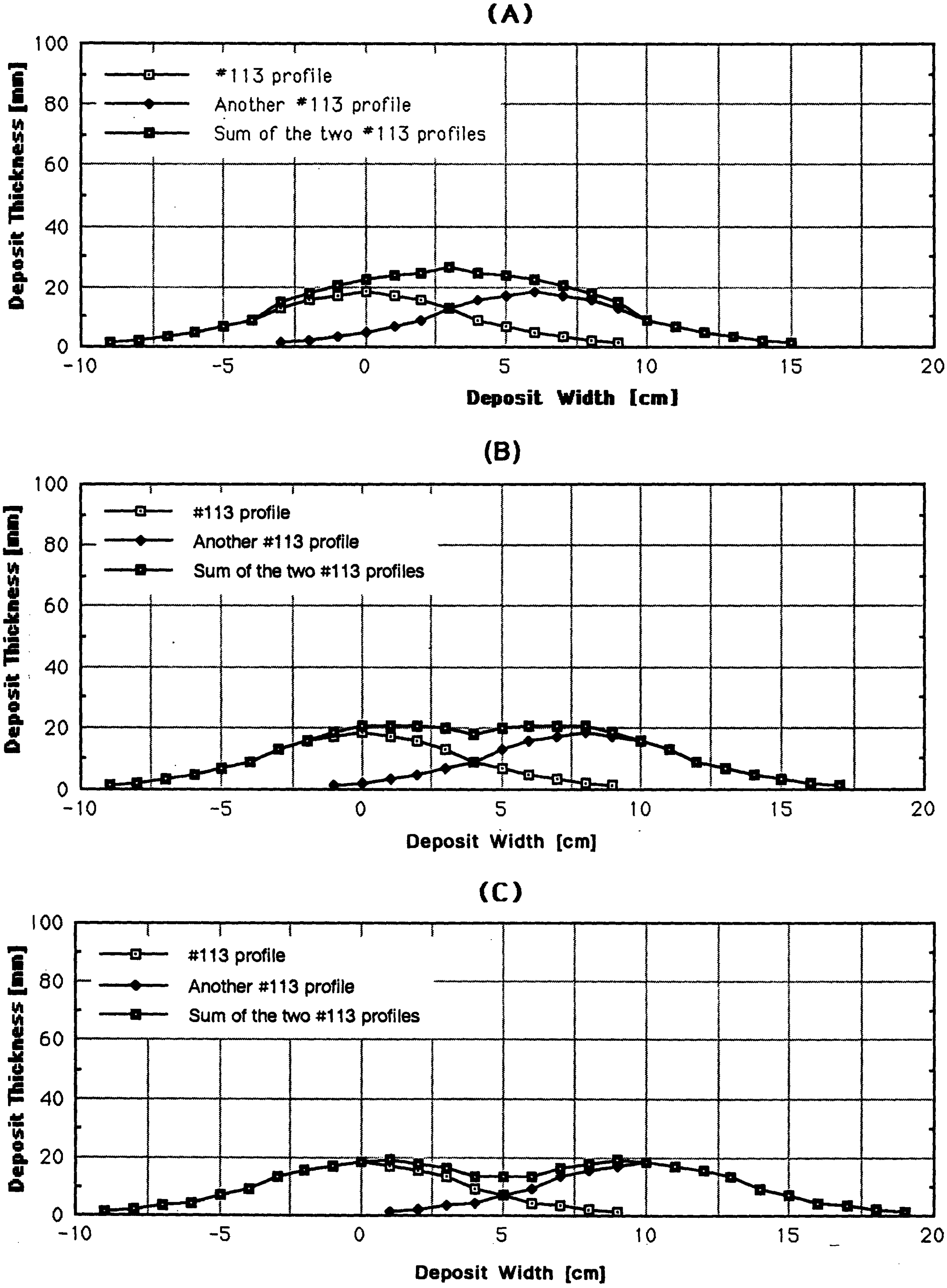

center spacing of (A) 6 cm, (B) 8 cm and (C) 10 cm. And (D) the sum of three profiles with 8 cm center-to-center spacing.

(D)

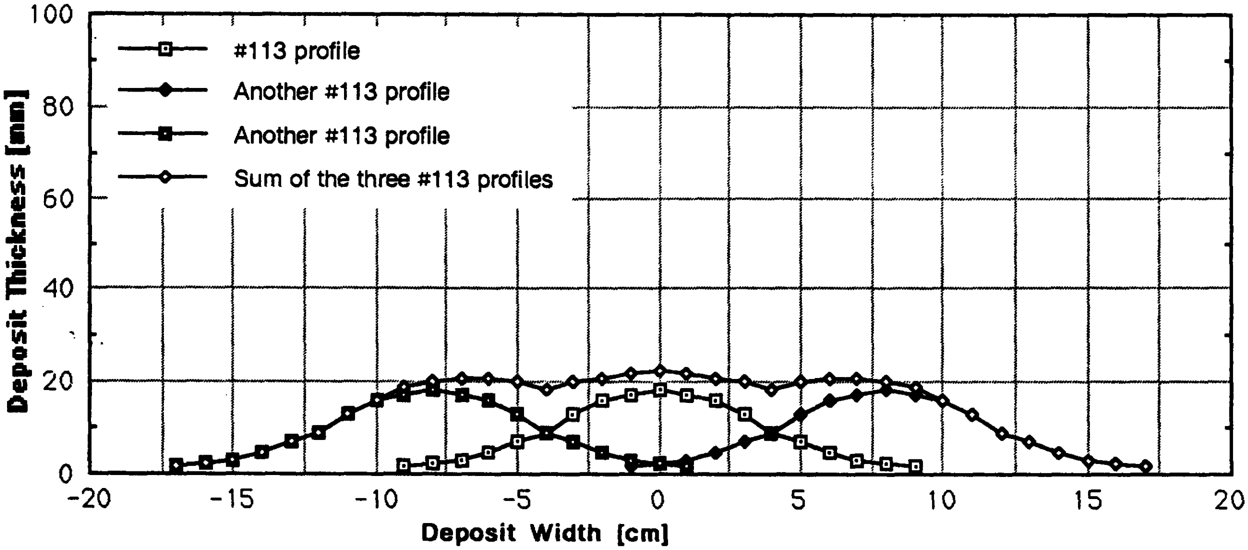

Figure 44. Continued........

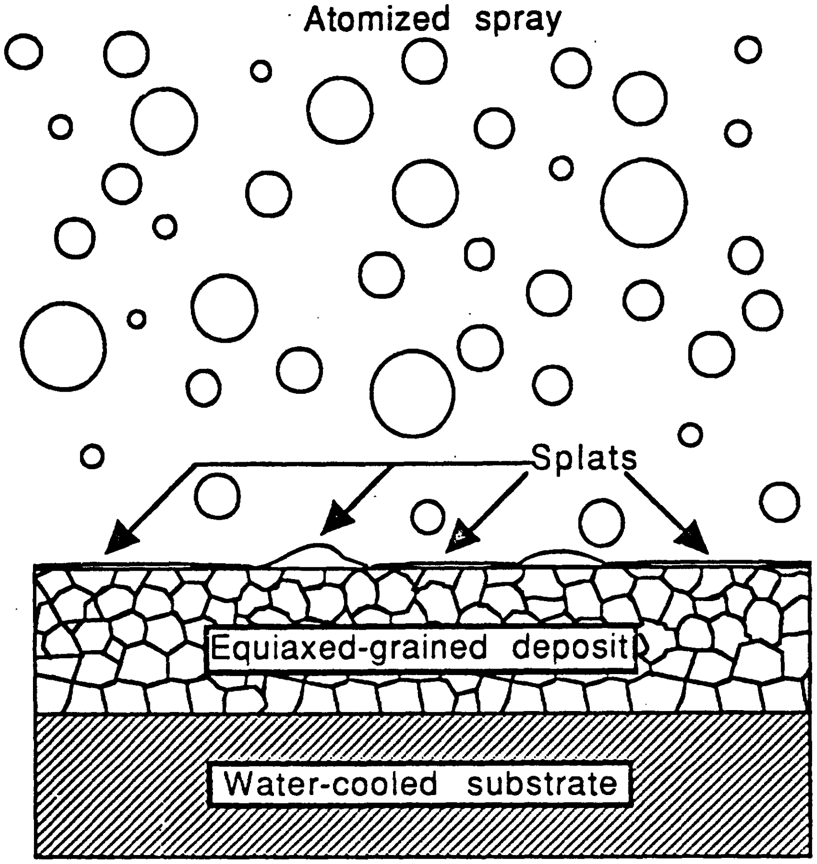

Figure 45. Schematic representation of the LDC spray deposition process.

powder metallurgy process, in which no liquid layer is involved, and from the ingot metallurgy process, in which the mass is essentially liquid. If this liquid layer is very thin, with the presence of high solid fraction in the depositing droplets during deposition, then a somewhat more porous structure is formed. On the other hand, if the layer is very large, the rapid solidification advantages are lost and a deposit with cast structure is formed. To achieve the proper conditions of a successful LDC run, the right combination of parameters, such as melt temperature and delivery rate, aspiration pressure, atomization gas pressures, gas/melt flow ratio, and flight distance must be chosen.

The combination of the droplets' heat content, the heat transfer to the atomization gas, and the heat extraction through the existing layer of the deposit and the substrate determine the thermal history of the deposit. Additionally, the spatial thickness distribution of the deposit, the droplet impact areas per unit of surface, and whether the substrate is water cooled affect the spatial thermal history of the deposit. These interactions complicate the prediction of the temperature distribution in the deposit and lead to different microstructures through the deposit.

The wide droplet size distribution related to the low atomization gas pressures may not affect negatively the final deposited microstructure since the larger liquid layer at the top of the deposit, which is formed by the larger droplets, facilitates the incorporation of most of the pre-solidified fine droplets into the deposit. The fine pre-solidified droplets may remelt partially or completely after impacting into the liquid layer; however, this is not considered to be a major factor.

All the deposits had microstructures that mostly consisted of equiaxed grains of 10 - 50 μm sizes. However, other types of microstructures were present at certain areas of the deposit. The kind and sizes of the microstructures depended on the fine scale thermal history of the deposit, which, as mentioned above, is not easy to predict.

During the early stages of the deposition, the first droplets impact on the cold substrate, splat and freeze before the following droplets are deposited.

If the undercooling of these splats is large enough and their heat transfer rate is such that the maximum recalescence temperature does not reach the solidus temperature T_S, then these splats solidify completely, essentially without segregation, as shown in Figure 46A. Due to the heat input from the depositing droplets and the reduced heat extraction rate through the substrate after a certain thickness of the deposit has formed, a columnar structure begins to grow at the top of the splats, as shown in Figure 46B. As the deposition continues and the liquid at the top of the deposit increases, the columnar structure changes into very small equiaxial structure (1µm), as shown in Figure 46C. This fine equiaxial structure then changes into relatively larger equiaxial grains with more consistent sizes (15-25µm) throughout the rest of the deposit, as shown in Figure 46D. The undercooled structure at the bottom, the columnar structure and the fine equiaxial grains should be limited to the bottom 5 mm of the deposit, while most of the rest of the deposit consisted of relatively coarser and more consistent equiaxial grains.

The fine droplets at the periphery of the spray plumes form porous layers both at the top and the bottom of the deposit. The thicknesses of these layers are variable and depends on the melt superheat and on the droplet size and distribution. The back side of the plume deposits fine droplets on the fresh surface of the advancing substrate and forms a porous layer of about 85% density there. The porous layer can be either agglomerates of powder when incorrect parameters are used as that at the bottom of run #78 shown in Figure 47, or a cohesive network, as shown in Figure 48. This layer, however, is always less than 10 mm thick, and is even kept smaller when the right parameter are chosen. This layer then advances under the more densely populated center of the spray, which deposits an equiaxial structure at the top of it. Sometimes, when the wrong parameters are used, due to the low heat transfer of the bottom layer and the high deposition rate at the center of the spray, a large top liquid layer is formed. The force from the atomization gas pressure pushes this large liquid layer to the sides over the early solidified layer existing there. Two separate structures of different sizes, at the top of each other, are seen to form there, as shown in Figure 49. As the substrate continues to advance, the fine droplets at the front end of the plume deposit a very thin porous layer at the top of the deposit.

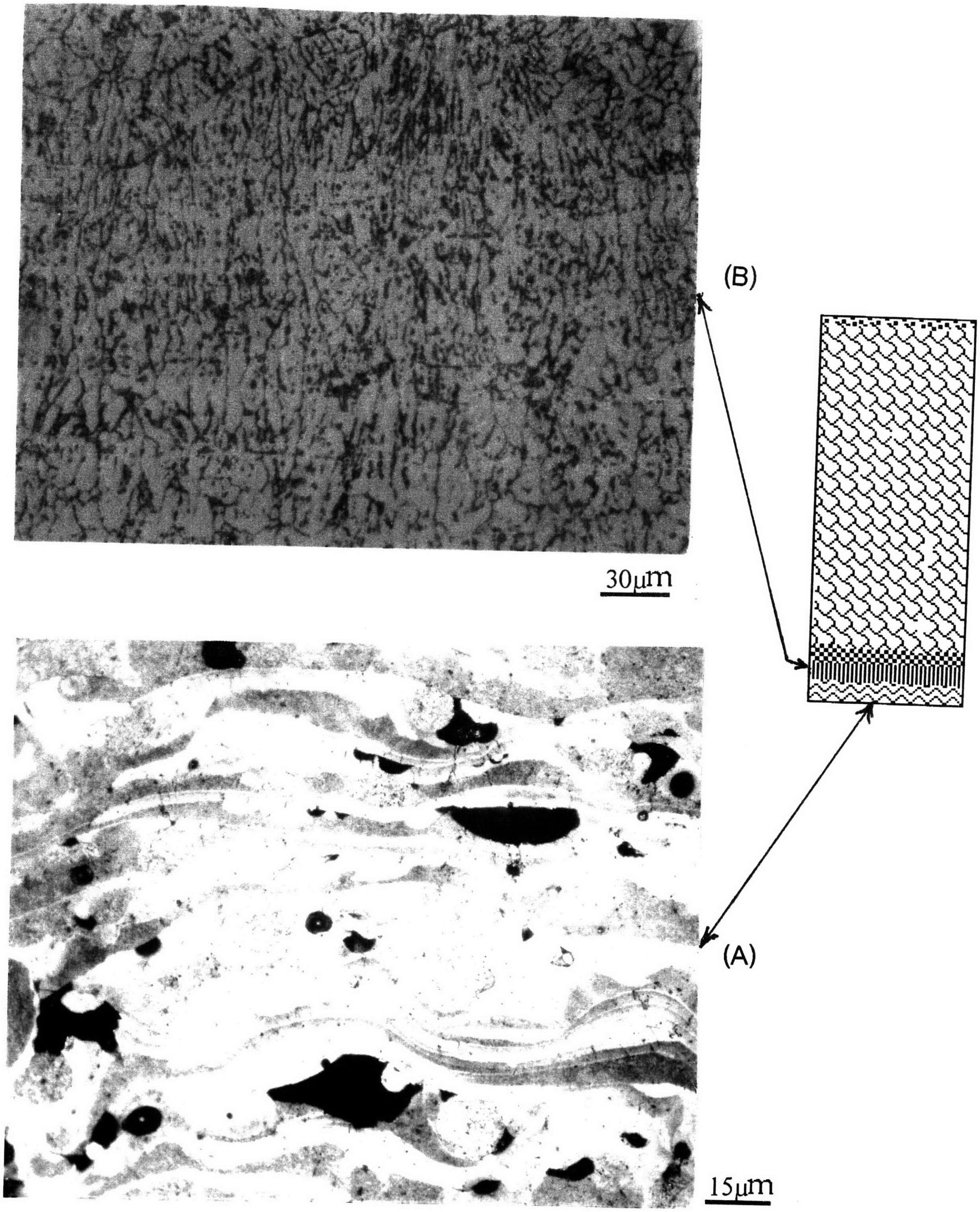

Figure 46. The different types of microstructure in the LDC deposit: (A) Undercooled splats, at the bottom, [X660] (B) Columnar structure, at the top of the splats, [X330].

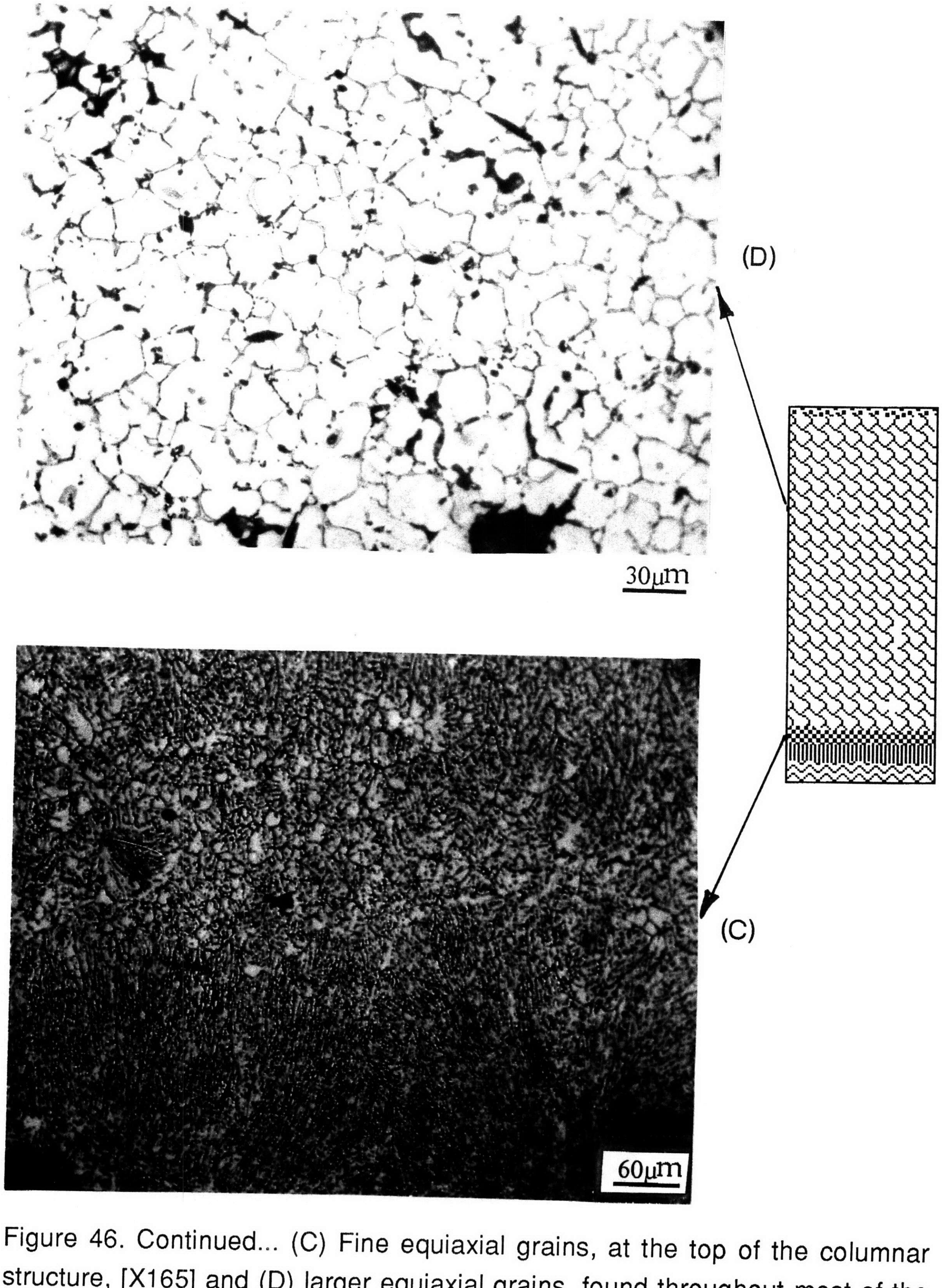

Figure 46. Continued... (C) Fine equiaxial grains, at the top of the columnar structure, [X165] and (D) larger equiaxial grains, found throughout most of the deposit, [X330].

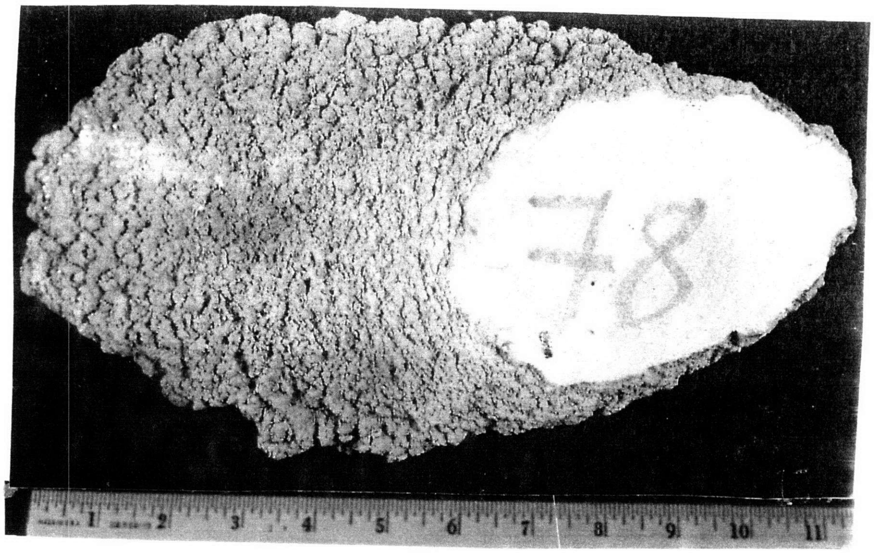

Figure 47. Agglomerates of unacceptable powder deposited by the spray back-tail at the bottom of run #78, which result from a wrong combination of process parameters.

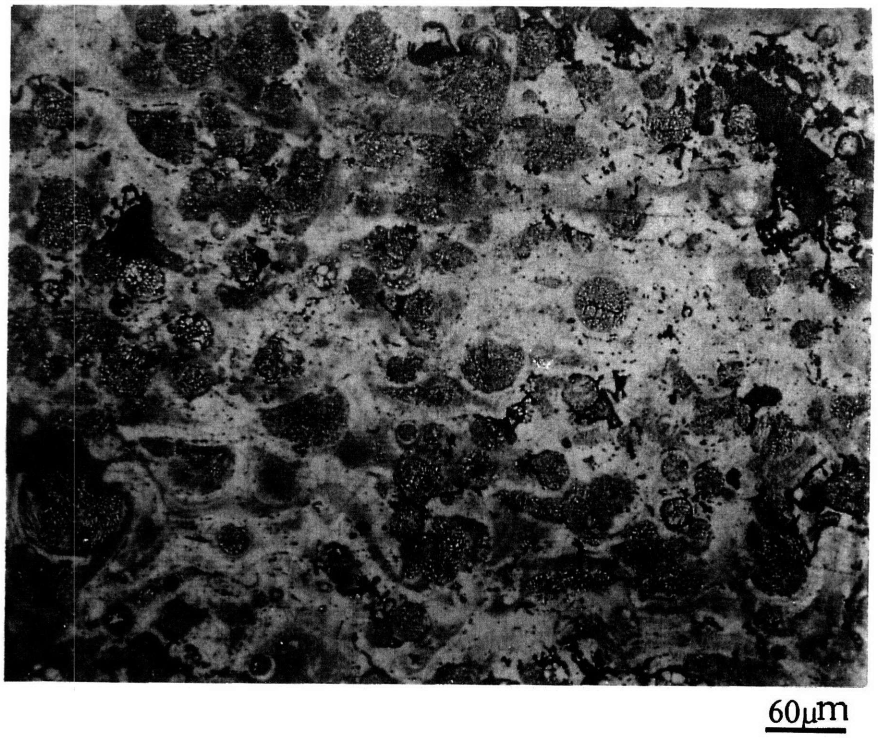

Figure 48. The cohesive bottom porous layer formed by the fine droplets from the back-tail of the spray plume, [X165].

Close to the end of the run, when the melt head level and the melt flow rate decrease, the spray tent apex angle increases until it is equal to the atomizer included angle but does not exceed it.[80] This wider spray plume is lightly populated only with fine droplets due to the high gas/melt flow ratio. A small porous layer, in the range of 1 mm, forms at the top of the deposit. This layer usually contains very fine pre-solidified particles that had frozen in flight and are found in the deposit, either completely spherical or partially remelted, as shown in Figure 50. These fine droplets with a high solid fraction constitute the characteristic rough top surface of the LDC deposit. If deviations from the required deposition procedure take place and there is an excess of liquid at the top of the deposit, then a smooth shiny surface will result.

5.1.10.1. Equiaxial Grains Structure

There is a competition between the columnar and equiaxial structures at the early stages of the deposition after a certain liquid layer has formed. The prevailing structure is influenced by the melt superheat, the temperature gradient across the deposited layer, the convection level in the liquid layer on the top of the deposit and the melt solidification temperature range. When the superheat and the temperature gradient are low, the convection in the melt is high, and the melt freezing temperature range is wide, the equiaxial grain structure prevails.[80] When these conditions are reversed the prevailing structure is the columnar one. In the LDC process, most of the deposit consists of an equiaxed grain structure, whose change in size from the bottom to the top of the deposit was negligible. The grain sizes were reported to change from the bottom to the top at a rate of 300 µm/m of the deposit thickness.[14] This increase is rather small and for a deposit of 20 mm thickness is about 6 micron. However, this 6 µm size is actually within the grain size variation seen with in a micrograph, and does not stand out.

The average as-deposited grain sizes in the equiaxial region of the deposit of this study were between 20 to 45 µm. The average grain sizes, maximum deposit thickness, and other characteristic parameters of selected runs are listed in Table 14. Substrate water cooling, smaller deposit thicknesses, lower melt flow rates, a higher G/M ratio and higher gas power

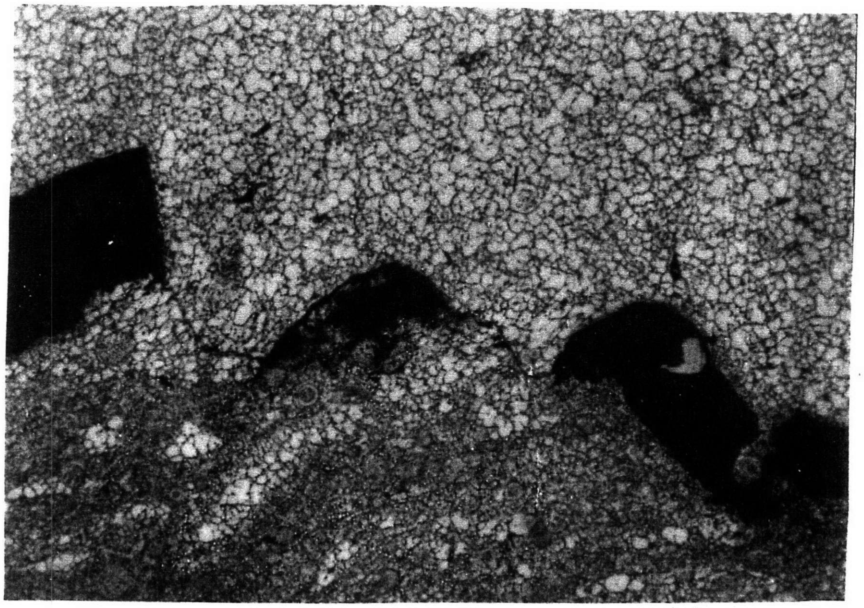

Figure 49. Two different microstructures at the zone where the large liquid layer at the top of the deposit is pushed and flows over an earlier solidified layer, [X82.5].

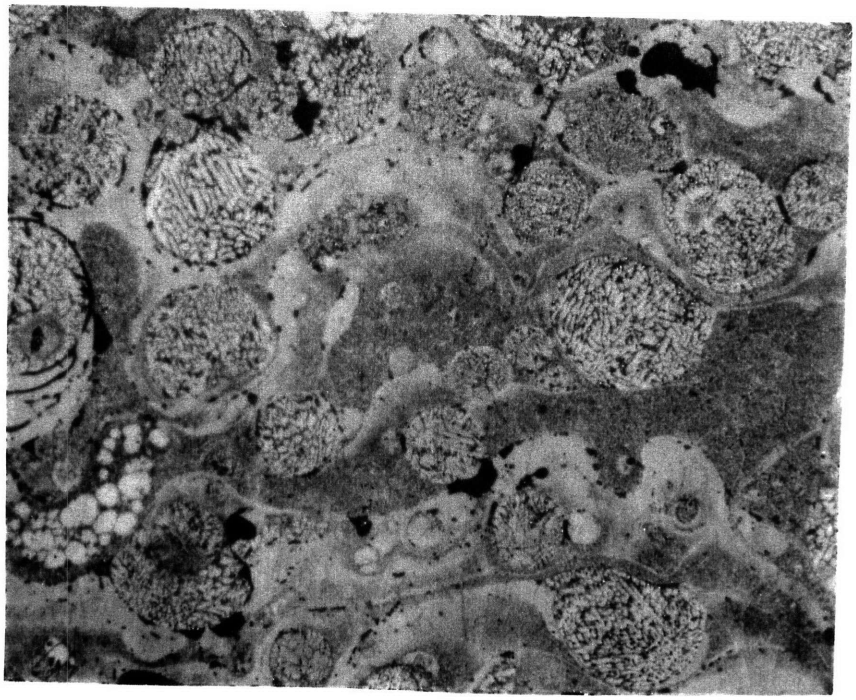

Figure 50. Pre-solidified droplets found in the deposit: either completely spherical or partially remelted after deposition, [X330].

(pressure) lead to smaller average as-deposited grain sizes in the equiaxial region. As can be seen from the table, none of these parameters seem to stand out as being dominant, and their effects seem to compensate each other. For instance, deposits of runs #77, #82 and #94 have the same average grain size while their processing parameters have different values. The difference in deposit thickness between runs #77 and #94 (39 mm and 15 mm, respectively) seems to be compensated by the higher G/M ratio and gas power of run #77. Comparing runs #82 and #94, the substrate water cooling and moderately higher G/M ratio and gas of run #82 compensate for its larger deposit thickness.

Table 14. The Average Equiaxial Grain Sizes and Other Characteristic Parameters of Selected LDC Runs.

Run #	Average grain size [μm]	Deposit thicknes s [mm]	Water Cooling	Melt flow rate [kg/min]	Gas/Melt flow ratio	Gas power [Watts]
69	22	33	yes	5.76	1.04	13,272
70	24	44	yes	5.69	1.09	13,874
75	42	30	no	3.69	1.67	13,572
77	27	39	no	5.07	1.85	20,802
81	33	26	yes	5.59	1.04	13,001
82	26	22	yes	5.89	1.22	15,967
94	26	15	no	4.74	1.18	12,510
98	38	20	yes	9.04	0.59	11,918
112	44	26	no	7.87	0.54	9,480

There are several mechanism that explain the formation of the equiaxed grains in a spray forming process. The nucleation of these mechanisms is heterogeneous. One of these mechanism is the one known as the "Big Bang Mechanism".[189] In this mechanism, the nuclei that form at the undercooled zone at the solid/liquid interface grow first as columnar grains. Then they break off from the interface due to the impacting droplets and drift into the molten thin layer becoming nuclei for the equiaxed structure.

In another mechanism, crystals that are heterogeneously nucleated at the solid liquid interface separate from the interface due to melt convection in the liquid layer. These crystals either get remelted completely or multiply into more crystals depending on their sizes and the local temperatures. These separated and multiplied crystals become nuclei to the equiaxial grains.

In another mechanism, nuclei of the equiaxial grains are formed by dendrite arm fragments that originate from either partially remelted dendrite arms or from mechanically fractured dendrites by splatting of the partially solidified droplets onto the top liquid layer. These dendrites originally form either in the partially solidified droplets in flight or inside the liquid layer.

Other nuclei of the equiaxed structures include the second phase particles and the pre-solidified droplets, which can act as nuclei for the equiaxed grains.[80]

The substantial undercooling in RS processes affects the structure and segregation in such a way that the dendrite arm spacings and the segregation patterns cannot be directly correlated to the cooling rate of the droplets in flight. The cooling during splatting is lower than the more than 10^3 °C/sec rate usually experienced by the droplets in flight. During the formation of the equiaxial grains, the partially solidified grains in the mushy zone do not grow as large as the prevailing solidification time would allow. This is because the solid in the mushy zone is interconnected and contains tiny pools of liquid in its interstices, and, thus, the maximum size attainable by these grains is restricted and is not dictated by the solidification time.[14]

5.1.11. Deposit Density and Porosity

As discussed earlier, small porous layers form both at the bottom and the top of the deposit, while most of the deposit core is of dense equiaxed structures. There were three kinds of porosities that were experienced in an LDC deposit; which are: 1) shrinkage porosity, which forms where grain boundaries meet and inhibit liquid feed into the solidification shrinkage, 2) gas porosity, which can come from either the entrapped gas or dissolved gas from the matrix, and 3) spaces (crevices) between splats due to the inability of the splats to fill the gaps between them because of their high solidification rates. These crevices are usually found only at the bottom of the deposit. Such porosity is usually of micron size and is well distributed. Micrographs of these porosities are shown in Figure 51A -C.

The porosities understandably lead to a lower deposit density, which is specially lower at the bottom and the top porous sections of the deposit. The as-deposited densities at certain sections of the deposits of selected runs were measured without removing the bottom or top porous layers, using the Archimede's principle. The samples were weighed first in air and then weighed while immersed in distilled water. The difference between these two weight measurements is equal to the weight of the water displaced by the immersed sample. Since the distilled water has 1 g/cm^3 density, the difference of the two weights is equal numerically to the volume of the displaced water and the sample. The density of the sample was then calculated. Dividing the calculated densities of the samples by the theoretical density of their alloys, the relative densities of the samples were determined.

The theoretical density of the alloys was approximated by assuming that the alloying elements were present in elemental form and contributed separately to the density of the alloy. The calculated theoretical densities of the different shipments of the commercial purity and the modified 3003 Al-alloys are listed in Table 8. The relative densities of certain sections of the selected deposits are listed in Table 15.

The density is seen to decrease from the center to the edges and from the front to the back of the deposit. This is due to the finer droplets at the periphery of the spray plume, which contribute to the lower density at the edges and the bottom` of the deposit. In general, the average density of these deposits were 95 % (± 4%), although certain parts of the deposit were completely dense while others were somewhat more porous.

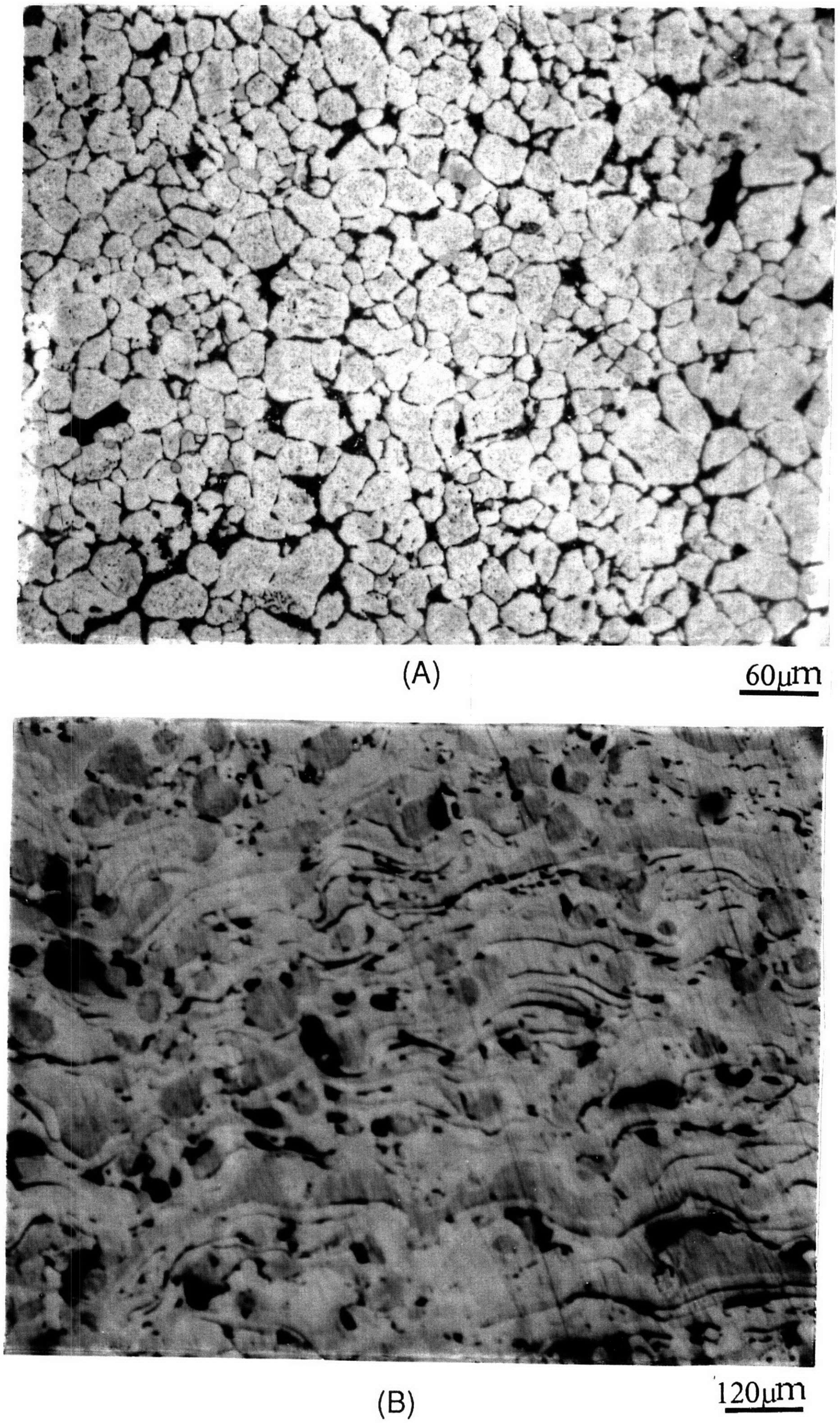

(A)

(B)

Figure 51. Different types of porosities found in the LDC deposit: (A) Solidification shrinkage, [X165] (B) crevices between splats, [X82.5] and (C) gas porosities, [X165] and [X1,800]

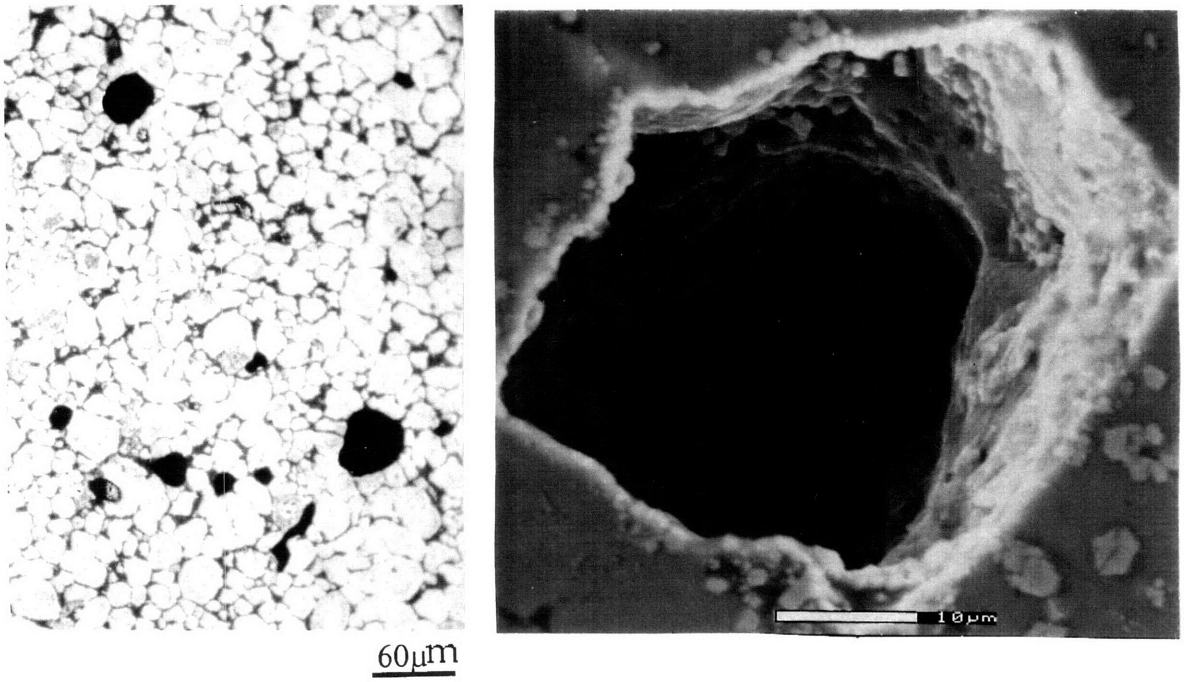

(C)

Figure 51. Continued ....

Table 15. The Relative Density of Certain Sections of Selected LDC Deposits.

Run #	#67	#69	#70	#82	#95	#96	#98	#99	#101	#112
Front center	—	93%	97%	95%	91%	97%	97%	97%	94%	99%
Front edge	—	—	—	—	—	—	—	—	—	98%
Back center	91%	85%	96%	91%	89%	94%	92%	94%	93%	98%
Back edge	82%	—	—	—	—	—	–	—	—	96%

Maintaining the fraction of liquid of about 50% in the atomized droplet at deposition was reported to achieve the desired maximum density in the LDC deposits.[3] This can be achieved by increasing the droplet size by lowering the atomization pressure, and also by setting the atomization parameters to appropriate values.

5.1.12. Deposit Solute Retention

Due to the high cooling rates in the RS processes, higher solid solubilities of the alloying elements are achieved, and new non-equilibrium crystalline and non crystalline phases are formed. The supersaturation of impurity elements is also increased, and their complex segregation phases were eliminated.

The extent of the solid solubility increases with increasing cooling rates and initial solute content. The higher solid solubility allows higher alloying additions which lead to superior strength-ductility combinations.[115] The maximum solid solubilities of a number of binary Al-alloys are listed in Table 16.[155] Elements that are susceptible to solubility extension in binary alloys, such as manganese, were seen to increase the solubility limits in ternary alloys of elements with low solubilities, such as iron, cobalt and nickel.[190]

Table 16. Maximum Solid Solubilities of Rapidly Solidified Binary Al-Alloys.[115]

	Maximum at equilibrium			
		Temperature		
Element	at.%	K	°R	Reported maximum, at.%
Cr	0.44	935	1670	>5–6
Cu	2.5	820	1460	17–18
Fe	0.025	930	1660	4–6
Mg	18.9	725	1290	36.8–40
Mn	0.7	925	1650	>6–9
Ni	0.023	915	1600	1.2–7.7
Si	1.59	850	1520	10–16
Zn	66.5	655	1170	38–···

During the heat treatment of the rapidly solidified alloys at low temperatures, their characteristic smaller grain sizes lead to high boundary diffusion rates due to the large available grains boundary areas. The solute elements, thus, tend to form fine second phases at the grain boundaries, which eventually grow in time. However, as the heat treatment temperature is increased, the lattice diffusion rate increases rapidly with temperature and becomes competitive with the boundary diffusion processes. Therefore, a more uniform second phase nucleation from the supersaturated solute elements is expected to occur in the grains as much as at the grain boundaries.

5.1.13. Deposit Oxygen Content

Carrying out the LDC spray deposition process in an inert atmosphere contributed to a reduction of the oxygen pickup by the sprayed droplets. The LDC atomization of the modified 3003 alloy resulted in an oxygen content of 90 to 100 ppm. This level is about one to two orders of magnitude lower than experienced in the powder metallurgy process. Although very few prior boundaries were observed in the first few undercooled splats at the bottom of the deposit, the absence of these prior boundaries in most of the deposit is an indication of the LDC success in this respect.

5.1.14. Second phases Particles

The high cooling rates associated with rapid solidification processes lead to refined second phases of simple compositions. These second phases can be divided into: 1) phases present at equilibrium but not stable at the processing temperatures, and composition in which they are observed, 2) phases that appear on further heat treatments of the solid, and 3) non equilibrium phases. Due to RS process, hypereutectic Al-alloys, such as Al-Fe alloy, deposited first an α-aluminum phase from the hypoeutectic equilibrium; and sometimes the eutectic phase morphologies changed from irregular Al-$FeAl_3$ phases to regular Al-$FeAl_6$.[115]

In some spray deposited Al-alloys, primary intermetallics were absent and the particles that precipitated were either intercellular or interdendritic in the aluminum matrix.[3] However, intermetallics that form during rapid solidification processes were different in chemistry, smaller in size, and uniformly distributed compared to those that form in IM products.[24] Refinement of the second phase and the eutectic by rapid solidification in Al-Si alloys resulted in dispersion hardening.[115]

Quenching during splatting in LDC spray deposition is lower than the 10^3 °C/sec found in the droplets in flight, and is inadequate to prevent some or all of the primary precipitation.[3] The main primary constituent phases in the 3003

Al-alloy, as discussed earlier in the literature review, are α-$Al_{12}(Mn,Fe)_3Si$, $(Mn,Fe)Al_6$, and Al_3Mn, while the modified 3003 may contain a host of the second phases listed earlier in Table 7. The LDC deposited 3003 had primary second phase particles of dendrite-like shaped needles that delineated the grain boundaries of the as-deposited structure. These phases, as shown by ESEM secondary electron imaging in Figure 52, were of 1 µm diameter and 5 - 10 µm length; whereas, the secondary constituent particles of the modified 3003 Al-alloy were more rounded and of larger volume, as shown in Figure 53. Some of these particles were of agglomerates of 2 µm size particles, as also shown in Figure 53.

Strong bonding of the second phases particles with the matrix reduces the dislocation motion and increases the stability and the strength of the alloy. In addition to the coherency, the other properties of the second phase particles that contribute to strengthening are the particle size, spacing, uniformity of distribution, resistance to deformation, and resistance to fracture.[3] The coherent particles increase the yield strength, while the incoherent particles distribute the plastic deformation and increase the tensile strength.[24]

5.2. Rolling

To characterize the mechanical properties of the commercial purity and the modified LDC 3003 Al-alloys, elimination of the as-deposited porosities and complete densification of the samples are required. This total densification can be achieved by mechanical means, which induces the surfaces of the pores to yield and the material surrounding them to plastically flow into the voids.[3] Shearing type mechanical loading, such as extrusion, was observed to achieve densification more efficiently than compression type loading, such as rolling.[191] In this study, however, rolling was selected since the LDC process was geared to produce sheets. Rolling samples with rectangular cross sections were cut and milled from the deposits. Usually the top and the bottom porous layers of the deposit were milled-off in order to obtain a sample with a dense, equiaxed structure. However, to investigate the effect of these porous layers on the mechanical properties, selected samples were rolled without

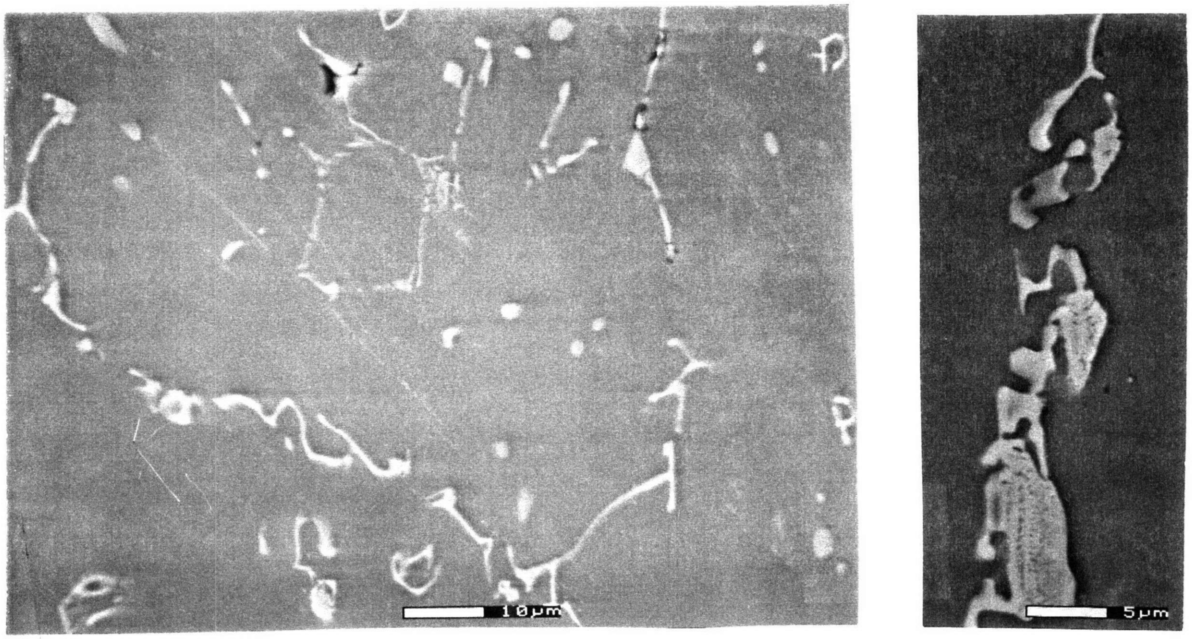

Figure 52. Primary second phase particles in dendrite-like form found at the polished surface of the LDC deposited commercial 3003 Al-alloy, [X1,000] and [X2,000].

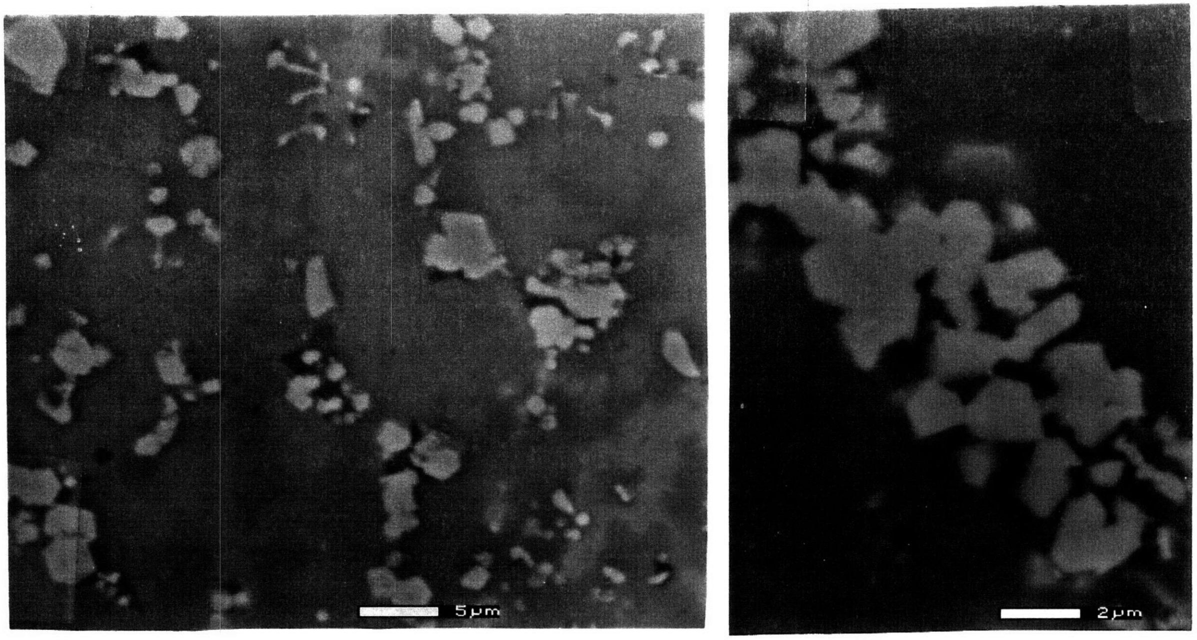

Figure 53. Primary second phase particles found in the LDC deposit of modified 3003 Al-alloy showed their roundedness and agglomeration, [X2,000] and [X5,000].

removing the bottom layer. A sample from the porous run #95 was also rolled for the same goal.

In general, the LDC deposits have good workability, no macrosegregation and fine second phase particles. They needed few processing steps to achieve complete densification. For deposits with initial densities in the range of 96-98%, hot rolling of 30-40% reduction was reported to attain theoretical density, although sometimes it was hard to eliminate small spherical porosities even with rolling reductions of 60%.[22]

The samples in this study were rolled at different temperatures to determine the effect of the rolling temperature on the annealing behavior and the mechanical properties of the alloys. The initial thickness of the rolling samples was between 10 and 16 mm. These samples were heated to the selected rolling temperatures in a box furnace that was already set to temperature. It took 15 to 30 minutes of heating for the samples to reach the rolling temperature.

The first and the second rolling reductions were usually kept under 15% and 20%, respectively, especially when the samples were cold rolled. At higher reductions, cracks were observed on the edges, and the top and the bottom surfaces of the samples. These cracks were especially severe in the modified LDC 3003 alloy. At rolling temperatures below 300 °C it was difficult to roll samples from this alloy even with an initial rolling pass reduction of 10%, since they split in the middle in an alligator type cracking, as shown in Figure 54. However, they were easily rolled at temperatures above 400 °C. After initial rolling at these high temperature to about 45% total reduction, and after an adequate closure of the initial porosities, the modified 3003 alloy was cold rollable without cracking. On the other hand, samples from the commercial purity LDC 3003 alloy were easily rolled at room temperature with an initial rolling reduction of 15%, and larger successive rolling pass reductions.

An investigation of the maximum first pass rolling reductions without cracking as a function of the rolling temperature of a LDC 2024 Al-alloy

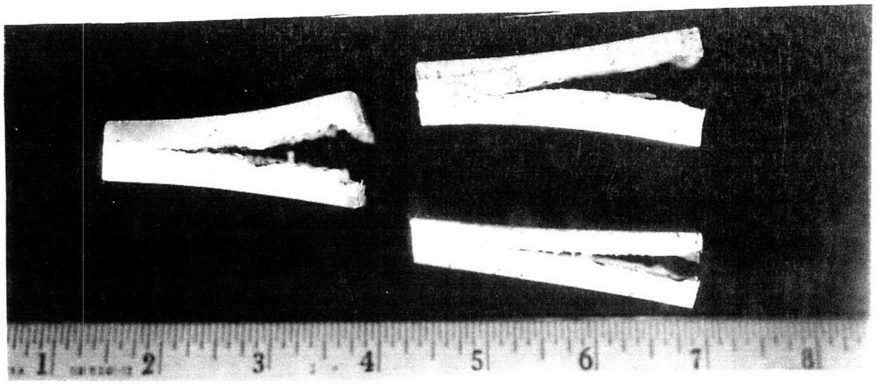

Figure 54. Alligator type cracking that occurs during the initial cold rolling step of the modified LDC 3003 alloy.

showed that reductions in the range of 40% at 350°C and 65% at 460°C were achieved.[T6] In this study, a maximum first pass rolling reduction of 25% at room temperature, without cracking, was realized in the commercial purity LDC 3003 alloy when several millimeter were milled off the porous bottom of the deposit.

A representative rolling schedule for the LDC 3003 alloys, which shows the number of rolling passes, the pass reduction percent, and the total reduction percent, is tabulated in Table 17.

Table 17. A Representative Rolling Schedule.

Rolling pass No.	1st	2nd	3rd	4th	5th	6th
Initial sample thickness [mm]	16.30	14.05	12.04	10.10	6.39	4.35
Final sample thickness [mm]	14.05	12.04	10.10	6.39	4.35	2.45
Pass reduction %	14 %	14 %	16 %	36 %	32 %	44 %
Total reduction %	14 %	26 %	38 %	60 %	73 %	85 %
Samples cut*		A1	A2	A3	A4	A5

* These samples are used to measure density and hardness as a function of the rolling reduction.

Pieces were cut from the rolling samples at different rolling passes to measure the density and the hardness as a function of the rolling reductions.

The relative densities of selected samples from the commercial purity 3003 rolled at different temperatures were plotted against the total rolling reduction in Figure 55. Complete densification of the samples was usually achieved at a total rolling reduction of about 70%, regardless of the hot rolling temperature.

The hardness of the rolled samples was also measured using the surface hardness scale (15T) of the Rockwell hardness machine since both the commercial purity and modified 3003 alloys were too soft for the other Rockwell hardness scales. Although the samples were heated in between rolling passes at different times of up to 30 minutes at the higher rolling temperatures, the hardness of the samples increased in general with increasing rolling reduction, as shown in Figure 56. However, the hardness of the samples rolled at 450 and 500 °C increased slightly with the rolling reduction up to a certain rolling reduction value and then decreased at higher rolling reductions. This behavior could be attributed to the repeated heating of the samples at these high temperatures, which eventually led to their softening. The hardness of the samples was higher the lower the rolling temperature. It was also observed that the equiaxed grains deformed into elongated, pancake shaped structures with aspect ratios that increased with the rolling reduction, as shown in Figures 57. The increasing hardness and the aspect ratio of the grains with rolling reduction indicate that the heating between the rolling passes relieved very little of the work hardening associated with rolling at lower temperatures.

To investigate the effect of rolling on the different microstructures present at different layers of the deposit, two rolling samples were sliced from the commercial purity 3003 deposit of run #69. These samples were rolled to 80% total reductions at 375°C and 450°C, respectively. The samples were rolled with their short transverse cross-section (sliced surface) facing the rolls. The hardness of these samples in the as-rolled condition was measured from the bottom to the top of the deposit and plotted in Figure 58. The hardness increased gradually from the bottom to the top of the deposit. This small differences in hardness can be attributed to the heating of the bottom layer by the depositing upper layers of the deposit .

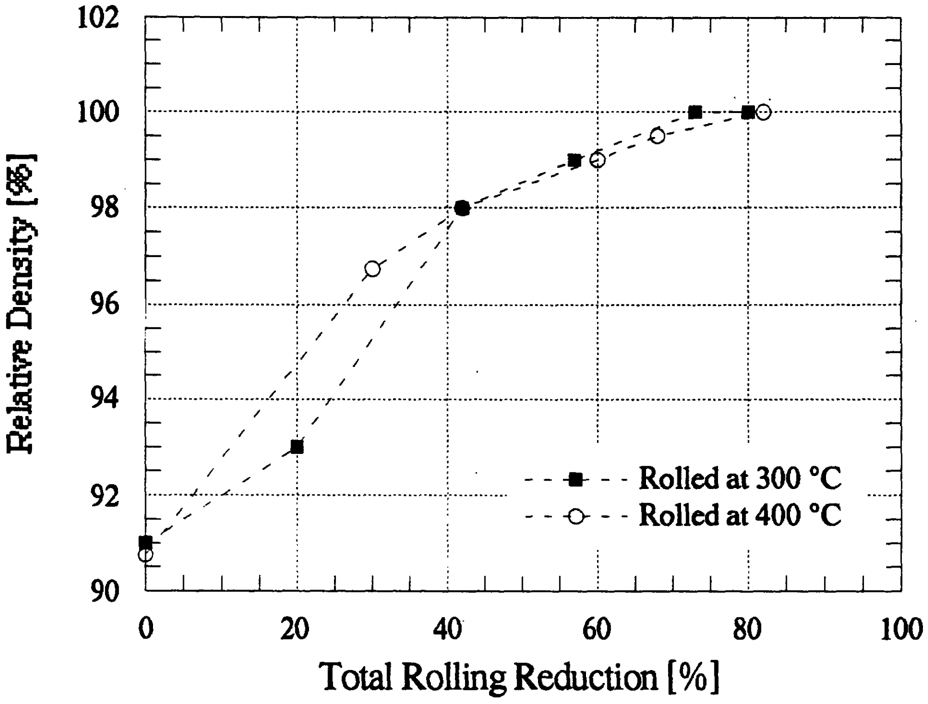

Figure 55. The relative density of selected samples at different rolling reductions %.

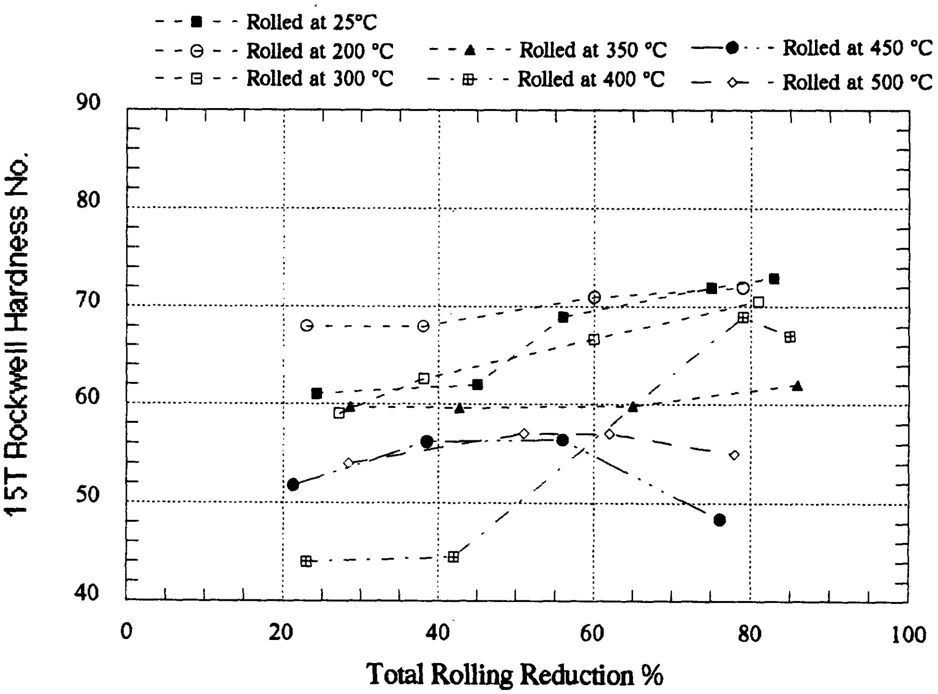

Figure 56. The hardness of samples rolled at different temperatures to different rolling reductions.

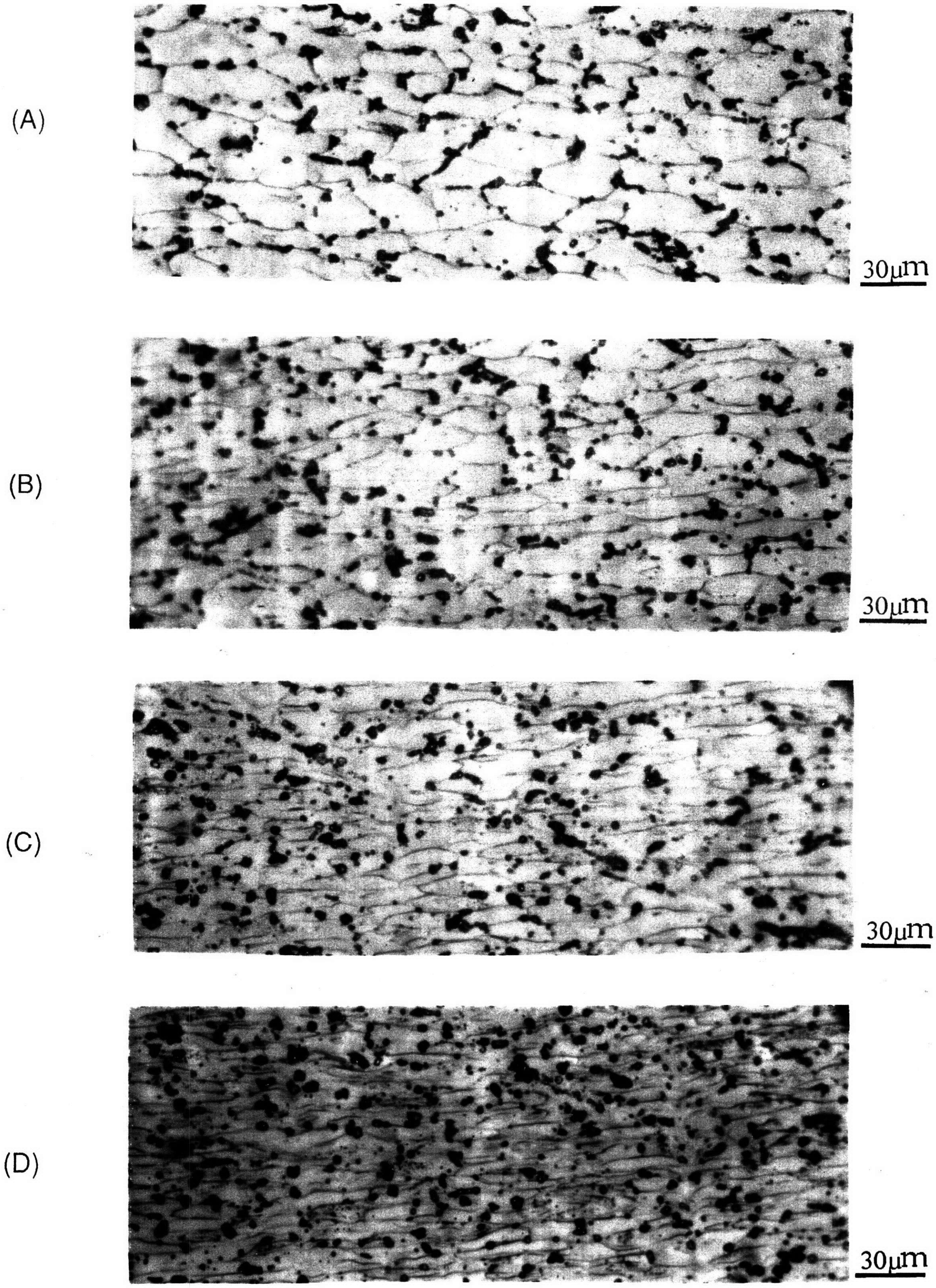

Figure 57. The change of the aspect ratio of the elongated grains with rolling reduction of (A) 45%, (B) 56%, (C) 75% and (D) 83%, [X330]

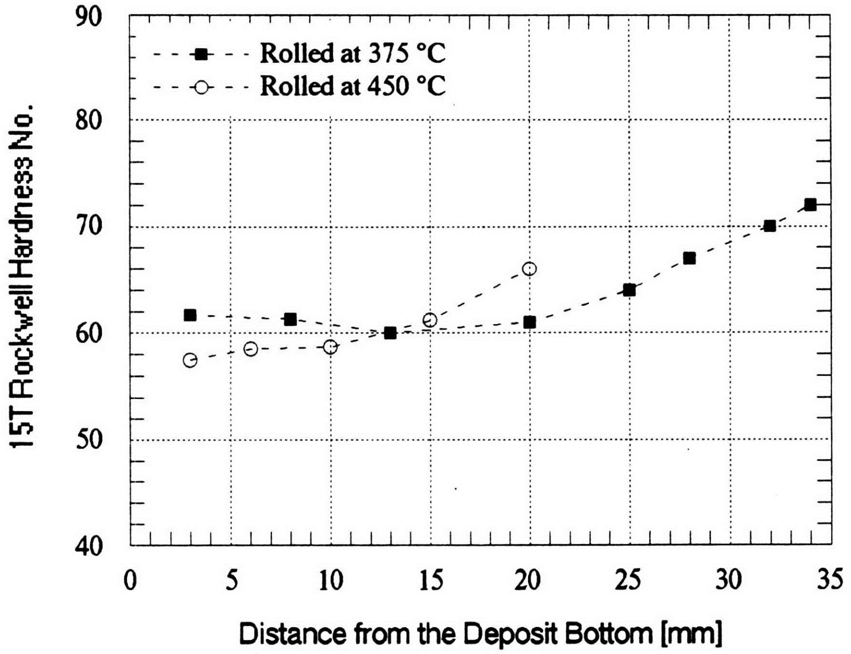

Figure 58. The hardness from the bottom to the top of the deposit thickness of samples rolled with their transverse cross section facing the rolls.

Rolling samples were also cut from run #95, which had a high concentration of pre-solidified particles and high porosity, as was shown in Figure 40, to determine the effect of this type of structure on the mechanical properties of the LDC alloys. After rolling this sample at 400°C to 85% total reduction, it was (essentially) completely densified, as shown in Figure 59. This indicates that the LDC alloys were easily rolled into dense structures regardless of their initial microstructure and porosity. The tensile properties of this sample were very good, as will be discussed later.

Samples for mechanical characterization from the commercial purity LDC 3003 Al-alloy were rolled at 25°, 200 °, 300°, 350 °, 400°, 450° and 500°C; whereas samples from the modified LDC 3003 Al-alloy were rolled at 400 °C and 500°C since rolling at lower temperatures was inhibited by cracking. However, some samples of the modified alloy were first rolled at 400°C to about 45% total reduction and then followed with cold rolling at either 25°C or 200°C to about 80% reduction.

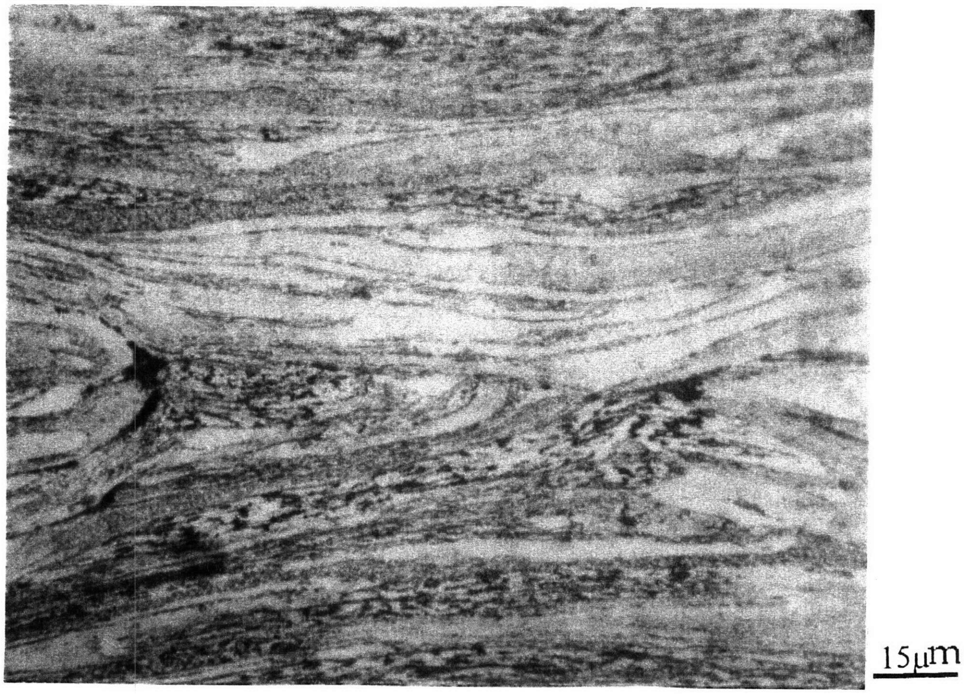

Figure 59. The densified microstructure of sample from the porous deposit of run #95 after rolling at 400°C to 85% reduction. [X660]

5.3. Preheating (Homogenization) Treatment

Al-Mn alloys are usually heated before rolling at high temperatures in the range of 600°C for up to 4 to 24 hours, in a process called homogenization. It was observed that this preheating reduced the Mn supersaturation in the matrix, eliminated the fine secondary precipitates that may have formed otherwise, and eventually led to the formation of very fine grained structures, as was explained in the literature survey. By reducing the number of the fine second phase particles and the matrix solute content, the eventual recrystallization of fine, uniform grains was encouraged, plus the grain boundary pinning by the fine second phases, which retarded recrystallization and eventually led to parasitic grain growth was reduced. Although fine recrystallized grains were formed in the homogenized samples, their strength was lower than those of the unhomogenized, due to the absence of strengthening by the fine second phases particles.

To determine the effect of homogenization on the commercial purity and modified LDC 3003 Al-alloys, samples from these alloys were homogenized at

600°C for 8 hours. Some of the as-deposited microstructures were, as expected, changed by the homogenization treatment. Optical microscope observations showed that the undercooled splats grew to extremely large equiaxed grains of about 250 µm size, while the columnar grains and the very fine equiaxed grains at the top of the splats grew to 120 µm size, as shown in Figure 60A-B. On the other hand, the mostly equiaxial structure of these deposits did not change in size and remained the same, as shown in Figure 61A; although the second phase particles grew larger as is evident from the Figure. However, around the entrapped gas porosities in this equiaxed zone, four large equiaxed grains of 120 µm sizes, which surround the pores at 90° from each other were observed to form, as shown in Figure 61B. The homogenized samples of the commercial purity and modified 3003 alloys were then rolled first at 400°C to 48.5% and 50% reductions, and then rolled at 25°C to 81% and 87%, respectively. The hardness of the homogenized, rolled samples also increased with rolling reductions, as shown in Figure 62. It could be seen that the hardness of these samples jumped high when cold rolled at reductions above 50%.

To investigate the morphological changes that take place during the preheating of the commercial purity and the modified LDC 3003 alloys, differential scanning calorimetry (DSC) samples were heated at 15°C/min to 600°C; however, no peaks were observed in the DSC curves of both alloys, as shown in Figure 63. This may be due to the fact that the DSC samples could have come from the equiaxed zone of the deposits, which, as was observed earlier, changed very little during the homogenization treatment. A similar behavior was reported for an Al-2.3 at% Mn alloy ribbon prepared by the single roller method.[192]

5.4. Annealing

Variable annealing behavior was observed in samples from both alloys rolled at different temperatures. Since the recrystallization of the IM and Directional Chill (DC) cast 3003 alloys was usually complete at 375°C to 400°C annealing temperatures,[143] samples from the LDC commercial purity

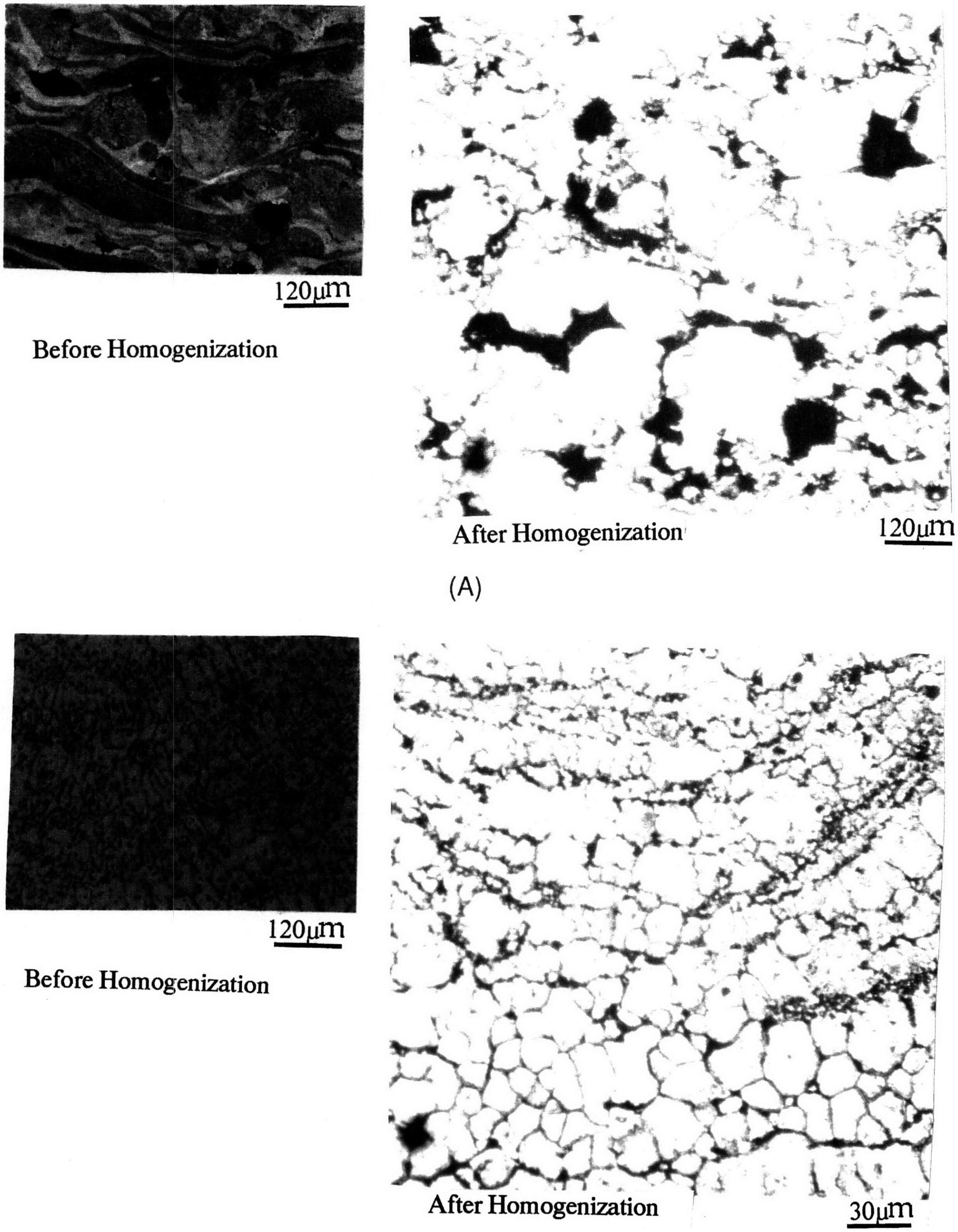

Figure 60. Optical micrograph comparing the various deposit microstructures before and after homogenization treatment: (A) undercooled splat and (B) columnar zones.

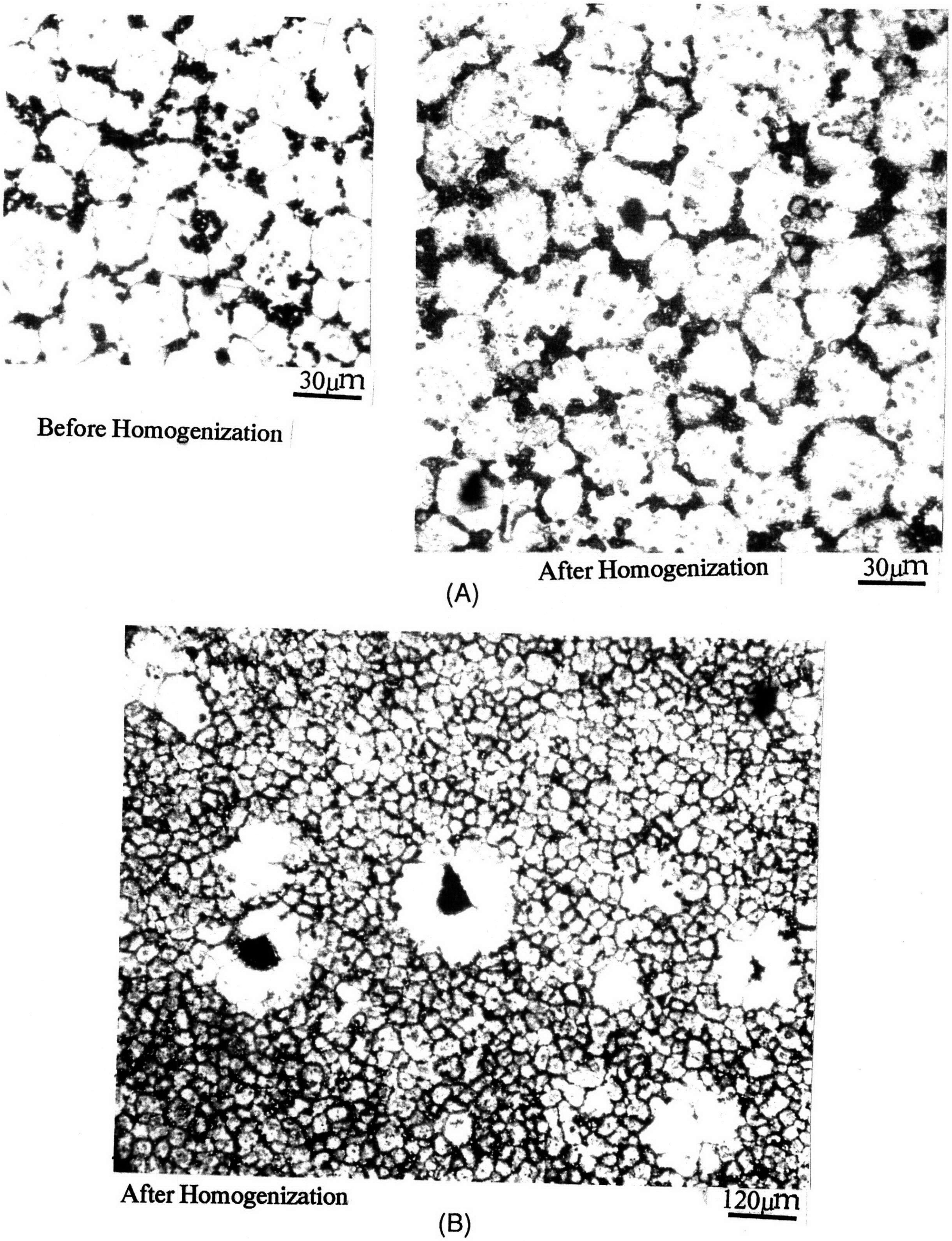

Figure 61. Optical micrograph comparing microstructures before and after homogenization showing that the treatment (A) did not induce changes in the grain sizes of the equiaxed zone, (B) although larger grains were formed around the pores of this zone.

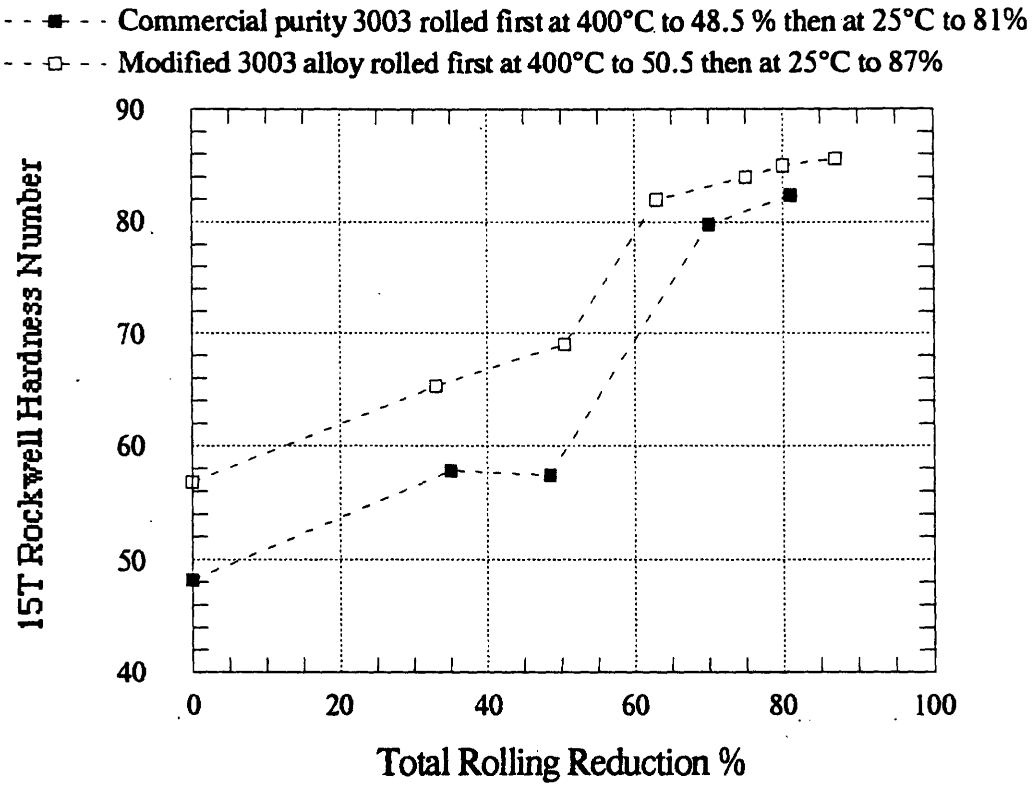

Figure 62. The hardness of the homogenized samples rolled at different temperature to different rolling reduction.

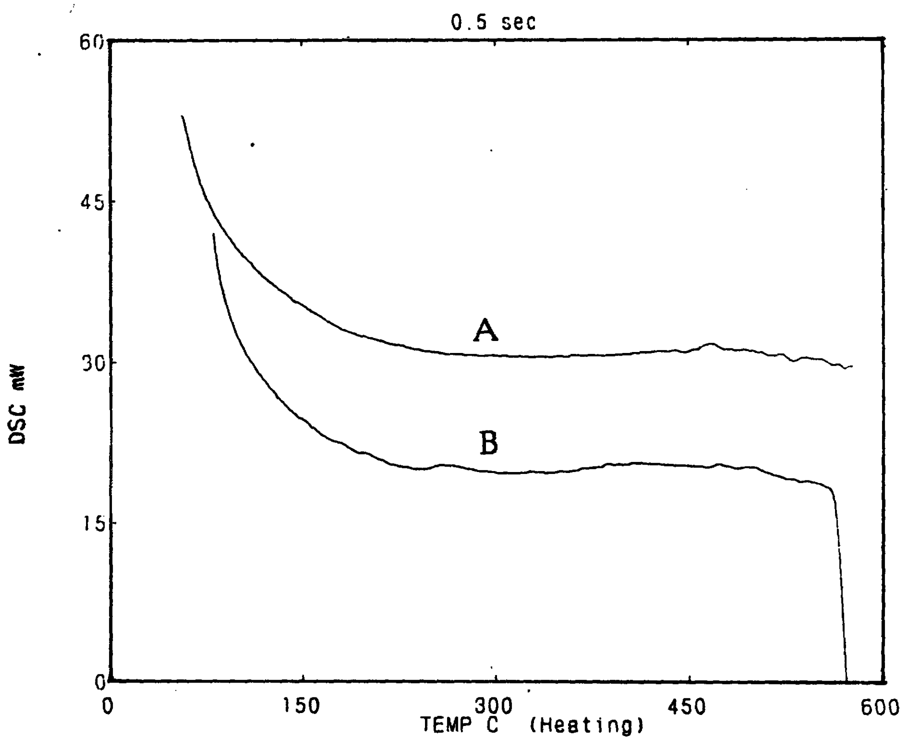

Figure 63. DSC curves of (A) the commercial purity and (B) the modified LDC 3003 alloys heated at 15°C/min to 600°C.

3003 alloy rolled at 375°C to 82.5% were annealed at 375°C and 400°C for variable times. The hardness measurements of these samples were plotted against the annealing time in Figure 64. It was observed that the profiles of the hardness curves for the two annealing temperatures were similar. Thus, to determine the annealing behavior of both the commercial purity and modified LDC 3003 alloys rolled at different temperatures, annealing of their samples was carried out at 400°C for period of times ranging from 30 minutes to 5 hours. To also determine the effect of temperature on annealing, other samples were annealed at temperatures of 200°, 300°, 400° and 500°C for 1 hour. The hardness of all the annealed samples was measured as an indicator of their annealing tendency and behavior. The hardness of the samples from the commercial purity LDC 3003 alloy, annealed for variable times and temperatures, are plotted in Figure 65A-B; whereas, the results for those from the modified LDC 3003 are plotted in Figure 66A-B. The hardness of annealed samples from both alloys, which were first homogenized and then rolled at different temperatures was also measured and plotted in Figure 67A-B.

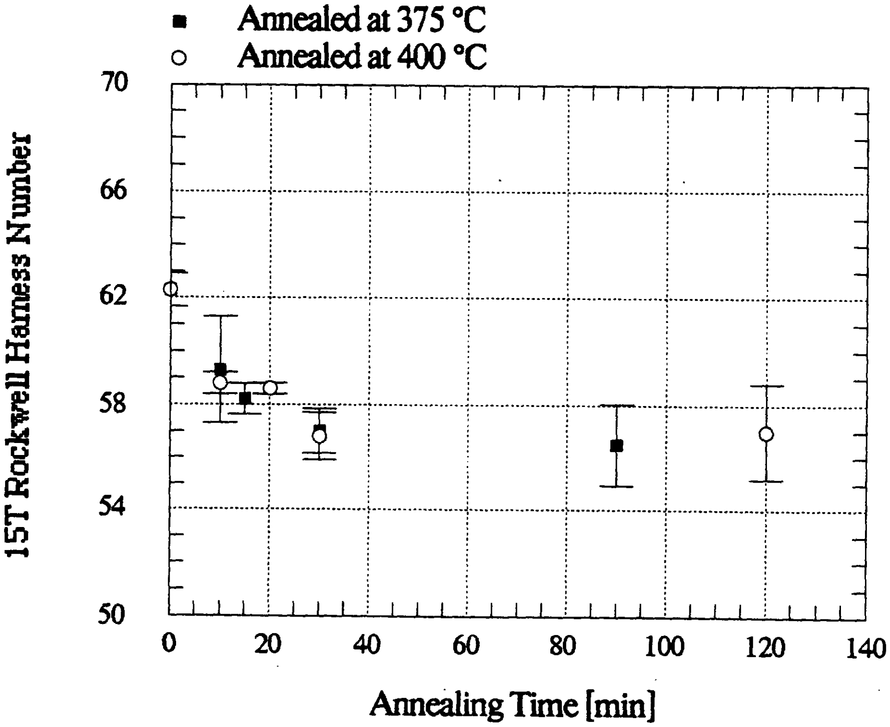

Figure 64. The hardness profiles of a commercial purity LDC 3003 alloy rolled at 375°C and annealed at 375°C and 400°C.

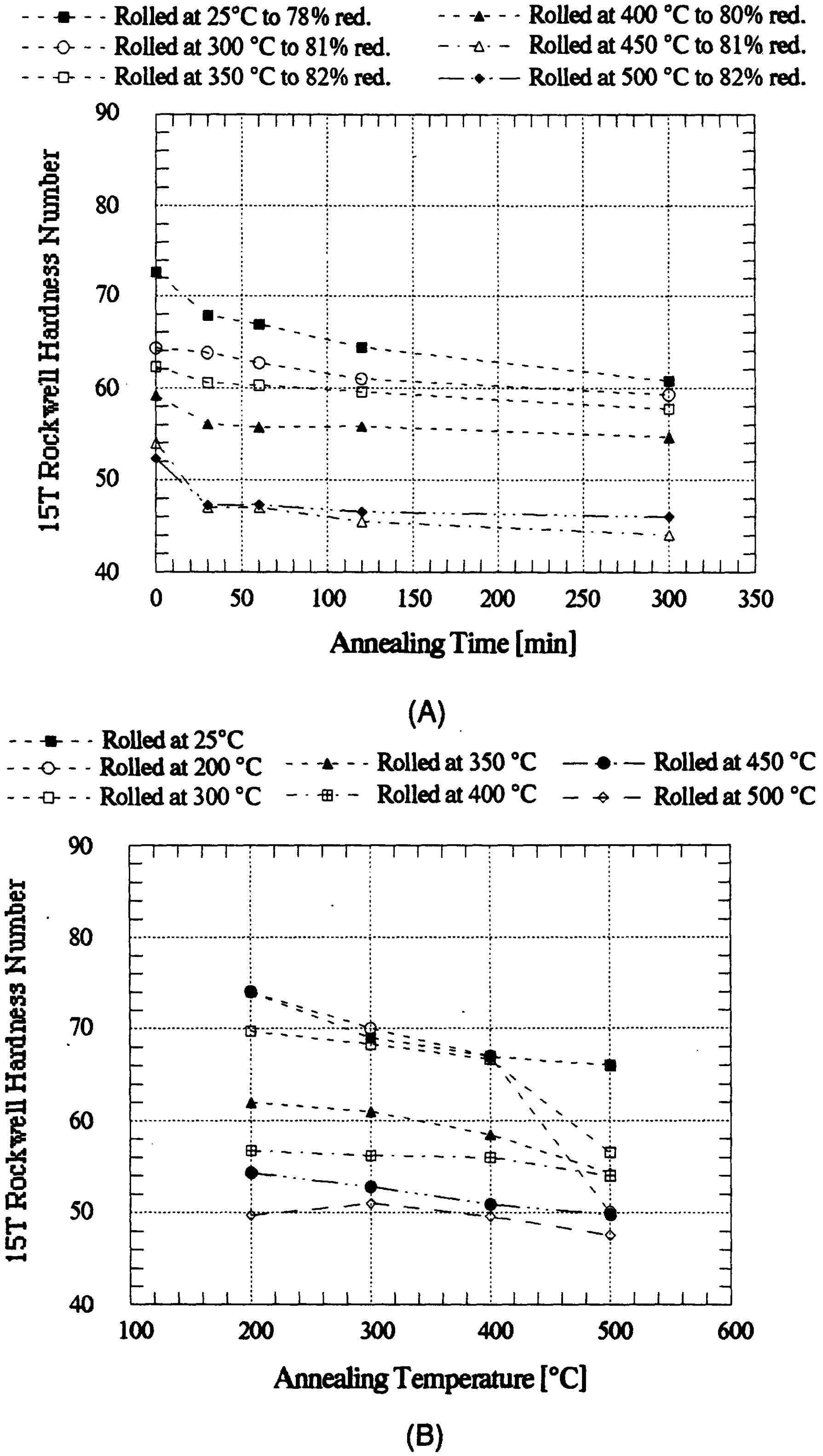

Figure 65. The hardness profiles of samples from the commercial purity 3003 that were rolled at different temperatures and annealed (A) at 400°C for variable times and (B) at different temperatures for 1 hour.

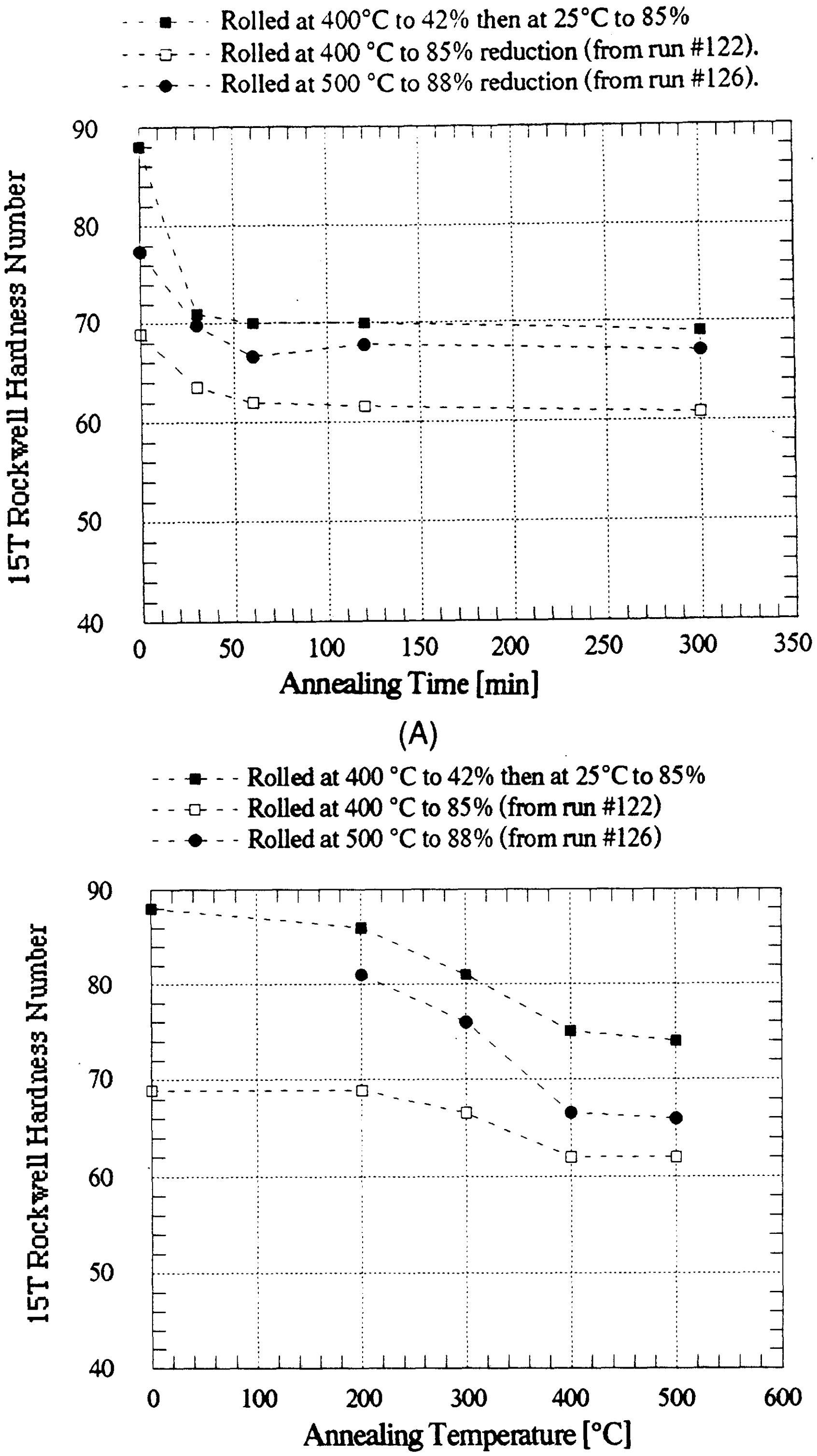

(A)

(B)

Figure 66. The hardness profiles of samples from the modified 3003 alloy that were rolled at different temperatures and annealed (A) at 400°C for variable times and (B) at different temperatures for 1 hour.

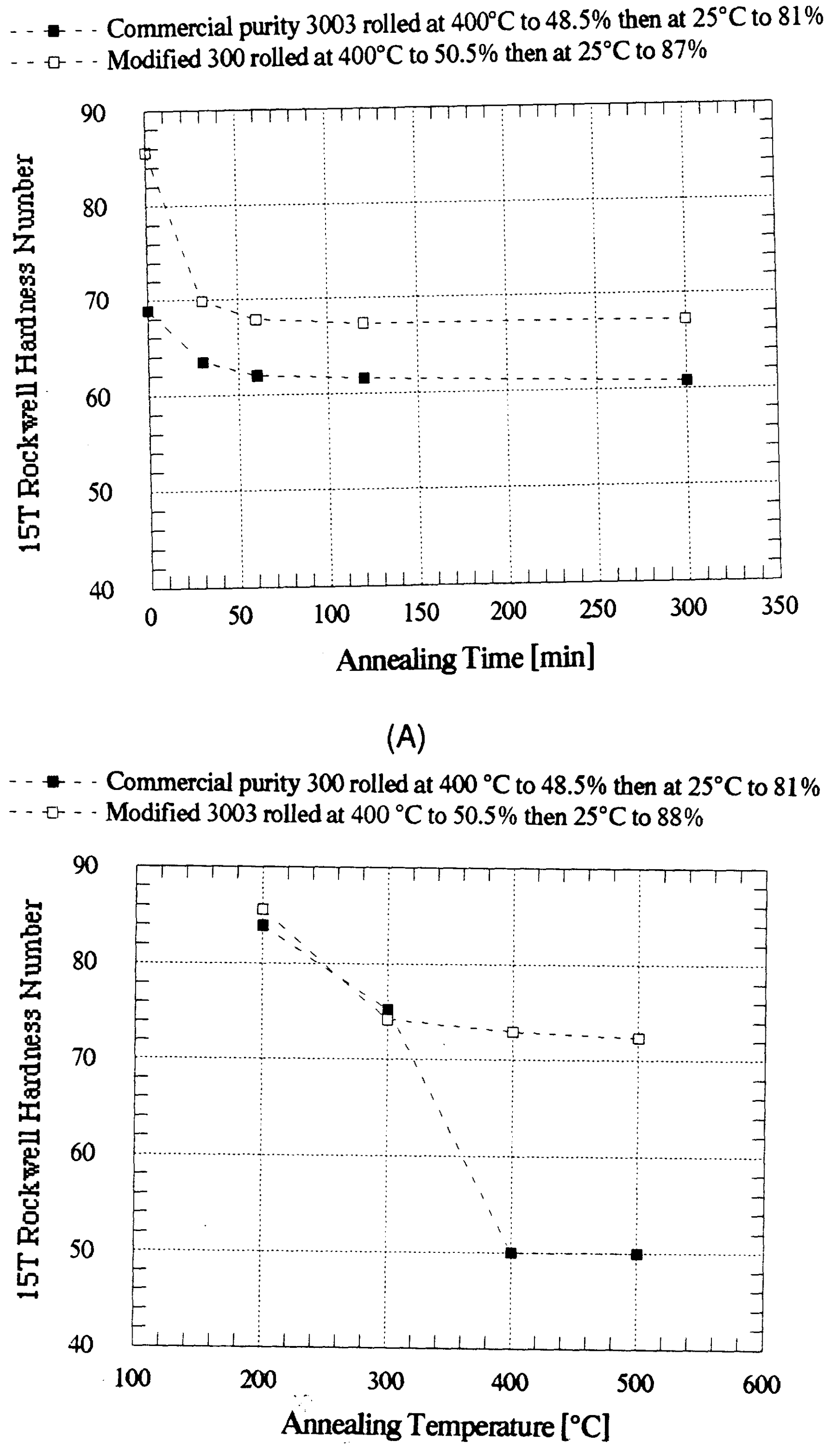

(A)

(B)

Figure 67. The hardness profiles of homogenized samples from both of the 3003 alloys that were first rolled at 400°c to about 50%, and then at 25°C to above 80%, and annealed (A) at 400°C for variable times and (B) at different temperatures for 1 hour.

The hardness curves of the samples of both the LDC 3003 alloys, which were annealed at 400°C for different period of times, had the same profiles, whether homogenized or not. The hardness drop rate at certain annealing time was observed to be constant regardless of the rolling temperatures. After the first 30 minutes to 1 hour of annealing at 400°C, the hardness drop with annealing time was smaller for all samples. However, as was shown earlier in Figure 56, the samples had as-rolled hardnesses, which were higher for samples rolled at lower temperatures due to their higher work hardening. And since the hardness profiles of these samples were similar, the samples rolled at lower temperatures had higher hardness at any annealing time. This behavior is associated with the difficulty of annealing out the work hardening from the cold rolling, and, in general, the resistance of the rapidly solidified 3003 to annealing. Similar hardness profiles were reported for a strip cast 3004 Al-alloy, which was annealed at similar temperatures.[150] It was reported that the chilled surface of a DC cast 3003 alloy needed about 30°C higher annealing temperature to recrystallize at the same time as the core of the cast, which experienced lower cooling rate.[143] It was also reported that large extrusions on a modified LDC 7075 Al-alloys led to high resistance to recrystallization of this alloy.[24]

For samples annealed at different temperatures for 1 hour, the hardness drop with temperature was in general small, although it increased slightly at higher temperatures. To investigate the effect of longer annealing times of these samples at low temperatures, samples from both alloys were annealed at 100°C, 200°C and 300°C for 100 hours. The hardness measurements of these samples did not show any change. Their microstructures also remained the same and, as will be discussed later, their mechanical properties remained almost the same as those in the as-rolled condition.

Optical microscopy investigation showed that the structures of the annealed samples consisted of recrystallized coarse and fine equiaxed grains, and/or elongated grains. However, none of the samples was observed to have completely recrystallized into equiaxed shape. Portions of the samples, which were originally from the equiaxed zone of the deposit, usually recrystallized into equiaxed structure after annealing at 400°C and 500°C for more than 1 hour. In the homogenized samples, these portions formed fine recrystallized equiaxial grains of 20 μm average size, whereas those of the unhomogenized samples recrystallized into larger elongated grains, as shown in Figure 68A-B, respectively. Other sections of the homogenized and non-homogenized samples of both alloys remained elongated even when annealed at 500°C for 5 hours, as shown in Figure 69A-B. The originally undercooled bottom splats of the sample were the most resistant to recrystallization. The samples that were annealed at temperatures up to 300°C for 100 hours contained mostly elongated grains; although very fine grains of about 1-2 μm were observed in a few areas, as shown in Figure 70. DSC analysis of the homogenized and non-homogenized, rolled samples from both the 3003 LDC alloys that were heated to 600°C at 15°C/min, showed no recrystallization peaks. This behavior was also observed in a LDC 2024 Al-alloy in the as-extruded condition.[145]

TEM micrographs of the annealed samples showed the presence of subgrains with lower dislocations visible in the sections of the samples that were recrystallized to equiaxed structure. On the other hand, the sections that did not completely recrystallized were observed to contain dislocations piled-up at the grain boundaries and around the second phase particles, as shown in Figure 71A-B, respectively.

The sizes and distribution of the second phase particles of the rolled and annealed samples of both alloys were investigated by TEM and by secondary electron imaging of an ESEM. The micrographs of the homogenized sample of the commercial purity 3003, shown in Figure 72, indicate that the homogenization treatment led to a higher volume fraction of larger primary constituent particles, as is evident when compared to those in Figure 52. After rolling and annealing both the homogenized and non-homogenized commercial purity alloys, the primary constituent particles were observed to have broken into finer, more rounded and more uniformly distributed particles, where their cylindrical and dendrite-like morphologies were eliminated, as shown in Figure 73A-B. The primary particles of the non-homogenized, rolled

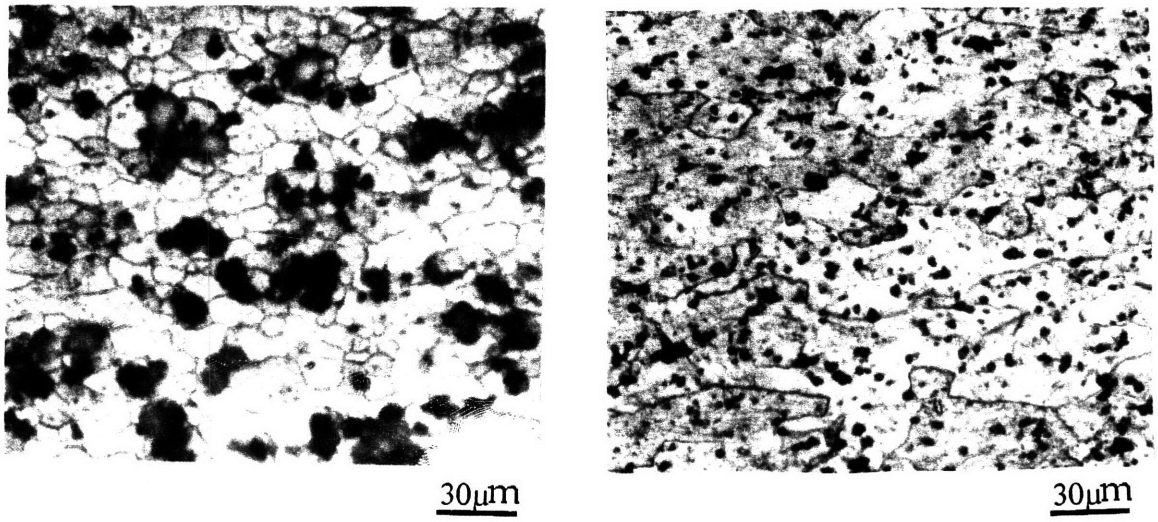

(A) (B)

Figure 68. Representative recrystallized structures, originally from the deposit equiaxed zone, of (A) homogenized and (B) non-homogenized samples from the LDC 3003 alloys annealed at a temperature of about 400°C for 1 hour or more.

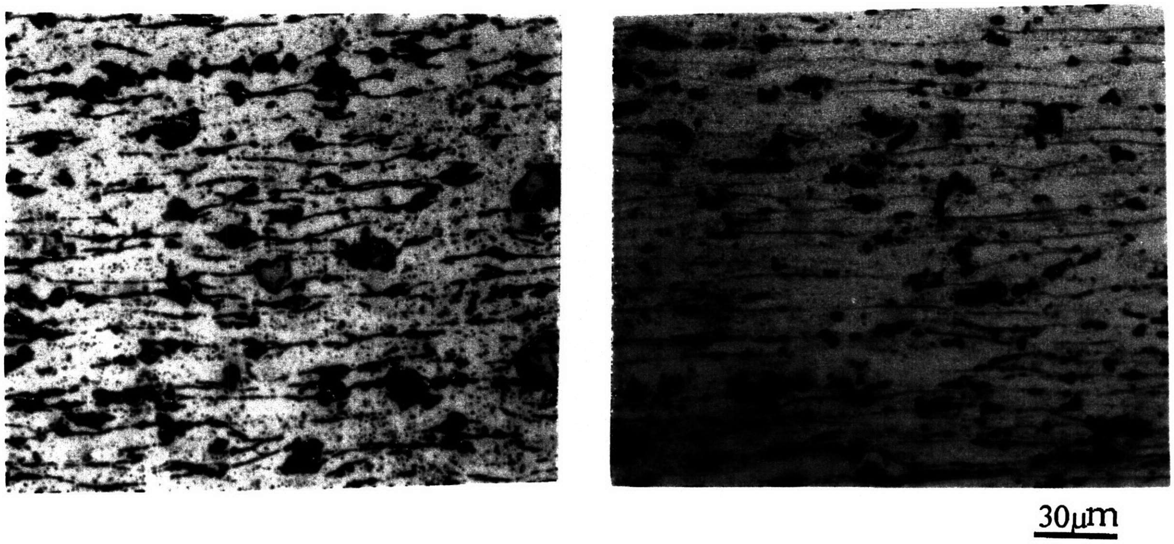

(A) (B)

Figure 69. Representative elongated structures, originally from the deposit bottom splats, of (A) homogenized and (B) non-homogenized samples from the LDC 3003 alloys annealed at a temperature of about 400°C for 1 hour or more.

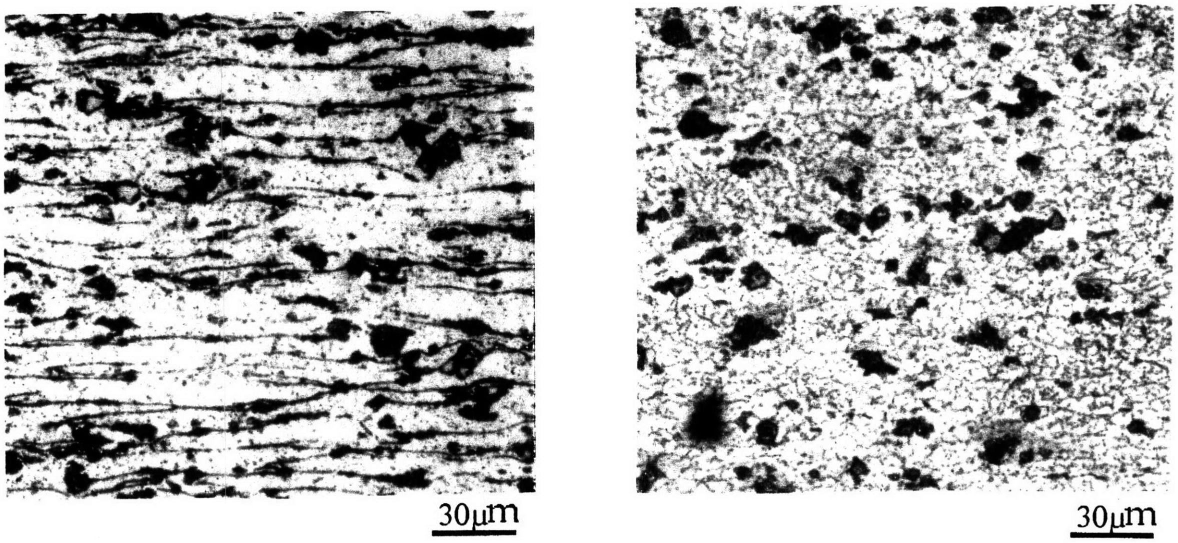

(A) (B)

Figure 70. The annealed structures of the modified 3003 alloy annealed at 300°C for 100 hours with (A) mostly elongated grains and (B) fine equiaxed grains.

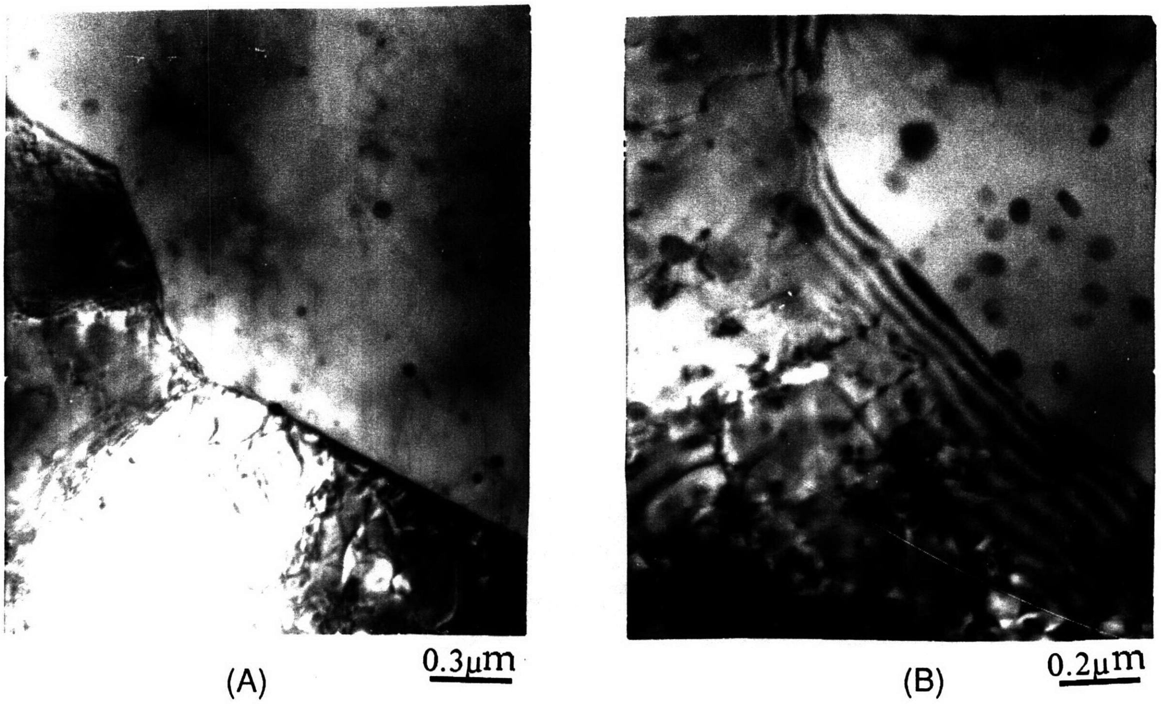

(A) (B)

Figure 71. TEM micrographs of annealed samples showing (A) sub-grains without lower dislocation content and (B) dislocation pile-ups at some grain boundaries and around second phase particles.

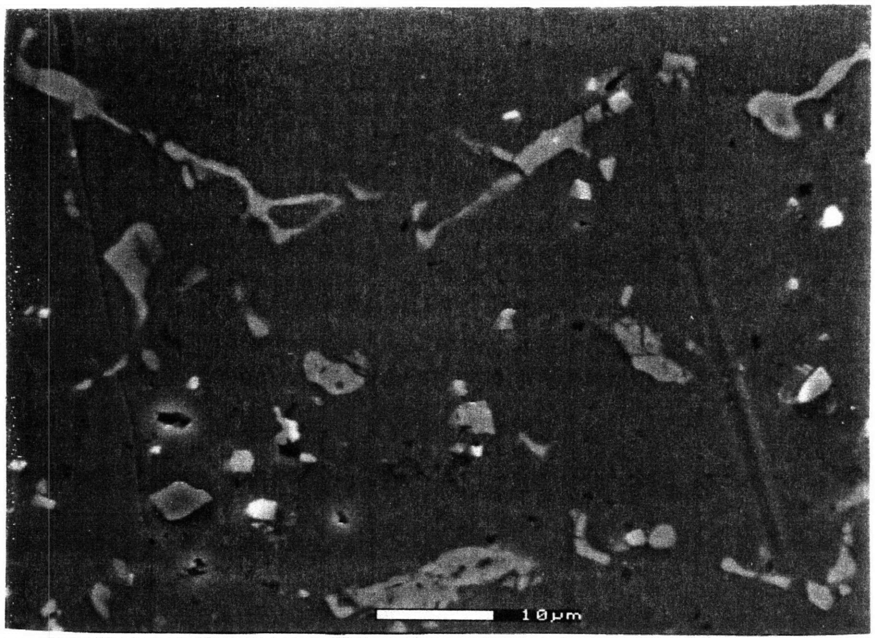

Figure 72. ESEM secondary electron imaging of the primary constituent particles of the commercial purity LDC 3003 alloy homogenized at 600°C for 8 hours.

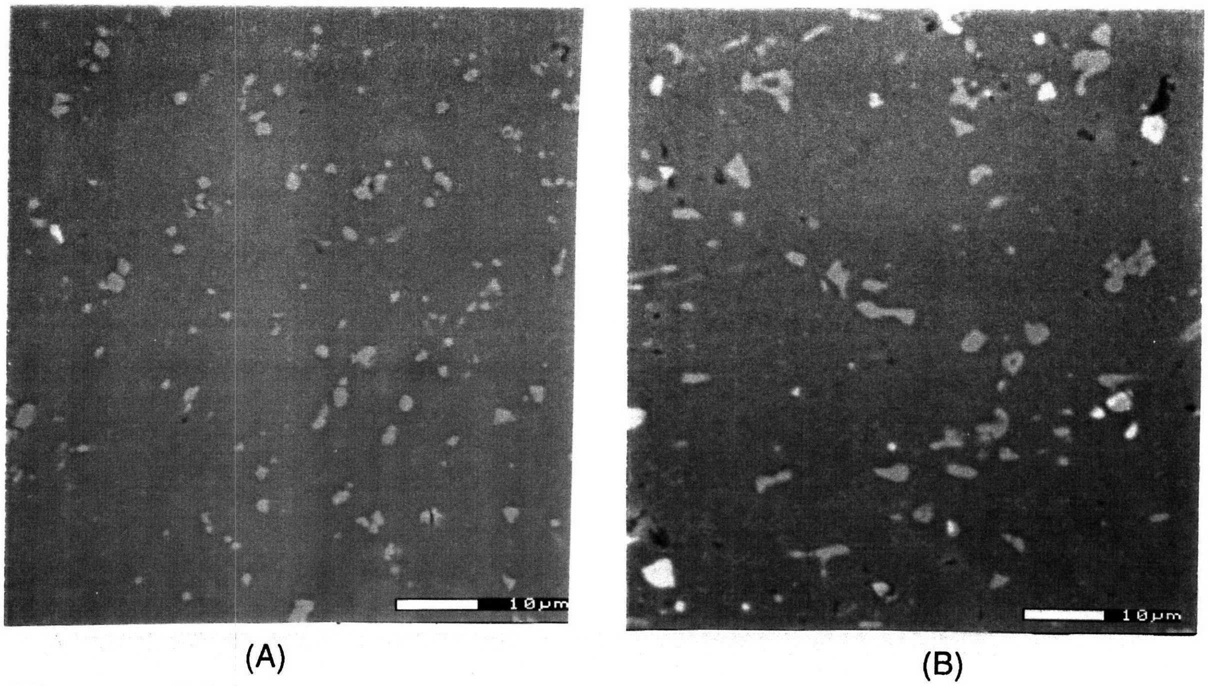

(A) (B)

Figure 73. ESEM micrographs of the primary constituent particles of (A) non-homogenized and (B) homogenized commercial purity 3003 alloy in the rolled and annealed conditions.

and annealed samples had average diameters of 1-3 μm, and were still smaller and at lower volume fraction than those of the homogenized samples.

The same trend of increased primary particles size and volume fraction was observed for the homogenized samples of the modified 3003 alloy in both the as-deposited and as-annealed conditions compared to the non-homogenized samples. ESEM micrographs of the modified 3003 alloy for selected TMT conditions are shown in Figure 74A-B. The second phase particles of the modified 3003 alloy were larger and had a higher volume fraction in all conditions compared to those of the commercial purity 3003 alloy. EDX analysis of the large particles of the commercial purity 3003 alloy showed the particles to be $Al_{12}(Mn,Fe)_xSi$, where the value of (x) varied between 3.4 to 3.8. These particles were most likely the α-$Al_{12}(Mn,Fe)_3Si$, which is usually of a higher fraction when the 3003 alloy is heated at temperatures above 400°C.[134,143,167] EDXA of the matrix of both alloys showed that the matrix of the non-homogenized commercial purity 3003, in the annealed condition, contained Mn, Fe and Si concentrations of about 5 times less than the readings in the matrix of the modified 3003 alloy of the same condition.

The fine secondary particles that formed during the heat treatments were not observed by the ESEM imaging on the polished surfaces of the samples due to particle pull-outs from grinding and polishing. However, TEM micrographs showed secondary particles of variable sizes and concentration, which, as expected, were at higher concentration in the modified 3003 alloy, as shown in Figure 75A-B. The sizes of these particles ranged from 20-100 nm for both the commercial purity and modified 3003 alloys. However, after the homogenization treatment, these particles were usually larger than 100 nm for both alloys. These secondary particles were observed to be of sizes greater than 100 nm and of different morphologies in the IM cast and single roller cast 3003 alloy.[139,192]

5.5. Tensile Properties

The mechanical properties of both the commercial purity and modified LDC 3003 Al-alloys in different rolling and annealing conditions were measured. The tensile tests were undertaken at room temperature. The results are

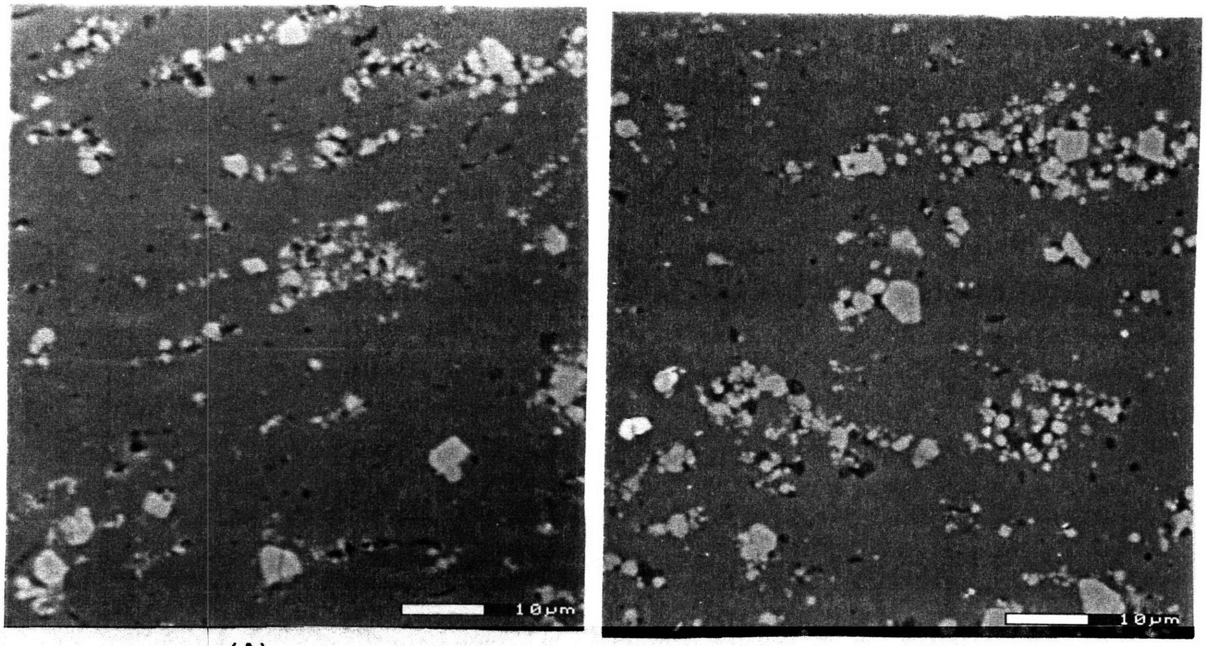

(A) (B)

Figure 74. ESEM micrographs of the primary constituent particles of (A) non-homogenized and (B) homogenized modified 3003 alloy in the rolled and annealed conditions.

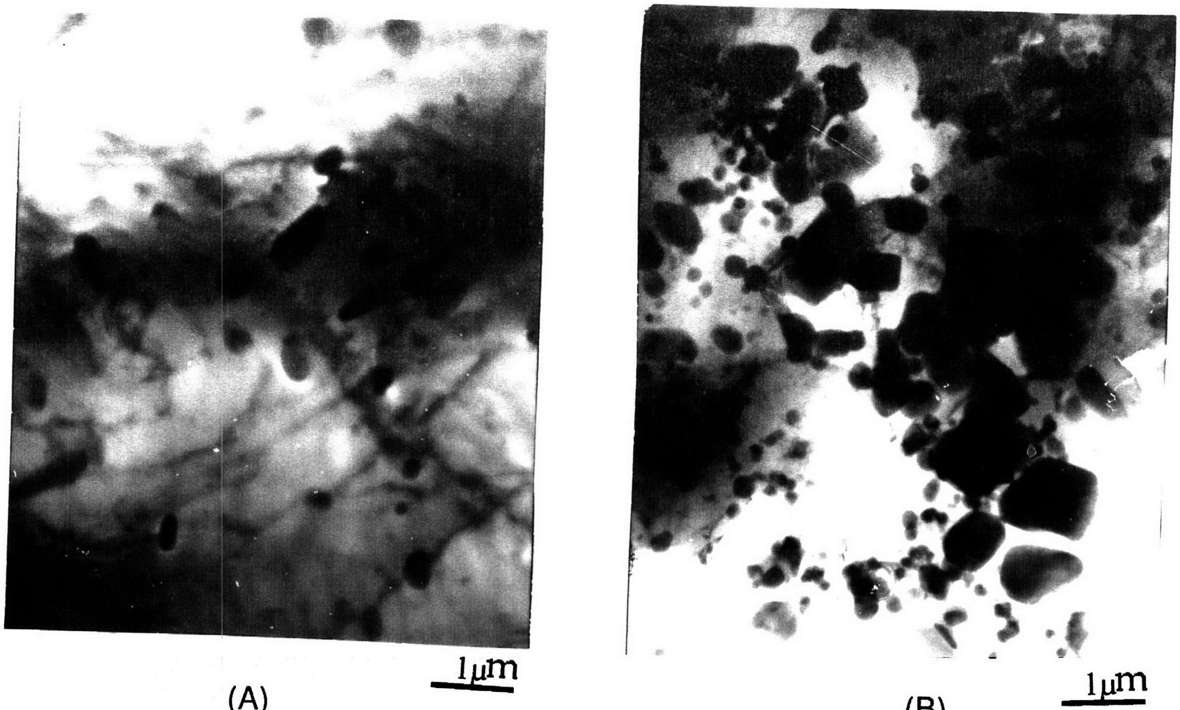

(A) (B)

Figure 75. TEM micrographs of the fine secondary particles in (A) commercial purity, and in (B), modified LDC 3003 alloys in the rolled and annealed condition.

compiled in separate Tables depending on the alloy type, the rolling temperature, the annealing temperature and time, and whether the samples were initially homogenized or not. The thermomechanical history, the relevant specimen dimensions, and the deposits from which the specimens were cut, are also listed. The mechanical properties of the unhomogenized, commercial purity LDC 3003 Al-alloy in the as-deposited and rolled conditions are listed in Table 18. The properties of this alloy when annealed at 400°C for 30 minutes are compiled in Table 19, whereas those of the samples annealed at 100°C or at 200°C for 100 hours are shown in Table 20A-B, respectively. On the other hand, the mechanical properties of the unhomogenized, modified LDC 3003 Al-alloy, annealed at 400°C for 1 hour, are compiled in Table 21. The properties of the samples annealed at 200°C or at 300°C for 100 hours are listed in Table 22A-B, respectively. The mechanical properties of the homogenized and annealed samples from both alloys are shown in Table 23.

Table 18: The Tensile Properties of the Unhomogenized Commercial Purity LDC 3003 Al-Alloy in the As-deposited and Rolled Condition, without Annealing.

Run No.	Rolled at [°C]	Sample cross section [inches X inches]	Gauge length [inches]	σ_y (0.2% offset) [ksi]	σ_{UTS} [ksi]	Elongation %
#69	—*	0.1745 x 0.1055	0.6915	9.2	20.4	26.5
		0.1525 x 0.1065	0.6960	8.6	20.0	25.9
#69	25°	0.1300 x 0.0945	0.5835	30.9	35.0	8.6
#99	200°	0.1633 x 0.0975	0.6885	31.2	34.3	10.0
#69	300°	0.1695 x 0.0840	0.6700	21.0	26.3	15.9
		0.1650 x 0.0770	0.6465	21.3	27.2	17.6
#69	350°	0.1475 x 0.0665	0.5800	19.9	26.5	21.0
		0.1570 x 0.0680	0.5350	18.7	27.0	25.0
#69	400°	0.1200 x 0.1075	0.5870	16.3	22.9	22.2
		0.0995 x 0.1020	0.5495	15.8	22.5	24.4
		0.1405 x 0.0625	0.5915	—	25.6	23.0
		0.1415 x 0.0550	0.5620	12.8	24.8	21.4
		0.1425 x 0.0605	0.6045	18.2	26.3	15.3
#82	450°	0.1545 x 0.0820	0.5455	14.2	21.0	26.0
		0.1120 x 0.0925	0.5675	17.4	21.6	19.5
#82	500°	0.1385 x 0.0855	0.4930	13.5	20.8	25.9
"		0.1515 x 0.0915	0.4940	12.6	20.7	31.0
#69		0.1495 x 0.0575	0.5810	14.5	22.7	29.1
"		0.1800 x 0.0530	0.5615	13.1	21.4	30.8
"		0.1445 x 0.0600	0.5900	13.4	23.1	24.1
"		0.1375 x 0.0460	0.5530	15.8	25.3	20.3

* these samples were cut from the dense equiaxed section and tested in the as-deposited condition.

Table 19: The Tensile Properties of the Unhomogenized Commercial Purity LDC 3003 Al-Alloy Annealed at 400°C for 30 Minutes.

Run No.	Rolled at [°C]	Sample cross section [inches X inches]	Gauge length [inches]	σ_y (0.2% offset) [ksi]	σ_{UTS} [ksi]	Elongation %
#69	25°	0.1360 x 0.1020	0.5900	19.5	27.8	18.0
		0.1115 x 0.0905	0.5750	21.3	26.8	15.0
		0.1400 x 0.0755	0.5745	15.7	24.1	23.2
		0.1335 x 0.0890	0.5925	18.3	24.6	20.4
#99	200°	0.1665 x 0.0960	0.7105	21.5	27.7	12.9
		0.1525 x 0.0875	0.6970	22.3	27.9	13.9
#69	300°	0.1635 x 0.0850	0.5540	19.4	26.3	23.7
"		0.1415 x 0.0810	0.5730	20.5	26.6	25.7
#67		0.1285 x 0.0835	0.5555	22.4	31.2	20.5
"		0.1400 x 0.0700	0.5650	26.0	35.5	19.8
#69	350°	0.1450 x 0.0695	0.5660	17.7	25.6	24.0
		0.1460 x 0.0640	0.5245	18.7	26.2	22.7
#69	400°	0.1460 x 0.0940	0.5340	15.7	22.1	25.6
		0.1335 x 0.0900	0.5500	15.1	22.0	28.4
		0.1475 x 0.0535	0.6880	14.7	26.2	21.3
		0.1405 x 0.0565	0.7355	14.6	25.2	23.2
		0.1470 x 0.0560	0.5930	16.2	26.4	21.8
		0.1470 x 0.0635	0.6000	19.5	25.9	22.7
#82	450°	0.1530 x 0.0930	0.5690	12.6	21.4	29.4
		0.1435 x 0.0900	0.5670	13.5	21.2	28.6
#82	500°	0.1450 x 0.0855	0.5550	—	20.2	32.7
"		0.1385 x 0.0825	0.5580	11.4	20.2	28.1
#69		0.1405 x 0.0580	0.5765	9.3	21.5	30.3
"		0.1615 x 0.0570	0.5745	10.8	21.7	31.3
"		0.1365 x 0.0530	0.5765	11.6	20.7	20.8
"		0.1265 x 0.0550	0.5530	11.1	21.6	25.0

Table 20A: The Tensile Properties of the Unhomogenized Commercial Purity LDC 3003 Al-Alloy Annealed at 100°C for 100 Hours.

Run No.	Rolled at [°C]	Sample cross section [inches X inches]	Gauge length [inches]	σ_y (0.2% offset) [ksi]	σ_{UTS} [ksi]	Elongation %
#99	25°	0.1555 x 0.0710	0.7500	30.8	39.6	10.3
		0.1605 x 0.0645	"	33.6	40.5	7.8
#96	200°	0.1480 x 0.0840	"	30.6	37.6	8.9
		0.1550 x 0.0900	"	29.2	38.6	8.4
#99	300°	0.1325 x 0.0595	"	23.5	29.8	11.0
		0.1460 x 0.0505	"	22.8	28.5	11.6
#99	350°	0.1665 x 0.0610	"	17.2	23.9	17.0
		0.1480 x 0.0640	"	18.3	26.1	16.5
#96	400°	0.1395 x 0.0820	"	15.7	21.9	21.3
		0.1330 x 0.0785	"	15.5	21.7	20.9
#99	450°	0.1615 x 0.0805	"	11.4	21.3	25.7
		0.1320 x 0.0795	"	12.2	20.2	24.3
#99	500°	0.1535 x 0.0595	"	10.8	20.4	24.0
		0.1520 x 0.0625	"	12.1	22.0	18.0

Table 20B: The Tensile Properties of the Unhomogenized Commercial Purity LDC 3003 Al-Alloy Annealed at 200°C for 100 Hours.

Run No.	Rolled at [°C]	Sample cross section [inches X inches]	Gauge length [inches]	σ_y (0.2% offset) [ksi]	σUTS [ksi]	Elongation %
#96	200°	0.1415 x 0.0865	0.7500	29.8	35	11.8
#99	300°	0.1795 x 0.0590	"	22.2	27.7	13.2
		0.1310 x 0.0640	"	23.3	28.3	11.0
#99	350°	0.1590 x 0.0655	"	16.3	22.1	20.0
		0.1445 x 0.0665	"	16.4	22.3	18.9
#96	400°	0.1485 x 0.0840	"	14.2	20.0	21.9
		0.1515 x 0.0845	"	14.3	20.5	20.6
#99	450°	0.1480 x 0.0895	"	12.6	21.1	28.8
		0.1400 x 0.0845	"	12.1	20.5	23.0
#99	500°	0.1330 x 0.0720	"	—	20.4	19.9
		0.1635 x 0.0610	"	12.0	21.1	23.9

Table 21: The Tensile Properties of the Unhomogenized Modified LDC 3003 Al-Alloy Annealed at 400°C for 1 Hour.

Run No.	Rolled at [°C]	Sample cross section [inches X inches]	Gauge length [inches]	σ_y (0.2% offset) [ksi]	σUTS [ksi]	Elongation %
#126*	400° / 25°	0.1580 x 0.0682	0.7500	20.4	38.8	12.3
		0.1395 x 0.0530	"	14.8	32.9	12.0
#126†	400°/200°	0.1650 x 0.0465	"	19.2	38.8	14.0
		0.1530 x 0.0565	"	25.7	43.5	15.2
#122	400°	0.1455 x 0.1003	"	13.4	29.5	15.7
		0.1755 x 0.0815	"	15.4	29.9	10.9
#126	500°	0.1305 x 0.0518	"	18.2	37.3	13.6
		0.1165 x 0.0510	"	18.0	33.8	14.6

* These samples were first rolled at 400°C to 42% total reduction then rolled at 25°C to 85% total reduction.

† These samples were first rolled at 400°C to 45% reduction then rolled at 200°C to 89% total reduction.

Table 22A: The Tensile Properties of the Unhomogenized Modified LDC 3003 Al-Alloy Annealed at 200°C for 100 Hours.

Run No.	Rolled at [°C]	Sample cross section [inches X inches]	Gauge length [inches]	σ_y (0.2% offset) [ksi]	σUTS [ksi]	Elongation %
#126*	400° / 25°	0.1080 x 0.0720	0.7500	32.8	40.3	2.9
		0.1425 x 0.0670	"	28.9	42.5	5.4
#126†	400°/200°	0.1540 x 0.0595	"	27.8	36.0	6.8
		0.1460 x 0.0617	"	27.7	37.7	8.9
#122	400°	0.1600 x 0.0990	"	20.5	31.9	10.7
		0.1622 x 0.1010	"	23.0	32.6	8.9
#126	500°	0.1455 x 0.0588	"	24.2	36.6	9.7
		0.1390 x 0.0540	"	26.6	37.7	8.5

* These samples were first rolled at 400°C to 42% total reduction then rolled at 25°C to 85% total reduction.

† These samples were first rolled at 400°C to 45% reduction then rolled at 200°C to 89% total reduction.

Table 22B: The Tensile Properties of the Unhomogenized Modified LDC 3003 Al-Alloy Annealed at 300°C for 100 Hours.

Run No.	Rolled at [°C]	Sample cross section [inches X inches]	Gauge length [inches]	σ_y (0.2% offset) [ksi]	σ_{UTS} [ksi]	Elongation %
#126†	400°/	0.1620 x 0.0500	0.7500	13.5	27.4	16.5
	200°	0.1605 x 0.0535	"	18.6	32.0	12.8
#122	400°	0.1640 x 0.0922	"	11.8	25.1	18.3
		0.1815 x 0.0855	"	12.6	25.0	15.2
#126	500°	0.1510 x 0.0573	"	12.2	25.9	16.7
		0.1530 x 0.0550	"	11.5	27.1	16.0

† These samples were first rolled at 400°C to 45% reduction then rolled at 200°C to 89% total reduction.

Table 23: The Tensile Properties of the Homogenized Commercial Purity and Modified LDC 3003 Al-Alloys Annealed at 400°C for 0.5 and 1 Hours, Respectively.

Run No.	Rolled at [°C]	Sample cross section [inches X inches]	Gauge length [inches]	σ_y (0.2% offset) [ksi]	σ_{UTS} [ksi]	Elongation %
#99†	400° /	0.1695 x 0.0885	0.7500	8.4	18.9	29.9
	25°	0.1595 x 0.0900	"	7.9	19.2	31.5
#126*	400°/25	0.1460 x 0.0805	"	13.4	29.3	8.9
	°	0.1615 x 0.0780	"	12.9	29.4	10.9

† The commercial purity LDC 3003, first rolled at 400°C to 48%, then rolled at 200°C to 81% reduction.
* The modified LDC 3003, first rolled at 400°C to 50% reduction then rolled at 25°C to 87% total reduction.

The above listed tensile properties were plotted against the rolling temperature to illustrate the effects of the rolling temperature and annealing conditions on the mechanical (tensile) properties of the alloys. The data of the commercial purity LDC 3003 Al-alloy are shown in Figure 76A-D, whereas those of the modified LDC 3003 are shown in Figure 77A-C. It was observed that all the samples, whether in the as-rolled condition or annealed, had higher strength and lower elongation when rolled at lower temperatures. This behavior is related to the high work hardening during cold rolling, which is typically observed in a mixed microstructure of hard second phase particles and a soft matrix, and to the lack of complete annealing at the selected temperatures and times. It was also observed that the difference between the yield and the ultimate tensile strength increased when the samples were rolled at higher temperatures. This behavior is also associated with the larger strain hardening of the specimens during the tensile test, since they are initially softer due to their higher rolling temperatures.

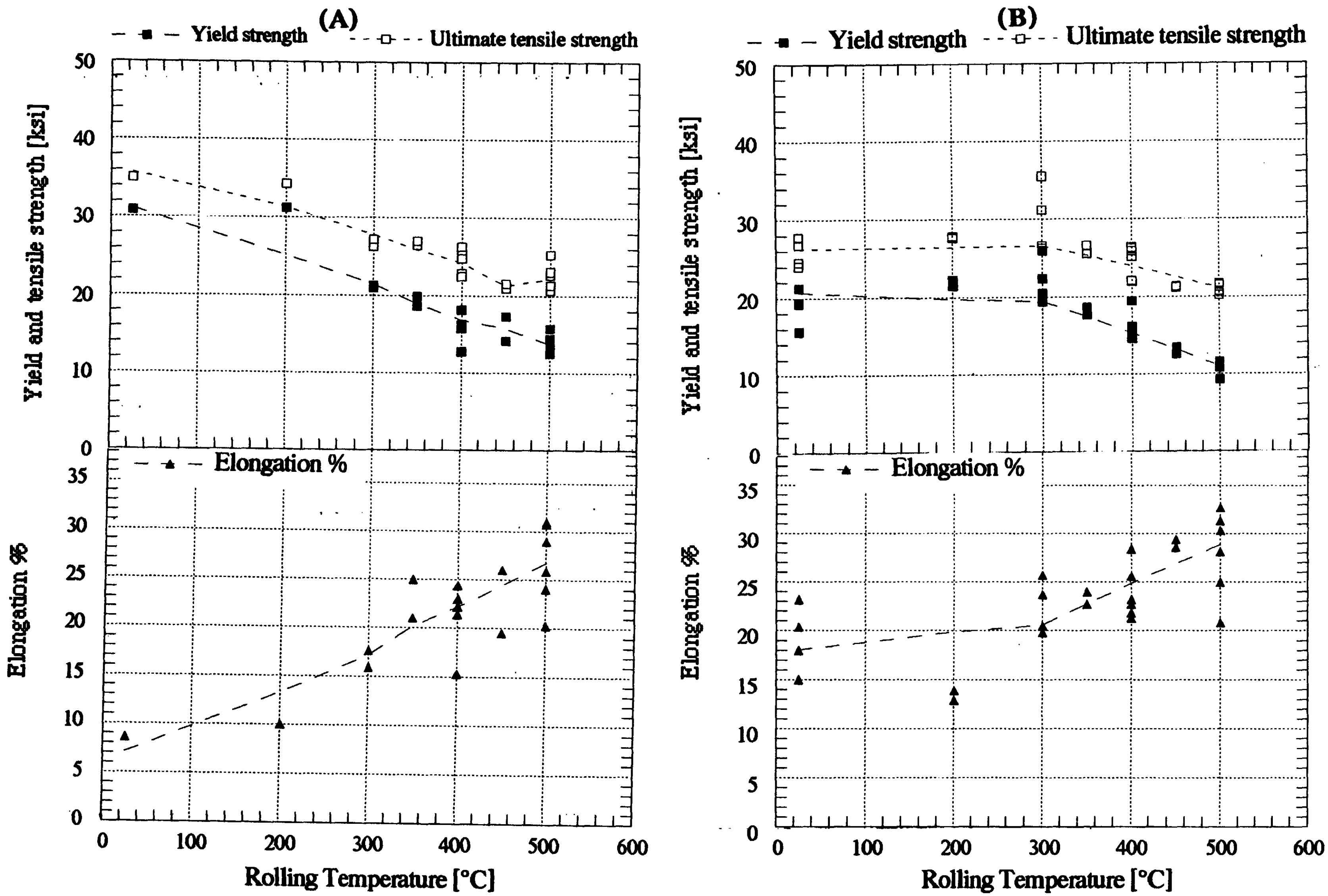

Figure 76. The mechanical properties of the commercial purity LDC 3003 Al-alloy plotted against the rolling temperature in (A) the as-rolled condition, or annealed at (B) 400°C for 30 minutes, (C) 100°C for 100 hours, and (D) 200°C for 100 hours.

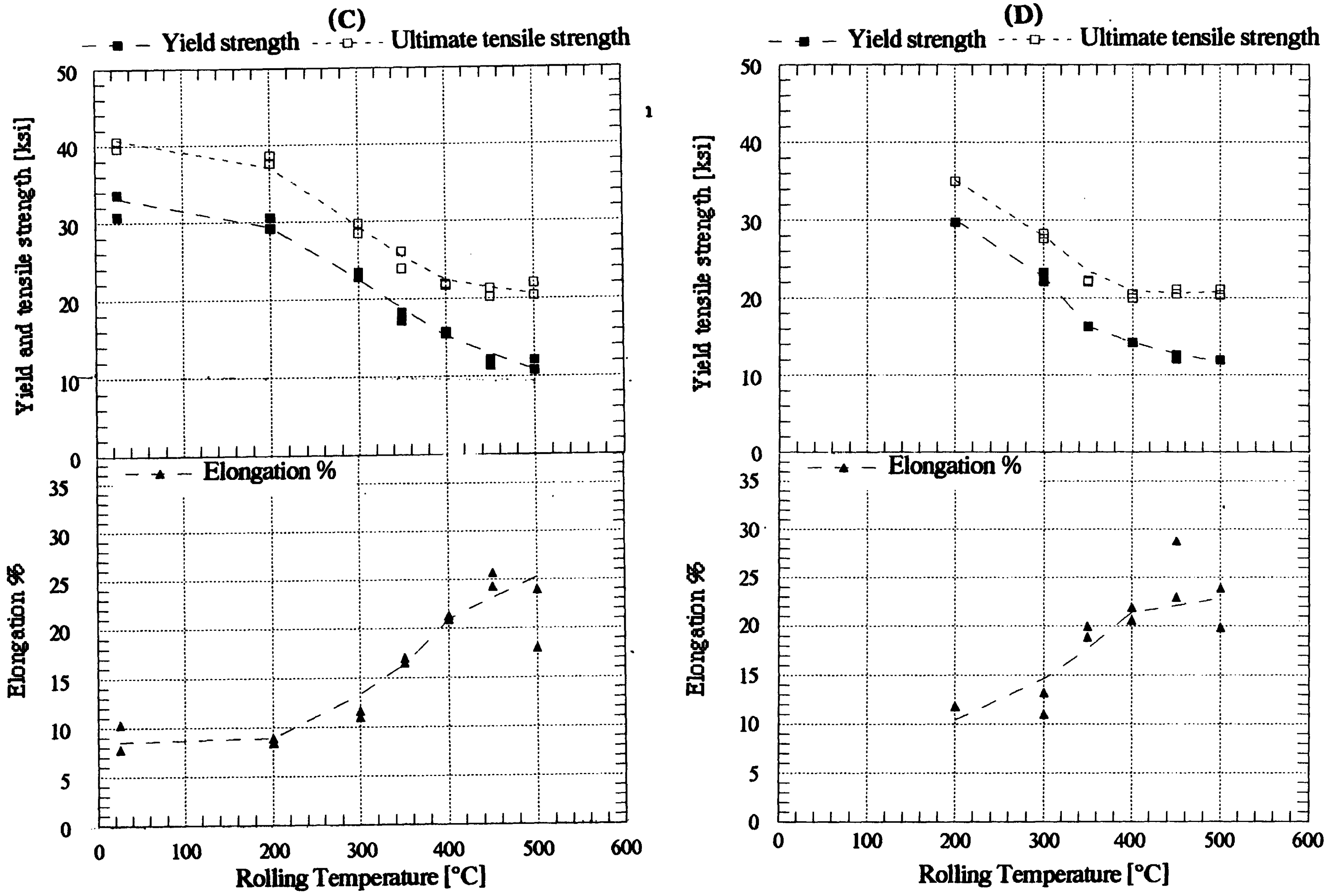

Figure 76. Continued......

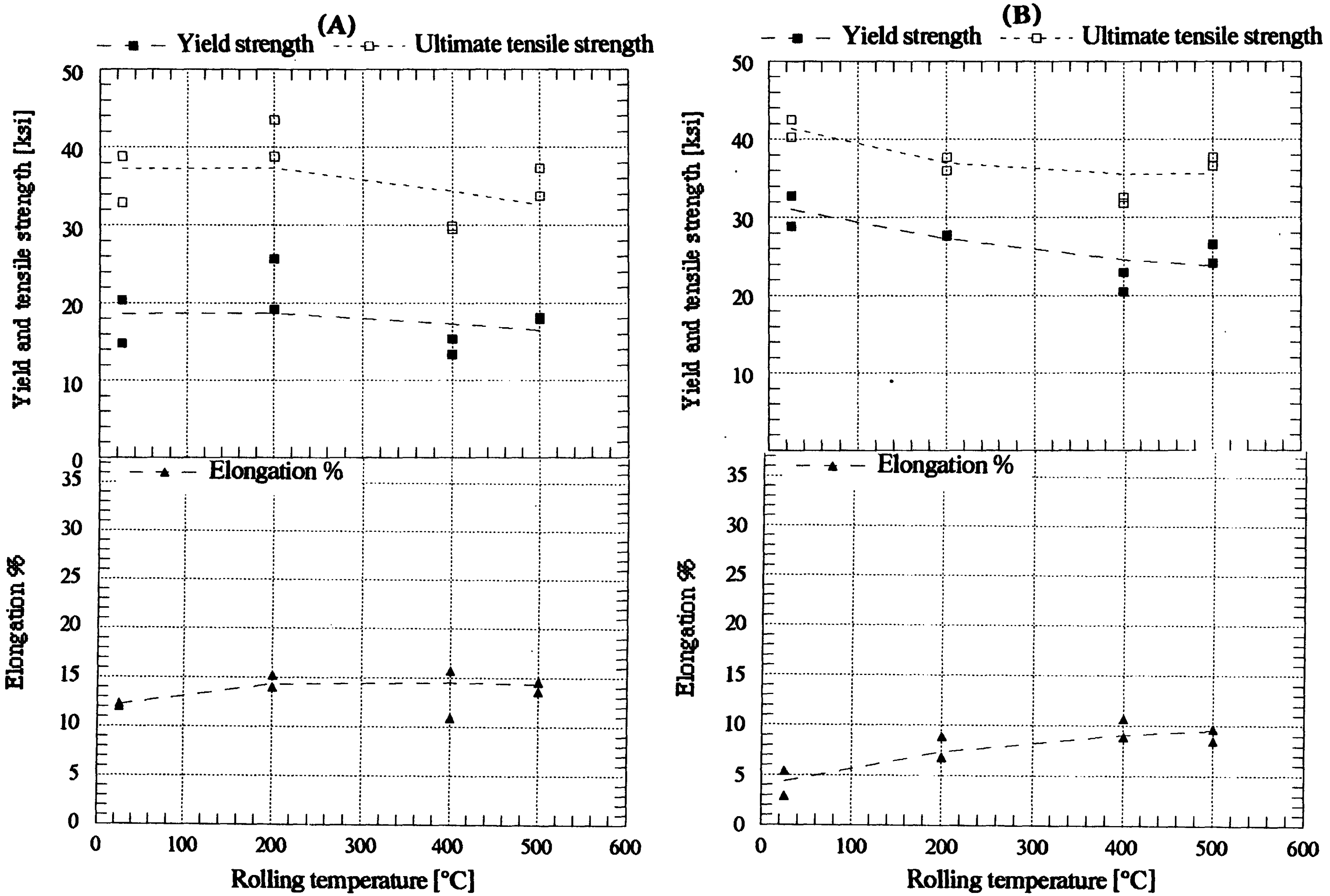

Figure 77. The mechanical properties of the modified LDC 3003 Al-alloy plotted against the rolling temperatures when annealed at (A) 400°C for 1 hour, (B) 200°C for 100 hours, and (C) 300°C for 100 hours..............

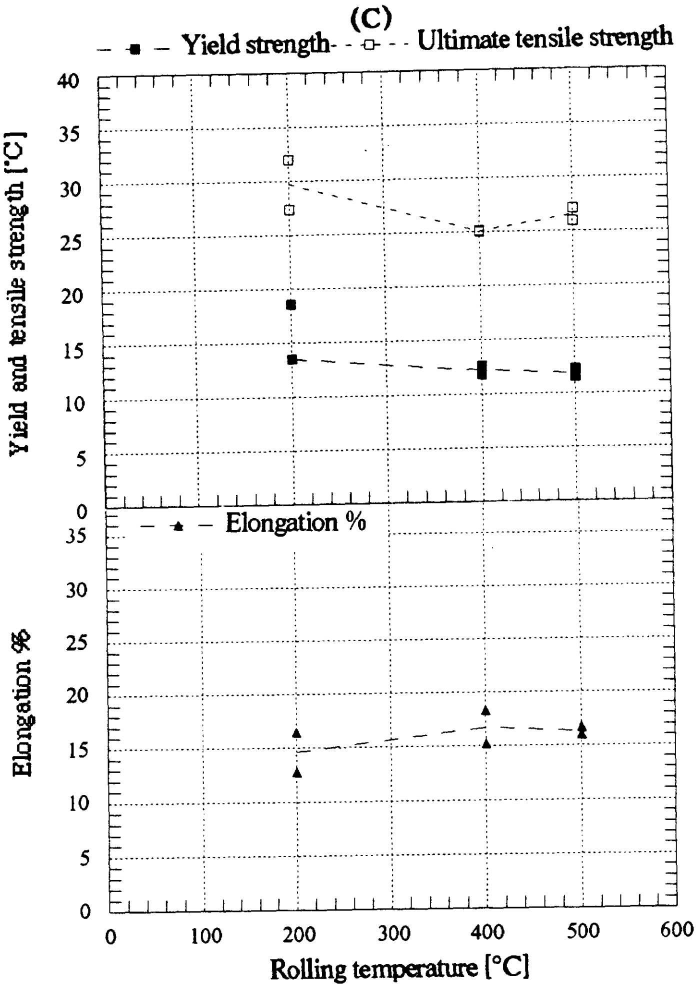

Figure 77. Continued....

good mechanical properties, as shown in Table 18. With these good initial as-deposited properties, the LDC commercial purity 3003 alloy was observed to have excellent ductilities, even in the as-rolled condition and specially when rolled at higher temperatures. After annealing the samples of this alloy at 100°C or 200°C for up to 100 hours, the mechanical properties remained the same as those of the alloy in the as-rolled condition. The microstructures of these samples were also observed to be similar to those of the rolled samples. On the other hand, the specimens annealed at 400°C for 30 minutes exhibited in reduced tensile strength and increased ductility compared to those in the as-rolled condition. This behavior is related to the recovery and partial recrystallization observed at high annealing temperatures.

The 3003 Al-alloy is one of the strain-hardenable aluminum alloys whose strength and ductility depend on its thermomechanical history. Different mechanical property limits were standardized (ASTM B 209) for the commercial 3003 Al-alloy depending on these thermomechanical treatments, also known as "tempers", as shown in Table 24. Compared to these standard values, the commercial purity LDC 3003 alloy had higher yield strength, tensile strength and elongation values than those of comparable tempers. For instance, the cold rolled LDC 3003 samples in the as-rolled condition had about 20% higher average strength, and 50% higher elongation compared to the fully hardened (H18) temper of the commercial purity 3003 alloy. Samples of the LDC 3003 alloy rolled at 500°C and annealed at 400°C for 30 minutes had more than 10% higher average elongation than those in the annealed and recrystallized (O) temper with the greatest ductility of the standardized values, while at the same time possessing about 50% higher yield strength and comparable tensile strength. These higher values are attributed to the rapid solidification grain and second phase refinement associated with the LDC process, which was also experienced in a variety of other LDC alloys.[3,9,15,26,80]

Samples from run #67 of the commercial purity LDC 3003 alloy, which were rolled at 300°C without removing the bottom layer of splats and fine columnar structure of the deposit and annealed at 400°C for 30 minutes, had the highest yield and tensile strengths of all the samples in its group, as shown in Table 19 and Figure 76B. This strength is thought to result from the bottom layer which experienced higher solidification rates than the rest of the deposit. This sample also possessed relatively high elongation of about 20%. Equipped with this information, samples from run #95, which had high porosity and a structure that mostly consisted of presolidified droplets (Figure 40) were rolled at 400°C. The goal was to investigate the effect of this usually undesired porous structure on the mechanical properties of the metal. The mechanical properties of these samples in the as-rolled condition or annealed at 400°C for 30 minutes are listed in Table 25. These samples had slightly higher strength and lower elongation compared to other samples of the commercial purity LDC 3003 Al-alloy of similar TMT history. However, the elongations of these samples were higher than the standard values for the 3003 alloy in partial strain hardened tempers. The results from both runs #67 and #95 led to the conclusion that the rapidly cooled bottom layers with relatively larger

Table 24. Mechanical Property Limits For Non-Heat Treatable Commercial Purity 3003 Al-Alloy (ASTM B 209).[193]

Temper	Specified Thickness, in.	Tensile Strength, ksi		Yield Strength (0.2 % offset), ksi		Elongation in 2 in. or 4 × Diameter, min, %
		min	max	min	max	
O	0.006–0.007	14.0	19.0	5.0	...	14
	0.008–0.012	14.0	19.0	5.0	...	18
	0.013–0.031	14.0	19.0	5.0	...	20
	0.032–0.050	14.0	19.0	5.0	...	23
	0.051–0.249	14.0	19.0	5.0	...	25
	0.250–3.000	14.0	19.0	5.0	...	23
H12 or H22	0.017–0.019	17.0	23.0	12.0	...	3
	0.020–0.031	17.0	23.0	12.0	...	4
	0.032–0.050	17.0	23.0	12.0	...	5
	0.051–0.113	17.0	23.0	12.0	...	6
	0.114–0.161	17.0	23.0	12.0	...	7
	0.162–0.249	17.0	23.0	12.0	...	8
	0.250–0.499	17.0	23.0	12.0	...	9
	0.500–2.000	17.0	23.0	12.0	...	10
H14 or H24	0.009–0.012	20.0	26.0	17.0	...	1
	0.013–0.019	20.0	26.0	17.0	...	2
	0.020–0.031	20.0	26.0	17.0	...	3
	0.032–0.050	20.0	26.0	17.0	...	4
	0.051–0.113	20.0	26.0	17.0	...	5
	0.114–0.161	20.0	26.0	17.0	...	6
	0.162–0.249	20.0	26.0	17.0	...	7
	0.250–0.499	20.0	26.0	17.0	...	8
	0.500–1.000	20.0	26.0	17.0	...	10
H16 or H26	0.006–0.019	24.0	30.0	21.0	...	1
	0.020–0.031	24.0	30.0	21.0	...	2
	0.032–0.050	24.0	30.0	21.0	...	3
	0.051–0.162	24.0	30.0	21.0	...	4
H18 or H28	0.006–0.019	27.0	...	24.0	...	1
	0.020–0.031	27.0	...	24.0	...	2
	0.032–0.050	27.0	...	24.0	...	3
	0.051–0.128	27.0	...	24.0	...	4
H112	0.250–0.499	17.0	...	10.0	...	8
	0.500–2.000	15.0	...	6.0	...	12
	2.001–3.000	14.5	...	6.0	...	18
F	0.250–3.000	...	...	...	...	...

"0" = Completely annealed and recrystallized, temper with the lowest strength and greatest ductility.
"H1?" = Strain hardened, the second numerical digit is a measure of the sample strain hardening: "2" = 1/4, "4" = 1/2, "6" = 3/4, "8" = full hardening
"H2" = Strain hardened and partially annealed

Table 25: The Tensile Properties of Samples from the Porous Run #95 of the Commercial Purity LDC 3003 Al-Alloy, Rolled at 400°C and Annealed at 400°C for 30 Minutes.

Run No.	Rolled at [°C]	Sample cross section [inches X inches]	Gauge length [inches]	σ_y (0.2% offset) [ksi]	σ_{UTS} [ksi]	Elongation %
#95 †	400°	0.1480 x 0.0755	0.6275	18.3	27.5	16.8
#95	400°	0.1580 x 0.0760 0.1360 x 0.0810	0.6510 0.6335	18.2 19.5	27.0 27.4	8.7 18.8

† This sample was tested in the as rolled condition

porosity may not be as negative and as detrimental to the mechanical properties of the alloy as thought.

For the modified LDC 3003 Al-alloy, the same trend of increasing ductility and decreasing strength with increasing rolling temperature was observed, although the rate of increase or decrease was not as high as in the commercial purity LDC 3003 alloy. This modified alloy was, in general, stronger than the commercial purity LDC alloy and had 20 - 40% higher ultimate tensile strength. However, the yield strengths of the two alloys were comparable for certain TMT conditions. Characteristic large strain hardening of the modified alloy led to ultimate tensile strength twice as high as the yield stress.

The elongation values of the modified LDC 3003 alloy, on the other hand, were lower and depended less on the rolling temperatures compared to that for the commercial purity LDC 3003 alloy. However, the samples annealed at 400°C for 1 hour and those annealed at 300°C for 100 hours had relatively high elongations of about 12-18%. These values, on the other hand, were higher than the standardized values of any strain hardened temper (HXX) of the 3003 alloy listed in Table 24. During the tensile tests, it was observed that all the specimen of the modified LDC 3003 alloy failed without necking and that all the elongation of this alloy took place during strain hardening.

After the onset of yield, the Portevin-LeChatelier effect of serrations appeared on all the stress/strain curves of the specimens of the modified LDC 3003 alloy. These serrations, which are characteristic of Al-alloys that contain Mg, reflect dynamic strain aging. The serrations continued from the yield point to the maximum tensile strength, where the specimens failed without necking. The tensile specimens failed at a plane either perpendicular or at a 45° angle from the strain direction. A mixture of brittle and ductile fractures was observed at the fracture surfaces of these samples, as shown in Figure 78.

The lack of necking and the partially "brittle" fracture of the tensile specimen of the modified LDC 3003 alloy were related to the large primary constituent particles, some of which crumbled and cracked during mechanical

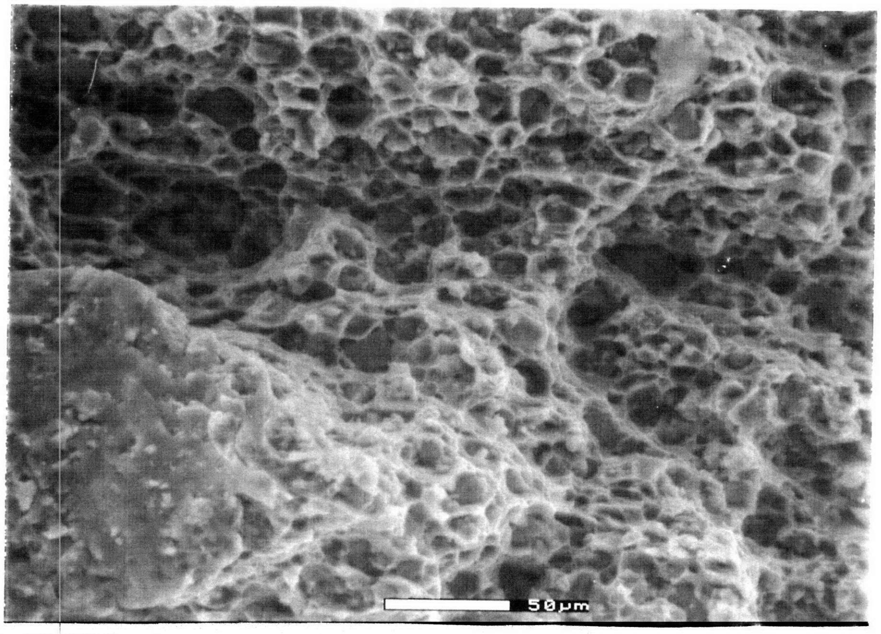

Figure 78. ESEM micrograph of the fracture surface of a tensile sample from the modified LDC 3003 Al-alloy showing a mixture of ductile and brittle fracture.

deformation, as shown in Figure 79. These particles were thought to be the α-(Fe-Si) particles, which have higher iron content and was reported to nucleate cracks by easily breaking-up during deformation, and lead to brittle fracture in Al-Mn alloys that have high silicon content.[177]

No serrations were observed in the stress/strain curves of the commercial purity LDC 3003 Al-alloy since it contained negligible amounts of Mg. In contrast to the modified LDC 3003 alloy, up to 50% of the elongation of the tensile samples of the commercial purity LDC 3003 alloy took place after necking, and the samples failed with characteristic ductile cup and cone fractures with dimpled fracture surfaces, as shown in Figure 80.

When both of the LDC 3003 alloys were homogenized, their strength values were reduced, while only the ductility of the commercial purity LDC 3003 alloy was increased. Compared to the unhomogenized samples with similar rolling and annealing history, the homogenization step led to 20-50% reductions in the strength of both Al-alloys; 38% increase in the elongation of the commercial purity LDC alloy, and no change in the elongation of the modified LDC 3003 alloy. The homogenized commercial purity LDC 3003 had

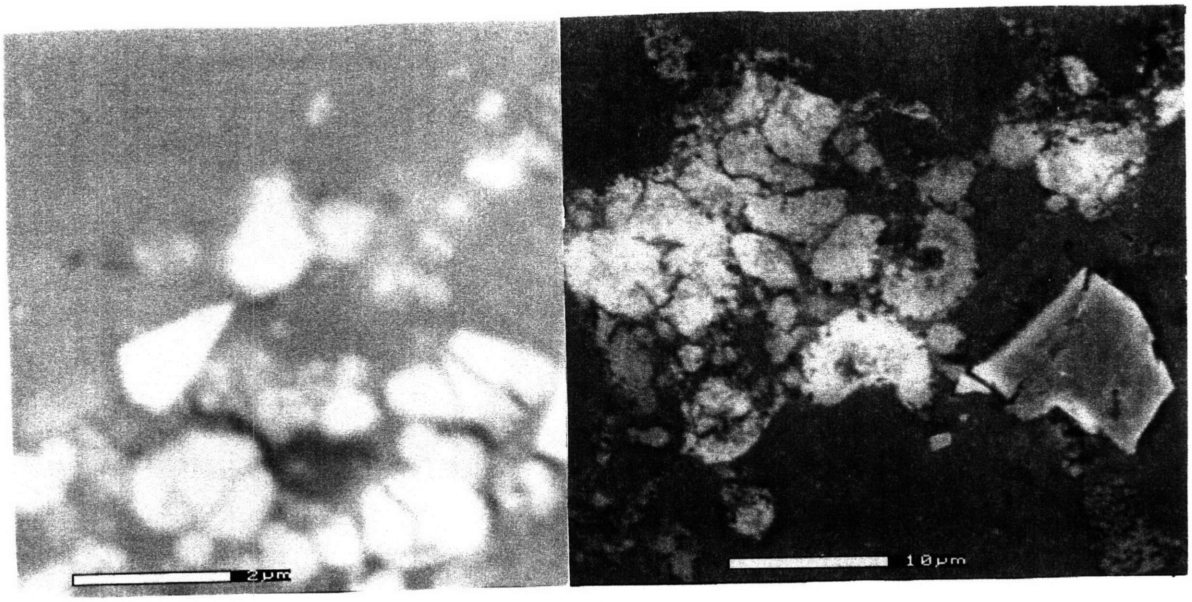

Figure 79. ESEM micrograph of rolled samples from the modified LDC 3003 Al-alloy showing the break-up of large primary constituent particles.

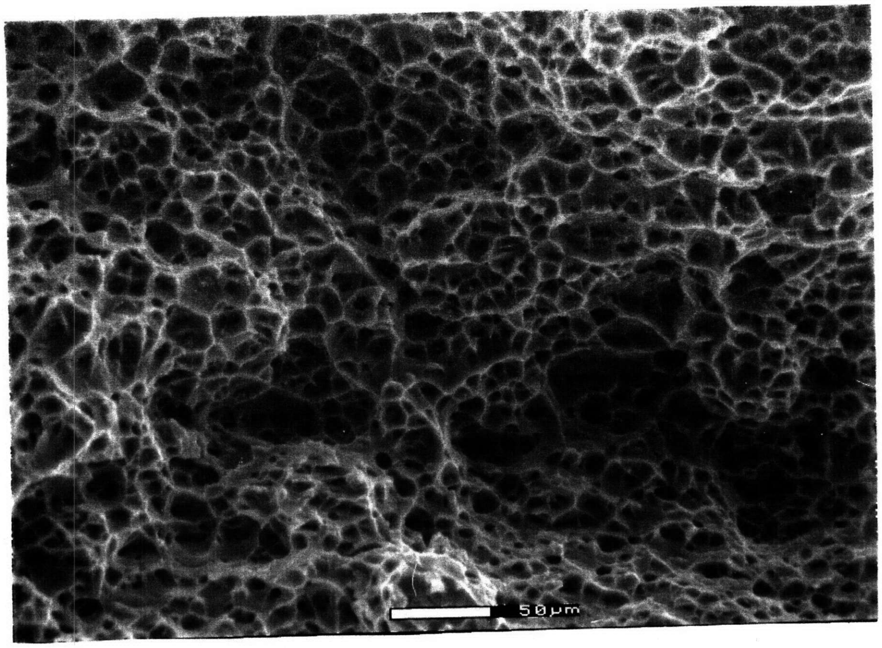

Figure 80. ESEM micrograph of the fracture surface of a tensile specimen from the commercial purity LDC 3003 Al-alloy showing dimpled ductile fracture.

mechanical properties similar to the standard values of the commercial 3003 tempers (Table 24). This indicates that the alloy had lost its rapid solidification properties during the homogenization. Compared to the tensile values of homogenized and non-homogenized direct chill (DC) cast 3003 Al-alloy,[143] which are listed in Table 26, the homogenized commercial purity LDC 3003 alloy had similar mechanical properties, although it had slightly higher strength and lower elongation. The unhomogenized commercial purity LDC 3003 alloy, however, was stronger than the DC cast alloy to an extent that depends on the rolling temperatures and the annealing conditions (although it had lower elongations).

Table 26. The Room Temperature Mechanical Properties of Homogenized and Unhomogenized Samples from Direct Chill Cast 3003 Al-Alloy in the Annealed Condition.[143]

Sample Description	σ_y (0.2% offset) [ksi]	σ_{UTS} [ksi]	Elongation %
Unhomogenized	7.4 7.9	17.6 17.8	31.5 30.5
Homogenized	6.6 7.5	16.6 16.8	34.0 31.5

The dependence of the mechanical properties of 3003 Al-alloy, as a strain-hardenable aluminum alloy, on its thermomechanical history complicates the comparison of the properties of the alloy at different fabrication conditions. In general, the commercial purity LDC 3003 Al-alloy showed to always possess higher strength and ductility than those specified for the commercial 3003 alloy of comparable tempers. Depending on the final application of the alloy, a proper thermomechanical treatment can be selected to achieve the necessary mechanical properties.

On the other hand, the modified LDC 3003 alloy with higher Fe and Si content, possessed good mechanical properties when annealed at higher temperatures for longer times. The tolerance of the 3003 alloy to concentration of the Fe and Si is certainly relaxed by the LDC process, since the modified LDC 3003 alloy has higher strength and comparable, if not better, ductility than the conventional IM 3003 alloy. However, This alloy did not have as high ductility as those achieved in the commercial purity LDC 3003 alloy, since it failed prior to necking. Its evident that the brittle constituent particles formed by the Fe and Si in the modified alloy are still detrimental to the ductility of the LDC aluminum alloy, although the LDC process had refined them and and led to ductilities in the range of 15-20%.

The improved ductilities of the LDC alloys are related to the refinement of their structures by this RS process, which eliminated the large dendritic structure and large brittle complex second phases particles present in cast materials. On the other hand, the higher strength of the LDC alloys is related to:

1) Solid solution strengthening, which arises from the internal dislocation stress field created by the solute atoms. The magnitude of the stress field depends on the sizes and concentrations of the solute atoms.

2) Grain refinement and substructure strengthening, which result from the blocking of dislocation glide by the grain and sub-grain boundaries. This was also explained in the Hall-Petch relationship, where smaller grain sizes were shown to lead to higher strength. This type of strengthening can apply in the aluminum alloys at low and intermediate temperatures .

3) Second phase particles strengthening, which depends on the second phase particle shape, size, distribution, volume fraction and interparticle spacing. This strengthening arises from the difficulty of moving dislocations through the particles or in between them, also known as the "Orowan Mechanism."[123] The transition elements can form intermetallic dispersoid phases, which are relatively stable at moderate temperatures. The strengthening by the second phase depends also on the degree of coherency between the second phase particles and the matrix, and the difference in elastic moduli between the particles and matrix. However, brittle particles, when coherent with the matrix, crack easily during the deformation and provide crack nuclei. The size reduction of these large, brittle inclusion by rapid solidification was observed to increase the ductility of the alloys.[3]

6. Summary and Conclusion.

The new gas delivery design with gas distribution vanes at the back entrance of the atomizers was successful in achieving more uniform gas pressure along the length of the atomizer gas exit. As a result, the aspiration pressure at the atomization zone, which is generated by the interaction of the atomization gas with the melt delivery slit, became more uniform along the length of the slit.

The uniformity of the aspiration pressure along the slit depended also on the atomization gas pressure and the vertical positioning (offset distance) between the gas exit level and the slit tip, since other parameters, such as the gas jet included angle, were kept constant. A smaller offset distance and lower gas pressure led to lower but very uniform aspiration pressure along the length of the slit; whereas higher atomization pressure and longer offset distance resulted in greater, less uniform aspiration, which is higher at the middle (center) of the slit. It was also observed that reduced length of the Hartman tubes of the second set of the new atomizers increased the uniformity of the aspiration pressure along the slit, as experienced with second set of the new atomizers.

Increasing the aspiration pressure was observed to increase the production (melt flow) rate, but it also results in a less uniform melt flow rate along the length of the slit, which is higher at its center due to higher aspiration there, and leads to poorer melt break-up efficiency. Increasing the atomization gas pressure to compensate for the increased aspiration and loss of melt break-up efficiency was observed to lead to the formation of feathering (agglomerates of powder) in the deposit. Increasing the melt exit length or area, while keeping the aspiration pressure low (-0.2 to -0.3 psi) and uniform along the slit, may be a better approach to increase the production rate rather than changing the aspiration pressure from its optimal values.

From the overspray powder analyses and the deposit morphology, it was observed that high atomization gas pressure (100 psi), which results in higher gas power (20 kW) and gas/melt mass flow rate ratios (1.35 - 1.85), led to excessive refinement of the droplets and their early eventual solidification in flight. This led to deposits with high feathering and porosity. Even when lower atomization gas pressure (70 psi) with lower gas power (13 KW) was used, smaller melt exit length (71 mm X 0.75 mm) led to lower melt flow rates (3.6 - 6.7 kg/min) and higher gas/melt mass flow rate ratios (1.04 - 1.67); and feathering were observed in those runs. However, a longer melt exit area (100 mm X 0.5 mm) led to higher melt flow rates (7.0 - 9.3 kg/min); and when low atomization gas pressure (70 psi) was used, smaller gas/melt mass flow rate ratios (<0.85) were realized and the extent of feathering was reduced.

A smaller average aspiration pressure along the slit also led to a more uniform deposit profile as that of Run #113. This run was made with an aspiration pressure of -0.28 psi, atomization gas pressure of 50 psig and gas/melt mass flow rate ratio of 0.55. If tandem sets of 100 mm long atomizers that can produce deposit profiles similar to that of run #113, were assembled in parallel at a center-to-center spacing of 80 mm, the profiles of their runs could be superimposed to produce flatter and wider deposits.

The microstructure of the 3003 Al-alloy deposit made by the LDC process consisted mostly of equiaxed grains of sizes between 20 - 50 µm. Other microstructural features, such undercooled splats, columnar grains and presolidified droplets were also observed in the deposits. Most of the second phase particles were very fine (<1 µm) although dendrite-shaped primary constituent particles of 2-10 µm length were present. Non-interconnected gas porosities, crevices between splats, and shrinkage porosities were also observed in the deposits. Deposit densities of 95±4% were measured in most parts of the deposits. A total oxygen contents of 0.009 to 0.010% were measured in these deposits, values which were one or two orders of magnitude lower than those observed in PM processes.

The primary constituent particles were broken to finer sizes (<2 µm), and the deposits were densified by mechanical deformation - rolling - of up to 70% reduction. The commercial purity LDC 3003 Al-alloy was easily rolled at room temperature; however, the modified LDC 3003 Al-alloy needed initial hot rolling to about 50% reduction at temperatures greater than 400°C before it could be cold rolled.

The annealing of both the commercial purity and the modified 3003 Al-alloys did not result in complete recrystallization to an equiaxed structure throughout the samples. The structures remained elongated in some sections of the sample even when annealed at 500°C for 5 hours. The resistance to recrystallization was observed to be more prevalent in the unhomogenized samples. On the other hand, portions of the samples were observed to recrystallize into fine equiaxed grains, especially when homogenized, while other portion resulted in larger, recrystallized, elongated grains, especially in the unhomogenized samples.

Due to the strain hardenability of the 3003 Al-alloy, both the commercial purity and the modified 3003 Al-alloys had higher tensile strengths when rolled at lower temperature, while their ductilities were higher when rolled at higher temperatures.

The commercial purity LDC 3003 Al-alloy possessed strength and ductility values higher than the standard values expected from the conventionally processed 3003 Al-alloy. High yield strength of about 30 - 33 ksi and ultimate tensile strength of about 40 ksi were registered for this alloy in the as-cold-rolled condition; whereas, elongations of up to 32% were realized in samples rolled at 500°C and annealed at 400°C for 30 minutes. The LDC 3003 alloy in the as-cold-rolled condition had more than 25% higher yield and tensile strengths compared to the values listed for the commercial 3003 Al-alloy in the full strain hardened temper (H18), while at the same time possessing elongations that are 50 - 80% higher. On the other hand, when this alloy was rolled at 500°C and annealed at 400°C for 30 minutes, it had ductilities more than 15% higher than those of the conventional 3003 Al-alloy in the completely annealed and recrystallized temper "O", with the highest elongation values, while at the same time possessing about 10% higher tensile strength.

The modified LDC 3003 Al-alloy had slightly higher ultimate tensile strength than the commercial purity LDC 3003 for any thermomechanical condition. However, its yield strengths were comparable and its elongations were well below those of the commercial purity LDC 3003 alloy. The highest yield and ultimate tensile strength values registered for this modified alloy were 33 and 43 ksi, respectively, whereas its highest elongation was 18%. The tensile specimens of this modified LDC alloy showed high strain hardening above the yield stress, which led to tensile stresses sometimes twice as high as the yield strength. These specimens also failed without necking, with a fracture surface that consisted of a mixture of brittle and ductile fractures. The larger primary constituent particles of this alloy were observed to crack during rolling and contributed to the brittle fracture ridges in the fracture surface, and may likely be the reason that the specimens failed without necking. This modified LDC 3003 alloy, however, had tensile properties that were higher than the values expected in standard 3003 Al-alloy, and also had comparable elongation values. This shows that the LDC processing was successful in increasing the tolerance of the 3003 Al-alloy for the increased Fe and Si contents in the alloy, and that impurity limits during recycling can be relaxed with this type of processing, which would reduce the cost of refinement.

The homogenization treatment of the deposits at 600°C for 8 hours of both the commercial purity and modified 3003 Al-alloys, prior to rolling, were observed to lead to mechanical properties of the commercial LDC 3003 alloy which are similar to the standardized values of the conventional 3003 Al-alloy. The tensile values of the modified alloy were lowered by 25% without any improvement in the elongation. This shows that the homogenization treatment brought about the loss of the characteristic rapid solidification properties of these alloys by increasing their grain sizes and second phase particles sizes and spacing, and by reducing the number of second phase particles and solute supersaturation. Although portions of the homogenized and rolled samples recrystallized to equiaxed grains of about 15-20 μm sizes, the strength values of the alloys were lowered due to the reduced fine second phase particles in these alloys.

The following conclusion were drawn from the work done in this study:

1. The new design of vanes, at the back of the nozzle where the gas enters, was successfully in achieving uniform gas delivery along the length of the linear atomizer gas exit. A more uniform aspiration pressure along the tip of the slit resulted subsequently from the uniform gas pressure along the atomizer exit. The uniformity of the aspiration pressure was increased with reduced atomization gas pressure and offset distance.

2. Increasing the length and/or the area of the melt exit was a better approach to increase the alloy production rate rather than to increase the aspiration pressure and risk creating non-uniform melt flow rates along the melt delivery slit.

3. Low aspiration pressures of -0.2 to -0.3 psi, atomization gas pressures of less than 70 psig, and a melt/gas mass flow rate ratio of about 0.6 were observed to be optimal for the atomization of the 3003 Al-alloy when a slit with a melt exit area of 100 mm X 0.5 mm and atomizers with gas exit areas of 2 (100 mm X 0.5 mm) are used.

4. A mild steel substrate with grit blasted surface of about 15 μm roughness promoted good adherence with the depositing droplet and the eventual deposit of the Al-alloys, whether water cooled or not.

5. The LDC deposits consisted mostly of fine, as-deposited, equiaxed grains of 20 - 50 μm sizes. However, other microstructures, such as undercooled splats, columnar structures, and presolidified droplets were also present. None of these microstructural features were detrimental to the mechanical properties, of the alloys. The layers with equiaxed grains were very stable even after exposure to 600 °C for 8 hours, whereas the other layers with different microstructures formed large grains of 120 - 250 μm sizes.

6. Deposits with high as-deposited densities of 95±4% were produced with the linear atomizer; however, different non-interconnected fine porosities from entrapped gas to shrinkage porosities were present.

7. Rolling to about 70% reduction achieved total densification in all the deposits. The commercial purity LDC 3003 alloy were easily rolled at room temperature; however, the modified 3003 Al-alloy cracked constantly when cold rolled unless first subjected to 50% hot rolling reduction at temperatures above 400°C.

8. Different layers of the spray deposited samples of both alloys responded differently to annealing. Some section recrystallized into equiaxed grains, which were finer when the sample was homogenized; whereas other portions remained in are elongated shape even when annealed at 500°C for 5 hours.

9. The commercial purity LDC 3003 Al-alloy had mechanical properties of up to 31 ksi yield strength, 40 ksi ultimate tensile strength and 32% elongation at different TMT. It was more than 25% stronger and more than 50% more ductile compared to the standard values for conventionally processed 3003 Al-alloys at comparable tempers.

10. The modified 3003 Al-alloys also possessed good mechanical properties of up to 33 ksi yield strength, 43 ksi ultimate tensile strength and 18% elongation. The ductilities of this alloy at different TMT, although not as good as those of the commercial purity LDC 3003 alloy, were sometimes better if not similar to those of the conventional 3003 alloy. This confirms that the LDC process increases the tolerance of these alloys to higher impurity levels, and should be ideal in scrap recycling, where it would reduce the cost of refinement.

11. The homogenization treatment of the LDC Al-alloys reduced the mechanical properties of the alloys to levels similar to those of the conventionally processed 3003 Al-alloy, and the characteristic rapid solidification properties were lost.

7. Future Work

Based on the results of this study and on the progress made so far with the LDC process, effort should be directed to the following areas:

1. The industrial scale application of the LDC process in the production of sheets and plates. Studies on the laboratory scale application of the LDC process on a variety of alloy systems have resulted in excellent mechanical properties. The only hurdle that needs to be addressed is the thickness profile of the deposits, which, as discussed, could be improved with the use of tandem sets of atomizers in parallel, and the use of the modified gas feeding design of the new atomizers discussed in this study.

2. The application of LDC processed Al-alloys should be extended to areas, where they can replace other alloy systems, such as Fe-alloys, due to their higher specific mechanical properties and easy workability.

3. The application of the LDC process in scrap metal recycling and its potential for increasing impurity tolerance in alloy systems, especially those with critical structural applications, such aerospace materials, should be further investigated.

REFERENCES

[1] M. A. Reynolds and J. G. Harris, *Aluminum*, Vol. 50, (1974) p. 592.

[2] M. V. Hyatt, *Aluminio*, vol. 46, (1977) p.81.

[3] E. J. Lavernia; Ph.D thesis, MIT, Cambridge, MA, Feb. (1986).

[4] M. Gupta, J. Marinkovich, F. A. Mohamed, and E. J. Lavernia, *Advances in Powder Metallurgy*, Vol 2, 1989, MPIF, Princeton, NJ, p.139.

[5] H. Jones, "Proceeding of the First International Conference on Rapid solidification Processing," R. Mehrabian, B. Kear and M. Cohen, eds., Claitors Publishing Division, Baton Rouge, 1977, pp. 28-45.

[6] S. L. Savage and H. Jones, " Proceeding on the Fourth International Conference on Rapid Quenching Metals," T. Masumoto and H. Suzuki, eds., Japan Institute of Metals, Sendai, vol. 1, (1982) pp. 159-163.

[7] S. J. Savage and F. H. Froes, *J. Metals*, April 1984, p. 20.

[8] N. J. Grants, *J. Metals*, January 1983, p. 20.

[9] I. Ucok, Ph.D Thesis, MIT, Cambridge, MA (1991).

[10] A. R. E. Singer and R. W. Evans, *Metals Technology*, Vol. 10, No.2, (1983), pp. 61-68

[11] H. Jones, "Rapid Solidification of Metals and Alloys", *The Institution of Metallurgist*, London, U.K. (1982)

[12] E. J. Lavernia, E. M. Gutierrez, J. Szekely and N. J. Grant, " Heat Flow Behavior During Deposition of a Nickel Base Superalloy by Liquid Dynamic Compaction", Proc. of the 1987 Annual Powder Met., Vol. 43, C. L. Freeby and H. Hjort eds., APMI, Princeton, NJ (1987) 683

[13] E. Gutierrez-Miravette, "The Mathematical Modelling of Rapid Solidification Processing", NASA Contractor Report 179551, Nov. 1986.

[14] E. Gutierrez-Miravette, E. J. Lavernia, G. M. Trapaga, J. Szekely, N. J. Grant, *Met. Trans.*, 20A (1989) 71

[15] E. J. Lavernia, G. W. McKewan, and N. J. Grant, Progress in Powder Metallurgy, Vol. 42, 1986 (Annual P. M. Conf. Proc.) ed., E. A. Carlson and G. Gains, MPIF, Princeton, NJ, p.457.

[16] E. J. Lavernia, J. C. Baram and N. J. Grant, *Metal Powder Rep.*, 42 (10) (1987) p. 688.

[17] N. J. Grant: in Casting of Near Net Shape Products, Y. Sahai, J. Battle, R. S. Carbonara, and C. E. Mobley, eds., TMS, Warrendale, PA, 1988, p. 203.

[18] Nicholas J. Grant, "Rapid Solidification Processing", Eds., R. Mehrabian, B. H. Kear and M. Cohen, Claitors Publ. Div., Baton Rouge, LA, (1977) p.230

[19] T. E. Tietz and I. G. Palmer, *Advances in Powder Technology*, 1982, ASM, Metals Park, Ohio, p.189

[20] Y. W. Kim, W. M. Griffith, and F. H. Froes., *Journal of Metals*, August, 1985

[21] D. H. Ro and H. Sunwoo, "Progress in Powder Metallurgy 1983", 39, MPIF Publication, 1984, p.109-124.

[22] B. A. Rickinson, F. A. Kirk, and D. R. G. Davies., *Powder Metallurgy*, vol. 24, No.1, 1981, pp. 1-6

[23] E. Y. Ting and N. J. Grant " metal powder production by gas atomization," *Progress in powder metallurgy*, Vol. 41, 1986

[24] E. Y. Ting, Ph.D Thesis, MIT, Cambridge, MA (1984)

[25] M. K. Veistinen, E. J. Lavernia, M. Abinante and N. J. Grant, *Materials letters*, Vol.5, No.5, September 1987

[26] W. Wang, ScD Thesis, MIT, Cambridge, MA (1982)

[27] Alan Lawley, *Int. Jour. of Powder Metall. and Powder Technology*, Vol. 13, No. 3, July 1977, p. 169.

[28] E. Klar, and W. M. Shafer, "Powder Metallurgy for High Performance Applications", J. J. Burke and V. Weiss, eds., Syracuse Univ. Press, Syracuse, NY, (1972) pp. 57-68.

[29] Alan Lawley: "Fundamentals of Particulate Metallurgy", R. S. Technology Sourcebook, R. L. Ashbrook, ed., ASM (1983) p. 47.

[30] J. K. Beddow, The Production of Metal Powders, Heyden and Son, Ltd., Philadelphia, PA (1978).

[31] A.R.E. Singer, J. S. Coombs and A. G. Leatham in "Modern Developments in Powder Metallurgy", Vol. 8, H. H. Housner and W. E. Smith eds., Plenum, New York, 1974. p. 263.

[32] J. A. Tallmadge, "Powder Metallurgy Processing, New Techniques and Analyses," H. Kuhn and A. Lawley, editors, p. 1, Academic Press, New York, 1978.

[33] J. S. Thompson, *J. Inst. Met.,* (1948), 74, pp. 101-130.

[34] E . J. Hall, U.S. Patents No. 1,501,449 and 1,545,253.

[35] Aluminum-Lithium Alloys, Proceedings of the Second International Aluminum-Lithium Conference, T. H. Sanders, Jr. and E. A. Starke, Jrs., eds., TMS-AIME, Warrendale, PA, 1984.

[36] J. R. Pickens: *J. Mat. Sci.*, vol. 16, (1981) pp. 1437-1457

[37] R. G. Brooks, A. G. Leatham, J. S. Coombs and C. Moore, *Metallurgia and Metal Forming,* vol. 9, April 1977, p. 1.

[38] J. B. See and G. H. Johnston, *Powder Technology*, Vol. 21, (1978) pp.119-133.

[39] V. Anand, M.S. Thesis, MIT, Cambridge, MA (1977)

[40] G. Rai, E. Lavernia, and N. J. Grant, *Journal of Metals*, Vol. 37, No.8, (1985), p.22-26.

[41] U. Backmark, N. Backstrom, and Lars Arnberg, " Production of Metal Powder by Ultrasonic Gas Atomization" Report, Swedish Institute for Metal Research (1985)

[42] P. Domalavage, C. Ashdown, R. C. O'Handley and N. J. Grant, *Materials Science and Engineering*, Vol. 57 (1983) L1-L2

[43] S. A. Miller and R. J. Murphy, *Scripta Metallurgica,* Vol. 13, (1979) pp. 673-676

[44] M. K. Veistinen, E. J. Lavernia, J. C. Baram and N. J. Grant, *The Int. Journal of Powder Technology*, Vol. 25, No.2, (1989) pp.89-92.

[45] T. W. Clyne, R. A. Ricks, and P. J. Goodhew, *International Journal of Rapid Solidification*, Vol. 1, (1984-85) pp. 59-80

[46] S. Kang and N. J. Grant, *Metallurgical Transaction A*, Vol. 18A, Dec. 1987, pp.2037-2045

[47] P. K. Domalavage, N. J. Grant, and Y. Gefen, *Metallurgica Transaction A*, Vol. 24A, August 1983, pp. 1599-1606

[48] J. P. Lyle and W. S. Cebulak, *Met. Trans.*, vol. 6A, (1975) p. 685.

[49] W. S. Cebulak, E. W. Johnson and H. Markus, *Inst. J. Powder Metall. And Powder Tech.*, vol. 12, (1976) p. 299.

[50] W. W. Webster, M.S. Thesis, MIT, Cambridge, MA (1982)

[51] P. U. Gummeson, *Powder Met.*, 15, (1972) pp.67-94 .

[52] E. J. Lavernia, E. M. Gutierrez, J. Szekely, and N. J. Grant, *International Journal of Rapid Solidification*, Vol. 4, (1988) pp. 89-124

[53] S. Hirose and M. E. Fine, *Met. Trans.*, vol. 14A, June 1983, pp. 1189-1197.

[54] W. C. Victor and E. A. Starke, Jr., *Met. Trans.*, vol. 14A, March 1983, pp. 435-447.

[55] J. A. Walker and E. A. Starke, Jr., *Met Trans.*, vol. 14A, March 1983, pp. 435-447.

[56] A. Gysler, R. Crooks, and E. A. Starke, Jr., "A Comparison of Microstructure and Tensile Properties of P/M and I/M Al-Li-X Alloys," in "Aluminum-Lithium Alloys," T. H. Sanders, Jr., and E. A. Starke, Jr., eds., AIME, New York, N.Y., 1981, pp. 263-291.

[57] V. Anand, A. J. Kaufman , and N. J. Grant, "Rapid Solidification Processing: Principles and Technologies", eds. R. Mehrabian et al. Claitors, Baton Rouge, 1980

[58] S. L. Langenbeck, "High Strength Powder Metallurgy Aluminum Alloys", Proceedings of the PM Committee of AIME Symposium, Dallas, TX, 1982, p. 87.

[59] R. G. Brooks, U.S. Patent No. 3,826,301, July 30, 1974.

[60] E. J. Lavernia, M.S. Thesis, MIT, Cambridge, MA,1984.

[61] E. J. Lavernia, G. Rai, and N. J. Grant, *The International Journal of Powder Technology*, Vol. 22, No. 1, (1986) p. 9-16

[62] K. Ogata, E. J. Lavernia, G. Rai, and N. J. Grant, *International Journal of Rapid Solidification*, Vol. 2, (1986) pp. 21-35

[63] E. Lavernia and N. J. Grant, "Structure and Properties of X2020 Aluminum Alloys Modified with Lithium produced by Liquid Dynamic Compaction", First International Conference on Rapidly Solidified Materials, San Diego, CA, 3-5 Feb. 1986.

[64] T. S. Chin, Y. Hara, E. J. Lavernia, R. C. O'Handley and N.J. Grant, *J. Appl. Physics*, 59:4 (1986) pp.1297-1300.

[65] J. Megasur , E. Lavernia, P. Domalavage, O. K. Harling and N. J. Grant, *J. Nuclear Materials,* Vols.122-123 (1984) p. 789

[66] ARE Singer, *Met. Materials*, (4) (1970) 246.

[67] B. Towler, "Flame Deposition", Oxford Univ. Press, Oxford, U.K. (1978)

[68] E. J. Lavernia and N. J. Grant, *Mater. Sci. Eng.*, 1988, Vol. 98, p.381.

[69] S. Annavarapu, D. Apelian and A. Lawley, *Metallurgica Transaction A*, Vol 21A, December 1990, pp. 3237-3256

[70] E. Kear, P. R. Holiday and A. R. cox, *Met. Trans. A*, V10A, 2/1979, p.191.

[71] R. G. Brooks, U.S. patent 3,909,921, issued to July 30, 1974.

[72] N. J. Grant, U. S. Patent No. 4,485,834. Issued to Dec. 4, 1984.

[73] A. G. Leatham and R. G. Brooks, *Modern Developments in powder Metallurgy*, Vol. 15-17, (1985) p.157-173

[74] H. C. Fiedler, T. F. Sawyer, and R. W. Kopp, "Spray-formed Rene 95," Technical Information Series (87CRD034), Class 1, Corporate Research and Development General Electric, Schenectady, New York, March 198

[75] B. Williams, *Metal Powder Report*, Vol. 38 No. 1, Jan. 1983, p. 15.

[76] B. L. Ferguson, [2] Metals Handbook, 9th Ed., Vol. 7, p. 531, American Society for Metals, Metals Park, Ohio, 1973.

[77] E. O. F. Nilsson, S. I. Nilsson and E. G. Hagelin, U.S. Patent No. 2997245 issued in Aug. 22, 1961.

[78] P. A. Toves, U.S. Patent 3067956, issued 1962.

[79] E. J. Lavernia and N. J. Grant, *Metal Powder Report*, Vol 41 (1986), No. 4, P. 255

[80] C. Y. Tsao; Ph.D thesis, MIT, Cambridge, MA (1990).

[81] G. Rai, E. J. Lavernia, and N. J. Grant. Progress in Powder Metallurgy, Vol. 41, 1985 Annual Powder Metallurgy Conf. Proc., eds, H.I. Sanderow, W.L. Grebelhausen and K.M. Kulkarni, M.P.I.F. Princeton N.J. (1986) p.55-65.

[82] T. H. Heter and R. H. Bolt, "Sonics", John Wiley and Sons, NY, 1962.

[83] P. A. Toves, U.S. Patent No. 3302892 (Feb. 7, 1967).

[84] E. Ting, "Metal Powder Production by Gas Atomization, " Fifth Intern'l Powder Metallurgy Conference, July 1985, San Francisco, CA.

[85] E. J. Lavernia and N. J. Grant, *Int. J. of Rapid Solid.*, Vol 2, (1986) pp 93-106

[86] P. J. Meschter, R. J. Lederich, J. E. O'Neil, E. J. Lavernia and N. J. Grant; Proc. of Int. Conf. on Al Alloys, Charlottesville, VA, 15-20, June (1986).

[87] C. A. Tsao, N. J. Grant, Proceed. 2nd International Conference on RSM, San Diego 7-8 March 1988, pp. 163-170

[88] X. Duan, T. Ando and N. J. Grant; *Advances in Powder Metallurgy*, Vol. 6, Aerospace, Refractory and Advanced Materials, (1991) p. 75.

[89] X. Duan, I. Ucok, T. Ando and N. J. Grant; Proc. of TMS Spring Meeting, San Diego, March (1992).

[90] I. A. Ibrahim; Ph.D thesis, MIT, Cambridge, MA (1989).

[93] S. Matsuo, T. Ando, M. Zody and N. J. Grant; *Advances in Powder Metallurgy*, Vol. 5, P/M Materials, (1991) p. 161.

[92] J. M. Nell, G. Rai, E. J. Lavernia, and N. J. Grant, "Microstructure and Properties of an IN-100 Tube Produced by Liquid Dynamic Compaction", 1986 Annual Powder Metallurgy Conf. Proceedings, Boston, MA, 18-21 May 1986, Progress in Powder Metallurgy, vol. 42, E. A. Carlson and G. Gainer eds., APMI Princeton, NJ (1986) p. 67.

[93] S. Tanigawa, Y. Hara, E. J. Lavernia, T. S. Chin, R. C. O'Handley and N. J. Grant, *IEEE Trans. Magnet.*, MAG, 22:5 (1986) p. 746.

[94] M. K. Veistinen, Y. Hara, E. J. Lavernia. A. C. O'Handley, and N. J. Grant, "Optimization of Liquid Dynamic Compaction for Fe-Nd-B Magnet Alloys" 1987 MRS Spring Meeting, Anaheim, CA, April 21-25, Vol. 96, (1987), p. 93-101.

[95] T. Kuji, R. C. O'Handley, and N. J. Grant, *Appl. Phys. Lett.*, 54:24 (1989) pp. 2487-2489.

[96] M. Gupta, F. Mohamed and E. J. Lavernia, "The Effect of Solidification Phenomena on the distribution of Ceramic Reinforcements During Spray Atomization and Deposition," , in "Metal and Ceramic Matrix Composites: Processing, Modeling and Mechanical Behavior", R. B. Bhagat, A. H. Kumar, and A. M. Ritter., eds., The Minerals, Metals and Materials Society, 1990, p.23

[97] A. Farah, M. Zody, "Tin coating via LDC", Internal Report, High Temperature Materials Laboratory, MIT, 1992.

[98] M. Zody, M.S. Thesis, MIT, Cambridge, MA, 1994.

[99] E. Klar and J. W. Fesko, "On the Particle Shape of Atomized Metal Powders", Progress in Powder Metallurgy, V37, National PM Conf. Proceedings, MPIF 1981, p. 47.

[100] K. P. Rao and S. P. Mehrotra, "Effect of Process Variables on Atomization of Metals", Mod. Dev. In PM/ Principle and Processes, MPIF, V12, 1980.

[101] W. E. Ballard, Brit. Welding J., Vol. 6, (1962) p. 362.

[102] O. S. Michiporenko and Y. I. Naida, *Sov. Powder Metall. Met. Ceram.*, 67 (7) (1968) 509.

[103] G. de Vahl Davis, Heat Transfer 1986, Proc. 8th Int. Heat Transfer Conf., San Francisco, CA, C. L. Tien, V. P. Carey, and J. K. Ferrel (eds.), 1(1986) 101.

[104] B. N. Putimtsev, *Sov. Powder Metall. Met. Ceram.*, 11, (1968) 839, Translated from Poroshkovaya Metall., 11(1) (1968).

[105] N. Dombrowski and P. C. Hooper, "The Effect of Ambient Density on Drop Formation in Sprays", Chem. Eng. Sci., V17, 1962, p.291.

[106] J. Szekely and N. J. Themelis, Rate Phenomena in Process Metallurgy, John Wiley and Sons (1971) 97.

[107] H. C. Lewis, D. G. Edwards, M. J. Goglia, R. I. Rice and W. L. Smith, *Ind. Eng. Chem.* 40 (1948) pp. 67-75.

[108] S. Nukiyama and Y. Tanasawa, *Trans. Soc. Mech. Engrs.*, 4 (14) (1938) 86.

[109] M. D. Bitron, *Ind. Eng. Chem.*, 47 (1) (1955) 23.

[110] H. Lubanska, *Journal of Metals*, 1970, Vol. 22, pp. 45-49.

[111] R. J. Grandzol and J. A. Tallmadge, *Int. J. of Powder Metall. Powder Tech.*, 11 (2) (1975) 103.

[112] K. Y Kim and W. R. Marshall, *AICHE Journal*, 17 (3) (1971) 575.

[113] J. Szekely, "Fluid Flow Phenomena in Metals Processing," Academic Press, NY, (1979) 261.

[114] "Aluminum: Properties, Physical Metallurgy and Phase Diagram," Kent R. Van Horn, ed., American Society for Metals, Metals Park, Ohio, 1967,

[115] J. E. Hatch, Aluminum, Properties and Physical Metallurgy, ASM, Metals Park, (1984).

[116] D. Altenpohl, "Aluminum Viewed From Within," Aluminum-Verlag, Dusseldorf, (1982).

[117] R. J. Towner: "Development of Aluminum Base Alloys", Annual Progress Report, Sept. 1961 - Sept. 1962. Project No. 593-32-004, Contract No. DA-36-034-ORD-355RD, Oct. 1962, DDC, Alexandria, VA.

[118] E. J. Lavernia, B. Poggiali, I. S. Servi, J. P. Clark, F. E. Katrak and N. J. Grant., *The international Journal of Powder Metallurgy*, Vol 23, No.1, 1987.

[119] X. Duan, T. Ando, and N. J. Grant, "Processing of a Modified 2024 Plus 2 wt% Fe and 2 wt% Ni Aluminum Alloy by Liquid Dynamic Compaction," Advances in Powder Metallurgy, Vol. 6, Aerospace, Refractory and Advanced Materials, 1991, (Proc. of the 1991 Powder Metall. Conf. and Exhibition, Chicago, IL, June 9-12, 1991), p.75.

[120] X. Duan, Y. Hao, M. Yoshida, T. Ando and N. J. Grant, submitted to *Int. J. of Powder Metallurgy* for Publication, Massachusetts Institute of Technology, Cambridge, MA 02139, 1992..

[121] R. E. Lewis, I. G. Palmer, J. C. Eckvall, I. F. Sakata and W. E. Quist: Proceedings of the Third Conference on Rapid Solidification Processing, R. Mehrabian, eds., National Bureau of Standards, Gaithersburg, MD, 1982, p. 613.

[122] P. R. Bridenbaugh, W. S. Cebulak, F. R. Billman, and G. H. Hildeman, *Light Metal Age*, October 1985, Vol. 43, No. 9/10, p.18.

[123] B. Chalmers, "Physical Metallurgy" 2nd edition, John Wiley and Son, 1962.

[124] G. H. Narayanan, W. E. Quist, B. L. Wilson and A. L. Wingert; "Low Density Aluminum Alloy Development," First Interim technical report, AFWAL, Contract No. F.33615-81-C-5053, Jan.-June 1982

[125] K. K. Sankaran, and N. J. Grant, *Mater. Sci. and Eng.* 44, (1980) pp.213-227.

[126] W. E. Quist, G. H. Narayanan, and A. L. Wingert, "Aluminum-Lithium Alloys for Aircraft Structure - An Overview," Aluminum-Lithium Alloys II, T. H. Sanders, Jr. and E. A. Starke, Jr., eds., AIME, Warrendale, PA, (1984) pp. 313-334.

[127] A. M. Senia, *Iron Age*, August 1, (1983) pp.47-50.

[128] E. J. Lavernia and N. J. Grant, *Jour. of Mat. Sci.*, Vol. 22 (1987) pp. 1521-1529.

[129] T. W. Clyne, R. A. Ricks, and P. J. Goodhew, *International Journal of Rapid Solidification*, 1984-85, Vol. 1, pp. 85-101

[130] P. J. Meschter, J. K. Gregory, R. J. Lederich, J. E. O'Neal, E. J. Lavernia, and N. J. Grant., "Microstructure and Properties of Rapid Solidification Processed Auminum-High Lithium alloys." 4th International Aluminum-Lithium Conference, Paris, 10-12 June 1987

[131] R. E. Sanders Jr., S. F. Bauman, and H. C. Stumpf, "Aluminum Alloy - Physical and Mechanical Properties", Vol. 3, E. A. Starke and T. H. Sanders, Eds., EMAS, Warley, (1986), pp.1441-1485.

[132] P. A. Hollinshead and T. Sheppard, *Materials Science and Technology*, Vol.3, December 1987, p.1019-1024.

[133] R. E. Hanneman, "Aluminum Alloy - Physical and Mechanical Properties", Vol. 1, E. A. Starke and T. H. Sanders, Eds., EMAS, Warley, (1986), p.45-50

[134] P. Furrer, G. Hausch, *Metal Science*, Vol.13 (1979) pp.155-162.

[135] F. Gatto, G. Camona, M. Conserva and P. Fiorini, *Mat. Sci. Eng.*, 3 (1968/69) pp. 56-61

[136] G. Marchand, *Can. J. of Technol.*, 31 (1953) 15.

[137] V. I. Dobatkin and Ya. G. Grishkovets, *Metal. Sci. Heat Treat. Metals*, 7-8 (1966) p.628.

[138] P. M. B. Rodrigues and P. Furrer, "Aluminum Alloy - Physical and Mechanical Properties", Vol. 2, E. A. Starke and T. H. Sanders, Eds., EMAS, Warley, (1986), pp.827-841.

[139] J. M. Howe, *Metall.Trans. A*, Vol.17A, April 1986, p. 593

[140] Y. Liu, L. Delaey and J. P. Baekelandt, "Aluminum Alloy - Physical and Mechanical Properties", Vol. 1, E. A. Starke and T. H. Sanders, Eds., EMAS, Warley, (1986), p.247.

[141] X. Xia, *Scripta Metall. et Mat.*, Vol.28, (1993) pp.1213-1218

[142] H. D. Merchant, J. G. Morris and D. S. Hodgson, *Materials Characterization*, Vol. 25, (1990) p.339.

[143] P. R. Sperry, *Trans. ASM*, 50 (1958) p.589

[144] M. Firth and W.M. Williams, *Canadian Metall. Q.*, Vol.8, No.4 (1969) p.331

[145] B. Andersson, "Aluminum Alloy - Physical and Mechanical Properties", Vol. 2, E. A. Starke and T. H. Sanders, Eds., EMAS, Warley, (1986), p.799.

[146] F.J. Kedves, M. Hordos and F. Schuszter, *Phys. Stat. Sol.* (A) 38, (1976) K123

[147] M. Ueki, S. Horie and T. Nakamura, "Aluminum Alloy - Physical and Mechanical Properties", Vol. 1, E. A. Starke and T. H. Sanders, Eds., EMAS, Warley, (1986), p.419.

[148] F. J. Kedves, M. Hordos, and L. Gergely, *Solid State Commun.,* 11, 1067 (1972)

[149] L. Chen and J.G. Morris, *Scripta Metall.,* Vol. 18 (1984) p.1365

[150] O.S. Es-Said and J.G. Morris, "Aluminum Alloy - Physical and Mechanical Properties", Vol. 1, E. A. Starke and T. H. Sanders, Eds., EMAS, Warley, (1986), p.451.

[151] H. Hug, *Metall,* Vol. 9, (1955) p. 176.

[152] J. L. Murray, A. J. McAlister, R. J. Schaefer, L. A. Bendersky, F. S. Biancaniello, and D.L. Moffat, *Metall. Trans. A,* Vol. 18A, March 1987, p.385.

[153] F. A. Shunk, " Constitution of Binary Alloys", Second Supplement, (McGraw Hill, New York, 1969) p. 29.

[154] E. H. Dix and W. D. Keith, Trans. Am. Inst. Mining Met. Engrs., Inst. Metals Div., 1927, pp.315-333.

[155] E.Nes, S.E. Naess and R. Hoier, *Z. Metallkde,* Bd. 63 (1972) H.5, p.248

[156] P. R. Sperry, Transactions, American Institute of Mining and Metallurgical Engineers, Vol. 203, 1955, p. 145.

[157] L. Chen and J. G. Morris, *Scripta Metallurgica,* Vol.18, (1984) p.1365.

[158] A. Jansson, *Metall. Trans. A,* Vol. 23A, November 1992, p.2953

[159] Y. Zhang, T. Yamane, S. Saji and J. Takahashi, *J. of Mat. Sci.,* Vol. 28, (1993) p.3235

[160] D. Shechtman, I. Blech, D. Gratias and J. W. Cahn, *Phys. Rev. Lett.,* 53 (1984) 1951.

[161] Y.F. Cheng, V. Hansen, and J. Gjonnes, *J. Mater. Res.*, Vol. 7, No. 12, Dec 1992, p.3235

[162] G. Marchand, *J. Inst. Met.,* 73 (1946) 747.

[163] Little, K. and Hume-Rothery, W. *J. Inst. Metals*, 74: 521-524, 1948.

[164] K. Nagahama and I. Miki, *Trans. J. I. M.*, Vol. 15, (1974), p. 185-192.

[165] P. L. Morris and B. J. Duggan, *Metal Science*, Jan. 1978, p. 1-7.

[166] D. B. Goel, Proc. Seventh Intern. Conf. for Electron Microscopy, Vol. 2 (1970) 537.

[167] X. Meng and D. O. Northwood, *Metallography*, Vol.21, (1988) p.293

[168] P. L. Morris and B. J. Duggan, *Metal Science*, Vol.12, No.1, (1978) p.1

[169] R. Sandstrom, *Acta Met.,* 25 (1977) 897.

[170] R. Sandstrom, B. Lehtinen, Emmy Hedman, I. Groza and S. Karlsson, *J. of Mat. Sci.*, Vol 13 (1978) p.1229

[171] P. Furrer, J.M. Vitek and E. Shapiro, "Strength of Metals and Alloys" Vol.2, 5th Int. Conf. , Achen, W. Germany, 1979, Pergamon Press, p.1419

[172] K. Lintermanns and H. A. Kuhn, "Aluminum Alloy - Physical and Mechanical Properties", Vol. 1, E. A. Starke and T. H. Sanders, Eds., EMAS, Warley, (1986), p.529.

[173] E. Nes, *Acta Metallurgica*, Vol., 24, (1975) p. 391

[174] C. S. Smith, *Trans. Met. Soc.*, AIME., 175, (1948) 15 .

[175] M. P. Anderson, G. S. Grest, R. D. Doherty, K. Li and D. J. Srolovitz, *Scripta Met.*, 23(1989)753.

[176] M. Hillert, *Acta Metall.*, 36, 3177 (1988).

[177] H. S. L. Phillips, *Journal, Institute of Metals*, Vol. 68, (1942) p.47

[178] K. Fukada, M. Mizouchi and T. Kajiyama, "Aluminum Alloy - Physical and Mechanical Properties", Vol. 1, E. A. Starke and T. H. Sanders, Eds., EMAS, Warley, (1986), p.483.

[179] N. Raghunathan, M. A. Zaidi and T. Sheppard, *Mater. Sci. and Techn.*, Vol. 2, September 1986, p.938.

[180] I. G. Palmer, R. E. Lewis, and D. D. Crooks, "The Design and Mechanical Properties of Rapidly Solidified Al-Li-X Alloys," Aluminum Lithium Alloys, T. H. Sanders, Jr., and E. A. Starke, Jr., eds., AIME, Warrendale, PA (1981) 241

[181] E. A. Starke and G. Lutjering, "Cyclic Plastic Deformation and Microstructure," ASM Materials Science Seminar, Fatigue and Microstructure, St. Louis, MO, 14-15 Oct. 1978, 205-243

[182] L. M. Groot, L. Katgerman, K. Klienjan, "Rapid Solidification Processing of Aluminum Alloys", presented at the 7th International Light Metal Congress, Leoben-Vienna, 1981.

[183] L. Katgerman, F. J. Kievits, H. Klienjan and W. E. Zalm, "Rapid Solidification Processing of Aluminum Alloys", presented at the 4th Yugoslav Int. Symp. on Aluminum, Titograd 1982.

[184] H. Jones, "Rapid Solidification Processing: Principles and Technologies", R. Mehrabian et al, eds. Claitor's, Baton Rouge, LA, 1980, P.306.

[185] A. M. Sumner, *Metallurgia and Metal Forming*, Sept. 1973, 40,(9) p.300

[186] T. C. Rollason and J. W. Martin *J. Mat. Sci.*, Vol. 5, (1970) 127.

[187] G. Phragmen, *Journal, Institute of Metals*, Vol.77, (1950) p.489

[188] C. E. Miller, Unpublished Work of High Speed Photography Analysis of the LDC Process, Submitted to ALCOA Laboratories. 1994.

[189] B. Chalmers, *J. Aus. Inst. Met.*, 8, p. 225 (1962).

[190] S. M. Kaufman, *Intl J. of Powder Met.*, 8, (1972), pp. 183-190.

[191] H. Jones, *Aluminum*, Vol. 54 (No. 4), 1978, p. 274.

[192] K. F. Kobayashi, H. Kawaura and P. H. Shingu, "Aluminum Alloy - Physical and Mechanical Properties", Vol. 1, E. A. Starke and T. H. Sanders, Eds., EMAS, Warley, (1986), p.247.

[193] "Annual Book of ASTM Standard", ASM, Section 2, Volume 02.02, (1995) p.133.

[194] C. Suryanarayana, S. F. H. Froes, S. Krishnamurthy and Y. Kim; *Int. J. Powder Metall.*, 26 (2) (1990) 117